Nikos E. Mastorakis Imre J. Rudas Yuriy S. Shmaliy *Editors* 

# Computational Problems in Science and Engineering II



### Computational Problems in Science and Engineering II

Nikos E. Mastorakis • Imre J. Rudas • Yuriy S. Shmaliy Editors

# Computational Problems in Science and Engineering II



Editors Nikos E. Mastorakis Technical University of Sofia Sofia, Bulgaria

Yuriy S. Shmaliy Universidad de Guanajuato Guanajuato, Mexico Imre J. Rudas Óbuda University Budapest, Hungary

ISBN 978-3-031-78415-6 ISBN 978-3-031-78416-3 (eBook) https://doi.org/10.1007/978-3-031-78416-3

© The Editor(s) (if applicable) and The Author(s), under exclusive license to Springer Nature Switzerland AG 2025

This work is subject to copyright. All rights are solely and exclusively licensed by the Publisher, whether the whole or part of the material is concerned, specifically the rights of translation, reprinting, reuse of illustrations, recitation, broadcasting, reproduction on microfilms or in any other physical way, and transmission or information storage and retrieval, electronic adaptation, computer software, or by similar or dissimilar methodology now known or hereafter developed.

The use of general descriptive names, registered names, trademarks, service marks, etc. in this publication does not imply, even in the absence of a specific statement, that such names are exempt from the relevant protective laws and regulations and therefore free for general use.

The publisher, the authors and the editors are safe to assume that the advice and information in this book are believed to be true and accurate at the date of publication. Neither the publisher nor the authors or the editors give a warranty, expressed or implied, with respect to the material contained herein or for any errors or omissions that may have been made. The publisher remains neutral with regard to jurisdictional claims in published maps and institutional affiliations.

This Springer imprint is published by the registered company Springer Nature Switzerland AG The registered company address is: Gewerbestrasse 11, 6330 Cham, Switzerland

If disposing of this product, please recycle the paper.

#### **Preface**

This book provides readers with modern computational techniques for solving a variety of problems from electrical, mechanical, civil, and chemical engineering. Mathematical methods are presented in a unified manner, so they can be applied consistently to problems in computational algebra, clustering metrics, scientific computing, image processing, composite materials, energy, environmental engineering, biomedical engineering, signal processing, automatic control, and more.

Sofia, Bulgaria Budapest, Hungary Guanajuato, Mexico Nikos E. Mastorakis Imre J. Rudas Yuriy S. Shmaliy

#### **About the Book**

This book features contributions from distinguished researchers on significant aspects of current numerical methods and computational mathematics. It presents actual results and innovative methods that provide numerical solutions, while minimizing computing times. It includes new and advanced methods and modern variations of known techniques that can solve difficult scientific problems efficiently.

#### **Contents**

1	Investigation of Low-Frequency Acoustic NDE to Detect Delaminations in Multilayer Polymer-Composite Structures S. Shevtsov, V. Chebanenko, and N. Snezhina	1
2	2-Normed Groups: Unraveling Computational Properties of 2-Norms	17
3	Bile Acid Loss Syndrome Screening: A Protocol Using Pooled Samples  João P. Martins, Miguel Felgueiras, Rui Santos, and Manuela Amorim	33
4	A Novel Enhancement for the Best Master Clock Algorithm Associated with the Precision Time Protocol for the Fractional Gaussian Noise Case Monika Pinchas	41
5	Designing an Efficient Solar Photovoltaic Tracking System for Sustainable Electricity Generation	51
6	<b>Toward Geometric Interpretation of Generalized Frequency</b>	71
7	Cluster Metric Sensitivity to Irrelevant Features	85
8	Orthogonal Geometry on Generalized Frequencies Yuichi Hasegawa and Kota Horizumi	97
9	A Hybrid Probabilistic –Fuzzy Programming for Integrated Production Planning and Raw Material Procurement in Post-Pandemic Time	113

x Contents

<b>10</b>	Curve Identification and Digitization for the Reconstruction	
	of Ship Hulls from 2D Drawings	129
	Argiris I. Delis, Ioannis K. Nikolos, Eleftherios S. Zografos,	
	Charilaos S. Zografos, Sotirios S. Sarakinos,	
	Alexandros N. Konstantinis, Petros Manousis,	
	and Dimitra N. Pochani	
11	Multiple Subset Problem as an Encryption Scheme for	
	Communication	147
	Yair Zadok, Nadav Voloch, Noa Voloch-Bloch, and Maor Meir Hajaj	
12	State Feedback Controller of a Self-Balancing Bicycle	157
	I. I. Siller-alcalá, J. U. Liceaga-Castro, R. A. Alcántara-ramírez,	
	and S. Calzadilla-Ayala	
Ind	ex	175
mu	<u>VA</u>	1/3

# Chapter 1 Investigation of Low-Frequency Acoustic NDE to Detect Delaminations in Multilayer Polymer-Composite Structures



S. Shevtsov, V. Chebanenko, and N. Snezhina

#### 1.1 Introduction

The growing use of reinforced polymer composites in industries such as the production of aircraft, ships, and cars requires guaranteed quality and strength reliability of manufactured defect-free structures, especially those experiencing high cyclic loads. One of the necessary conditions for this is the use of means for identifying and localizing possible defects that occur during the production process and are not fixed by visual inspection. Problems and achievements in the development of such means are considered in detail in review articles [1-3]. The experience gained by the world's leading manufacturers of composite structures shows that the most common defects are separation of adjacent layers inside composite laminates, which are formed during cure due to the presence of residual air or evaporation of volatile substances contained in the resin [4–11], peel-up and push-down delaminations at the entry and exit of the tool when drilling holes and at the edges of the composite part [1, 6, 12–16], as well as internal defects resulting from accidental low-velocity impacts when moving the finished structure [6, 13, 17– 19]. The negative effect of such defects on the characteristics of both short-term and long-term fatigue strengths of composite structures was already established in early works [20, 21], studied in detail in later works [2, 3, 22, 23], which substantiate the development of new methods of non-destructive diagnostics, the list of which currently includes methods based on the analysis of natural vibration modes of the defected structures [6, 10, 24, 25], the use of acoustic emission [1, 13, 26], shadow

Composite Materials and Structures Lab, Federal Research Center "Southern Scientific Center of the Russian Academy of Sciences", Rostov-on-Don, Russia

Department of Aircraft Engineering, Don State Technical University, Rostov-on-Don, Russia

S. Shevtsov (⋈) · V. Chebanenko

N. Snezhina

moire interferometry, infrared, radiographic, microwaves, and X-rays tomography [1, 7, 27], and the most common types of acoustic methods in practice, discussed below.

In the first works devoted to the use of acoustic vibrations for diagnosing, localizing, and estimating the size of delaminations, a modal analysis of samples of a beam configuration [4, 7, 22, 25] and flat rectangular plates was performed [5, 23, 28].

More recent studies using the propagation of selected Lamb waves modes in beams [8] ( $A_0$  and  $S_0$  modes) [17] ( $S_0$  mode) [18] ( $SH_0$  mode) and plates [14] ( $SH_0$  mode) have demonstrated significantly higher sensitivity and resolution due to the use of the characteristics of the reflected wave [8, 14], the time of flight of the wave through the section of the plate with delamination [17, 18]. The experiments in these works were carried out using plate-like or angle beam wedge piezoelectric transmitters and receivers placed in optimal positions on the sample surface. Due to the fact that their application is impossible on real composite structures with complex surface curvature, new designs of non-contact sensors, and actuators are being developed. In particular, these are integrated piezoelectric plate active sensors (PWAS) [15, 29], embedded sensor networks [30, 31], microfiber composite (MFC) sensors [32], multichannel MEMS sensor arrays [33], conventional broadband laser Doppler vibrometers [15, 33], and the scanning ones (SLDV) [10, 31]. They can be used effectively with non-contact air-coupled (ACT) [19, 34] and vacuum actuated [33], Lamb wave sources.

Simultaneously with the development of experimental methods aimed at increasing the sensitivity, accuracy, and reliability of methods for identifying the parameters of defects such as delaminations in composites, their digital twins are being improved—methods for analytical and numerical, most often, finite element (FE) modeling of acoustic wave propagation processes in layered composites with defects, presented in works [2, 22, 31, 35, 36]. These achievements have become the basis for the analysis and improvement of acoustic methods for non-destructive testing of layered composites with different structural anisotropy: quasi-isotropic [18, 35], transversely isotropic [11, 27, 31, 33], orthotropic materials [13, 19], cross-ply laminates [10, 17, 36], and different types of wave attenuation [29, 37–39]. The experimental and theoretical parts of the work contain a study of a symmetrical balanced eight-layer carbon fiber reinforced plastic (CFRP) laminate laid out according to the scheme [-45°,45°,90°,0°]<sub>S</sub>, which have a transversal isotropy and material elastic and damping characteristics borrowed from Refs. [38, 40].

It should be noted that in all of the above-mentioned works that model the acoustic diagnostics of delaminations, their geometry is presented in the form of thin, almost flat, rectangular prisms. This makes solving the problem much easier, but in practice, such delaminations never arise. Assuming that the presented material will be of interest to specialists in the field of polymeric composite manufacturing, we will focus our attention on the study of the possibility of diagnosing lenticular delaminations, which most often occur during the manufacture of polymer composites with layered reinforcement. This required the use of a numerical approach,

which consisted of solving the transient problem of acoustic wave propagation in a defective plate using the finite element method. The developed technique should not require time-consuming experiments and computer simulations to obtain a large amount of baseline data on the acoustic characteristics of each newly manufactured defect-free composite structure.

Focusing on the target consumer of the presented technique in the manufacture of aircraft composite structures led to the abandonment of complex testing equipment, the choice of a simple Doppler laser vibrometer for recording acoustic propagation, and the choice of the low-frequency range of excited waves, which make it possible to reliably detect and localize delaminations of the accepted size with low-noisy measurement results. Below are the results of an experimental and complementary numerical study of the propagation of wave packets with a carrier frequency of 10 kHz in a flat carbon fiber plate with artificially created delaminations.

This article is organized as follows. In Sect. 1.2, we describe the research object, a carbon fiber (CFRP) panel with embedded artificial defects. The results presented in Sect. 1.3 allow us to reasonably select the mode of excited waves at the available carrier frequency. The description of the FE model and its simulation method presented in Sect. 1.4 demonstrates the design of the model geometry, choice of the governing equations, solvers, and post-processing capabilities. A comparison of the results of FE simulations and experiments, as well as the applicability of the method in production conditions, is given in Sect. 1.5. Section 1.6 contains the summary of the results obtained during the study, an assessment of their reliability, and the possibility of use in composite production practice.

#### 1.2 Experiment

The object of the study was laid out according to the scheme  $[-45^{\circ},45^{\circ},90^{\circ},0^{\circ}]_{S}$  is an eight-layer square CFRP panel with side dimensions of  $62 \times 62$  cm and a thickness of 2 mm. Along the diagonals of the square at a distance of 22 cm from the center of their intersection, lenticular delaminations with a diameter of 15 and 30 mm, and a maximum thickness of 0.1 and 0.3 mm, were created. A porous absorber of reflected waves is laid along the perimeter of the plate (see Fig. 1.1a, b). All elastic properties of the CFRP laminate were determined experimentally according to the requirements of ASTM standards and the numerical refinements presented in Ref. [40]. Their values are collected in Table 1.1.

Due to the fact that the real range of propagation of Lamb waves is limited by geometric and material attenuation, the Rayleigh damping model was used in the calculations. The values of the Rayleigh damping parameters, mass damping  $\alpha_{dM}$  and stiffness damping  $\alpha_{dK}$ , were borrowed from Ref. [38].

The influence of waves reflected from the edges of the panel was reduced by using the exponentially increasing dependence of the coefficients  $\alpha_{dM}$  and  $\alpha_{dK}$  at a distance of more than 30 cm from the center of the panel.

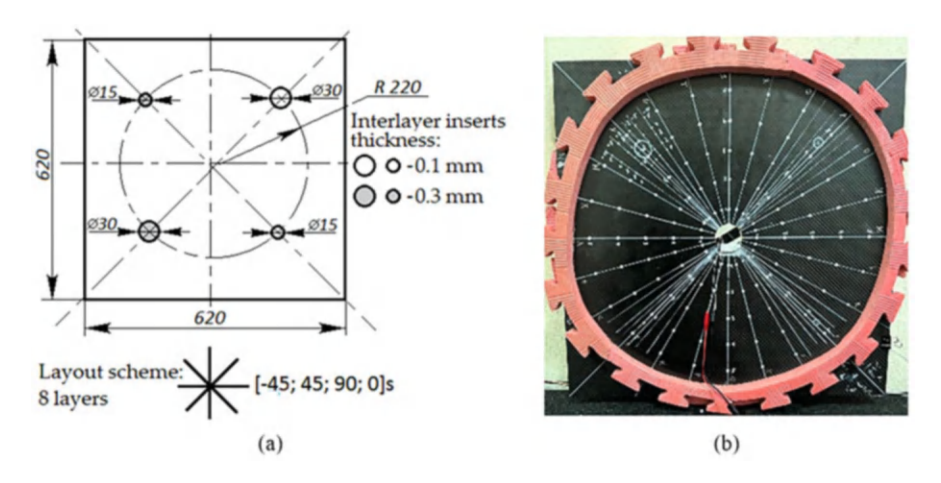


Fig. 1.1 CFRP panel under study: (a) scheme with dimensions and (b) photo of the manufactured panel

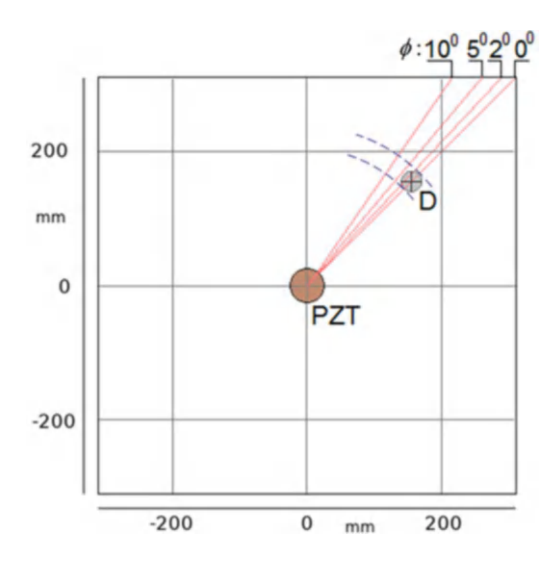
**Table 1.1** Mechanical properties of CFRP material

In-plane Young's moduli $E_x$ , $E_y$	44 GPa
Transversal Young's modulus $E_z$	12 GPa
In-plane shear modulus $G_{xy}$	24 GPa
Interlaminar shear moduli $G_{xz}$ , $G_{yz}$	4.8 GPa
Poisson's ratio v <sub>xy</sub>	0.14
Poisson's ratios $v_{xz}$ , $v_{yz}$ ,	0.26
Mass density ρ	1500 kg/m <sup>3</sup>

The wave packets in the test panel were formed using a STEMINC SMD50T21F45R omnidirectional tablet-like piezoelectric transducer with a diameter of 50 mm and a thickness of 2.1 mm, which was installed in the center of the panel. The control signal was generated by a RIGOL DG1022 signal generator and amplified by Apex Microtechnology PA94 piezo drivers. The out-of-plane velocity field on the panel surface during the propagation of Lamb waves was sensed by a Polytec PDV 100 laser vibrometer with a measuring laser spot diameter of 2 mm. The vibrometer signals were processed by a LeCroy 422 WaveSurfer digital oscilloscope, capable of averaging and finding the maximum absolute value of the recorded out-of-plane velocity when the wave packet passed through the observed surface areas. Further processing of the saved observation sessions was carried out by the MATLAB scripts.

The values of the out-of-plane vibration velocity on the surface of a studied square panel were monitored along the lines passing through its center at different angles to the diagonals near artificially created delaminations (see Fig. 1.2). However, due to the limited capabilities of the laser vibrometer used, these measurements were performed on a discrete set of points lying on these lines with subsequent smoothing of the results along the measurement trajectories and inside the surface area surrounding the delamination.

Fig. 1.2 Vibration velocity monitoring zone of Lamb waves propagating in the vicinity of panel delamination



#### 1.3 Dispersion Analysis of Lamb Waves Propagation

The calculation of dispersion dependences was carried out for a flat plate of constant thickness from a homogeneous anisotropic ideally elastic material using the Christoffel equation according to the technique presented in Ref. [41]. As a result, the dispersion dependences of phase velocities c and wavelengths  $\lambda$ , defined as  $\lambda = c/f$ , where f is the carrier frequency of the wave packet, for antisymmetric A<sub>0</sub>, symmetric S<sub>0</sub> Lamb waves, and horizontally polarized shear waves SH<sub>0</sub> were determined. Their analysis clearly shows that the waves S<sub>0</sub> and SH<sub>0</sub> have wavelengths that are much larger than the dimensions of the delaminations existing in the panel, and therefore only A<sub>0</sub> waves excited at frequencies of at least 10 kHz, the length of which ~4 cm is comparable to the size of the delaminations, can be used for acoustic diagnostics. These dependencies obtained for different angles of deviation from the diagonal of a square plate practically coincide, which confirms the fact of the transversal isotropy of the panel material (see Fig. 1.3). The experimental and finite element (FE) simulation results presented in Fig. 1.3 show that even at the lowest frequency of 10 kHz, artificial delaminations existing in the rear panel and their virtual copies in the FE model can be reliably identified.

#### 1.4 The Finite Element Model of the Studied System

The model used a circular delamination shape that was as close as possible to the real one. To eliminate the defacement of the composite layers adjacent to delamination, its geometry was modeled in two stages. Initially, the generatrix of the upper surface

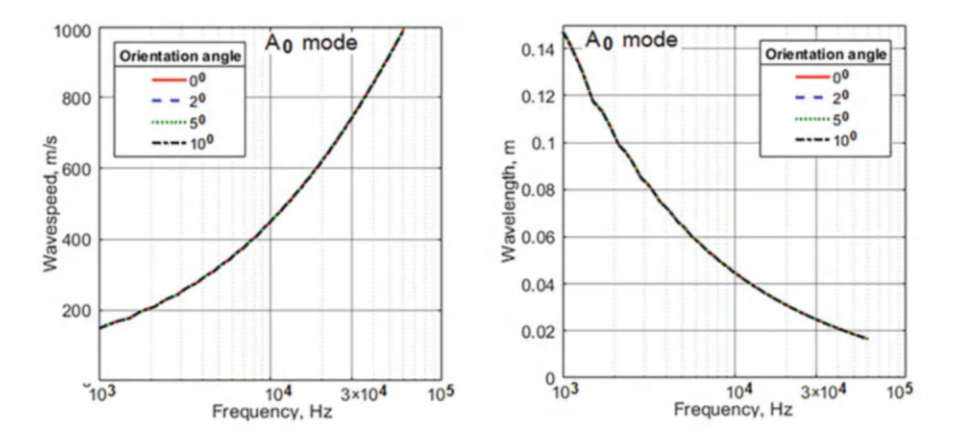


Fig. 1.3 The dispersion curves for phase velocities and wavelengths of A<sub>0</sub> Lamb wave mode in the studied CFRP panel

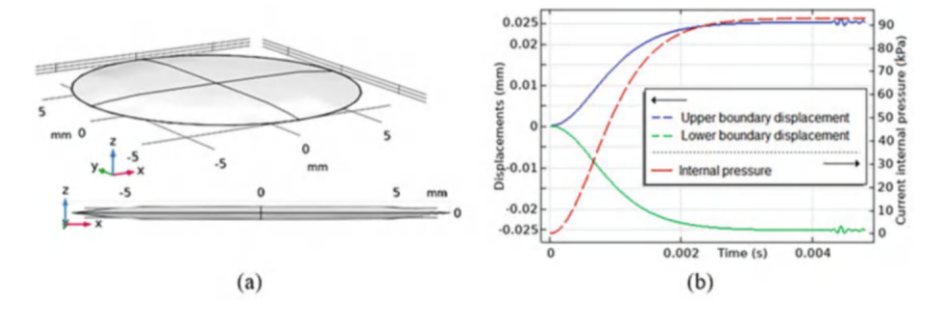
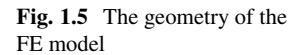


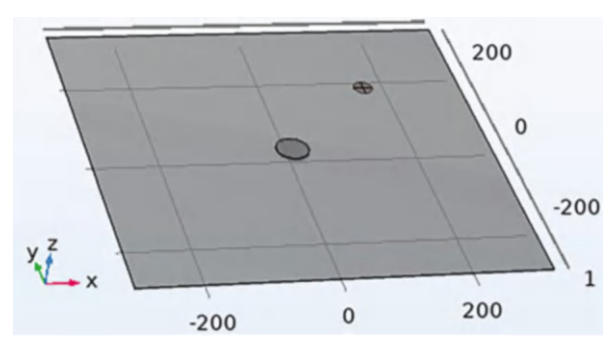
Fig. 1.4 The solid 3D model of a thin lenticular inclusion (a) and expansion of the delamination thickness during the application of internal pressure (b)

of the lenticular inclusion was combined from two parts: the dependences of the thickness coordinate on the radius according to the equations of the ellipse and the square of the hyperbolic tangent. Further, this generatrix and its reflection from the horizontal plane combined with it were used to construct a lenticular-shaped solid body. This solid body of the required diameter, but very small thickness (the range 0.02–0.05 mm), was placed between adjacent layers of the laminate and cut out from them using a Boolean operation (see Fig. 1.4a).

To achieve the required thickness of the delamination, a gradually increasing and then steady pressure was applied inside the thin empty inclusion, which deformed the walls bounding it, bending them outward. The plot of the internal pressure in the empty delamination, combined with the plot of the change in its thickness from the initial value of 0.05 mm to 0.1 mm, is shown in Fig. 1.4b. After stabilization of the delamination thickness to the desired value, acoustic waves were excited.

The simulation of the propagation of acoustic waves generated by a PZT disk placed in the center of the CFRP plate was carried out in the Comsol Multiphysics





v.6 finite element analysis (FEA) system using the coupled equations of the anisotropic linear elastic body dynamics and piezoelectricity. The geometry of the object of the FE modeling fully corresponded to its real prototype (see Fig. 1.5).

One simplifying assumption adopted in this study should be pointed out here. The composite plate under study consists of two layers that are in absolute contact over the entire area except for an empty cavity of a circular shape in plan, simulating delamination. Each of these layers is a balanced four-layer laminate, laid out according to the scheme shown in Fig. 1.1a. This scheme ensures that the same transversal isotropy is obtained not only for each of these layers but also for the entire assembled panel. This fact significantly simplifies the computational complexity of the delamination detecting and localization problem. Naturally, when delamination is formed between other, differently oriented laminas, the effect of delamination on the propagation of Lamb waves will be different, most likely more complex. However, in this article, we will limit ourselves to only the presented case.

The FE meshing took into account the specifics of the geometry of the modeled area, namely, the thinness of the panel, the presence of local delamination, and the area of contact between the panel and the disk piezoelectric transducer. To do this, a triangular meshing of increased density was created on the middle plane under the PZT disk and on the lower boundary of the empty inclusion (see Fig. 1.6). Further, as from a source, the created 2D mesh was extruded onto the upper and lower layers of the plate, creating four layers of prismatic elements on each.

The problem of modeling wave propagation in a defective composite plate was formulated and solved using the following Comsol modules:

 Solid Mechanics/Linear Elastic Material—simulation of processes in the anisotropic CFRP panel with delamination

$$\rho \partial^2 \mathbf{u} / \partial \mathbf{t}^2 = \nabla \cdot (\mathbf{C} : \nabla \mathbf{u})$$

where  $\rho$  is the density of the material, **u** is the displacement vector, and  $\mathbf{C} = \mathbf{C}(\mathbf{Y}, \nu, \mathbf{G})$  is the stiffness tensor, the components of which are functions of the elastic, shear moduli, and Poisson ratios. The Voigt notation (11, 22, 33, 23, 13, 12) was used in the model of the material;

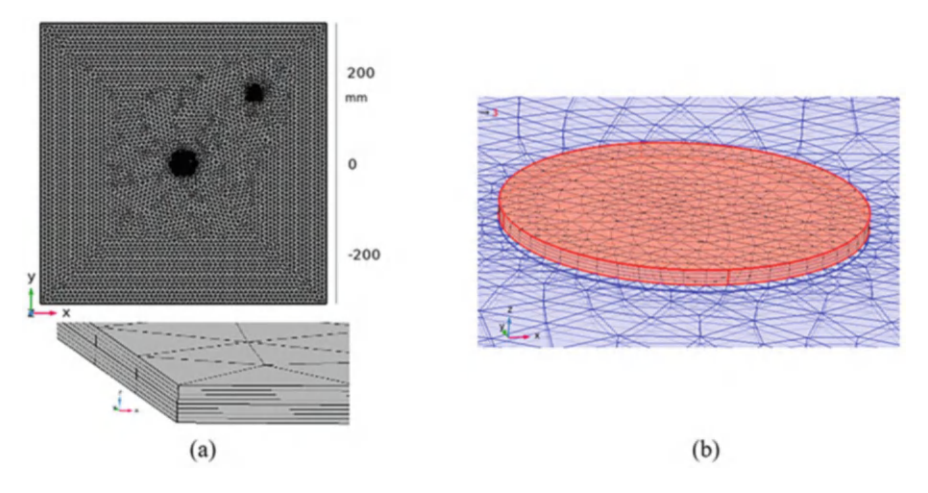


Fig. 1.6 FE meshing of the studied CFRP panel (a) and PZT transducer (b)

 Solid Mechanics/Piezoelectric Material (Stress-Charge form)—simulation of processes in a piezoelectric actuator

$$\begin{cases} \sigma = c_{\mathbf{E}}\varepsilon + e^{T}\mathbf{E} \\ \mathbf{D} = e\varepsilon + \varepsilon_{0,\text{vac}}\varepsilon_{r,\mathbf{S}}\mathbf{E} \end{cases}$$

where  $\sigma$  is the stress tensor,  $c_{\rm E}$  is the stiffness matrix, e is the coupling matrix,  $\varepsilon$  is the strain tensor,  $\varepsilon_{0,{\rm vac}}$  is the vacuum permittivity, and  $\varepsilon_{\rm r,S}$  is the piezoelectric relative permittivity matrix;

Electrostatics/Charge Conservation, Piezoelectric 1, which includes the conservation of electric charge

$$\nabla \cdot \mathbf{D} = \rho_{V}$$

and the relation between electric field  $\mathbf{E}$  and potential V

$$\mathbf{E} = -\nabla V,$$

where  $\rho_V$  is the volumetric electric charge density, as well as boundary conditions, including setting a variable control potential on the upper plane of the PZT disk (see Fig. 1.7) and grounding its lower plane;

Multiphysics/Piezoelectric Effect module, which couples the two previous modules. All material constants of the PZT-5H piezoelectric, including density, elasticity, coupling, permittivity matrices, and loss factor value, were imported from Comsol's database.

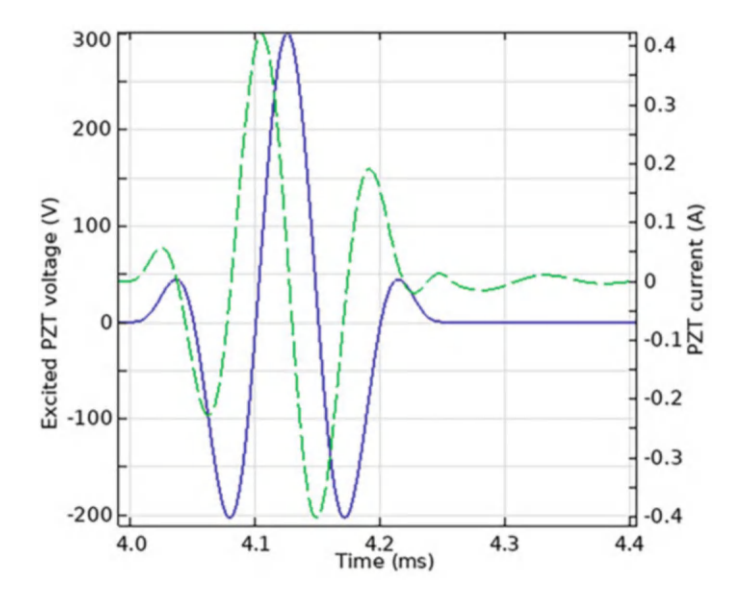


Fig. 1.7 Time dependence of the electric potential applied to the PZT actuator

Accounting for the inverse piezoelectric effect, that is, generation of voltages on the conductive planes of the disk, was provided by the adoption of the internal resistance of the voltage source equal to 60 Ohms.

All external boundaries of the modeled panel are assumed to be free, except four points at the vertices of the square, which prohibit rotations and displacements of the plate in its plane.

To take into account the presence of a porous absorber, the values of the Rayleigh attenuation parameters  $\alpha_{dM}$  and  $\alpha_{dK}$  increased exponentially with distance from the center of the disk exciter, starting from a distance of 27 cm.

When solving the transient problem of the wave packet propagation in a panel, the time integration step was chosen to be approximately 20 times smaller than the period of excited oscillations at the carrier frequency. This choice ensured stable convergence of the solution for all studied delamination sizes with variations in the carrier frequency and the number of waves in the tone burst.

Each session of process simulation, including the slow expansion of an empty inclusion to the required thickness and the subsequent launch of 3–5 wave packets, took about an hour of computation time when using a computer with an i7 processor. The saved spatiotemporal dependencies of out-of-plane displacements and velocities allowed us to easily analyze their distributions over the surface of the tested structure at each moment in time using post-processing tools.

#### 1.5 Numerical and Experimental Results

The FE tool has much more powerful imaging capabilities for presenting results than an experiment. So we start by discussing them. An example of the results of solving the problem of wave propagation in a defective plate is shown in Fig. 1.8, which shows the fields of out-of-plane displacements of panel points at two-time instances: before the wave reaches the defect zone and after it passes through the zone before the start of reflection from the boundaries of the plate. In both screenshots, displacement distortion above the delamination area is noticeable. This is a consequence of the fact that the out-of-plane displacement (bending) of the plate surface above the delamination significantly exceeds the wave displacements, the magnitude of which determined the permissible range of depicted displacements. In Fig. 1.8a, the attenuation of the wave amplitude is observed as it moves away from the exciter, and in Fig. 1.8b—the reverse propagation of reflected waves with significantly reduced amplitude.

Figure 1.9 clearly shows a significant increase in the out-of-plane velocities of wave  $A_0$ , as it passes over the defect, which confirms the possibility of experimental diagnostics of delamination using a laser vibrometer that measures the out-of-plane velocity on the vibrating surface. To quantify the effect of delamination on the  $A_0$  wave, a similar problem was solved for a defect-free panel. The time dependences of the vibration velocity amplitude shown in Fig. 1.10 for wave radial propagation lines  $\phi = 0^{\circ}$ ,  $2^{\circ}$ ,  $5^{\circ}$ ,  $10^{\circ}$  demonstrate that the initially increased wave amplitude decreases when the propagation line deviates from  $0^{\circ}$ , and at the angles of more than  $5^{\circ}$ , the character of the out-of-plane velocity is practically indistinguishable from that for a defect-free panel.

The selected surface elements, on which the vibration velocity was averaged at the selected time points, had a round shape corresponding to the shape of the existing delamination and were located on these radial lines at the same distance from the vibration source to eliminate the dependence of the vibration velocity on geometric and material attenuation.

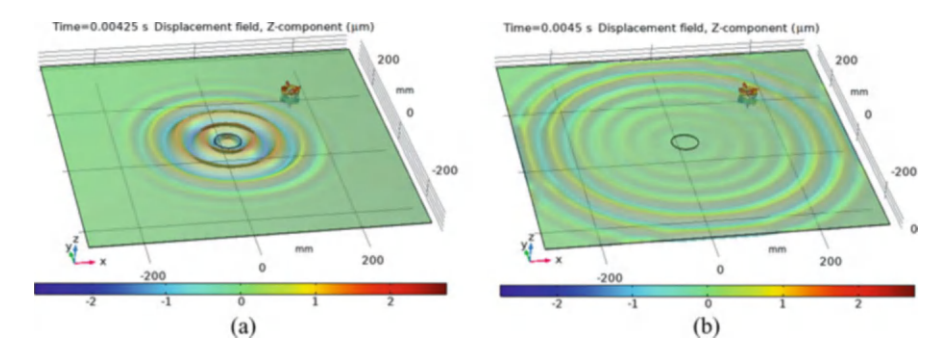


Fig. 1.8 The out-of-plane displacement field on the panel surface, fixed at two different points in time before (a) and after (b) wave reflection from the edge of the panel

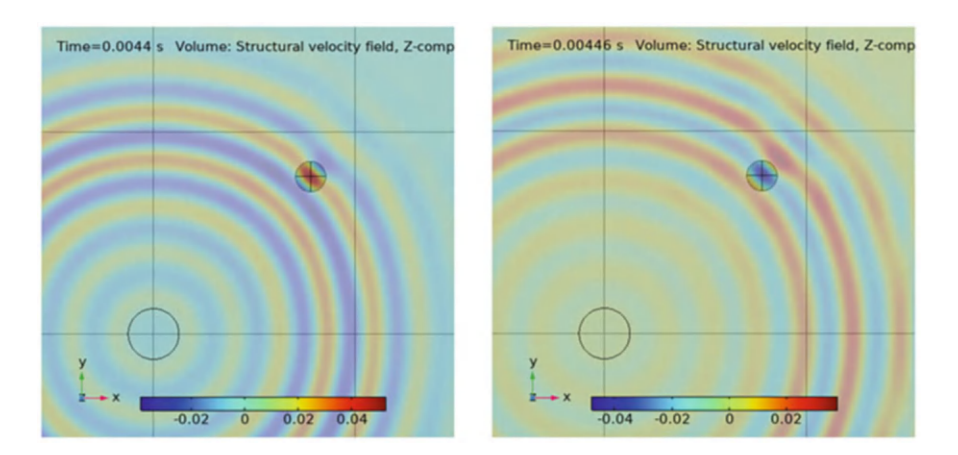


Fig. 1.9 The field of out-of-plane velocities of the panel surface, fixed at two different points in time

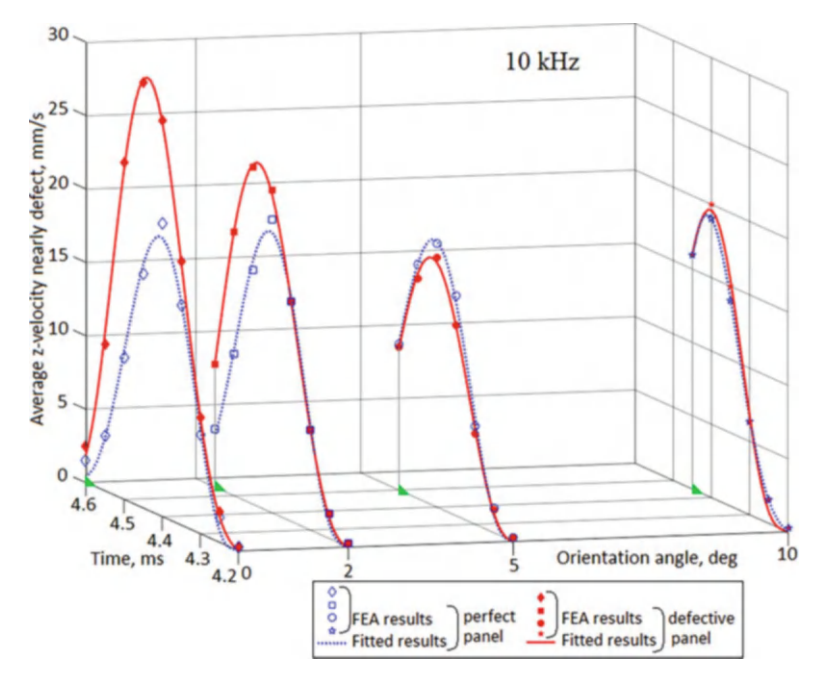


Fig. 1.10 Dependences of average out-of-plane velocities of Lamb waves A<sub>0</sub> passing through the analyzed areas of the surface on the orientation angles and propagation time of the tone burst

The capabilities of the Comsol FE system make it possible to analyze the evolution of the simulated processes in any area, including points, lines, and 2D and 3D areas at any time intervals. However, in real production conditions, it is difficult to use such sophisticated scientific equipment as a scanning laser vibrometer.

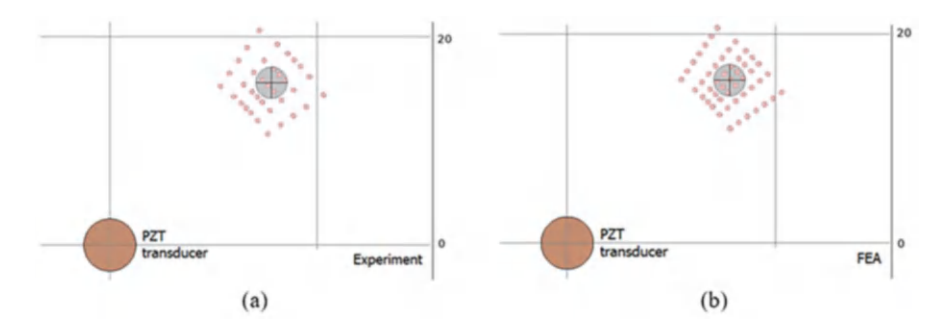


Fig. 1.11 Points on the panel surface to monitor the maximum out-of-plane velocities in experiments (a) and FEM (b)

Therefore, to compare the results of calculations with the experimental data on the out-of-plane vibrations velocity obtained at discrete points on the surface of the analyzed structure using the simple Doppler laser vibrometer, the modeled maximum vibration velocity values were calculated at the set of points shown in Fig. 1.11. Figure 1.12 shows both level lines map and 3D plots of the experimentally measured and FEM-calculated maximum modules of vibration velocity after their smoothing by the Curve Fitting tool (cftool MATLAB) using cubic interpolation. In the level line maps, the location of the delamination is indicated by a red circle.

Comparisons of the maps depicted in Fig. 1.12 show that there are some differences between the experimentally and numerically obtained, partly caused by the insufficient accuracy of pointing the spot of the laser vibrometer to the points of the panel surface. In addition, the position and diameter of the circle on the map of level lines in Fig. 1.12b are precisely specified for the FE model, while in Fig. 1.12a, the parameters of the circle (i.e., delamination) are not available for visual observation and correspond to the expected ones provided by the accuracy of introducing artificial delamination between the layers of the laminate. However, despite these differences, both distributions are qualitatively and quantitatively very similar. Thus, directly above the delamination, an increase in the wave amplitude by about 1.5 times is observed. Outside the circle denoting the delamination contour, there is some decrease in intensity and distortion of the wave propagation pattern.

Comparative analyses of the results presented in Figs. 1.10 and 1.12 show a significant local increase (more than 1.5 times) of the maximum amplitudes of out-of-plane vibration velocity in the zone of delamination location. This fact allows us to assert that the investigated method for detecting local delaminations, based on the generation of asymmetrical Lamb waves at low frequencies and measure of out-of-plane vibration velocity along the surface of a CFRP panel, can be used in production practice with appropriate excitation and measurement means.

It should, however, be noted that the use of the proposed method for diagnosing large-sized composite structures of complex 3D geometry requires the use of

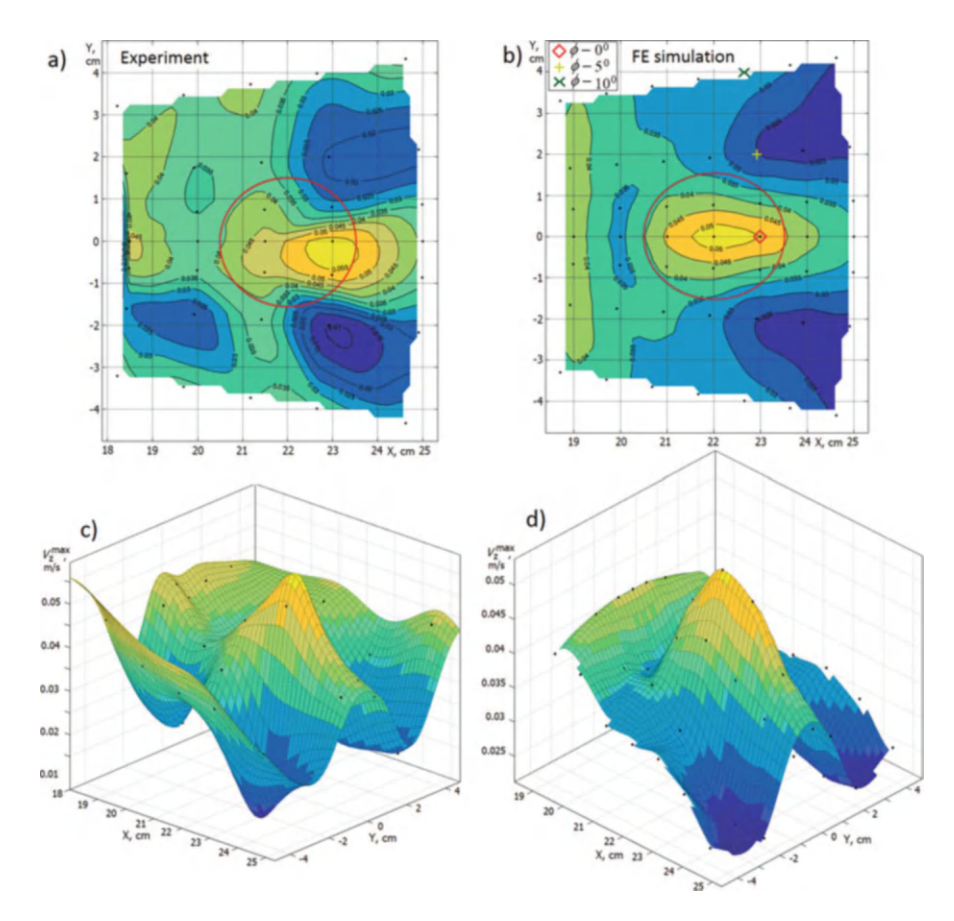


Fig. 1.12 Smoothed level lines maps (a, b) and 3D plots (c, d) of the experimentally measured (a, c) and FEM-calculated (b, d) maximum modules of vibration velocity on the panel surface area above the delamination location

advanced non-contact exciters of significant power, capable of generating waves of greater amplitude, thereby increasing the viewing area and reducing the overall time of monitoring the surface being inspected. In addition, an urgent technical problem is the development of effective methods for damping waves reflected from the edges of the structure under study and complicating the search for possible defects near such edges.

The next stage in improving and generalizing the results presented in the article will be the study of cases of the delaminations location between laminas with different fiber orientations at different distances from the surface available for study in structures with anisotropy more complex than transversal isotropy investigated here.

#### 1.6 Conclusions

The article presents the results of the proposed low-frequency acoustic NDE of layered composite structures to identify and localize possible delaminations. The object of theoretical and experimental studies was a flat square CFRP panel of constant thickness with transversal isotropy of the material, between the fourth and fifth layers of which thin round Teflon inclusions were introduced, imitating delamination. Dispersion analysis of phase velocities and wavelengths, performed using experimental data on the elastic moduli of the used symmetrical balanced laminate, showed the possibility of using only anisotropic Lamb waves  $A_0$  in the available frequency range. A finite element analysis of the propagation of waves generated by an omnidirectional piezoelectric transducer installed in the center of the panel made it possible to establish that the out-of-plane velocity amplitudes on its surface in the vicinity of the delamination increase up to 1.5 times. The possibility of detecting and localizing delaminations of the studied geometries and sizes was also proved using a simplified method for monitoring the velocities averaged over small areas of the surface, analyzed by a laser vibrometer. The experimental studies carried out confirmed the process regularities revealed numerically.

**Acknowledgments** The authors acknowledge the Russian Academy of Science that provides financial support for project No. AAAA–A16-116012610052-3 and the Joint Center for Scientific and Technological Equipment of SSC RAS No. 501994 for providing necessary equipment.

#### References

- J. Babu et al., Assessment of delamination in composite materials: A review. Proc. Inst. Mech. Eng. B J. Eng. Manuf. 230(11), 1990–2003 (2016)
- P. Chaupal, P. Rajendran, A review on recent developments in vibration-based damage identification methods for laminated composite structures: 2010–2022. Compos. Struct. 311, 116809 (2023)
- A. Ghavamian, F. Mustapha, B.H.T. Baharudin, N. Yidris, Detection, localisation and assessment of defects in pipes using guided wave techniques: A review. Sensors 18(12), 4470 (2018)
- G.C. Pardoen, Effect of delamination on the natural frequencies of composite laminates. J. Compos. Mater. 23(12), 1200–1215 (1989)
- A. Chattopadhyay, C. Nam, Y. Kim, Damage detection and vibration control of a delaminated smart composite plate. Adv. Compos. Lett. 9(1), 096369350000900101 (2000)
- 6. P. Tan, L. Tong, Delamination detection of composite beams using piezoelectric sensors with evenly distributed electrode strips. J. Compos. Mater. **38**(4), 321–352 (2004)
- B.O. Baba, R.F. Gibson, The vibration response of composite sandwich beam with delamination. Adv. Compos. Lett. 16(2), 096369350701600204 (2007)
- N. Hu, Y. Liu, Y. Li, X. Peng, B. Yan, Optimal excitation frequency of Lamb waves for delamination detection in CFRP laminates. J. Compos. Mater. 44(13), 1643–1663 (2010)
- Z. Li et al., Delamination detection in composite T-joints of wind turbine blades using microwaves. Adv. Compos. Lett. 25(4), 096369351602500401 (2016)
- A. Migot, V. Giurgiutiu, Numerical and experimental investigation of delamination severity estimation using local vibration techniques. J. Intell. Mater. Syst. Struct. 34(9), 1057–1072 (2023)

- E. J. Nabiswa, M. Chierichetti, Structural health monitoring of composite structures using guided Lamb waves, AIAA SciTech Forum, 2023, p. 1709
- V.H.C. De Albuquerque, J.M.R. Tavares, L.M. Durão, Evaluation of delamination damage on composite plates using an artificial neural network for the radiographic image analysis. J. Compos. Mater. 44(9), 1139–1159 (2010)
- T. Lorriot, H. Wargnier, J.C. Wahl, A. Proust, L. Lagunegrand, An experimental criterion to detect onset of delamination in real time. J. Compos. Mater. 48(18), 2175–2189 (2014)
- R. James, H. Mei, V. Giurgiutiu, SH-mode guided-wave impact damage detection in thick quasi-isotropic composites, in *Proc. SPIE Health Monitoring of Structural and Biological* Systems XIV, vol. 11381, (2020), pp. 84–101
- 15. A.N. Shpak et al., Influence of a delamination on Lamb wave excitation by a nearby piezoelectric transducer. J. Intell. Mater. Syst. Struct. **32**(3), 267–283 (2021)
- I. Zhilyaev, E. Chigrinets, S. Shevtsov, S. Chotchaeva, N. Snezhina, ANN-based estimation of the defect severity in the drilling of GFRP/Ti multilayered composite structure. J. Compos. Sci. 6(12), 370 (2022)
- C. Ramadas, A. Hood, J. Padiyar, K. Balasubramaniam, M. Joshi, Sizing of delamination using time-of-flight of the fundamental symmetric Lamb modes. J. Reinf. Plast. Compos. 30(10), 856–863 (2011)
- H. Mei, R. James, V. Giurgiutiu, Damage detection in laminated composites using pure SH guided wave excited by angle beam transducer, in *Proc. SPIE Health Monitoring of Structural* and Biological Systems XIV, vol. 11381, (2020), pp. 65–76
- H. Zhang, J. Sun, X. Rui, S. Liu, Delamination damage imaging method of CFRP composite laminate plates based on the sensitive guided wave mode. Compos. Struct. 306, 116571 (2023)
- C.T. Herakovich, On the relationship between engineering properties and delamination of composite materials. J. Compos. Mater. 15(4), 336–348 (1981)
- 21. A. Blythe, B. Fox, M. Nikzad, B. Eisenbart, B.X. Chai, Stiffness degradation under cyclic loading using three-point bending of hybridised carbon/glass fibres with a polyamide 6, 6 nanofibre interlayer. J. Compos. Sci. 6(9), 270 (2022)
- O.K. Ihesiulor, K. Shankar, Z. Zhang, T. Ray, Validation of algorithms for delamination detection in composite structures using experimental data. J. Compos. Mater. 48(8), 969–983 (2014)
- A. Muc, Computational and variational formulations of unilateral problems for structures made of composite materials (Laminates, Functionally Graded Materials). WSEAS Trans. Appl. Theor. Mech. 17, 118–123 (2022)
- L.H. Yam, Z. Wei, L. Cheng, Nondestructive detection of internal delamination by vibrationbased method for composite plates. J. Compos. Mater. 38(24), 2183–2198 (2004)
- 25. P. Tan, L. Tong, Experimental and analytical identification of a delamination using isolated PZT sensor and actuator patches. J. Compos. Mater. **41**(4), 477–492 (2007)
- J. Yousefi, R. Mohamadi, M. Saeedifar, M. Ahmadi, H. Hosseini-Toudeshky, Delamination characterization in composite laminates using acoustic emission features, micro visualization and finite element modeling. J. Compos. Mater. 50(22), 3133–3145 (2016)
- Z. Su, L. Ye, Selective generation of Lamb wave modes and their propagation characteristics in defective composite laminates. Proc. Inst. Mech. Eng. L. J. Mater. Des. Appl. 218(2), 95–110 (2004)
- X. Zhang, X. Yin, W. Li, J. Lv, H. Zhang, Delamination detection on composite laminates using the modal displacement unevenness coefficient. J. Compos. Mater. 56(28), 4329–4338 (2022)
- M. Gresil, V. Giurgiutiu, Prediction of attenuated guided waves propagation in carbon fiber composites using Rayleigh damping model. J. Intell. Mater. Syst. Struct. 26(16), 2151–2169 (2015)
- V. Giurgiutiu, A. Cuc, Embedded non-destructive evaluation for structural health monitoring, damage detection, and failure prevention. Shock Vib Dig 37(2), 83 (2005)
- 31. J.C.P. Allen, C.T. Ng, Damage detection in composite laminates using nonlinear guided wave mixing. Compos. Struct. **311**, 116805 (2023)

 A.H. Daraji, J. Ye, J.M. Hale, Optimisation of active SHM system based on optimal number and placement of piezoelectric transducers. J. Intell. Mater. Syst. Struct. 34(4), 425–439 (2023)

- 33. A.W.F. Volker et al., Non-contact MEMS-sensor array inspection of composites and metallic parts using Lamb waves. J. Nondestr. Eval. Diagn. Progn. Eng. Syst. 6(4), 041002 (2023)
- T. Wandowski, D. Mindykowski, P. Kudela, M. Radzienski, Analysis of air-coupled transducerbased elastic waves generation in CFRP plates. Sensors 21(21), 7134 (2021)
- X. Zeng et al., Lamb wave-based damage localization and quantification algorithms for CFRP composite structures. Compos. Struct. 295, 115849 (2022)
- Y. Yu, X. Liu, Y. Wang, Y. Wang, X. Qing, Lamb wave-based damage imaging of CFRP composite structures using autoencoder and delay-and-sum. Compos. Struct. 303, 116263 (2023)
- 37. C. Ramadas, Three-dimensional modeling of Lamb wave attenuation due to material and geometry in composite laminates. J. Reinf. Plast. Compos. **33**(9), 824–835 (2014)
- 38. S. Shevtsov et al., On the directivity of Lamb waves generated by wedge PZT actuator in thin CFRP panel. Materials **13**(4), 907 (2020)
- T. Mace, J. Taylor, C.W. Schwingshackl, Measurement of the principal damping components of composite laminates. Compos. Struct. 302, 116199 (2022)
- 40. L. Chinchan, S. Shevtsov, A. Soloviev, V. Shevtsova, J.P. Huang, Mechanical testing of polymeric composites for aircraft applications: Standards, requirements and limitations, in Advanced Materials: Physics, Mechanics and Applications, (Springer, 2014), pp. 201–222
- 41. J.L. Rose, Ultrasonic Guided Waves in Solid Media (University Press, Cambridge, 2014)

## Chapter 2 2-Normed Groups: Unraveling Computational Properties of 2-Norms



Alireza Pourmoslemi, Tahere Nazari, and Mehdi Salimi

#### 2.1 Introduction

Generalization of normed linear spaces is one of the most remarkable topics of modern mathematics. For many years, mathematicians have tried to generalize these spaces. The first attempt was to introduce K-normed spaces in 1937 [1]. The concept of 2-metrics was introduced in 1963 [2], and following the path, 2-normed spaces are investigated as a proper generalization of normed linear spaces [3]. The notion of *n*-metrics and *n*-norms are introduced in 1969 [4–6]. In the same year, investigating convergence of sequences in 2-normed spaces, the term 2-Banach spaces was appeared in a doctoral dissertation entitled 2-*Banach Spaces* [7, 8]. For more on 2-normed spaces in the 1980s and 1990s, see [9–13]. Recently, many mathematicians have turned their attention to the theory of 2-normed spaces, and significant results, including *fixed point theory* [14–18], *approximate and linear mapping* [19–23], 2-inner product spaces [24–27], and probabilistic normed spaces [28–30] (for more details about probabilistic 2-normed spaces see [31], chapter 11) have been investigated in this regard.

**Definition 1** Let V be a vector space over the field  $\mathbb{R}$  with dimension  $\geq 2$  and let

$$||\cdot,\cdot||:V\times V\to\mathbb{R}^+\cup\{0\}$$

be a function satisfying the following properties:

A. Pourmoslemi · T. Nazari

Department of Mathematics, Payame Noor University, Tehran, Iran

e-mail: a\_pourmoslemy@pnu.ac.ir

M. Salimi (⊠)

Mathematics Department, Kwantlen Polytechnic University, Surrey, BC, Canada

e-mail: mehdi.salimi@kpu.ca

18 A. Pourmoslemi et al.

1.  $||u, v|| \ge 0$  for all  $u, v \in V$  and ||u, v|| = 0, if and only if u and v are linearly dependent.

- 2. ||u, v|| = ||v, u|| for all  $u, v \in V$ .
- 3.  $\|\alpha u, v\| = |\alpha| \|u, v\|$ , for all  $u, v \in V$  and  $\alpha \in \mathbb{R}$ .
- 4.  $||u, v + s|| \le ||u, v|| + ||u, s||$ , for all  $u, v, s \in V$ .

Then the function  $||\cdot,\cdot||$  is called a 2-norm over V, and the pair  $(V,\|\cdot,\cdot\|)$  will be called a 2-normed space.

In this chapter, we tend to define 2-norms on groups. Normed groups that are in fact groups with a right-invariant metric and are subject to topological groups have recently received attentions. Since their inception in the 1930s through the Birkhoff-Kakutani theorem, the results derived from these concepts have not garnered significant attention, leading to a limited body of work. Nevertheless, there is a current resurgence of interest among researchers, particularly in areas such as probabilistic normed groups [32–34]. The recent focus in [35] has inspired scholars to explore the application of analytical principles within algebraic structures, notably groups. Moreover, the recent attention sparked by the definition of Inner Product Groups has prompted a reevaluation of the concept. Inner product groups, which are abelian groups equipped with an inner product, have been the subject of investigation, particularly in the context of quantum mechanics and representation theory [36]. In our investigation, we delved into 2-norms on groups with the aim of highlighting the significance of prioritizing 2-normed groups within the category of 2-normed spaces. Given the incomplete and fragmented study of the analytical characteristics of these groups, normed groups were selected as the foundational algebraic structures for the reconstitution of the analytical attributes of 2-normed vector spaces.

In 1936, a notable theorem was established:

A Hausdorff group G is homeomorphic with a metric space if and only if G adheres to the first countability axiom.

Additionally, it is demonstrated that such a group possesses a right-invariant metric. This theorem is recognized as Birkhoff-Kakutani's metrization theorem for groups, as referenced in [37] and [38]. An essential concept in the study of semigroups is the characterization of metrics, where a metric d on a semigroup G is termed left-invariant if d(gx, gy) = d(x, y) and right-invariant if d(xg, yg) = d(x, y) for all  $g, x, y \in G$ . When a metric satisfies both conditions, it is referred to as invariant. In 1950, invariant metrics on groups were examined to address a problem posed by Banach [39]. This chapter focuses on norms within groups closely associated with those possessing invariant metrics, which have recently gained significance in the realm of topological groups [40–42]. Some scholars interchangeably use the term "length function" instead of "norm" for groups [43–45]. We start with some notions that will be needed in this chapter. First, we define the notion of 2-metric groups and related concepts, with respect to the definition of 2-metric spaces [2, 3] as follows:

**Definition 2** ([3]) Let  $\mathcal{L}$  be a group and let a real-valued mapping d on  $\mathcal{L} \times \mathcal{L} \times \mathcal{L}$  satisfying the following conditions:

1. For each pair of distinct elements v, s in  $\mathcal{L}$ , there exists an element t in  $\mathcal{L}$  such that  $d(v, s, t) \neq 0$ .

- 2. If at least two of  $v, s, t \in \mathcal{L}$  are the same, then d(v, s, t) = 0.
- 3. The symmetry: d(v, s, t) = d(s, t, v) = d(v, t, s) for all  $v, s, t \in \mathcal{L}$ .
- 4. The rectangle inequality:  $d(v, s, t) \le d(v, s, z) + d(v, z, t) + d(z, s, t)$  for all  $v, s, t, z \in \mathcal{L}$ .

Then d is said to be a 2-metric on  $\mathcal{L}$ . When d is a 2-metric on  $\mathcal{L}$ , the ordered pair  $(\mathcal{L}, d)$  is called a 2-metric group.

**Definition 3 ([3])** Let  $(\mathcal{L}, d)$  be a 2-metric group:

- 1. A sequence  $\{v_n\}$  is called convergent to v in  $(\mathcal{L},d)$  if for every  $t\in\mathcal{L}$ ,  $\lim_{n\to\infty}d(v_n,v,t)=0$  and written as  $\lim_{n\to\infty}v_n=v$ .
- 2. A sequence  $\{v_n\}$  is called Cauchy in  $(\mathcal{L}, d)$  if for every  $t \in \mathcal{L}$ ,  $\lim_{n,m\to\infty} d(v_n, v_m, t) = 0$ , that is, for each  $\varepsilon > 0$  and  $t \in \mathcal{L}$ , there exists  $n_0$  such that  $d(v_n, v_m, t) < \varepsilon$  for all  $n, m \ge n_0$ .
- 3.  $(\mathcal{L}, d)$  is called a complete 2-metric group, if every Cauchy sequence in  $(\mathcal{L}, d)$  is a convergent sequence.

**Definition 4** Let  $(\mathcal{L}, d)$  be a 2-metric group and  $v, s \in \mathcal{L}, r \geq 0$ . The set

$$B(v, s, r) = \{t \in \mathcal{L} : d(v, s, t) < r\}$$

is called a 2-ball centered at v and s with radius r. The topology generated by the collection of all 2-balls as a subbasis is called a 2-metric topology on group  $\mathcal{L}$ .

Now, the definition of normed groups is presented by hoping to generalize them to 2-normed groups.

**Definition 5** ([35]) Let  $\mathcal{L}$  be a group with identity element e. A function  $\|.\|: \mathcal{L} \to \mathbb{R}$  is called a group norm if the following holds for all  $v, s \in \mathcal{L}$ :

- 1.  $||v|| = ||v^{-1}||$  (symmetry).
- 2.  $||vs|| \le ||v|| + ||s||$  (triangle inequality).
- 3.  $||v|| \ge 0$  (positivity) and ||v|| = 0 iff v = e.

Then  $\mathcal{L}$  equipped with a group norm  $\|.\|$  is said to be a normed group.

In the realm of science and engineering, the application of computational methods for Normed Groups encompasses diverse areas of study. Distance Computations play a pivotal role, utilizing computational methods to determine distances between points within groups. This facilitates tasks such as measuring similarity [46–48] and clustering data points [49], essential in data analysis and pattern recognition [50–52]. Furthermore, optimization techniques are instrumental in optimizing functions defined on normed and metric spaces, enabling the effective resolution of optimization problems across various domains including machine learning [53–56], and operations research [57, 58]. These methods find applications in Signal Processing [59–61], contributing to advancements in communication systems,

20 A. Pourmoslemi et al.

image processing, and digital signal analysis. The integration of computational methods in the study of normed groups underscores their significance in enhancing efficiency, accuracy, and innovation across scientific and engineering disciplines.

#### 2.2 2-Normed Groups

In this section, we explore and introduce 2-normed groups, a concept that warrants thorough investigation. To establish a foundation for this study, it becomes imperative to revisit and redefine fundamental concepts akin to those prevalent in 2-normed spaces, adapting them to suit the unique characteristics of 2-normed groups. Given the absence of linearity in groups in a general context, a novel approach is taken to redefine essential notions such as linear dependence and independence within the framework of groups.

Subsequently, we delve into the formal definition of 2-normed groups, accompanied by illustrative examples that shed light on the interplay between norms and 2-norms within group structures. Furthermore, we extend our examination to encompass the application of 2-norms in the context of direct product groups, introducing a specialized 2-norm tailored to this scenario.

To enrich our understanding, we now elucidate the concepts of *dependent* and *independent* subsets and elements within the realm of 2-normed groups, paving the way for a comprehensive exploration of their properties and implications.

**Definition 6** Let  $\mathcal{L}$  be a group and  $\{v_1, v_2, \ldots, v_n\}$  be a subset of  $\mathcal{L}$ . Then,  $\{v_1, v_2, \ldots, v_n\}$  is a *dependent subset* of  $\mathcal{L}$  if there exist  $z_1, z_2, \ldots, z_n \in \mathbb{Z}$  such that at least one of  $z_1, z_2, \ldots, z_n$  is not zero and  $v_1^{z_1} v_2^{z_2} \ldots v_n^{z_n} = e$ . (Note that  $v_i^0 = e$ , for  $i = 1, \ldots, n$ .) In this case,  $v_1, v_2, \ldots, v_n$  are *dependent elements*. Otherwise,  $\{v_1, v_2, \ldots, v_n\}$  is an *independent subset* of  $\mathcal{L}$  and  $v_1, v_2, \ldots, v_n$  are *independent elements*.

The prerequisites needed to define 2-normed groups are now stated. In the next definition, 2-normed groups will be defined.

**Definition 7** Let  $\mathcal{L}$  be a nontrivial group with identity element e. A function  $\|., .\|$ :  $\mathcal{L} \times \mathcal{L} \to \mathbb{R}$  is called a group 2-norm if the following holds for all  $v, s, t \in \mathcal{L}$ :

- 1.  $||v, s|| \ge 0$  and ||v, s|| = 0 iff  $\{v, s\}$  is dependent.
- 2. ||v, s|| = ||s, v||.
- 3.  $||v^{-1}, s|| = ||v, s||$ .
- 4.  $||vs, t|| \le ||v, t|| + ||s, t||$ .

The pair  $(\mathcal{L}, \|., .\|)$  is called a 2-normed group.

In the above definition, if (4) holds, we speak of a semi-2-norm, and if (2) and (3) and (4) hold, one speaks of a pseudo-2-norm, and if (1), (2), and (4) hold, we speak of a group pre-2-norm. We say that a group 2-norm is abelian if ||vs,tz|| = ||sv,zt|| for all  $v, s, t, z \in \mathcal{L}$ .

2 2-Normed Groups 21

Note that if the group 2-norm is abelian, then

$$||vs(ab)^{-1}, t|| \le ||va^{-1}, t|| + ||sb^{-1}, t||,$$

for all  $v, s, t, a, b \in \mathcal{L}$ .

Now, let  $(\mathcal{L}, \|., .\|)$  be a 2-normed group. The conditions (2) and (4) imply that

$$||v, st|| < ||v, s|| + ||v, t||,$$

for all  $v, s, t \in \mathcal{L}$ .

Some of the basic properties of 2-norms on groups are given as follows.

**Proposition 1** Let  $(\mathcal{L}, \|...\|)$  be a 2-normed group. For all  $v, s, t \in \mathcal{L}$ , we have:

- 1.  $||v, s|| = ||vs^{-1}, s||$ .
- 2.  $||vt^{-1}, vs^{-1}|| = ||vt^{-1}, st^{-1}||$ .
- 3.  $||vt, st|| \le ||v, s|| + ||s, t|| + ||v, t||$ .
- 4.  $||v, t|| ||s, t||| \le ||vs^{-1}, t|| \le ||v, t|| + ||s, t||$ .
- 5. |||v,t|| ||s,t||| < ||vs,t|| < ||v,t|| + ||s,t||.

In particular, if  $m = min\{||v, t|| + ||s, t||\}$ , then

$$-2m \le ||vs, t|| - ||vs^{-1}, t|| \le 2m.$$

Now, here are some examples of 2-normed groups:

**Example 1** 1. Let  $\mathcal{L} = \left\{ \begin{pmatrix} 1 & a & b \\ 0 & 1 & c \\ 0 & 0 & 1 \end{pmatrix} : a, b, c \in \mathbb{Z} \right\}$  denote the discrete Heisenberg group. Putting

$$||v,s||_H = |a\acute{c} - c\acute{a}|,$$

where 
$$v = \begin{pmatrix} 1 & a & b \\ 0 & 1 & c \\ 0 & 0 & 1 \end{pmatrix}$$
 and  $s = \begin{pmatrix} 1 & \acute{a} & \acute{b} \\ 0 & 1 & \acute{c} \\ 0 & 0 & 1 \end{pmatrix}$ . One can see that  $||v, s||_H$  is a 2-norm

on f.

The following Python codes simply compute the 2-norm of two Heisenberg groups.

class HeisenbergGroup:

A. Pourmoslemi et al.

```
return f"HeisenbergGroup({self.a}, {self.b},
                  {self.c})"
          def __mul__(self, other):
               new a = self.a + other.a
               new b = self.b + other.b
               new c = self.c + other.c + self.a * other.b
               - self.b * other.a
               return HeisenbergGroup(new_a, new_b, new_c)
          def __pow__(self, n):
               result = HeisenbergGroup(0, 0, 0)
               base = self
               while n > 0:
                    if n % 2 == 1:
                         result = result * base
                    base = base * base
                    n //= 2
               return result
          def two_norm(self, other):
               return abs(self.a * other.c - self.c * other.a)
     # Example usage
     g1 = HeisenbergGroup(1, 2, 3)
     g2 = HeisenbergGroup(4, 5, 6)
     print(f"Heisenberg group 1: {g1}")
     print(f"Heisenberg group 2: {g2}")
     print(f"2-norm of g1 and g2: {g1.two_norm(g2)}")
     For example, as a result of the above codes, we have:
     Heisenberg group 1: HeisenbergGroup(1, 2, 3)
     Heisenberg group 2: HeisenbergGroup(4, 5, 6)
     2-norm of g1 and g2: 15
2. Let \mathbf{R}_{+}^{*} denote the group of positive real numbers with multiplication as the group
  operation and \mathcal{L} = \mathbf{R}_{+}^{*} \times \mathbf{R}_{+}^{*}. By setting
            ||v, s|| := |(\log a)(\log b) - (\log b)(\log a)| \qquad (\forall v, s \in \mathcal{L}),
  when v = (a, b) and s = (\hat{a}, \hat{b}), \mathcal{L} will be a 2-normed group.
3. Let \mathbb{Z} \times \mathbb{Z} = \{(a, b) | a, b \in \mathbb{Z}\}. Then, with a binary operation
```

 $(a, b) + (\acute{a}, \acute{b}) = (a + \acute{a}, b + \acute{b}).$ 

2 2-Normed Groups 23

and by setting a 2-norm

$$||(a,b), (\acute{a}, \acute{b})|| = |\sqrt{2}a\acute{b} - \sqrt{2}b\acute{a}|,$$

 $\mathcal{L} = \mathbb{Z} \times \mathbb{Z}$  is a 2-normed group.

4. Let  $P_n$  denote the group of all real polynomials of degree  $\leq n$ , on the interval [0, 1] with addition as the group operation, and let  $\{v_0, v_1, ..., v_{2n}\}$  be distinct fixed elements on [0, 1]. Now, define

$$||f,g|| = \sum_{i=0}^{2n} |f(v_i)g(v_i)|, \qquad (2.1)$$

where f and g are independent. It is clear that (2.1) is a group 2-norm on  $P_n$ .

**Proposition 2** Let  $\mathcal{L}$  be a group having two pseudo-norms  $\|.\|_1$  and  $\|.\|_2$ . For all  $v, s \in \mathcal{L}$ , define

$$||v, s|| = ||v||_1 \cdot ||s||_2$$
.

Then,  $\|.,.\|$  is a pseudo-2-norm on  $\mathcal{L}$ .

**Proposition 3** Let  $\mathcal{L}$  be a group. If |.,.| is a group pre-2-norm on  $\mathcal{L}$ , then

$$||v, s|| := \max\{|v, s|, |v^{-1}, s|\},\$$

is a group 2-norm on L.

**Proof** It is sufficient to show that  $||vs,t|| \le ||v,t|| + ||s,t||$  for all  $v,s,t \in \mathcal{L}$ . Assuming

$$\max\{|v, t| + |s, t|, |v^{-1}, t| + |s^{-1}, t|\} = |v, t| + |s, t|,$$

we have

$$||vs, t|| = \max\{|vs, t|, |(vs)^{-1}, t|\}$$

$$\leq \max\{|v, t| + |s, t|, |v^{-1}, t| + |s^{-1}, t|\}$$

$$= |v, t| + |s, t|$$

$$\leq \max\{|v, t|, |v^{-1}, t|\} + \max\{|s, t|, |s^{-1}, t|\}$$

$$= ||v, t|| + ||s, t||.$$

It completes the proof.

24 A. Pourmoslemi et al.

**Remark 1** If  $(\mathcal{L}, \|., .\|)$  is a 2-normed group, then

$$\|\sum_{i=1}^n v_i, s\| \le \sum_{i=1}^n \|v_i, s\|,$$

for all  $v_i$ ,  $s \in \mathcal{L}$  and i = 1, 2, ..., n.

In the next definition, we redefine concepts such as convergent sequences, Cauchy sequences, and 2-Banach groups. Although these definitions are similar to the definitions in 2-normed spaces, we found it necessary to write them here because these concepts are defined for groups for the first time. Moreover, we get the following results for 2-normed groups, similar to those in 2-normed spaces that needed to be discussed here:

#### **Definition 8**

- 1. A group 2-norm is said to be n-homogeneous if  $||v^n, s|| = n||v, s||$  for all  $v, s \in$  $\mathcal{L}$  and  $n \in \mathbb{N}$ .
- 2. A sequence  $\{v_n\}$  in a 2-normed group  $\mathcal{L}$  is called a Cauchy sequence if there are independent  $s, t \in \mathcal{L}$  such that

$$\lim_{m,n\to\infty} ||v_n v_m^{-1}, s|| = 0 = \lim_{m,n\to\infty} ||v_n v_m^{-1}, t||.$$

3. A sequence  $\{v_n\}$  in a 2-normed group  $\mathcal{L}$  is called a convergent sequence if there is a  $v \in \mathcal{L}$  such that

$$\lim_{n\to\infty} ||v_n v^{-1}, s|| = 0,$$

for all  $s \in \mathcal{L}$ , and write  $\lim_{n \to \infty} v_n = v$ . 4. A 2-normed group, in which every Cauchy sequence is a convergent sequence, is called a 2-Banach group.

Remark 2 The uniqueness of the limit of a converges sequence can be verified as follows.

Suppose that  $\{v_n\}$  is convergent to two distinct limits v and s in  $\mathcal{L}$ . Choose  $t \in \mathcal{L}$ such that  $||vs^{-1}, t|| \neq 0$  and take  $n_1 \in \mathbb{N}$  sufficiently large such that  $||v_{n_1}v^{-1}, t|| < \infty$  $\frac{1}{2} \|vs^{-1}, t\|$  and  $\|v_{n_1}s^{-1}, t\| < \frac{1}{2} \|vs^{-1}, t\|$ . Then

$$\begin{aligned} \|vs^{-1}, t\| &\leq \|vv_{n_1}, t\| + \|v_{n_1}s^{-1}, t\| \\ &< \frac{1}{2}\|vs^{-1}, t\| + \frac{1}{2}\|vs^{-1}, t\| = \|vs^{-1}, t\|. \end{aligned}$$

Hence, whenever it exists,  $\lim_{n\to\infty} v_n$  must be unique.

Now, let  $(\mathcal{L}, \|., .\|)$  be a 2-normed group,  $v \in \mathcal{L}$ , and  $\|v, s\| = 0$  for all  $s \in \mathcal{L}$ . Suppose that  $v \neq e$ , and let  $s_1, s_2$  be independent elements in  $\mathcal{L}$ . So, v and  $s_1$  are dependent, and there exist  $z_1, z_2 \in \mathbb{Z}$  such that  $(z_1, z_2) \neq (0, 0)$  and  $v^{z_1} s_1^{z_2} = e$ . Similarly, there exist  $z_1, z_2 \in \mathbb{Z}$  such that  $(z_1, z_2) \neq (0, 0)$  and  $v^{z_1} s_2^{z_2} = e$ . Hence  $s_1$  and  $s_2$  are dependent, which is a contradiction. Therefore we have the following lemma.

**Lemma 1** Let  $(\mathcal{L}, \|., .\|)$  be a 2-normed group. If  $\|v, s\| = 0$  for all  $s \in \mathcal{L}$ , then v = e.

**Lemma 2** For a convergent sequence  $\{v_n\}$  in a 2-normed group  $\mathcal{L}$ ,

$$\lim_{n\to\infty} ||v_n, s|| = ||\lim_{n\to\infty} v_n, s||,$$

for all  $s \in \mathcal{L}$ .

**Proof** Since  $\{v_n\}$  is a convergent sequence, there is an element  $v \in \mathcal{L}$  such that  $\lim_{n \to \infty} ||v_n v^{-1}, s|| = 0$  for all  $s \in \mathcal{L}$ . Then,

$$\lim_{n \to \infty} ||v_n, s|| - ||v, s||| \le \lim_{n \to \infty} ||v_n v^{-1}, s|| = 0,$$

for all  $s \in \mathcal{L}$ . So,

$$\lim_{n \to \infty} ||v_n, s|| = ||v, s|| = ||\lim_{n \to \infty} v_n, s||,$$

for all  $s \in \mathcal{L}$ .

**Theorem 1** Let  $(\mathcal{L}, \|., .\|)$  be a 2-normed group. Then the 2-norm  $\|., .\|$  is a continuous map.

**Proposition 4** In a 2-normed group  $(\mathcal{L}, \|., .\|)$ , the following statements are equivalent:

- 1.  $||vt, st|| \le ||v, s|| + ||s, t|| + ||v, t||$ , for all  $v, s, t \in \mathcal{L}$ .
- 2.  $d(v, s, t) \le d(v, s, z) + d(v, z, t) + d(z, s, t)$ , for all  $v, s, t, z \in \mathcal{L}$ .

**Proof** From (1) we have

$$d(v, s, t) = \|vt^{-1}, st^{-1}\|$$

$$\leq \|vz^{-1}, sz^{-1}\| + \|sz^{-1}, tz^{-1}\| + \|tz^{-1}, vz^{-1}\|$$

$$= d(v, s, z) + d(v, z, t) + d(z, s, t),$$

for all  $v, s, t, z \in \mathcal{L}$ , and conversely,

A. Pourmoslemi et al.

$$||vt, st|| = d(v, s, t^{-1})$$

$$\leq d(v, s, e) + d(v, e, t^{-1}) + d(e, s, t^{-1})$$

$$= ||v, s|| + ||v, t|| + ||s, t||.$$

Hence, the two statements are equivalent.

**Lemma 3** *Let*  $\vartheta$  *from a 2-normed group*  $(\mathcal{L}, \|., .\|_{\mathcal{L}})$  *into a 2-normed group*  $(\mathcal{K}, \|., .\|_{\mathcal{K}})$  *be a bounded homomorphism. Then*  $\vartheta$  *is continuous.* 

**Proof** From boundedness of  $\vartheta$ , there exists  $\eta > 0$  such that  $\|\vartheta(v), \vartheta(s)\|_{\mathcal{K}} \le \eta \|v, s\|_{\mathcal{L}}$  for all  $v, s \in \mathcal{L}$ . Then for  $t \in \mathcal{L}$  and  $\varepsilon > 0$  there exist  $\delta = \frac{\varepsilon}{\eta}$  such that  $\|\vartheta(v)\vartheta(s)^{-1}, \vartheta(t)\|_{\mathcal{K}} < \varepsilon$  whenever  $\|vs^{-1}, t\| < \delta$ , i.e.,  $\vartheta$  is continuous.

The presented lemma establishes a crucial relationship within the realm of 2-normed groups, emphasizing the continuity of a bounded homomorphism  $\vartheta$  between two 2-normed groups  $(\mathcal{L}, |., .|\mathcal{L})$  and  $(\mathcal{K}, |., .|\mathcal{K})$ . Delving deeper into the implications of this lemma reveals the foundational concepts at play. The boundedness of  $\vartheta$  ensures the existence of a positive constant  $\eta$  that governs the relationship between the norms of elements in  $\mathcal{L}$  and  $\mathcal{K}$ . This bound guarantees that the homomorphism  $\vartheta$  maintains a controlled transformation between the two 2-normed groups, thereby preserving their essential properties.

Furthermore, the proof of continuity for  $\vartheta$  elucidates the intricate interplay between the boundedness of the homomorphism and its continuous nature. By establishing a direct link between the norms of elements in  $\mathcal{L}$  and  $\mathcal{K}$ , the proof showcases how the continuity of  $\vartheta$  is inherently tied to the boundedness condition, ensuring a smooth and consistent mapping between the two 2-normed groups.

In essence, this lemma not only highlights the fundamental role of continuity in the context of bounded homomorphisms but also underscores the intricate connection between these properties in maintaining the structural coherence of 2-normed groups. This insight into the interplay between boundedness and continuity enriches our understanding of the dynamics within 2-normed groups and their homomorphisms.

It is easy to see that a subgroup C of a 2-normed group  $(\mathcal{L}, \|., .\|)$  is also a 2-normed group with the same 2-norm. Furthermore, the product  $(\mathcal{L}_1 \times \mathcal{L}_2, \star, e)$  of two groups  $(\mathcal{L}_1, \circ, e_{\mathcal{L}_1})$  and  $(\mathcal{L}_2, \bullet, e_{\mathcal{L}_2})$ , where

$$(v_1, v_2) \star (s_1, s_2) = (v_1 \circ s_1, v_2 \bullet s_2),$$

is also a group. The following lemma shows that we can extend 2-norms from groups to their product.

**Lemma 4** Direct product of two 2-normed groups  $(\mathcal{L}_1, \|..., \|_1, \circ, e_{\mathcal{L}_1})$  and  $(\mathcal{L}_2, \|..., \|_2, \bullet, e_{\mathcal{L}_2})$  is a 2-normed group with respect to 2-norms defined on  $(\mathcal{L}_1, \circ)$  and  $(\mathcal{L}_2, \bullet)$ , respectively.

**Proof** Letting  $\mathcal{L}_1 \times \mathcal{L}_2 = \{(v_1, v_2), \ v_1 \in \mathcal{L}_1, v_2 \in \mathcal{L}_2\}$ , define a 2-norm on  $\mathcal{L}_1 \times \mathcal{L}_2$  by

$$||(v_1, v_2), (s_1, s_2)|| = ||(v_1, s_1)||_1 + ||v_2, s_2||_2,$$

where  $v = (v_1, v_2), s = (s_1, s_2) \in \mathcal{L}_1 \times \mathcal{L}_2$ .

Now, let  $\mathcal L$  and  $\mathcal K$  be 2-normed groups. The homomorphic image of a homomorphism  $\varpi:\mathcal L\to\mathcal K$  can be defined as

$$Img(\varpi) = {\{\varpi(v), v \in \mathcal{L}\}} \subseteq \mathcal{K}.$$

Every homomorphic image of a group  $\mathcal{K}$  is also a subgroup, and every subgroup of a 2-normed group is a 2-normed group as well. Hence, the homomorphic image of a 2-normed group is a 2-normed group.

**Lemma 5** Let  $\mathcal{L}$  be a group and  $(\mathcal{K}, \|., .\|)$  be a 2-normed group. If  $\varpi : \mathcal{L} \to K$  is a homomorphism, then

$$\|v, s\|_{\mathcal{L}} := \|\varpi(v), \varpi(s)\|_{\mathcal{K}} \quad (\forall v, s \in \mathcal{L})$$

is also a 2-norm on  $\mathcal{L}$ .

**Proof** Let  $v, s \in \mathcal{L}$ , then

$$||v, s||_{\mathcal{L}} = ||\varpi(v), \varpi(s)||_{\mathcal{K}} \ge 0,$$

and  $\|v, s\|_{\mathcal{L}} = 0$  implies that  $\|\varpi(v), \varpi(s)\|_{\mathcal{K}} = 0$ , which gives  $\varpi(v)$  and  $\varpi(s)$  are dependent. From this, we deduce that v and s are dependent. It is evident that  $\|v, s\|_{\mathcal{L}} = \|s, v\|_{\mathcal{L}}$  and  $\|v^{-1}, s\|_{\mathcal{L}} = \|v, s\|_{\mathcal{L}}$ . It remains to prove that  $\|vs, t\|_{\mathcal{L}} \le \|v, t\|_{\mathcal{L}} + \|s, t\|_{\mathcal{L}}$ . Indeed,

$$\|vs, t\|_{\mathcal{L}} = \|\varpi(vs), \varpi(t)\|_{\mathcal{K}}$$

$$= \|\varpi(v)\varpi(s), \varpi(t)\|_{\mathcal{K}}$$

$$\leq \|\varpi(v), \varpi(t)\|_{\mathcal{K}} + \|\varpi(s), \varpi(t)\|_{\mathcal{K}}$$

$$= \|v, t\|_{\mathcal{L}} + \|s, t\|_{\mathcal{L}}.$$

**Theorem 2** ([62]) If  $\mathcal{L}$  is a finitely generated abelian group, then

$$\mathcal{L} \cong \mathbb{Z}^n \times \mathbb{Z}_{n_1} \times \mathbb{Z}_{n_2} \times ... \times \mathbb{Z}_{n_k},$$

with  $1 < n_k \mid n_{k-1} \mid \dots n_1$  and  $n \ge 0$ . Moreover, this expression is unique.

**Theorem 3** Let  $\mathcal{L}$  be a finitely generated abelian group with  $o(\mathcal{L}) = n < \infty$ . Then there exists a pseudo 2-norm  $\|.,.\|$  on  $\mathcal{L}$ .

28 A. Pourmoslemi et al.

**Proof** If  $o(\mathcal{L}) = n < \infty$ , then

$$\mathcal{L} = < l_1 > \times < l_2 > \times ... \times < l_m > = \prod_{i=1}^{m} < l_i >,$$

where  $o(l_i) = p_i^{n_i}$  for i = 1, 2, ..., m. Each  $l_i$  is a generator of cyclic group of order  $p_i^{n_i}$  where each  $n_i$  is positive integer and each  $p_i$  is prime and

$$o(l_1) \le o(l_2) \le \dots \le o(l_m),$$
  
 $o(\mathcal{L}) = p_1^{n_1} p_2^{n_2} \dots p_m^{n_m} = n.$ 

Let  $v \in \mathcal{L}$ . Then v can be written as  $v = l_1^{\alpha_1} l_2^{\alpha_2} ... l_m^{\alpha_m}$  such that  $o(l_i) \leq p_i^{n_i}$ . There exists a group pseudo-2-norm  $\|.,.\|_i$  on  $< l_i >$  and  $\|l_i^{p_{n_i}}, l_j^{p_{n_j}}\|_i = 0$  for each i = 1, 2, ..., m, since every cyclic group is generated by  $< l_i >$ . Define a pseudo 2-norm  $\|.,.\|$  on  $\mathcal{L}$  by

$$\|v,s\| = \|l_1^{\alpha_1} l_2^{\alpha_2} ... l_m^{\alpha_m}, l_1^{\beta_1} l_2^{\beta_2} ... l_m^{\beta_m}\| = \sum_{i=1}^m \|l_i^{\alpha_i}, l_i^{\beta_i}\|_i,$$

where each  $\|.,.\|_i$  is a pseudo-2-norm. It is easy to check that  $\|v,s\| \ge 0$  and  $\|v,s\| = \|s,v\|$ . Let  $v,s,t \in \mathcal{L}$ ; then,

$$v = l_1^{\alpha_1} l_2^{\alpha_2} ... l_m^{\alpha_m} = v_1 v_2 ... v_m,$$

$$s = l_1^{\beta_1} l_2^{\beta_2} ... l_m^{\beta_m} = s_1 s_2 ... s_m,$$

$$t = l_1^{\gamma_1} l_2^{\gamma_2} ... l_m^{\gamma_m} = t_1 t_2 ... t_m,$$

where  $l_i^{\alpha_i} = v_i$ ,  $l_i^{\beta_i} = s_i$ , and  $l_i^{\gamma_i} = t_i$ .

$$\|vs, t\| = \|(v_1v_2...v_m)(s_1s_2...s_m), t_1t_2...t_m\|$$

$$= \|v_1s_1...v_ms_m, t_1t_2...t_m\|$$

$$= \sum_{i=1}^m \|v_is_i, t_i\|_i$$

$$\leq \sum_{i=1}^m \|v_i, t_i\|_i + \sum_{i=1}^m \|s_i, t_i\|_i$$

$$= \sum_{i=1}^m \|l_i^{\alpha_i}, l_i^{\gamma_i}\|_i + \sum_{i=1}^m \|l_i^{\beta_i}, l_i^{\gamma_i}\|_i$$

$$\begin{split} &=\|l_1^{\alpha_1}l_2^{\alpha_2}...l_m^{\alpha_m}, l_1^{\gamma_1}l_2^{\gamma_2}...l_m^{\gamma_m}\| \\ &+\|l_1^{\beta_1}l_2^{\beta_2}...l_m^{\beta_m}, l_1^{\gamma_1}l_2^{\gamma_2}...l_m^{\gamma_m}\| \\ &=\|v,t\|+\|s,t\|. \end{split}$$

It remains to prove that  $||v^{-1}, s|| = ||v, s||$ . Indeed,

$$||v^{-1}, s|| = ||(l_1^{\alpha_1} l_2^{\alpha_2} ... l_m^{\alpha_m})^{-1}, l_1^{\beta_1} l_2^{\beta_2} ... l_m^{\beta_m}||$$

$$= ||(v_1 v_2 ... v_m)^{-1}, s_1 s_2 ... s_m||$$

$$= \sum_{i=1}^m ||v_i^{-1}, s_i||_i$$

$$= \sum_{i=1}^m ||v_i, s_i||_i$$

$$= ||v, s||.$$

#### 2.3 Conclusion

The research presented in this chapter contributes to the exploration of 2-normed groups. Through the definition of the 2-norm on groups and the illustration of various examples, the computational potential of 2-norms on groups is demonstrated. The establishment of theorems to investigate the relationship between 2-normed groups and the presentation of additional results concerning homomorphisms on such groups and 2-norms on the direct product of groups further enriches the understanding of this mathematical framework. These findings provide insights into the properties and applications of 2-normed groups, thereby advancing the existing knowledge in this study area.

#### References

- B. Vulich, On a generalized notion of convergence in a Banach space. Ann. Math. 38(1), 156– 174 (1937)
- 2. S. Gähler, 2-metrische Raume und ihre topologische Struktur. Math. Nachr. **26**, 115–148 (1963)
- 3. S. Gähler, Linear 2-normierte raume. Math. Nachr. 28, 1–43 (1964)
- S. Gähler, Untersuchungen über verallgemeinerte m-metrische Räume. I. Mathematische Nachrichten. 40, 165–189 (1969)
- S. Gähler, Untersuchungen über verallgemeinerte m-metrische Räume. II. Mathematische Nachrichten. 40, 229–264 (1969)

 S. Gähler, Untersuchungen über verallgemeinerte m-metrische Räume. III. Mathematische Nachrichten. 41, 23–26 (1969)

- 7. A. White, 2-Banach spaces. Doctorial Diss. St. Louis University (1968)
- 8. A. White, 2-Banach spaces. Math. Nachr. 42, 43–60 (1969)
- R. Freese, Y.J. Cho, Geometry of Linear 2-Normed Spaces (Nova Science Publishers, Inc., New York, 2001)
- R. Freese, Y.J. Cho, Characterizations of linear 2-normed spaces. Math. Japan 40, 115–122 (1994)
- 11. Z. Lewandowska, Linear operators on generalized 2-normed spaces. Bulletin mathématique de la Société des Sciences Mathématiques de Roumanie (1999), pp. 353–368
- K.S. Ha, Y.J. Cho, S.S. Kim, M.S. Khan, Strictly Convex Linear 2-Normed Spaces. Math. Nachr. 146(1), 7–16 (1990)
- 13. A. White, Y.J. Cho, Linear mappings on linear 2-normed spaces. Bull. Korean Math. Soc. 21, 1–6 (1984)
- K. Tamilvanan, A.H. Alkhaldi, R.P. Agarwal, A.M. Alanazi, Fixed point approach: ulam stability results of functional equation in non-archimedean fuzzy φ-2-normed spaces and non-archimedean banach spaces. Mathematics 11(2), 270 (2023). https://doi.org/10.3390/ math11020270
- 15. P. Senthil Kumar, P. Thiruveni, D. Dhamodharan, Some results on common fixed point in fuzzy 2-normed linear space. Adv. Appl. Math. Sci. **21**(11), 6425–6435 (2022)
- 16. J. Brzdęk, K. Ciepliński, A fixed point theorem in n-Banach spaces and Ulam stability. J. Math. Anal. Appl. 470(1), 632–646 (2019). https://doi.org/10.1016/j.jmaa.2018.10.028
- I-i. EL-Fassi, A new fixed point theorem in quasi-(2, β)-Banach spaces and some of its applications to functional equations. J. Math. Anal. Appl. 512(2), 126–158 (2022). https://doi.org/10.1016/j.jmaa.2022.126158
- 18. G.U. Reddy, Some fixed point results in 2-normed spaces. Nonlinear Stud. 30(2) (2023)
- A. Bahyrycz, J. Brzdek, E.-S. El-Hady, Z. Lesniak, On Ulam stability of functional equations in 2-normed spaces—A survey. Symmetry 13(11), 2200 (2021). https://doi.org/10.3390/ sym14071365
- H.A. Almurieb, E.S. Bhaya, Best neural simultaneous approximation. Indones. J. Electr. Eng. Comput. Sci. 20(3), 1584–1590 (2020). https://doi.org/10.11591/ijeecs.v20.i3.pp1584--1590
- 21. H.-Y. Chu, On the Mazur–Ulam problem in linear 2-normed spaces. J. Math. Anal. Appl. **327**(2), 1041–1045 (2007)
- 22. K. Cleplinski, Approximate multi-additive mappings in 2-Banach spaces. Bult. Iranian Math. Soc. 41, 785–792 (2015)
- 23. J. Gao, On the stability of the linear mapping in 2-normed spaces. Nonlinear Funct. Anal. Appl. 14, 801–807 (2009)
- 24. H. Mazaheri, R. Kazemi, Some results on 2-inner product spaces. Novi Sad. J. Math. 37(2), 35–40 (2007)
- N. Minculete, R. Păltănea, Weak n-inner product spaces. Ann. Funct. Anal. 12(2), 22 (2021). https://doi.org/10.1007/s43034-020-00108-3
- 26. H. Batkunde, Norms on Quotient spaces of the 2-inner product space. Contemp. Math. Appl. **3**(2), 80–87 (2021)
- S. Vijayabalaji, S. Sivaramakrishnan, P. Balaji, Cubic n-inner product space, in *Soft Computing Techniques in Engineering, Health, Mathematical and Social Sciences* (CRC Press, Boca Raton, 2021), pp. 121–136
- T.B. Chandra, K. Omer, and G. Mehmet, Certain aspects of rough I-statistical convergence in probabilistic n-normed space. Filomat 37(24), 8113–8130 (2023). https://doi.org/10.2298/ FIL2324113T
- A. Pourmoslemi, S. Rajabi, M. Salimi, A. Ahmadian, Fuzzy routing protocol for D2D communications based on probabilistic normed spaces. Wireless Pers. Commun. 122(3), 2505–2520 (2022). https://doi.org/10.1007/s11277-021-09009-7
- A. Pourmoslemi, M. Salimi, Probabilistic n-normed spaces, Dn-compact sets and Dn-bounded sets. Chaos, Solitons Fractals 42(5), 2729–2734 (2009). https://doi.org/10.1016/j.chaos.2009. 03.179

- 31. B. Guillen, H. Panackal, Probabilistic Normed Spaces (Imperial College Press, London, 2014)
- K. Nourouzi, A.R. Pourmoslemi, Probabilistic normed groups. Iran. J. Fuzzy Syst. 14(1), 99– 113 (2017)
- A. Pourmoslemi, M. Ferrara, B.A. Pansera, M. Salimi, Probabilistic norms on the homeomorphisms of a group. Soft Comput. 24, 7021–7028 (2020). https://doi.org/10.1007/s00500-020-04818-7
- A. Pourmoslemi, K. Nourouzi, Mazur-Ulam theorem in probabilistic normed groups. Int. J. Nonlinear Anal. Appl. 8(2), 327–333 (2017). https://doi.org/10.22075/IJNAA.2017.1281.1318
- 35. N.H. Bingham, A.J. Ostaszewski, Normed versus topological groups: dichotomy and duality. Dissertationes Math. **472**, 138 (2010)
- 36. A. Pourmoslemi, T. Nazari, M. Salimi, Inner product groups and Riesz representation theorem. Symmetry 13(10), 1946 (2021). https://doi.org/10.3390/sym13101946
- 37. G. Birkhoff, A note on topological groups. Compos. Math. 3, 427–430 (1936)
- 38. S. Kakutani, Über die Metrisation der topologischen Gruppen (German). Proc. Imp. Acad. 12(4), 82–84 (1936)
- 39. V.L. Klee, Invariant metrics in groups (solution of a problem of Banach). Proc. Am. Math. Soc. 3, 484–487 (1952)
- 40. D.R. Farkas, The algebra of norms and expanding maps on groups. J. Algebra **133**(2), 386–403 (1990)
- A.A. Pavlov, Normed groups and their application to noncommutative differential geometry (Russian). Zap. Nauchn. Sem. S.-Peterburg. Otdel. Mat. Inst. Steklov. (POMI) 266 (2000).
   Teor. Predst. Din. Sist. Komb. i Algoritm. Metody. 5, 234–244, 340. Translation in J. Math. Sci. (N. Y.) 113(5), 675–682 (2003)
- 42. B.J. Pettis, On continuity and openness of homomorphisms in topological groups. Ann. Math. **52**(2), 293–308 (1950)
- 43. R.C. Alperin, N. Kenneth, Complete trees for groups with a real-valued length function. J. London Math. Soc. 2(1), 55–68 (1985)
- 44. N. Harrison, Real length functions in groups. Trans. Am. Math. Soc. 174, 77–106 (1972)
- 45. R.C. Lyndon, Length functions in groups. Math. Scand. 12, 209–234 (1963)
- A. Evangelos, T. Ebrahimi, Towards a point cloud structural similarity metric, in 2020 IEEE International Conference on Multimedia & Expo Workshops (ICMEW) (IEEE, Piscataway, 2020), pp. 1–6
- Y. Xiaohan, Y. Gao, M. Bennamoun, S. Xiong, A Lie algebra representation for efficient 2D shape classification. Pattern Recognit. 134, 109078 (2023). https://doi.org/10.1016/j.patcog. 2022.109078
- 48. G. Subhroshekhar, A.Y.R. Low, Y.S. Soh, Z. Feng, B.K.Y. Tan, Dictionary learning under symmetries via group representations. Preprint. arXiv:2305.19557 (2023)
- T.M. Ghazal, Performances of k-means clustering algorithm with different distance metrics. Intell. Autom. Soft Comput. 30(2), 735–742 (2021). https://doi.org/10.32604/iasc.2021. 019067
- X. Bai, X. Wang, X. Liu, Q. Liu, J. Song, N. Sebe, B. Kim, Explainable deep learning for efficient and robust pattern recognition: a survey of recent developments. Pattern Recognit. 120, 102–108 (2021). https://doi.org/10.1016/j.patcog.2021.108102
- F. Xiao, CED: a distance for complex mass functions. IEEE Trans. Neural Networks Learn. Syst. 32(4), 1525–1535 (2020). https://doi.org/10.1109/TNNLS.2020.2984918
- L. Zhou, H. Wang, S. Lin, S. Hao, Z.-M. Lu, Face recognition based on local binary pattern and improved pairwise-constrained multiple metric learning. Multimedia Tools Appl. 79, 675–691 (2020). https://doi.org/10.1007/s11042-019-08157-0
- B. Subramanian, A. Paul, J. Kim, K.-W.-A. Chee, Metrics space and norm: Taxonomy to distance metrics. Scientific Programming 2022 (2022). https://doi.org/10.1155/2022/1911345
- 54. A. Bellet, A. Habrard, M. Sebban, *Metric Learning* (Springer Nature, Berlin, 2022)
- P. Ribino, C. Di Napoli, L. Serino, Norm-based reinforcement learning for QoS-driven service composition. Information Sci. 646, 119377 (2023). https://doi.org/10.1016/j.ins.2023.119377

32 A. Pourmoslemi et al.

S.H. Sababe, On 2-inner product spaces and reproducing property. Korean J. Math. 28(4), 973–984 (2020). https://doi.org/10.11568/kjm.2020.28.4.973

- 57. T. Eelbode, J. Bertels, M. Berman, D. Vandermeulen, F. Maes, R. Bisschops, M.B. Blaschko, Optimization for medical image segmentation: theory and practice when evaluating with Dice score or Jaccard index. IEEE Trans. Med. Imaging 39(11), 3679–3690 (2020). https://doi.org/ 10.1109/TMI.2020.3002417
- W. Jiang, K. Huang, J. Geng, X. Deng, Multi-scale metric learning for few-shot learning. IEEE Trans. Circuits Syst. Video Technol. 31(3), 1091–1102 (2020). https://doi.org/10.1109/TCSVT. 2020.2995754
- 59. X. Huang, Y. Xu, J. Hua, W. Yi, H. Yin, R. Hu, S. Wang, A review on signal processing approaches to reduce calibration time in EEG-based brain–computer interface. Front. Neurosci. **15**, 733546 (2021). https://doi.org/10.3389/fnins.2021.733546
- 60. E. Binz, S. Pods, *The Geometry of Heisenberg Groups: With Applications in Signal Theory, Optics, Quantization, and Field Quantization.* No. 151 (American Mathematical Society, Providence, 2008)
- 61. V.P. Sinha, Symmetries and Groups in Signal Processing: An Introduction (Springer Science & Business Media, Berlin, 2010)
- 62. J.B. Fraleigh, A First Course in Abstract Algebra, 7th edn. (Addison Wesley, Boston, 2003)

# Chapter 3 Bile Acid Loss Syndrome Screening: A Protocol Using Pooled Samples



João P. Martins , Miguel Felgueiras , Rui Santos , and Manuela Amorim .

#### 3.1 Introduction

# 3.1.1 Pooled Samples

In 1943, the foundational concepts of group testing were introduced [1]. This method involved combining individuals into pools to screen for a binary characteristic with prevalence rate p, such as the presence or absence of the syphilis antigen, aimed at cost reduction. A negative result on a pooled mixture of blood from n individuals indicated that all n individuals were free from the disease. Conversely, a positive result suggested that at least one individual within the pool had the disease,

J. P. Martins (⊠)

ESS, Polytechnic of Porto, Porto, Portugal

CEAUL, Faculdade de Ciências, Universidade de Lisboa, Lisbon, Portugal

CEISUC/CIBB, University of Coimbra, Coimbra, Portugal e-mail: jom@ess.ipp.pt

M. Felgueiras

CEAUL, Faculdade de Ciências, Universidade de Lisboa, Lisbon, Portugal

ESTG, Polytechnic Institute of Leiria, Leiria, Portugal

CIDMA, University of Aveiro, Aveiro, Portugal

R. Santos

CEAUL, Faculdade de Ciências, Universidade de Lisboa, Lisbon, Portugal

ESTG, Polytechnic Institute of Leiria, Leiria, Portugal

M. Amorim

ESS, Polytechnic of Porto, Porto, Portugal

REQUIMTE/LAQV, Polytechnic of Porto, Porto, Portugal

© The Author(s), under exclusive license to Springer Nature Switzerland AG 2025 N. E. Mastorakis et al. (eds.), *Computational Problems in Science and Engineering II*, https://doi.org/10.1007/978-3-031-78416-3\_3

J. P. Martins et al.

without specifying which ones. Subsequently, individual tests were recommended to differentiate between positive and negative individuals [2, 3].

Finding the ideal batch size n, which minimizes the anticipated number of tests, stands as a pivotal metric for monetary expenses, considering that the cost of sample mixing is generally negligible [4]. The anticipated number of tests required to detect infected units within groups of n members from a total of N individuals is (for simplicity, assume that  $\frac{N}{n} \in \mathbb{N}$ )

$$E[T] = N\left(\frac{1}{n} + 1 - (1-p)^n\right)$$
(3.1)

Thus, a simple quantification of the efficiency of pooled versus individual tests is the relative cost RC

$$RC = \frac{E[T]}{N} = \frac{n+1}{n} - (1-p)^n, \quad n \ge 2$$
(3.2)

which can be used to find the most efficient value for n, given an infection prevalence p.

Resort to a pool-testing strategy can expedite screening processes and enhance testing rates, particularly during periods of limited test availability and slow reporting. Pool testing has demonstrated efficacy across diverse infectious disease screening scenarios [5]. Nevertheless, the potential reduction in sensitivity (the likelihood of accurately classifying an infected individual) hinders the widespread adoption of this approach especially in developed nations [6]. This decrease in sensitivity arises from dilution effects resulting from the combination of healthy and infected samples. Therefore, determining the batch size requires consideration of the sources of testing error, quantified by the test sensitivity  $\varphi_s$  and test specificity  $\varphi_e$ , cf. Ref. [7]. When testing error is a possibility, straightforward calculations show that Eq. (3.2) should be rewritten as  $(n \ge 2)$ 

$$RC = \frac{E[T]}{N} = \frac{n\varphi_s + 1}{n} + (1 - \varphi_s - \varphi_e)(1 - p)^n$$
(3.3)

In Eq. (3.3), the values of  $\varphi_s$  and  $\varphi_e$  should be interpreted not as the individual test performance but as measures of the pooled sample test performance.

Since Dorfman's work, pooling samples strategies have been extended to count variables and to continuous variable [7]. In these cases, its application is not straightforward, as it depends on setting a threshold of classification of the pooled sample as described in what follows for the continuous case.

Let  $X_i$ , with  $i = 1, \dots, n$ , be n independent Bernoulli trials ( $X_i \in Ber(p)$ ) with probability p, where the random variable (r.v.)  $X_i$  denotes the presence ( $X_i = 1$ )

or the absence  $(X_i = 0)$  of the infection in the *i*-th individual. In addition, let the continuous variable *Y* represent the value of a diagnostic test, and let us assume that it can be described by a known distribution *Y* if  $X_i = 0$ . Finally, let *t* be the threshold of the binary classification (healthy versus infected) based on the observation of *Y*. Thus, we can set the following classification rule:

- If  $Y < t \rightarrow X = 0$  (a negative result, i.e., the individual is classified as healthy).
- If  $Y > t \to X = 1$  (a positive result, i.e., the individual is classified as infected).

The opposite inequalities can also be applied. Nevertheless, the reasoning is the same. Sensitivity and specificity, which are inversely correlated, can be computed and clearly will depend on the chosen cut-point t [7].

When dealing with pooled samples, the diagnostic test is performed on 1/n of the mixture of the n samples. The distribution is no longer D, but the distribution of the mean of n (independent) random variables identically distributed to Y, say  $Y_n$ . Let  $X_n$  be the classification of a pooled sample of size n. Under these conditions, we can define the following classification rule:

- If  $Y_n \le t_n \to X_n = 0$  (a negative result, i.e., all individuals are classified as healthy).
- If  $Y_n > t_n \to X_n = 1$  (a positive result, i.e., at least one individual is infected).

Hence, if the observed value  $Y_n$  exceeds a given threshold  $t_n$ , individual tests are required to identify which are the infected individuals. Application of pooling strategies is recommended mainly for low prevalence contexts (a positive pooled result implies the performance of n+1 tests instead of the standard n individual tests).

# 3.1.2 Bile Acid Loss Syndrome

Bile acid loss syndrome, arising from disrupted bile acid reabsorption in the terminal ileum, manifests with symptoms like diarrhea. 7-Alpha-hydroxy-4-cholesten-3-one (C4) acts as a semiquantitative serum marker for bile acid synthesis in humans. C4, a precursor of cholic acid in the classic bile acid synthesis pathway from cholesterol, is indicative of the rate-limiting enzymatic step catalyzed by 7-alpha-hydroxylase (CYP7a1). In individuals with bile acid loss, CYP7a1 expression is elevated, leading to increased serum C4 levels, which remain relatively steady. Normal C4 values have been established, with serum concentrations above 50–60 ng/mL suggesting bile acid loss in both children and adults. There are several techniques to measure bile acid loss (e.g., 75Se-Homocholic acid taurine scintigraphy) [8].

In this study, we investigate the viability of employing a pooling strategy for binary classification using C4 as a biomarker [9]. We verify this approach through simulation, establishing guidelines for sample size n and threshold  $t_n$  selection, while also analyzing the estimated gains and error rates.

J. P. Martins et al.

#### 3.2 Methods

#### 3.2.1 C4 Distribution

The normal values distribution of C4 in healthy individuals was modeled as a lognormal distribution, with a mean of 22.8 ng/mL and a standard deviation of 15.8 ng/mL, as determined by Freudenberg et al. [10]. Their study on children yielded conclusions consistent with other research conducted on adults. Additionally, neither sex nor age demonstrated predictive significance for C4 levels. Information regarding the C4 values of the 12 unhealthy individuals found in that study was extracted by digitizing a plot using WebPlotDigitizer software [11].

In recent years, there have been no studies establishing an incidence rate for this bile acid loss syndrome. Since there is a clear association between this syndrome and short bowel syndrome (SBS) [12], studies on the prevalence of SBS were used. SBS is a rare disease with prevalences lower than 1% [13]. Therefore, it was decided to set a value of 2% for the prevalence rate on the subsequent simulation study, so that the estimates regarding sample size are conservative (as a lower prevalence tends to result in a larger pooled sample size) [7].

#### 3.2.2 Simulation

The receiver operating characteristic (ROC) curve illustrates the changes in  $\varphi_s$  and  $\varphi_e$ , as the cut-point traverses all possible values, ranging from categorizing all individuals as infected to the opposite extreme of classifying all as healthy. The area under the ROC curve (AUC) is perhaps the most used metric for evaluating the diagnostic precision of binary classification methods. To avoid instances where the test on a pooled sample has low diagnostic power, only cases where the respective ROC curve exhibits an AUC of at least 0.9 were considered.

A simulation study was performed through the R software [14] using the pROC package [15]. AUC values ranging from 0.9 to 0.99 were included, with increments of 0.01. For each AUC value, pooled sample sizes ranged from 2 to 50 were considered. The largest sample size (and subsequently the lowest RC) corresponding to each AUC was recorded, along with the threshold at which the highest AUC was achieved within that sample size. All scenarios were analyzed using  $10^4$  replicas.

#### 3.3 Results

The optimal (highest) sample size corresponding to each value of the AUC is depicted in Fig. 3.1.

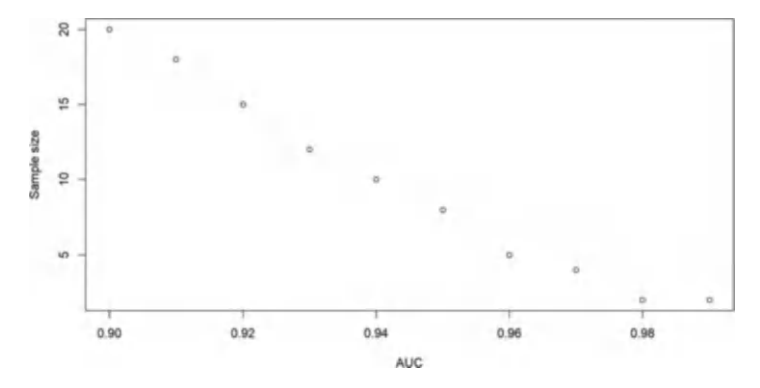


Fig. 3.1 Maximum pooled sample size for each AUC value

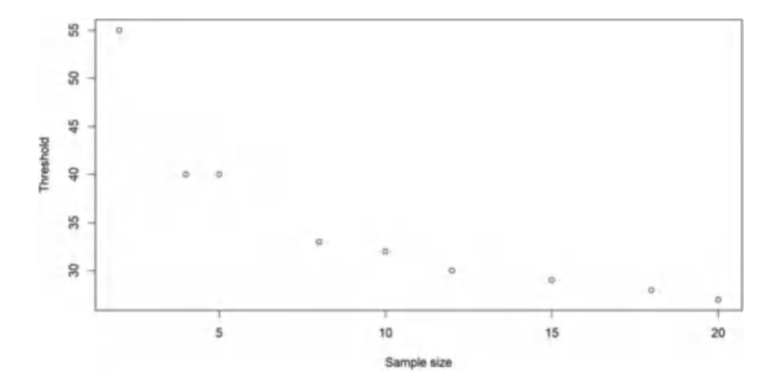


Fig. 3.2 Best threshold for the selected pooled sample sizes

Sample size diminishes linearly from 20 to 2, as AUC increases, demonstrating a strong linear trend (coefficient of determination  $r^2 = 0.977$ ). Interestingly, the sample size remains constant at n = 2 for AUC values of 0.98 and 0.99.

The threshold associated with the previous sample size is presented in Fig. 3.2. It exhibits a decreasing trend, as the sample size increases.

The performance of the diagnostic strategy can be assessed through sensitivity and specificity. The values of these measures for the pooled sample sizes presented in Fig. 3.1 are displayed in Fig. 3.3. Higher values of AUC are related to higher values of sensitivity and specificity. However, neither sensitivity nor specificity is consistently higher than the other for all considered AUC values. For an AUC of 0.98 and 0.99, the sensitivity attained is 100%, coupled with a specificity of 98.2%. These values surpass 0.90 across all AUC values, except for the specificity of the pooling strategy with an AUC of 0.90.

The RC of each strategy is presented in Fig. 3.4. The relative cost of each approach does not follow a consistent pattern across the range of AUC variation.

J. P. Martins et al.

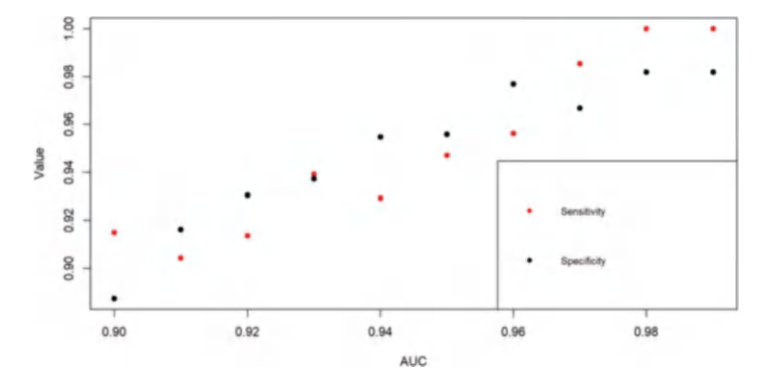


Fig. 3.3 Sensitivity and specificity of the best-pooled sampling strategy (with the lowest relative cost) verifying a predefined AUC value

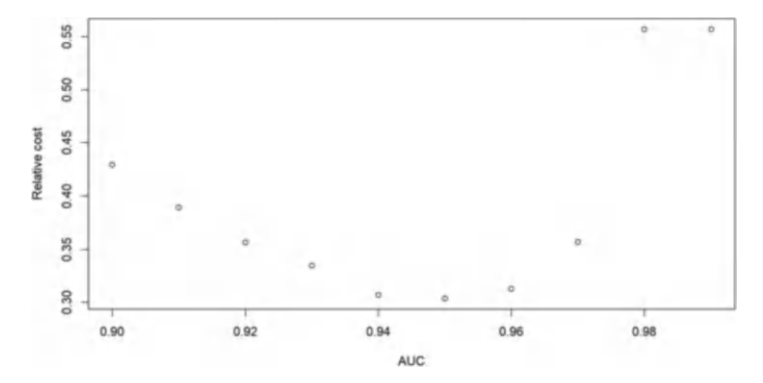


Fig. 3.4 Relative cost of the pooled sampling strategy for each AUC value

However, in all cases, the savings are high. The relative cost ranges from 0.303 (n = 8) to 0.557 (n = 2).

#### 3.4 Discussion

This is to our knowledge the first work presenting a protocol for a pooling strategy concerning a diagnostic test that is based on a continuous variable and uses real data. Several studies have focused on utilizing pooled samples in estimation tasks, and the rationale is evident [16]. It aims to mitigate the expected decrease in sensitivity compared to individual testing, caused by the dilution effect. However, it was unexpected to discover that with a pooled sample size of 2, achieving 100% sensitivity is feasible while also achieving significant cost savings (with a cost reduction higher than 40%). On the other hand, if an AUC of 0.95 (n=8) is considered, the reduction attains the value of 70%. The true RC may be even lower

than what we have reported. For instance, the prevalence rate might be not as high as the assumed value of 2%.

The threshold for each sample size decreases with the pooled sample size n. As the prevalence is low, the dilution effect increases with n resulting in a lower threshold to identify the presence of an unhealthy individual in the pooled sample. From Fig. 3.4, it is clear that increasing the pooled sample size does not necessarily mean a reduced cost. The relative cost depends on another factor beyond the sample size: the positive rate of the pooled tests. A high number of positive pools result in a great number of tests.

Unlike individuals without the bile acid loss syndrome, there is no probability distribution for C4 values in individuals with this syndrome. Therefore, it was necessary to simulate these values through random selection of individual values, which constitutes a limitation of this study.

#### 3.5 Conclusion

This work showed for the first time with real data that how pooled sample strategies can be implemented in a real context, when the diagnostic test depends on a continuous variable.

It is important to continue to develop these strategies to save resources [17]. Although these types of strategies are not a standard approach, especially in developed countries, they can also assume an important role in particular situations (such as pandemics) where even in those countries resources can be limited and pooling schemes can be part of the solution [18–20].

**Acknowledgments** This work is partially financed by national funds through FCT—Fundação para a Ciência e a Tecnologia under the project UIDB/00006/2020. DOI: 10.54499/UIDB/00006/2020 (https://doi.org/10.54499/UIDB/00006/2020).

#### References

- R. Dorfman, The detection of defective members of large populations. Ann. Math. Stat. 14(4), 436–440 (1943)
- S.Y. Kim, J. Lee, H. Sung, H. Lee, M.G. Han, C.K. Yoo, S.W. Lee, K.H. Hong, Pooling upper respiratory specimens for rapid mass screening of COVID-19 by real-time RT-PCR. Emerg. Infect. Dis. 26(10), 2469–2472 (2020). https://doi.org/10.3201/eid2610.201955
- K. Kusonmano, M. Netzer, C. Baumgartner, M. Dehmer, K.R. Liedl, A. Graber, Effects of pooling samples on the performance of classification algorithms: A comparative study. Sci. World J. 2012(1), 1–10 (2012). https://doi.org/10.1100/2012/278352
- S.C. Liu, K.S. Chiang, C.H. Lin, W.C. Chung, S.H. Lin, T.C. Yang, Cost analysis in choosing group size when group testing for potato virus Y in the presence of classification errors. Ann. Appl. Biol. 159(3), 491–502 (2011). https://doi.org/10.1111/j.1744-7348.2011.00513.x

- N. Grobe, A. Cherif, X. Wang, Z. Dong, P. Kotanko, Sample pooling: Burden or solution? Clin. Microbiol. Infect. 27(9), 1212–1220 (2021). https://doi.org/10.1016/j.cmi.2021.04.007
- N. Bogere, F. Bongomin, A. Katende, K. Ssebambulidde, W. Ssengooba, H. Ssenfuka, E. Kigozi, S. Biraro, D.P. Kateete, I. Andia-Biraro, Performance and cost-effectiveness of a pooled testing strategy for SARS-CoV-2 using real-time polymerase chain reaction in Uganda. Int. J. Infect. Dis. 113(12), 355–358 (2021). https://doi.org/10.1016/j.ijid.2021.10.038
- R. Santos, M. Felgueiras, J.P. Martins, L.F. Liliana Ferreira, Accuracy measures for binary classification based on a quantitative variable. REVSTAT-Stat. J. 17(2), 223–244 (2019). https://doi.org/10.57805/REVSTAT.V1712.266
- A. Baena García, F. Partida Palma, S. García Martínez, M. De Bonilla Candau, M. Pajares Vinardell, 75Se-Homocholic acid taurine scintigraphy (75SeHCAT<sup>®</sup>), a standard benchmark test in bile acid malabsorption? Revista Española de Medicina Nuclear e Imagen Molecular (English Edition) 38(5), 305–311 (2019). https://doi.org/10.1016/j.remnie.2019.02.008
- N. Labarile, S. Ghosh, S.C. Ng, J. Walters, M. Iacucci, Tests that now deserve to be more widely adopted in IBD clinical practice. Ther. Adv. Gastroenterol. 13(1), 175628482094408 (2020). https://doi.org/10.1177/1756284820944088
- F. Freudenberg, F. Gothe, F. Beigel, C. Rust, S. Koletzko, Serum 7-alpha-hydroxy-4-cholesten-3-one as a marker for bile acid loss in children. J. Pediatr. 163(5), 1367–1371.e1 (2013). https://doi.org/10.1016/j.jpeds.2013.06.083
- A. Rohatgi, WebPlotDigitizer (4.6). https://automeris.io/WebPlotDigitizer (2022). Accessed Jan 2024
- P. Vijayvargiya, M. Camilleri, A. Taylor, I. Busciglio, E.V. Loftus, L.J. Donato, Combined fasting serum C4 and primary bile acids from a single stool sample to diagnose bile acid diarrhea. Gastroenterology 159(5), 1952–1954.e2 (2020). https://doi.org/10.1053/j.gastro.2020.07.001
- M. Winkler, K. Tappenden, Epidemiology, survival, costs, and quality of life in adults with short bowel syndrome. Nutr. Clin. Pract. 38(S1), S17 (2023). https://doi.org/10.1002/ ncp.10964
- 14. R Core Team, R: A Language and Environment for Statistical Computing. (R Foundation for Statistical Computing, 2021). https://www.R-project.org/. Accessed Jan 2024.
- X. Robin, N. Turck, A. Hainard, N. Tiberti, F. Lisacek, J.-C. Sanchez, M. Müller, pROC: An open-source package for R and S+ to analyze and compare ROC curves. BMC Bioinf. 12(1), 77 (2011). https://doi.org/10.1186/1471-2105-12-77
- J.P. Martins, R. Santos, M. Felgueiras, Estimation of prevalence in rare disease using pooled samples. J. Phys. Conf. Ser. 1564(1), 012028 (2020). https://doi.org/10.1088/1742-6596/1564/ 1/012028
- 17. P. Mandhan, M. Sharma, S. Pandey, N. Chandel, N. Chourasia, A. Moun, D. Sharma, R. Sukar, N. Singh, S. Mathur, A. Kotnala, N. Negi, A. Gupta, A. Kumar, R. Suresh Kumar, P. Kumar, S. Singh, A regional pooling intervention in a high-throughput COVID-19 diagnostic laboratory to enhance throughput, save resources and time over a period of 6 months. Front. Microbiol. 13(1), 858555 (2022). https://doi.org/10.3389/fmicb.2022.858555
- A.M. Abdelrazik, M.N.E. Said, H.M. Abdelaziz, Evaluation of pooling strategy of SARS-CoV-2 RT-PCR in limited resources setting in Egypt at low prevalence. Comp. Clin. Pathol. 32(3), 375–381 (2023). https://doi.org/10.1007/s00580-023-03445-6
- R. Barathidasan, F.M. Sharmila, R.V. Raj, G. Dhanalakshmi, G. Anitha, R. Dhodapkar, Pooled sample testing for COVID-19 diagnosis: Evaluation of bi-directional matrix pooling strategies. J. Virol. Methods 304(6), 114524 (2022). https://doi.org/10.1016/j.jviromet.2022.114524
- I. Praharaj, A. Jain, M. Singh, A. Balakrishnan, R. Dhodapkar, B. Borkakoty, M. Ashok, P. Das, D. Biswas, U. Kalawat, J. Turuk, A. Sugunan, S. Prakash, A. Singh, R. Barathidasan, S. Subhadra, J. Sabat, M. Manjunath, P. Kanta, et al., Pooled testing for COVID-19 diagnosis by real-time RT-PCR: A multi-site comparative evaluation of 5- & 10-sample pooling. Indian J. Med. Res. 152(1), 88 (2020). https://doi.org/10.4103/ijmr.IJMR\_2304\_20

# Chapter 4 A Novel Enhancement for the Best Master Clock Algorithm Associated with the Precision Time Protocol for

the Fractional Gaussian Noise Case



Monika Pinchas (1)

#### 4.1 Introduction

Precision time protocol (PTP) [1] is a two-way packet message exchange protocol between a Master and a Slave, used for frequency and time synchronization required in many areas such as electrical grid networks, cellular base station synchronization, industrial control, communication in financial markets [2, 3], and Industrial Internet of things (IIoT) [4]. The path between the Master and the Slave is named the uplink, while the path between the Slave and the Master is called the downlink. The downlink and the uplink have different paths, and each consists of a fixed delay in addition to a random delay [3]. This random delay is known in the literature as packet delay variation (PDV) [3]. The PDV may rise in response to high network traffic, which might negatively affect the clock skew and offset estimator's performance. A long-range dependence (LRD) process could be used to characterize the network [5–8]. The fractional Gaussian noise (fGn) model, which is a part of the LRD process, is used in this study with the Hurst exponent parameter H in the range of  $0.5 \le H < 1$ . Please note that the fGn model reduces to the white Gaussian model for H = 0.5.

There might be multiple Master clocks in the network. Using the best Master Clock Algorithm (BMCA) [9], each Slave clock will select the best available Master clock among all the clocks on a PTP network. To determine the best Master clock, the BMCA considers via the Announcement message from each potential Master the user-configurable priority, clock accuracy, clock stability, and network distance when multiple paths are available to a potential Master [10, 11]. But, it does not consider the PDV. It is pretty evident that the Slave's clock skew performance depends on the Master's clock accuracy and stability. But it also depends on the

M. Pinchas (⋈)

Department of Electrical and Electronic Engineering, Ariel University, Ariel, Israel e-mail: monikap@ariel.ac.il

42 M. Pinchas

PDV. Suppose for a moment that we have two potential Master clocks named Master A and Master B, and we wish to select one of them to be the Master clock for the Slave. Master A has better clock accuracy and stability compared to Master B. But, the PDV from the uplink and downlink paths from Master A to the Slave is much higher than that observed from the uplink and downlink paths from Master B to the Slave. Thus, the PDV from the uplink and downlink paths from Master A to the Slave may cause such degradation in the Slave's clock skew performance from the mean square error (MSE) point of view that it is even worse compared to the Slave's clock skew performance if Master B would have been selected as the best Master clock. Therefore, some information related to the PDVs on the uplink and downlink paths between the potential Master clock and Slave clock is crucial for selecting the most appropriate Master clock for the Slave and thus should be taken into consideration in the BMCA.

Link congestion occurs in cases of traffic overloading, when a link or network node handles data above its capacity. It is common knowledge that network congestion causes serious degradation in synchronization performance [12]. But, as stated in Ref. [12], the BMCA does not consider it in its algorithm. Thus, a modified BMCA was proposed by Murakami and Horiuchi [12] that introduced a link congestion estimation to the BMCA to switch to a redundant Master in case of link congestion, which would otherwise cause a deterioration of the synchronization quality.

In Ref. [13], a method was proposed to select the best Master with a sequence table of the predefined Master. This proposed method cuts the convergence time generated while comparing the message for selecting a Master with the BMCA and assigning the role of ports. In other words, this proposed method can resynchronize the network faster than the existing BMCA. Consequently, the network can provide streaming services with low latency.

Converged wired and wireless network deployment opens up mobile use cases, but it also brings unstable network devices and erratic communication channels. Thus, according to Ref. [14], there may be cases where the Master, chosen by the BMCA, cannot achieve the best synchronization quality because of hierarchical factors, such as that most of the network devices are connected via an unstable radio link. In other words, the synchronization hierarchy impacts the synchronization quality [14]. However, the BMCA does not take this into account. Schüngel et al. [14] proposed an Advanced Grand Master Selection (AGMS) method that also considers architectural aspects. In contrast to Ref. [12], which considers the dynamic characteristics of network traffic in some way, Ref. [14] claims that the AGMS emphasizes static and probabilistic network aspects, such as the actual architecture and link uncertainty. So, up until now, the PDV was not considered when choosing the optimal Master selection based on the dynamic features of network traffic, unless it resulted in link congestion.

In this work, an enhancement part for the BMCA is derived that contains some information on the PDVs seen from the Master-to-Slave and Slave-to-Master paths that should be taken into consideration when selecting the best Master clock for the Slave. A lower value for the enhancement part means that the Slave will

suffer from a lower PDV compared to the case where the enhancement part is higher. Therefore, when two potential Masters have the same user-configurable priority, clock accuracy, and clock stability but different values for the calculated enhancement part for the BMCA, the BMCA should select the Master associated with the lowest value for the enhancement part. Potential Masters usually have excellent clock characteristics, and differences in their clock characteristics may lead to a degradation in the clock skew performance of the Slave. However, this degradation in the clock skew performance is usually small compared to the degradation in the clock skew performance caused by the PDV. Thus, the PDV must also be a factor considered by the BMCA when selecting the best Master clock. It should be pointed out that the enhancement part for the BMCA is valid for the fGn case for the Hurst exponent H in the range of  $0.5 \le H < 1$ , which depends neither on the constant time offset between the Master and Slave clocks nor on the clock skew between them. In addition, it does not depend on the constant delays between the Master and Slave. It should be noted that for the Gaussian (H = 0.5) case, the proposed enhancement part for the BMCA equals approximately twice the two-way round PDV variances. Thus, searching for a lower value for the enhancement part makes sense. With the proposed enhancement part for the BMCA, the BMCA may better select the optional Master in the Ethernet network based also on the PDV, which has not been done up to now.

# 4.2 System Description

We consider the system from Refs. [15] and [16] in this paper, described in Fig. 4.1 (recalled from Ref. [15]), where  $t_1$ ,  $t_2$ ,  $t_3$ , and  $t_4$  are the PTP timestamps. In the following, we denote those timestamps as  $t_1[j]$ ,  $t_2[j]$ ,  $t_3[j]$   $t_4[j]$ , where j is the j-th Sync period for  $j = 1, 2, 3, \ldots, J$ , and J is the total amount of Sync periods. In the following, we denote  $T_{sync}$  as the Sync message period. The relationship between the four PTP timestamps are given based on Refs. [3, 15–18] as:

$$t_{1}[j] + d_{ms} + w_{1}[j] = t_{2}[j](1+\alpha) + Q$$
  

$$t_{4}[j] - d_{sm} - w_{2}[j] = t_{3}[j](1+\alpha) + Q$$
(4.1)

where  $w_1[j]$  and  $w_2[j]$  are the PDVs for the j-th Sync period seen from the Master-to-Slave and Slave-to-Master paths, respectively. Please note that the Master-to-Slave and Slave-to-Master paths are also known as Forward and Reverse paths, respectively. The parameters  $\alpha$  and Q are the clock skew and clock offset between the Master and Slave clocks, respectively. In addition,  $d_{ms}$  and  $d_{sm}$  are the Forward and Reverse fixed delays, respectively.

In this work, we adapt the assumptions made in Refs. [15] and [16] that are as follows:

44 M. Pinchas

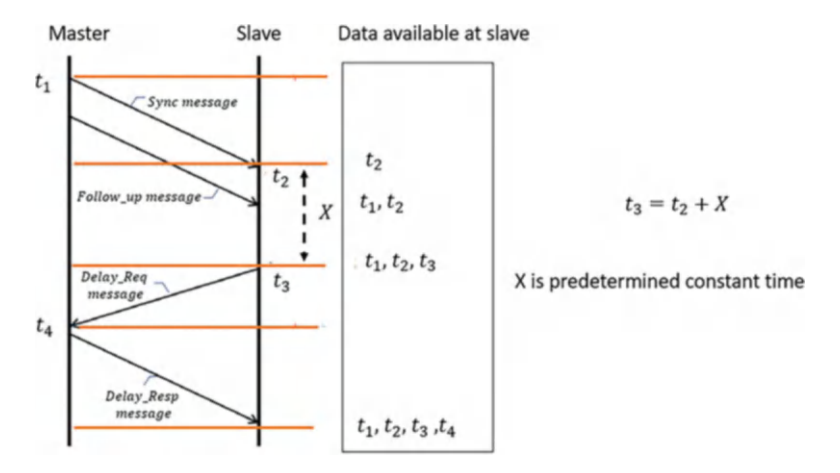


Fig. 4.1 PTP\_diagram

1. The PDV is characterized as an fGn noise with zero mean, based on Ref. [5], given as:

for 
$$j=m$$
: 
$$E\left[w_{n}\left[j\right]w_{n}\left[m\right]\right]=\sigma_{mn}^{2}$$

for  $j \neq m$ :

$$E\left[w_{n}\left[j\right]w_{n}\left[m\right]\right] = \frac{\sigma_{w_{n}}^{2}}{2} \left(\left\|j - m| - 1|^{2H_{p}} - 2|j - m|^{2H_{p}} + \left\|j - m| + 1|^{2H_{p}}\right)\right)$$

$$(4.2)$$

where n=1, 2, E[.] is the expectation operator, and p=F, R. Please note that the Hurst exponent parameters  $H_F$  and  $H_R$  are in the range of  $0.5 \le H_F$ ,  $H_R < 1$ , where  $H_F$  and  $H_R$  are the Hurst exponent parameters for the Forward and Reverse paths, respectively.

2. The Forward and Reverse PDVs are independent. Namely, we have:

$$E[w_1[n] w_2[m]] = 0;$$
 for every  $n, m$  (4.3)

In a real-world Ethernet network, the assumption of independent PDVs is realistic. As already was mentioned earlier in this work, there may be several potential Master clocks available in the Ethernet network to serve as the best Master clock for a Slave. Each such Master sends periodically an Announcement message to the Slave, where the content in the Announcement message is used in the BMCA. Those Announcement messages do not contain any information on the PDVs seen from the Master-to-Slave and Slave-to-Master paths. In the next

section, we derive the enhancement part for the BMCA containing information on the PDVs seen from the Master-to-Slave and Slave-to-Master paths that should be taken into consideration when selecting the best Master for the Slave. A lower value for the enhancement part means that the Slave will suffer from a lower PDV compared to the case where the enhancement part has a high value.

#### 4.3 The Enhancement Part for the BMCA

Based on (4.1), we may write:

$$t_{2}[j] - t_{1}[j] = w_{1}[j] + d_{ms} - Q - \alpha t_{2}[j]$$

$$t_{4}[j] - t_{3}[j] = w_{2}[j] + d_{sm} + Q + \alpha t_{3}[j]$$
(4.4)

Now, adding the first equation with the second equation from (4.4), we obtain:

$$(t_4[j] - t_3[j]) + (t_2[j] - t_1[j]) = (w_2[j] + w_1[j]) + (d_{sm} + d_{ms}) + \alpha (t_3[j] - t_2[j])$$

$$(4.5)$$

According to Refs. [15] and [16], X is a constant predefined parameter (please refer to Fig. 4.1). Thus, by using the additional notations:

$$X = t_{3}[j] - t_{2}[j]$$

$$\xi[j] = w_{2}[j] + w_{1}[j]$$

$$D = d_{sm} + d_{ms}$$
(4.6)

we may write (4.5) as:

$$(t_4[j] - t_3[j]) + (t_2[j] - t_1[j]) = \xi[j] + D + \alpha X \tag{4.7}$$

Please note that D,  $\alpha$ , and X are constant parameters. The (j + 1) -th sync period related to (4.7) can be written as:

$$(t_4[j+1] - t_3[j+1]) + (t_2[j+1] - t_1[j+1]) = \xi[j+1] + D + \alpha X$$
(4.8)

Next we define:

$$T_l[i] = t_l[i+1] - t_l[i]; l = 1, 2, 3, 4$$
 (4.9)

46 M. Pinchas

By subtracting (4.8) with (4.7) and applying (4.9), we obtain:

$$(T_4[j] - T_3[j]) + (T_2[j] - T_1[j]) = \varsigma[j]$$
 (4.10)

where

$$\zeta[i] = \xi[i+1] - \xi[i]$$
 (4.11)

Next, we calculate the variance of (4.11). By using (4.6), we have:

$$E\left[\varsigma^{2}[j]\right] = E\left[\left(\xi[j+1] - \xi[j]\right)^{2}\right]$$

$$= E\left[\left(\left(w_{2}[j+1] + w_{1}[j+1]\right) - \left(w_{2}[j] + w_{1}[j]\right)\right)^{2}\right]$$
(4.12)

Now, by using the assumption 2 from the Sect. 4.2, we can rewrite (4.12) with the help of (4.3) as:

$$E\left[\varsigma^{2}[j]\right] = E\left[w_{2}^{2}[j+1] + w_{1}^{2}[j+1] - 2\left(w_{2}[j+1]w_{2}[j]\right) + w_{1}[j+1]w_{1}[j]\right] + w_{2}^{2}[j] + w_{1}^{2}[j]$$

$$(4.13)$$

Next, by applying assumption 1 from Sect. 4.1, (4.13) can be written with the help of (4.2) as:

$$E\left[\varsigma^{2}[j]\right] = 2\sigma_{w_{2}}^{2} + 2\sigma_{w_{1}}^{2} - \sigma_{w_{2}}^{2}\left(-2 + 2^{2H_{R}}\right) - \sigma_{w_{1}}^{2}\left(-2 + 2^{2H_{F}}\right)$$

$$= \sigma_{w_{2}}^{2}\left(4 - 2^{2H_{R}}\right) + \sigma_{w_{1}}^{2}\left(4 - 2^{2H_{F}}\right)$$
(4.14)

Thus, by using (4.10) and (4.14), we have:

$$E\left[\left(\left(T_{4}[j] - T_{3}[j]\right) + \left(T_{2}[j] - T_{1}[j]\right)\right)^{2}\right] = E\left[\varsigma^{2}[j]\right]$$

$$= \sigma_{w_{2}}^{2}\left(4 - 2^{2H_{R}}\right) + \sigma_{w_{1}}^{2}\left(4 - 2^{2H_{F}}\right)$$
(4.15)

Our next step is to use the following approximation:

$$E\left[\left(\left(T_{4}\left[j\right] - T_{3}\left[j\right]\right) + \left(T_{2}\left[j\right] - T_{1}\left[j\right]\right)\right)^{2}\right]$$

$$\simeq \frac{1}{J-1} \sum_{j=1}^{J-1} \left(\left(T_{4}\left[j\right] - T_{3}\left[j\right]\right) + \left(T_{2}\left[j\right] - T_{1}\left[j\right]\right)\right)^{2}$$
(4.16)

Thus, based on (4.16) and (4.15), we obtain the "Enhancement Part" for the BMCA:

$$\frac{1}{J-1} \sum_{j=1}^{J-1} ((T_4[j] - T_3[j]) + (T_2[j] - T_1[j]))^2 \simeq \sigma_{w_2}^2 \left(4 - 2^{2H_R}\right) + \sigma_{w_1}^2 \left(4 - 2^{2H_F}\right)$$
(4.17)

Please note that for the white Gaussian case ( $H_R = H_F = 0.5$ ), the "Enhancement Part" in (4.17) turns to:

$$\frac{1}{J-1} \sum_{j=1}^{J-1} ((T_4[j] - T_3[j]) + (T_2[j] - T_1[j]))^2 \simeq 2\sigma_{w_2}^2 + 2\sigma_{w_1}^2$$
 (4.18)

which equals approximately twice the two-way round PDV variances.

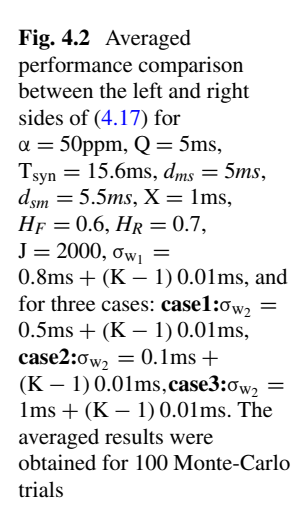
#### 4.4 Simulation

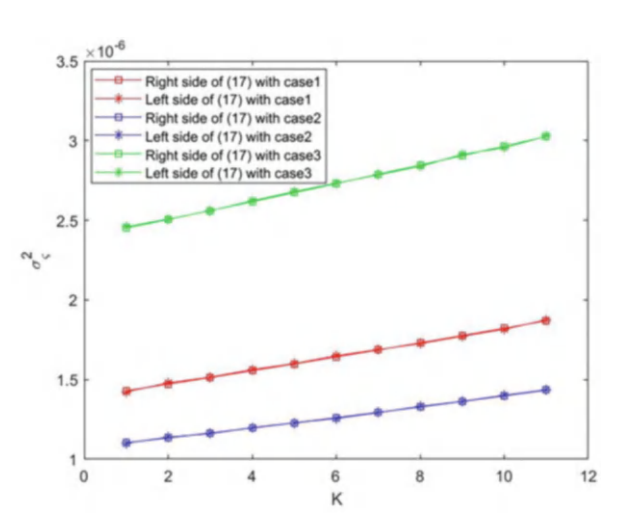
In this section, we test the "Enhancement Part" (4.17). In other words, we compare the averaged results obtained from the left and right sides of (4.17) for various PDV variances for the uplink and downlink paths for the total amount of sync periods of 200 and 2000 via simulation, considering the fGn case with different Hurst exponent parameters for the uplink and downlink paths, different fixed delays on the Forward and Reverse paths, and applying a clock skew of 50ppm with a clock offset of 5ms. According to Figs. 4.2 and 4.3, the left and right sides of (4.17) supply approximately the same averaged results, meaning that (4.17) holds. According to Figs. 4.2 and 4.3, the expression in (4.17) can indeed supply some insight into the traffic load in the network. Namely, when the two-way round PDV is high, the "Enhancement Part" (4.17) will supply a higher value compared to the case where the two-way round PDV is low. Thus, using (4.17) in the BMCA could be very useful.

#### 4.5 Conclusion

In this paper, an enhancement part for the BMCA was obtained that contains some information on the two-way round PDV variances for the fGn case with the Hurst exponent H in the range of  $0.5 \le H < 1$ , which depends neither on the constant time offset between the Master and Slave clocks nor on the clock skew between them. It

48 M. Pinchas





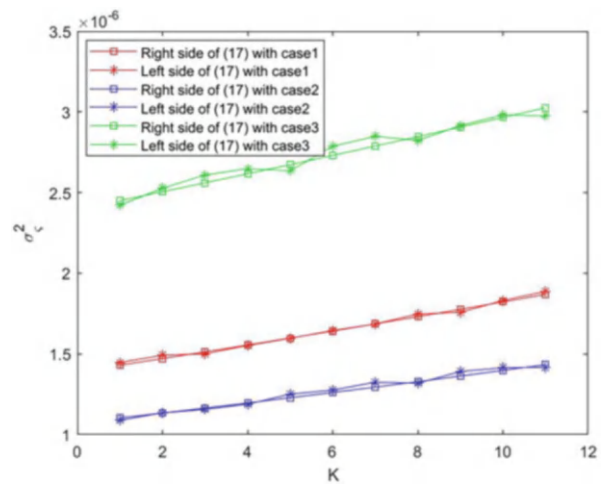


**Fig. 4.3** Averaged performance comparison between the left and right sides of (4.17) for  $\alpha=50 \mathrm{ppm},\ Q=5 \mathrm{ms},\ T_{\mathrm{syn}}=15.6 \mathrm{ms},\ d_{ms}=5 \mathrm{ms},\ d_{sm}=5.5 \mathrm{ms},\ X=1 \mathrm{ms},\ H_F=0.6,\ H_R=0.7,\ J=200,\ \sigma_{\mathrm{w}_1}=0.8 \mathrm{ms}+(\mathrm{K}-1)\,0.01 \mathrm{ms},\ \mathrm{and}\ \mathrm{for}\ \mathrm{three}\ \mathrm{case1:}\sigma_{\mathrm{w}_2}=0.5 \mathrm{ms}+(\mathrm{K}-1)\,0.01 \mathrm{ms},\ \mathrm{case2:}\ \sigma_{\mathrm{w}_2}=0.1 \mathrm{ms}+(\mathrm{K}-1)\,0.01 \mathrm{ms},\ \mathrm{case3:}\sigma_{\mathrm{w}_2}=1 \mathrm{ms}+(\mathrm{K}-1)\,0.01 \mathrm{ms}.$  The averaged results were obtained for 100 Monte-Carlo trials

also does not depend on the fixed delays seen on the Master-to-Slave and Slave-to-Master paths. Thus, considering the enhancement part in the BMCA may lead to a better selection of the optional Master in the Ethernet.

#### References

- A. Douglas, IEEE 1588-2019 IEEE Standard for a Precision Clock Synchronization Protocol for Networked Measurement and Control Systems. https://standards.ieee.org/standard/1588-2019.html, 2019
- 2. A.G. Bordogna, R.S. Blum, S. Kishore, M. Bordogna, Min-imax optimum joint frequency and phase recovery in IEEE 1588. IEEE Trans. Commun. **63**(9), 3350–3362 (2015)
- A.K. Karthik, R.S. Blum, Robust clock skew and offset estimation for IEEE 1588 in the presence of unexpected deterministic path delay asymmetries. IEEE Trans. Commun. 68 (2020). https://doi.org/10.1109/TCOMM.2020.2991212
- 4. H. Puttnies, P. Danielisx, D. Timmermann, PTP-LP: Using linear programming to increase the delay robustness of IEEE 1588 PTP, in *IEEE Global Communications Conference*, (2018)
- L. Ming, W. Zhao, On bandlimitedness and lag-limitedness of fractional Gaussian noise. Physica A 392, 1955–1961 (2013). https://doi.org/10.1016/j.physa.2012.12.035
- 6. L. Ming, Generalized fractional Gaussian noise and its application to traffic modeling. Physica A **579** (2021). https://doi.org/10.1016/j.physa.2021.126138
- L. Ming, Multi-fractal traffic and anomaly detection in computer communications, 1st edn. (CRC Press, Boca Raton, 2022). https://doi.org/10.1201/9781003268802
- 8. L. Ming, Fractal teletraffic modeling and delay bounds in computer communications, 1st edn. (CRC Press, Boca Raton, 2022). https://doi.org/10.1201/9781003354987
- IEEE standard for a precision clock synchronization protocol for networked measurement and control systems amendment 3: Precision Time Protocol (PTP) En-hancements for Best Master Clock Algorithm (BMCA) Mechanisms, IEEE Std 1588a-2023 (Amendment to IEEE Std 1588-2019 as amended by IEEE Std 1588b-2022 and IEEE Std 802.1588g-2022), pp. 1–54, 6 Dec. 2023, https://doi.org/10.1109/IEEESTD.2023.10347018, 2023
- chrome-extension://efaidnbmnnnibpcajpcglclefindmkaj/ media/assets/internet/documents/precision-time-protocol-application-note-en.pdf
- 11. https://notes.networklessons.com/ptp-best-master-clock-algorithm
- 12. T. Murakami, Y. Horiuchi, A master redundancy technique in IEEE 1588 synchronization with a link congestion estimation, in *IEEE ISPCS*, (2010)
- 13. Y. Jeon, J. Lee, S. Park, An efficient method of reselecting Grand Master in IEEE 802.1as, in *IEEE APCC*, (2014), pp. 303–308
- M. Schüngel, S. Dietrich, L. Leurs, D. Ginthör, S.-P. Chen, M. Kuhn, Advanced grandmaster selection method for converged wired and wireless networks, in 22nd IEEE International Conference on Industrial Technology (ICIT), Valencia, Spain, (2021), pp. 1007–1014. https:// doi.org/10.1109/ICIT46573.2021.9453490
- Y. Avraham, M. Pinchas, A novel clock skew estimator and its performance for the IEEE 1588v2 (PTP) case in fractional Gaussian noise generalized fractional gaussian noise environment. Front. Phys. 9 (2021). https://doi.org/10.3389/fphy.2021.796811
- 16. Y. Avraham, M. Pinchas, Two novel one-way delay clock skew estimators and their performances for the fractional Gaussian noise generalized fractional Gaussian noise environment applicable for the IEEE 1588v2 (PTP) case. Front. Phys. 10 (2022). https://doi.org/10.3389/fphy.2022.867861
- A.K. Karthik, R.S. Blum, Robust phase offset estimation for IEEE 1588 PTP in electrical grid networks, in 2018 IEEE Power & Energy Society General Meeting, (2018). https://doi.org/ 10.1109/PESGM.2018.8586488
- A.K. Karthik, R.S. Blum, Optimum full information, unlimited complexity, in-variant, and minimax clock skew and offset estimators for IEEE 1588. IEEE Trans. Commun. 67, 3624– 3637 (2019). https://doi.org/10.1109/TCOMM.2019.2900317

# Chapter 5 Designing an Efficient Solar Photovoltaic Tracking System for Sustainable Electricity Generation



Hassan Abdulmouti, Zakwan Skaf, Fady Alnajjar, Rasha Abousamra, and Ahana Fatima Alex

#### 5.1 Introduction

The growing demand for greener and cleaner sources of power in the world due to the recent alarming rate of pollution growth and the depletion of fossil fuels has raised the focus on solar power plants. Many countries have set their focus on increasing the production of electrical power by solar power plants. The solar power is virtually unlimited, and many energies can be extracted from it. Noting the potentiality of solar energy by bringing to the fore the fact that the Earth receives 160,000 TW of solar insolation, while the present global demand is only 16 TW [1–25]. However, even the solar energy has all these advantages, the conversion of solar energy in the usable form is still not very economical. It needs to be complemented with a successful storage device that can stabilize the fluctuating supply due to

H. Abdulmouti (⋈) · Z. Skaf

Mechanical Engineering Division, Sharjah Men's College, Higher Colleges of Technology,

Sharjah, United Arab Emirates

e-mail: habdulmouti@hct.ac.ae; zskaf@hct.ac.ae

F. Alnajjar

Department of Computer Science and Software Engineering, College of IT, United Arab Emirates University (UAEU), Al Ain, United Arab Emirates

e-mail: fady.alnajjar@uaeu.ac.ae

R. Abousamra

Business College, Higher Colleges of Technology, Sharjah, United Arab Emirates

e-mail: rabousamra@hct.ac.ae

A. F. Alex

Department of Electrical and Electronics Engineering, Manipal Academy of Higher Education,

Dubai, United Arab Emirates

e-mail: ahana.fatima@dxb.manipal.edu

© The Author(s), under exclusive license to Springer Nature Switzerland AG 2025 N. E. Mastorakis et al. (eds.), *Computational Problems in Science and Engineering II*, https://doi.org/10.1007/978-3-031-78416-3\_5

52 H. Abdulmouti et al.

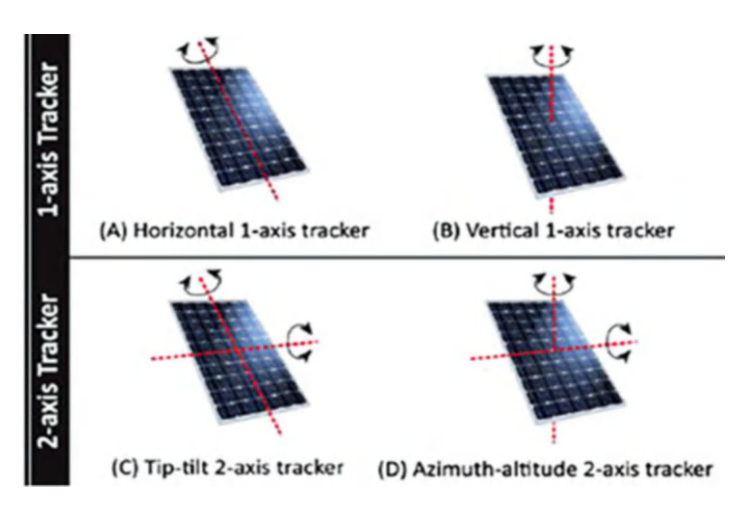


Fig. 5.1 Types of solar tracker [42]

climatic and seasonal variations. From this perspective, many countries have set their road maps for dependable and long-term usage of solar power [26–41].

Solar collectors keep the solar panels directly oriented toward sunlight, when the sun is moving concerning the Earth. Solar panels are used to increase the production of electricity from the sun. However, trackers improve the amount of solar energy that is incident on the surface of the solar panels. In photovoltaic (PV) systems, trackers are used to minimize the angle of incidence for maximum utilization of solar energy. It increases the capability of power generation. Solar trackers have optics that directly accept the solar insolation, so trackers must be placed correctly for the power generation. There are two major kinds of solar tracking systems as shown in Fig. 5.1, and they are, namely, single-axis solar tracking system (vertical-axis tracking, horizontal-axis tracking system) and dual-axis tracking system.

The design of a solar tracker is simple and can be employed with a low labor cost that makes it convenient for countries around the globe [43–59].

This paper is an investigation to bring to light the applicability of the dual-axis solar tracker system as a solar tracker for a typical house. Therefore, a solar plant that incorporates trackers is designed. The electronic system has an actuator and a motor arrangement that can easily track the sun depending on Arduino. Using a time reference, the panel is moved perfectly for 12 h to face the sun always, maximizing energy production for later usage. When the panel is oriented properly, it can provide enough surplus energy to supply the motor with the supplemental power it needs to run. With the application of an oriented and well-calibrated solar tracker, it is expected to increase production by 20–30%. This increases the overall energy yield and thereby the economy of a solar power plant. Furthermore, this paper also discusses optimizing the kind of solar tracker that should be used to minimize the cost and maximize the effectiveness. The calculated cost shows that it needs about 8.9 years to get the initial cost back, which is a very good and economical period.

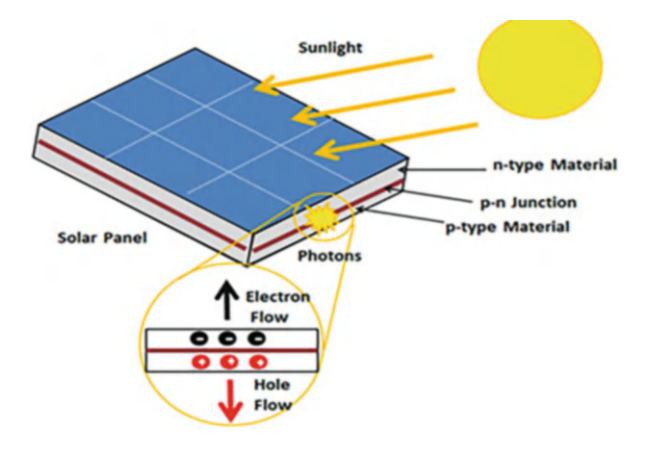
### 5.2 Methodology and Technology Elements

Phosphorus-doped (N-type) silicon is typically used as the bottom layer of a silicon PV cell, with boron-doped (P-type) silicon serving as the top layer. When these two substances come into contact, an electrical field is generated close to the cell's outermost surface; this is known as the P–N junction [60]. Figure 5.2 shows the photovoltaic effect. The highest efficiency solar cells are made from the micro morph triple junction Ge/GaAs/Gain Asp materials. The triple junction photovoltaics are very intricate, and the cost is very high. Hence, these triple junctions' cells find their application only in the satellite, where the energy consumption is very critical. For terrestrial usage, these cells are used in the high concentration mode, so that the usage of costly cells can be reduced.

By using reflectors, the sunlight can be concentrated 250–500 times. The sun is tracked day long with the help of automated arms running in servo motors to utilize most of the energy from it [62]. Photovoltaic cells are connected in series and parallel with low resistance wire to increase the voltage, current, and power supply. Photovoltaic modules are the building blocks of the solar panel. They are sealed in an environmentally safe covering. They are connected to form a larger combination of solar panels. Multiple PV modules are combined into one pre-wired, ready-to-install panel. Any number of PV modules and panels together make up the entire power-generating device, known as a photovoltaic array [63–83].

To generate more voltages, currents and power, photovoltaic cells can be wired in series and/or parallel circuits. Modules are the basic unit of a PV system, and they are made up of PV cell circuits that are sealed in an environmentally safe laminate. One or more PV modules are combined into one pre-wired, easily installed panel in the field [84–106]. A dual-axis solar tracking system is used in this design, because it has better effectiveness than the fixed solar PV panel and is 32.17% more effective in power production [107]. Figure 5.3 shows the dual-axis tracking system, which is a horizontal tilted single-axis solar tracker (HTSAT) and a vertical tracker system

**Fig. 5.2** Photovoltaic effect [61]



54 H. Abdulmouti et al.

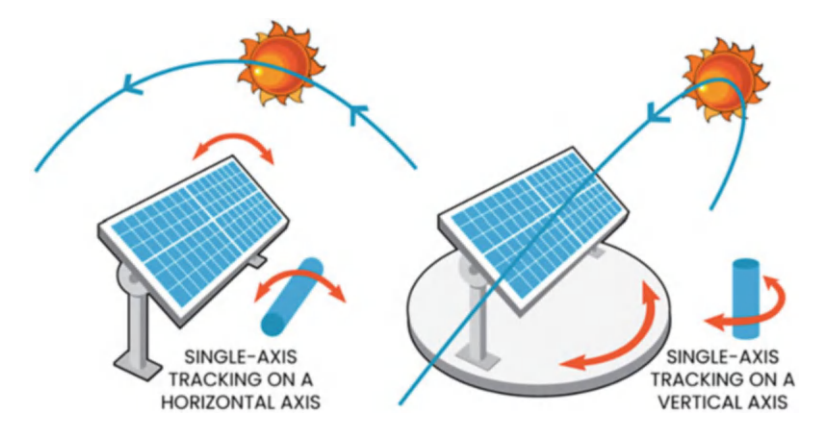


Fig. 5.3 Single-axis tracking system [108]

as they have a small angle of tilt to be stable; they are provided with a concrete structure that adds up in the total cost, and these are not known to be a scalable model [109–115].

The quality of the battery is defined based on the energy density and power density. The life of the batteries is dependent on the number of charge–discharge cycles. In contrast to this, it is possible to make a cell continuously discharge the fuel that is known as the fuel cell [116–120]. Figure 5.4 shows the flow chart of the microcontroller programming.

There are two basic types of viewers: single- and dual-axis viewers. Single-axis trackers are adjusted each month, so seasonal changes in sun position can be taken into account. The dual-axis solar tracking system is used to track the daily movement of the sun across the sky. The dual-axis trackers use one axis to track the daily movement of the sun and the other axis to track seasonal movement, eliminating the need for monthly adjustments. Single-axis solar tracker increases solar energy efficiency by approximately 25%, and dual-axis tracker increases by approximately 40%. Figure 5.5 shows the block diagram of the design that depends on the location of the sun. The movement of the sun is located using the angle of incidence detected using the sensor system in the Light-Dependent Resistor (LDR).

The design is based on the principle that the sun's rays move according to the angle of incidence. For this purpose, it is aimed to benefit from the sun's rays with maximum efficiency throughout the day. The data thus obtained are sent to the Arduino UNO that feeds them to the servo motors. The two servo motors in this work help the axes to move according to the sun angles. The two servo motors implemented in the design are controlled by the Arduino UNO to help in the movement of the solar panel as per the position of the sun. Several different mechanisms work on a set of principles to align the panel directly to the sun or to navigate the panel directly to the sun aimed at receiving maximum sunlight throughout the day. The dual-axis solar system is used in this design. The major design step here is the use of a time reference with which the panel is moved

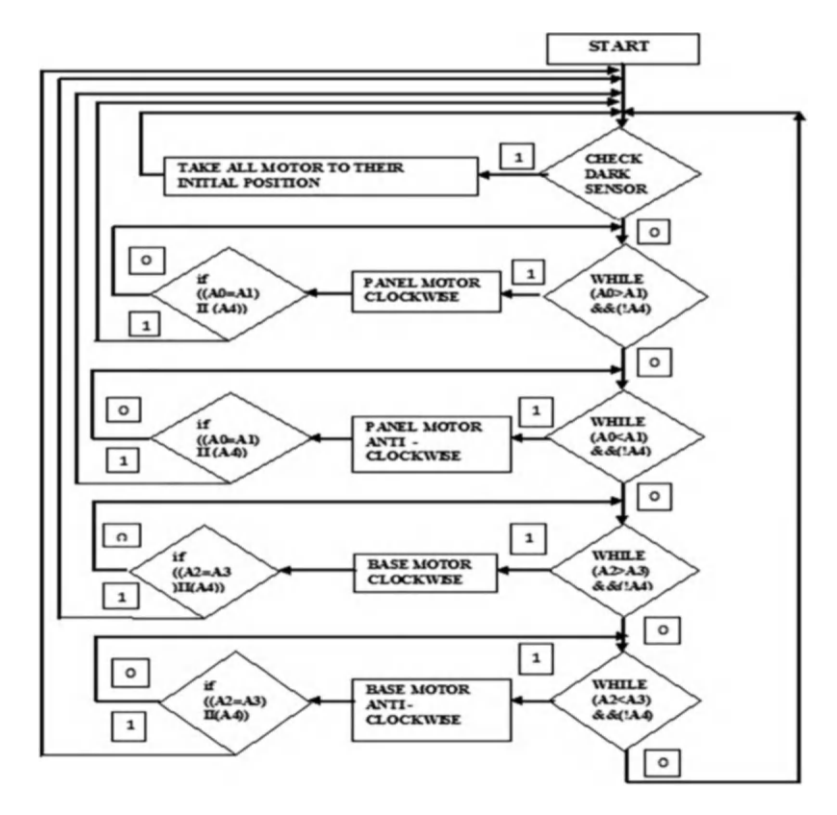


Fig. 5.4 Microcontroller programming flow chart [121]

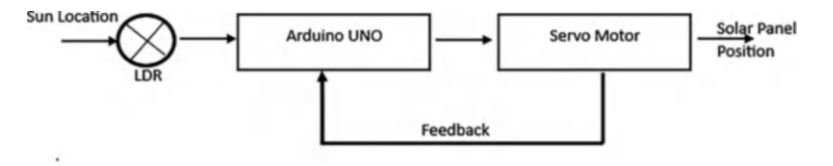


Fig. 5.5 The block diagram of the design

perfectly for 12 h, so that it always faces the sun, maximizing energy production for later usage. Figure 5.6 shows the circuit diagram connections of the LDR and the servo motors to the Arduino shield including the connection table. From the diagram, it can be seen that the LDRs are placed at four positions, so that the received light intensity is equal at all times. This four-quadrant sensor system is more efficient and helps in collecting solar energy effectively.

The energy received from the solar panel can be stored by either charging the battery or powering the Arduino. The design circuit for the solar tracker is implemented by using microcontroller coding. From the circuit, Arduino UNO that has an output of 5 V is the heart of other components connected, since it is the

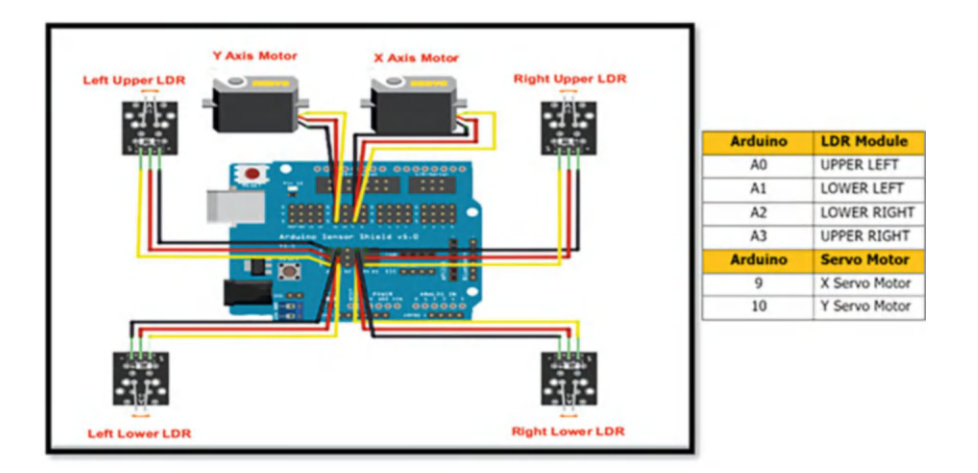


Fig. 5.6 The circuit diagram connections

microcontroller that controls the solar tracker. The LDR input is followed by a 1 K ohm resistor to control any overflow of current. The signal or input data for the servo motor are received from the Arduino pin 9 and pin 10 leg. The complete coding used in the design of the solar tracker is provided as an annexure. The system is thus designed to provide continuous tracking of solar energy and helps in collecting the energy to the fullest. This design opens the door to maximum tracking of solar energy. The basics of programming support the construction of this work. All the materials used in this work are shown in Table 5.1. The details of the major components used are as follows. A solar panel system was used to satisfy all the electricity needs, which is sufficient for the power requirements of a house or even a building. Arduino UNO was the software used to get physical information from various sensors and to get output from various stimuli, such as motors, LEDs, and buzzers. IO Expanding Shield for UNO was used to install many input and output units on the board with Arduino boards. A two-axis solar system prototype was also designed in this study. Using the above-mentioned component, a prototype was made that can maneuver itself with the movement of the light source to get maximum light out of the source, so it can excite and produce electricity. Hard card cardboard was used to make a simple working prototype of the system. Servo was used for the axis rotation, the spacer and nuts and bolts for the assembly operation, and cut-outs for hardware like LDR, Arduino, and servo motors. The Arduino interface is coded with the LDR, and a code is written to operate the assembly design efficiently. Figure 5.7 shows the final prototype that was made.

**Table 5.1** Materials used in the design

Name of the product	Pcs
Tower Pro SG90 RC MN(9gr) Servo Motor	2
6 V 250 mA Solar Panel—Solar Cell	1
KY—018 LDR Light Sensor Board	4
UNO R3 Board for Arduino	1
Expansion Shield for Arduino V5.0	1
10 mm M3 Metal Female—Male Spacer	16
M3 6 mm Head Metric Screw	4
M3 10 mm Head Metric Screw	11
M3 Nut	22
Double-Sided Tape	1
Extension cable (for LDR)	4
USB Cable	1
M3 Nylon nut	1
300 grt sandpaper	1
0.28-inch LED voltmeter	1
Small screwdriver	1
Wooden sheets (Wood parts)	1
Spare parts package	1

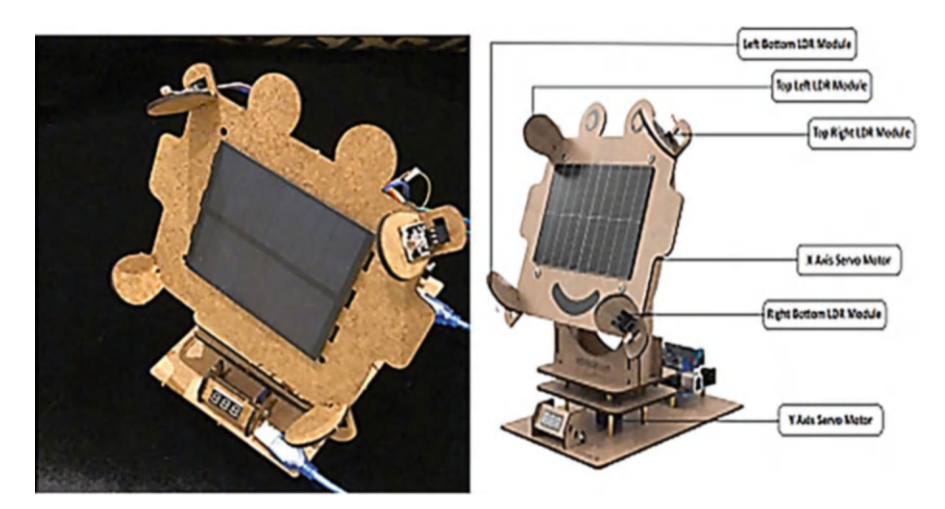


Fig. 5.7 Final prototype

# **5.3** Results and Inferences

The energy calculations for a complete house as a case study were conducted depending on the gadgets or devices that need to be powered by solar PV. The step-by-step process of calculations is elaborated in this section. Table 5.2 shows

58 H. Abdulmouti et al.

Items	Watt	Hours of use/day	No	Power (Wh)
TV	300	12	1	3600
CF bulbs	20	10	10	2000
Water pump	100	0.5	1	50
Fridge	200	12	1	2400
Water heater	600	2	2	2400
AC	500	6	2	6000
Ceiling fan	50	10	5	2500
Kitchen devices	100	5	5	2500
Other appliances	100	5	5	2500
Total Load Wh				23,950

**Table 5.2** Power calculation of components for a house

the appliances that are usually available in a typical house and the power required calculation for these devices.

#### 5.3.1 Solar Panel Selection and Calculation

For the total given load (23.95 kWh), the solar panels of monocrystalline 230 watts with  $I_{sc}$  of 6 A and  $V_{oc}$  of 30 V are selected. They are the most common and most efficient commercially available solar panels in the market for household usage where their efficiency can reach above 20%. Another major factor for selecting this kind of solar panel is that it is of high quality at a low price, has a cutting-edge design, and requires no maintenance. These panels also provide nonstop electricity for a long time. It is most used by the domestic and commercial sectors. The sun hours for a typical day in UAE is 8.8 h. The safety factor is 1.3. Hence, the load is calculated to be:

Total Load = 
$$23.95 \times 1.3 = 31.14 \text{ kWh}$$

Knowing the panel wattage of 230, the number of solar panels needed for the given load is calculated:

Total panels needed = 
$$\frac{\text{Total Load}}{\text{Power of a panel} \times \text{Sun hours}} = \frac{31.14}{0.23 \times 8.8} = 15.38$$
(5.1)

Therefore, 16 panels with 230 watts each are needed to meet the load requirements.

### 5.3.2 Battery System Calculation and Selection

Once the solar panel quantity is finalized, the next step is to identify and finalize the storage facilities such as batteries. Here, a standard 24 V battery with a depth of discharge (DoD) of 50% is selected. A lead acid battery is used for the given case. This type of battery is used because of its advantages such as deep cycle, flooded lead acid, and reliability and dependability. Also, it is easily available and has a minimum discharge rate. Moreover, it is economical considering the advantages it has. Standard off-grid sizing calls for a day of autonomy are also considered at this point, which means no energy would be coming out of panels during these days because of either rain or clouds. The term "days of autonomy," which is defined as the number of days that the battery can provide the site's loads without assistance from generation sources, has been used by the industry as one approach to describe the quantity of battery storage for the site's specific needs. A power backup of one day without any source input is assumed, so the days of autonomy would be 1. As days of autonomy can significantly increase the battery size, it must be selected cautiously. DoD indicates the percentage of the battery that has been discharged relative to the overall capacity of the battery. A battery's "cyclic life" is the number of charge/discharge cycles in its useful life. At the end of the day, the batteries would be down to 50% of their state of charge or half drained. Lead acid batteries can go down to 20% DoD, hence 50% standard DoD is applied for the given study.

Battery Bank size (kWh) = 
$$\frac{\text{Daily Energy Consumtions} \times \text{Days of autonomy}}{1 \times \text{DOD} \times \text{battery loss}}$$
$$= \frac{31.14 \times 1}{1 \times 0.5 \times 0.9} = 69.19 \text{ kWh}$$
(5.2)

Which is the power that the battery bank would have in total when fully charged. But typically, battery capacity is taken in terms of Ampere hour that depends on voltage ultimate. Assuming a 24 V battery bank.

Ampere hours (kWh) = 
$$\frac{1000 \times \text{Energy storage needed (kWh)}}{\text{Battery voltages}}$$
$$= \frac{1000 \times 69.19 \text{ (kWh)}}{24} = 2882.92 \text{ Ah}$$
 (5.3)

A Surrette S-550 battery, which is 6 V, 428 Ah, is used. Four batteries in series are connected to make up 24 V at 428 Ah. Consider a system or a mini battery pack of four batteries that produces 428 Ah at 24 V. A 2882.92 Ah is required, hence the subsystem of four batteries is connected to get the desired Ampere hours.

H. Abdulmouti et al.

Sub-system needed = 
$$\frac{2882.92 \text{ Ah}}{428 \text{ Ah}} = 6.74 \approx 7$$
  
Batteries Needed =  $7 \times 4 = 28$  Batteries (5.4)

#### 5.3.3 Invertor Calculations and Selections

Off-grid, invertor calculations are pretty much simpler as the maximum required load (wattage) is calculated. All appliances in Table 5.2 are included, considering they turn on at the same time. It should be noted that appliances need more connections and consequently more power at the start. For example, an AC having 500 watts would need around 4000 watts for that instance when turned on. Hence, inventors are used with a rated power output that can usually produce three times the rated power output. Considering this factor, the wattage of the inverter is calculated as

$$(300 + 20^* 10 + 100 + 200 + 600^* 2 + 500^* 2 + 50^* 5 + 100^* 5 + 100^* 5)$$
  
  $\times 1.3 = 5525$  watts. (5.5)

Hence, a GIANDEL (a pure sine wave power) 24 V, 5525 W, inverter is used. The advantages of this inverter are that it has a strong and durable aluminum build making it strong and reliable and has a cooling fan to keep it cool while working. Also, it has an LED display for overload warnings and remote handling capability. It can handle over-voltage, low voltage, overload, short circuit, and polarity reverse protection.

#### 5.3.4 Wire Calculation and Selection

A solar cable is required to connect the solar components for each solar project. The most crucial cable in any PV solar system is the solar cable, often known as a "PV Wire" or "PV Cable." Solar cables are used to transfer the electricity that the solar panels produce to other locations. The size difference between solar cable 4 mm and solar cable 6 mm is the largest.

For this design, a wire capable of supporting up to 230 watt/32  $V = 7.18 \, A$  is requested. The benefit and advantage of using a 24 V system is that it reduces the current needed, and hence, a wire with less gauge can be used as well. The basic formula for the calculation of required amperes is.

$$Current = Power/Vmn (5.6)$$

Components	Description	Price per unit (\$)	Quantity	Cost (\$)
Solar panels	Artheon AEL 24 V/230 watt	230 watt 200 16		3200
Batteries	Surrette S-550/6 V at 428Ah 250		28	7000
Inverter	GIANDEL 24 V, 2400 W 350 1		1	350
Wire coil 75Ft	10 AWG wire	200	1	200
Mounting structure	Sheet metal structure	500	1	500
Installation cost	Miscellaneous	250	1	500
				11,750 \$

**Table 5.3** Components cost for a house

Where  $V_{mn}$  is the maximum amount of voltage that a solar panel can deliver that usually is 70–80% of  $V_{oc.}$  A 10 AWG wire at least is required as per the stander wiring selection tables here. Hence, a 30-foot-long wire with a drop of 2% is used.

# 5.4 Cost Analysis

One important factor about green energy systems is that they need some heavy initial costs to be installed; but once they are installed, they could go a long way to saving money. The solar system is not that expensive to be installed, but anyhow it needs some payback time to return the initial investment. In this section, the initial cost of installing the solar system is calculated.

# 5.4.1 Components' Costs

Table 5.3 shows the components that need to be estimated to analyze the cost of a house. From the table, it is clear that an initial investment of around 11,750 dollars is required for this system. This cost includes all the mandatory and miscellaneous costs involved in building this system.

# 5.4.2 Cost of Electricity

It is essential to calculate the cost of electricity to find out the breakeven point. For this study, the cost of electricity in terms of kWh or a unit is considered. The price of 1 kWh of electricity in the United Arab Emirates is approximately 0.15\$. Considering this cost of electricity, the cost of daily electricity consumption is taken from Table 5.2 to be approximately 24 kWh of electricity consumed daily. By this figure, the yearly electricity consumption is calculated for this home thus designed.

62 H. Abdulmouti et al.

```
Cost per kWh = 0.15$
Daily consumption = 24 Kwh
Yearly consumption = 24 * 365 = 8760 kWh
Cost of electricity consumed per year = 8760 * 0.15 = 1314$
```

#### 5.4.3 Breakeven Calculation

Calculating how long it will take to "break even" on the solar energy investment, the solar panel payback period is a useful tool. Simply divide the cost of the system by the annual amount that could be saved to determine the payback period in years.

Breakeven = Initial investment on the solar system/cost of electricity consumed per year (5.7)

Breakeven = 11,750/1314 = 8.9 years

Hence, it needs about 8.9 years to get the initial cost back, which is a very good and economical period.

Furthermore, as a dual-axis solar tracker is used for this case, it is expected to increase production by 20–30%, and this would increase the efficiency of solar panels to about 52.78%. This increases the overall energy yield and thereby the economy of a solar power plant. So, the number of panels needed would decrease.

#### 5.4.4 Recommendation

It is highly recommended to use the dual-axis solar tracker system associated with the solar panels for a typical house to collect more solar energy. It is easy to install and operate this tracker. This method can be adopted worldwide to increase the efficiency of solar systems. It is cheap, and it offers a great return on a small investment.

#### 5.5 Conclusions

The requirement for clean and green sources of energy has created a total shift toward the solar power plant. However, the big problem is that there is a limited amount of technology to make this source of energy economically feasible.

A dual-axis solar tracker system as a solar tracker for a typical house is developed and designed. The methods are utilized to meet the current electricity demands and to increase electricity production by following the axis of the sun using a motorized solar panel with a tracking system that follows the sun's motion from the east in the morning to the west in the evening to harness the maximum intensity of solar irradiation. The electronic system has an actuator and a motor arrangement that can easily track the sun depending on Arduino. Using a time reference, the panel is moved perfectly for 12 h to face the sun always, maximizing energy production for later usage. When the panel is oriented properly, it can provide enough surplus energy to supply the motor with the supplemental power it needs to run. With the application of an oriented and well-calibrated solar tracker, it is expected to increase production by 20-30%, and this would increase the efficiency of solar panels to about 52.78%. This increases the overall energy yield and thereby the economy of a solar power plant. Hence, the number of panels needed would decrease. Furthermore, this paper also discusses optimizing the kind of solar tracker that should be used to minimize the cost and maximize the effectiveness. The calculated cost shows that it needs about 8.9 years to get the initial cost back, which is a very good and economical period. This method can be adopted worldwide to increase the efficiency of solar systems. It is cheap, and it offers a great return on a small investment.

#### References

- A.Z. Hafez, A.M. Yousef, N. Harag, Solar tracking systems: Technologies and trackers drive types. A Review, Renewable and Sustainable Energy Reviews, 01 June 2018. [Online]. Available: https://www.sciencedirect.com/science/article/abs/pii/S1364032118301886. Accessed 25 Oct 2022
- Abdulmouti, H.: Innovative environment-friendly systems for a modern town, in 12th International Conference on Sustainable Energy & Environmental Protection (SEEP'19). UOS, Sharjah, UAE. 18–21 Nov 2019
- 3. R.I. Salawu, T.A. Oduyemi, An electronic sun finder and solar tracking system. Sol. Wind Technol. 3, 215–218 (1986). https://doi.org/10.1016/0741-983X(86)90037-8
- 4. H. Abdulmouti, Z. Skaf, W. Minhas, S. Almheiri, Aquaponics System Display at Sharjah Campuses – The Campus of Tomorrow. 2023 Advances in Science and Engineering Technology Conferences (ASET). The International Conference on Renewable and Sustainable Energy. Dubai, UAE. 20–23 Feb 2023
- G.J. Tsekouras, F.D. Kanellos, Optimal operation of ship electrical power system with energy storage system and photovoltaics: Analysis and Application. WSEAS Trans. Power Syst. E-ISSN: 2224-350X, 2013
- 6. G.J. Tsekouras, F.D. Kanellos, J. Prousalidis, Simplified method for the assessment of ship electric power systems operation cost reduction from energy storage and renewable energy sources integration. IET Electr. Syst. Transp 5(2), 61–69 (2015). https://doi.org/10.1049/ietest.2013.0011. The Institution of Engineering and Technology 2015
- 7. H. Abdulmouti, A.A. Aljasmi, M.A. Almarzooqi, H.H. Alyasi, M.J. Khair, Y.M. Almulla, A.A. Almulla, Generating power from solar sphere design. Advances in Science and Engineering Technology International Conferences (ASET), The International Conference on Sustainable Environment and Urban Infrastructure. Dubai, United Arab Emirates, 2019, pp. 1–4, https://doi.org/10.1109/ICASET.2019.8714441. ISBN: 978-1-5386-8271-5. (PoD) ISBN: 978-1-5386-8272-2. Date of Publisher: 16 May 2019. Publisher: IEEE Xplore. 26–27 Mar 2019

- H. Abdulmouti, S. Alsuwaidi, A. Jamal, Smart environmental friendly court yard. The International Multi-Conference on Advances in Science and Engineering Technology (ASET'2018): The Engineering Innovations in Healthcare International Conference and The HCT 2nd Annual Radiology Symposium, Sharjah. UAE. 21–22 Mar 2018
- H. Abdulmouti, K. Ali, A. Ali, M. Ali, S. Abdullah, R. Abdalla, Smart innovation applications for a GreenHouse using sustainable and renewable energy in the UAE. International Multi-Conference on Advances in Science and Engineering Technology (ASET'2018): The International Conference on Renewable and Sustainable Energy. 6th 7th Feb 2018 in Dubai. UAE. Publisher: IEEE. https://doi.org/10.1109/ICASET.2018.8376782. Electronic ISBN: 978-1-5386-2399-2. Print on Demand (PoD) ISBN: 978-1-5386-2400-5. IEEE Xplore Digital Library: 11 June 2018
- H. Abdulmouti, F. Alnajjar, The effect of solar sphere thickness on the fluid to generate power, in *Proceedings of the 9th World Congress on Mechanical, Chemical, and Material Engineering (MCM'23)*. Brunel University, London, UK. Paper No. HTFF 201 https://doi.org/10.11159/htff23.201. pp. 1–10. 06–08 Aug 2023
- 11. H. Abdulmouti, F. Alnajjar, The effect of fluid type and volume on concentrated solar sphere power generatio, in *The 9th World Congress on Mechanical, Chemical, and Material Engineering (MCM'23)*. Brunel University, London, UK. Paper No. HTFF 140 https://doi.org/10.11159/htff23.140. pp. 1–11. 06–08 Aug 2023
- 12. H. Abdulmouti, PIV of flow convection induced by solar sphere to generate power, in *ENERGY 2023: The Thirteenth International Conference on Smart Grids, Green Communications, and IT Energy-aware Technologies, (ICNS 2023)*, Copyright (c) IARIA, 2023, ISBN: 978-1-68558-054-4, pp. 5–12, Barcelona, Spain. 13–17 Mar 2023
- H. Abdulmouti, S. Alblooshi, Z. Skaf, S. Abdulnaser, Exploring the flow of solar sphere using PIV. 2023 Advances in Science and Engineering Technology International Conferences (ASET), Dubai, United Arab Emirates. pp. 1–6, https://doi.org/10.1109/ ASET56582.2023.10180584. 2023
- H. Abdulmouti, A. Bourezg, R. Ranjan, Exploring the applicability of agrivoltaic system in UAE and its merits. in 2023 Advances in Science and Engineering Technology International Conferences (ASET), Dubai, United Arab Emirates, pp. 1–6, https://doi.org/10.1109/ ASET56582.2023.10180741. 2023
- B. Cirak, Modelling and simulation of photovoltaic systems using MATLAB/Simulink. WSEAS Trans. Power Syst. https://doi.org/10.37394/232016.2023.18.6. E-ISSN: 2224-350X Vol. 18, 2023
- H. Abdulmouti, Passive cooling module to improve the solar photovoltaic (PV) performance, in The 4th International Conference on Environment, Chemical Engineering & Materials. Athens, Greece, 27–29 Dec 2022. WSEAS Trans. Power Syst. 18, 11–17 (2023)
- H. Abdulmouti, Z. Skaf, S. Alblooshi, Smart green campus: The campus of tomorrow, in 2022 International Conference on Renewable and Sustainable Energy – 2022 Advances in Science and Engineering Technology (ASET) International Conferences. HCT, Feb 21–24, 2022. Dubai. UAE. pp. 1–8, https://doi.org/10.1109/ASET53988.2022.9735087. Publisher: IEEE. Date Added to IEEE Xplore: 18 Mar 2022
- 18. H. Abdulmouti, Producing electricity by concentrated solar energy, in *The 2nd International Conference on Advances in Energy Research and Applications (ICAERA'21)*. 24–26 Nov 2021. Seoul, South Korea
- V.D. Gil-vera, C. Quintero-López, Predictive modeling of photovoltaic solar power generation. WSEAS Trans. Power Syst. 18, 71 (2023). https://doi.org/10.37394/232016.2023.18.8.
   E-ISSN: 2224-350X
- A. Aktaş, Y. Kirçiçek, Eliminate the disadvantages of renewable energy sources, in Solar Hybrid Systems, (2021)
- M.U.H. Joardder, M.H. Masud, Solar pyrolysis, in Clean Energy for Sustainable Development, (2017)
- 22. J. Hartsough, Solar tracking systems: Maximize yield by following the sun. 12 Mar 2017. Solar Tracking Systems: Maximize yield by following the sun (sinovoltaics.com)

- A.Z. Hafez, A.M. Yousef, N.M. Harag, Solar tracking systems: Technologies and trackers drive types—A review. Renew. Sust. Energ. Rev. 91, 754–782., ISSN 1364-0321 (2018). https://doi.org/10.1016/j.rser.2018.03.094
- N. AL-Rousan, N.A.M. Isa, M.K.M. Desa, Advances in solar photovoltaic tracking systems: A review. Renew. Sustain. Energy Rev. 82(Part 3), 2548–2569 (2018). https://doi.org/10.1016/j.rser.2017.09.077. ISSN 1364-0321
- J. Yoshitake, Solar tracker". Encyclopedia Britannica, 17 Mar 2023. https://www.britannica.com/technology/solar-tracker. Accessed 8 Jan 2024
- 26. M.S. Sabry, *Determining the Accuracy of Solar Trackers*. Appalachian State University (2013). http://libres.uncg.edu/ir/asu/f/Sabry,%20Muhammad\_2013\_Thesis.pdf
- 27. J. Goldemberg, S.-B. Bioethanol, Energy and sustainable development, in *Worlds Apart: Globalization Environment*, (2003), pp. 53–65
- M.N. Kaya, M.H. Aksoy, F. Kose, Renewable energy in Turkey: Potential, current status and future aspects. Ann. Fac. Eng. Hunedoara 15(1), 65 (2017)
- J. Narendrasinh, A.N.P. Parmar, V.S. Gautam, Passive solar tracking system. Int. J. Emerg. Technol. Adv. Eng. 5(1), 8 (2015)
- Kolluru VR. Design and Development of FPGA Based Controllers for Photovoltaic Power System; 2016
- M. Clifford, D. Eastwood, Design of a novel passive solar tracker. Sol. Energy 77(3), 269–280 (2004)
- 32. A. Kaysal, The design of two axis solar tracking system based on fuzzy logic control and efficiency analysis. Int. J. Adv. Res. Electr. Electron Instrum. Eng. 5(12), 10 (2016)
- H.H. Gad, A.Y. Haikal, H.A. Ali, New design of the PV panel control system using FPGAbased MPSoC. Sol. Energy 146, 243–256 (2017)
- 34. E.M. Assaf, Design and implementation of a two axis solar tracking system using plc techniques by an inexpensive method. Int. J. Acad. Sci. Res. 2(3), 54–65 (2014)
- 35. G. Deb, A.B. Roy, Use of solar tracking system for extracting solar energy. Int. J. Comput. Electr. Eng. **4**(1), 42 (2012)
- 36. B.E. Hines, W. Gross, Tracking solar collector with non-uniform solar cells and empirical tracking system including solar angle information. 2008, Google Patents
- 37. J.-N. Juang, R. Radharamanan, Design of a solar tracking system for renewable energy, in *Proceedings of Zone 1 Conference of the American Society for Engineering Education (ASEE Zone 1)*, (IEEE, 2014)
- 38. N. AL-Rousan, A.L.-R. Mohammad, S. Adnan, H. AL-Najjar, Choosing the efficient tracking method for real time tracking system in Jordan and it's neighbors to get maximum gained power based on experimental data, in *Proceedings of international conference on renewable* energy research and applications (ICRERA), (IEEE, 2012)
- 39. T. Tudorache, L. Kreindler, Design of a solar tracker system for PV power plants. Acta Polytech. Hung. 7(1), 23–39 (2010)
- 40. Y.E. Wu, K.C. Huang, Design and implementation of dual-axis solar tracking system with GSM fault reporting capability. Adv. Mater. Res. **42**, 724 (2013) Trans Tech Publ
- 41. K. Jazayeri, S. Uysal, M. Jazayeri, MATLAB/simulink based simulation of solar incidence angle and the sun's position in the sky with respect to observation points on the Earth, in Proceedings of International Conference on Renewable Energy Research and Applications (ICRERA), (IEEE, 2013)
- 42. B. Casey, Crystalline vs thin film solar panels, Solaris [Online]. Available: https://www.solaris-shop.com/blog/crystalline-vs-thin-film-solar-panels/. Accessed 01 Nov 2022
- 43. J. Marlein, M. Burgelman, Empirical JV modelling of CIGS solar cells. in *Proceedings of NUMOS (International Workshop on Numerical Modelling of Thin Film Solar Cells, Gent (B)*, 28–30 March 2007). pp. 227–233 (2007)
- 44. M.S. Al-Soud, E.S. Hrayshat, A 50 MW concentrating solar power plant for Jordan. J. Clean. Prod. 17(6), 625–635 (2009)
- S. Kalogirou, A. Sencan, Artificial Intelligence Techniques in Solar Energy Applications (INTECH Open Access Publisher, 2010) https://cdn.intechopen.com/pdfs-wm/12231.pdf

- 46. K. Chong, C. Wong, General formula for on-axis sun-tracking system and its application in improving tracking accuracy of solar collector. Sol. Energy **83**(3), 298–305 (2009)
- 47. A. Sözen, T. Menlik, S. Ünvar, Determination of efficiency of flat-plate solar collectors using neural network approach. Expert Syst. Appl. **35**(4), 1533–1539 (2008)
- 48. S. Racharla, K. Rajan, Solar tracking system–A review. Int. J. Sustain. Eng. 10(2), 72–81 (2017)
- 49. E. Anderson, C. Dohan, A. Sikora, *Solar Panel Peak Power Tracking System*, vol 12 (Worcester Polytechnic Institute, 2003), pp. 28–30
- 50. M. Sabry, B. Raichle, Characteristics of residential tracker accuracy in quantified direct beam irradiance and global horizontal irradiance. J. Technol. Innov. Renew. Energy 3(2), 44 (2014)
- 51. A.L.L.V.M. Andreev, A. Luque, *Concentrator Photovoltaics*, Springer Series in Optical Sciences (Springer, 2007)
- 52. K.K. Aman Garg, R. Parveen, M.S. Kumar, Saini, solar tracking: An efficient method of improving solar plant efficiency. Int. J. Electr. Electron Eng. 07(01), 5 (2015)
- 53. O.R. Otieno, Solar Tracking for Solar Panel in Department of Electrical and Information Engineering (University of Nairobi, 2015), p. 61
- 54. R. Zogbi, D. Laplaze, Design and construction of a sun tracker. Sol. Energy **33**(3–4), 369–372 (1984)
- 55. S. Pattanasethanon, The solar tracking system by using digital solar position sensor. Am. J. Eng. Appl. Sci. **3**(4), 678–682 (2010)
- P. Roth, A. Georgiev, H. Boudinov, Cheap two axis sun following device. Energy Convers. Manag. 46(7), 1179–1192 (2005)
- J. Kamala, A. Joseph, Solar tracking for maximum and economic energy harvesting. Int. J. Eng. Technol. 5, 5030–5037 (2014)
- S.A. Chabuk, N. Mahadev, G. Pritam, P.S. Magdum, Dual axis solar tracking using microcontroller. Int. Res. J. Eng. Technol. (IRJET) 04(03), 5 (2017)
- Robles Algarín, C, Ospino Castro A, and Casas Naranjo J, Dual-Axis Solar Tracker for Using in Photovoltaic Systems. 2017
- 60. Buy an Arduino solar tracker system with electronic components solarx affordable price. https://www.robotistan.com/. [Online]. Available: https://www.robotistan.com/solarx-gunes-takip-sistemi-elektronikli. Accessed 01 Nov 2022
- 61. Buy Inverter & Batteries, solar solutions- genusinnovation. Genus, 16 Sept 2022 [Online]. Available: https://www.genusinnovation.com/. Accessed 01 Nov 2022. Edition 3/2021 IMU [Online]. Available: https://media-01.imu.nl/storage/sinovoltaics.com/13706/sinovoltaics-energy-storage-manufacturer-ranking-report-edition-3-2021.pdf. Accessed 01 Nov 2022
- De Rooij D, Single Axis Trackers [Online]. Available https://media-01.imu.nl/storage/ sinovoltaics.com/13706/sinovoltaics-energy-storage-manufacturer-ranking-report-edition-3-2021.pdf. Accessed 01 Nov 2022
- 63. S.R. Nayak, C.R. Pradhan, Solar tracking application. IOSR J. Eng 2(12781281), 4 (2012)
- A. Samantha, R. Varma, S. Bhatt, Chronological single axis solar tracker. Int. J. Eng. Trends Technol. (IJETT) 21, 204 (2013)
- 65. Design & implementation of a dual-axis solar tracking system Researchgate. [Online]. Available: https://www.researchgate.net/publication/ 276876652\_Design\_Implementation\_of\_a\_Dual\_Axis\_Solar\_Tracking\_System. Accessed 01 Nov 2022
- 66. V.D. Gil-Vera, C. Quintero-López, Predictive modeling of photovoltaic solar power generation, in WSEAS Transactions on Power Systems, (2023), pp. 71–81
- 67. C. Bekir, Modelling and simulation of photovoltaic systems using MATLAB/Simulink. WSEAS Trans. Power Syst. 18, 49–56 (2023). https://doi.org/10.37394/232016.2023.18.6
- A. Sathis, Arduino Based Solar Tracking System. University Malay Pahang (2016). http://umpir.ump.edu.my/16192/2/Arduino%20based%20solar%20tracking%20system-Abstract-FKP-Sathis%20Vatumalai-CD%2010396.pdf

- 69. M. Bharati, R. Divyakumari, B. Swamy, Solar power tracking system and power saving in highway street light. Int. J. Innov. Res. Comput. Commun. Eng. 5(4), 10 (2017)
- H.S. Akbar, A.I. Siddiq, M.W. Aziz, Microcontroller based dual axis sun tracking system for maximum solar energy generation. Am. J. Energy Res. 5(1), 23–27 (2017)
- M. Ghassoul, Design of an automatic solar tracking system to maximize energy extraction. Int. J. Emerg. Technol. Adv. Eng. 3(5) (2013)
- C. Alexandru, A novel open-loop tracking strategy for photovoltaic systems. Sci. World J. 2013 (2013)
- F. Khosrojerdi, S. Taheri, A.-M. Cretu, An adaptive neuro-fuzzy inference system-based MPPT controller for photovoltaic arrays, in *Proceedings of Electrical Power and Energy Conference (EPEC)*, (IEEE, 2016)
- 74. E. Kiyak, G. Gol, A comparison of fuzzy logic and PID controller for a single-axis solar tracking system. Renewables: Wind, Water, Solar 3(1), 7 (2016)
- 75. A. Louchene, A. Benmakhlouf, A. Chaghi, Solar tracking system with fuzzy reasoning applied to crisp sets. Rev. Energ. Renouv. **10**(2), 231–240 (2007)
- 76. K.H. Reddy, S. Ramasamy, P., Ramanathan hybrid adaptive neuro fuzzy based speed controller for brushless DC motor. Gazi Univ. J. Sci. **30**(1), 93–110 (2017)
- I. Altas, A. Sharaf, A novel maximum power fuzzy logic controller for photovoltaic solar energy systems. Renew. Energy 33(3), 388–399 (2008)
- M. Alata, M. Al-Nimr, Y. Qaroush, Developing a multipurpose sun tracking system using fuzzy control. Energy Convers. Manag. 46(7), 1229–1245 (2005)
- 79. P. Takun, S. Kaitwanidvilai, C. Jettanasen, Maximum power point tracking using fuzzy logic control for photovoltaic systems, in *Proceedings of international multiconference of engineers and computer scientists*. Hongkong; 2011. Citeseer
- D.F. Sendoya-Losada et al., Design and implementation of a photovoltaic solar tracking using fuzzy control for Surcolombiana university. ARPN J. Eng. Appl. Sci. 12(7), 6 (2017)
- Z. Xinhong, W. Zongxian, Y. Zhengda, Intelligent Solar Tracking Control System Implemented on an FPGA (Nios II Embedded Processor Design Contest—Outstanding Designs, 2007)
- A.A. Aldair, A.A. Obed, A.F. Halihal, Design and implementation of neuro-fuzzy controller using FPGA for sun tracking system. Iraq. J. Electr. Electron Eng. 12, 2 (2016)
- J.-H. Chen, H.-T. Yau, T.-H. Hung, Design and implementation of FPGA-based Taguchichaos-PSO sun tracking systems. Mechatronics 25, 55–64 (2015)
- 84. J.-H. Chen, H.-T. Yau, J.-H. Lu, Implementation of FPGA-based charge control for a self-sufficient solar tracking power supply system. Appl. Sci. 6(2), 41 (2016)
- 85. N. AL-Rousan, M. Al-Rousan, A. Shareiah, et al., A fuzzy logic model of a tracking system for solar panels in northern Jordan based on experimental data, in *Proceedings of International Conference on Renewable Energy Research and Applications (ICRERA)*, (IEEE, 2012)
- 86. R.K. Arya, Approximations of Mamdani type multi-fuzzy sets fuzzy controller by simplest fuzzy controller. Int. J. Comput Cognit. **4**, 35–47 (2006)
- 87. C.-H. Huang, H.-Y. Pan, K.-C. Lin, Development of intelligent fuzzy controller for a two-axis solar tracking system. Appl. Sci. 6(5), 130 (2016)
- M. Benghanem, A. Mellit, S. Alamri, ANN-based modelling and estimation of daily global solar radiation data: A case study. Energy Convers. Manag. 50(7), 1644–1655 (2009)
- M.A. Cheikh, M. Haddadi, A. Zerguerras, Design of a neural network control scheme for the maximum power point tracking (MPPT). Revue des énergies renouvelables 10(1), 109–118 (2007)
- 90. M. Panait, T. Tudorache, A simple neural network solar tracker for optimizing conversion efficiency in off-grid solar generators, in *Proceedings of International Conference on Renewable Energies and Power Quality*, (2008)
- 91. I. Kayri, M.T. Gencoglu, Prediction of power production from a single axis photovoltaic system by artificial neural networks, in *Proceedings of 14th International Conference on Engineering of Modern Electric Systems (EMES)*, (IEEE, 2017)

- 92. D. Mathur, Maximum power point tracking with artificial neural network. Int. J. Emerg. Sci. Eng 2, 2319–6378 (2014)
- 93. E.T. El Shenawy, M.K., M.A. Mohamad., Artificial intelligent control tracking system. Appl. Sci. Res. 8(8), 3971–3984 (2012)
- R. Arulmurugan, N. Suthanthiravanitha, Model and design of a fuzzy-based Hopfield NN tracking controller for standalone PV applications. Electr. Power Syst. Res. 120, 184–193 (2015)
- 95. C.A. Otieno, G.N. Nyakoe, C.W. Wekesa, A neural fuzzy based maximum power point tracker for a photovoltaic system, in *Proceedings of AFRICON*, (IEEE, 2009)
- 96. D. Zhao, E. Xu, Z. Wang, Q. Yu, L. Xu, L. Zhu, Influences of installation and tracking errors on the optical performance of a solar parabolic trough collector. Renew. Energy **94**, 197–212 (2016). https://doi.org/10.1016/j.renene.2016.03.036
- 97. A.S.C. Roong, S.-H. Chong, Laboratory-scale single axis solar tracking system: Design and implementation. Int. J. Power Electron. Drive Syst. 7, 254–264 (2016). https://doi.org/10.11591/ijpeds.v7.i1.pp254-264
- B.A.D.J.C.K. Basnayake, W.A.D.M. Jayathilaka, Y.W.R. Amarasinghe, R.A. Attalage, A.G.B.P. Jayasekara, Smart solar tracking and on-site photovoltic efficiency measurement system [2016, Moratuwa]. Moratuwa Eng. Res. Conf. (MERCon) (2016), pp. 54–59, https:// doi.org/10.1109/MERCon.2016.7480115
- 99. N.K. Kumar, V. Subramaniam, E. Murugan, Power analysis of non-tracking PV system with low power RTC based sensor independent solar tracking (SIST) PV system. Mater. Today Proc. (2016)
- Edition 3/2021 IMU. [Online]. Available: https://media-01.imu.nl/storage/sinovoltaics.com/ 13706/sinovoltaics-energy-storage-manufacturer-ranking-report-edition-3-2021.pdf. Accessed 01 Nov 2022
- 101. M. Theebhan, C.Y. Long, T.T. Tiong, Design and development of a solar thermal collector with single axis solar tracking mechanism. MATEC Web Conf. 78, 1–8 (2016)
- 102. J. Wang, J. Zhang, Y. Cui, X. Bi, Design and implementation of PLC-based automatic sun tracking system for parabolic trough solar concentrator. MATEC Web Conf. 77, 1–4 (2016). https://doi.org/10.1051/matecconf/20167706006
- 103. S. Avarand, M. Pirmoradian, Solar tracking system with momentary tracking based on operational amplifiers in order to be used in photovoltaic panels for following the sun. Bull La Société R Des Sci Liège 85, 269–277 (2016)
- 104. H. Moradi, A. Abtahi, R. Messenger, Annual performance comparison between tracking and fixed photovoltaic arrays, in *43rd IEEE Photovolt Spec Conf* (2016), pp. 3179–3183
- 105. F. Sallaberry, R. Pujol-Nadal, M. Larcher, M.H. Rittmann-Frank, Direct tracking error characterization on a single-axis solar tracker. Energy Convers. Manag. 105, 1281–1290 (2015). https://doi.org/10.1016/j.enconman.2015.08.081. F. Sallaberry, A.G. De Jalón, J.-L. Torres, R. Pujol-Nadal. Optical losses due to tracking error estimation for a low concentrating solar collector. Energy Convers. Manag, 92 (2015), pp. 194–206, https://doi.org/10.1016/j.enconman.2014.12.026
- 106. L. Li, H. Li, Q. Xu, W. Huang, Performance analysis of azimuth tracking fixed mirror solar concentrator. Renew. Energy 75, 722–732 (2015). https://doi.org/10.1016/ j.renene.2014.10.062
- 107. M.A. Green, E.D. Dunlop, M. Yoshita, N. Kopidakis, K. Bothe, G. Siefer, X. Hao, Solar Cell Efficiency Records. PVEducation. [Online]. Available: https://www.pveducation.org/pvcdrom/appendices/solar-cell-efficiency-results2. Accessed 26 Oct 2022
- 108. How PV cells work. [Online]. Available: http://www.fsec.ucf.edu/en/consumer/solar\_electricity/basics/how\_pv\_cells\_work.htm. Accessed 26 Oct 2022
- 109. Niclas, Manage risks and maximize ROI for your solar energy projects, Manage risks and maximize ROI for your PV and energy storage projects [Online]. Available: https:// sinovoltaics.com/. Accessed 01 Nov 2022
- Photovoltaic effect. Energy Education. [Online]. Available: https://energyeducation.ca/encyclopedia/Photovoltaic\_effect. Accessed 27 Oct 2022

- 111. F.R. Ahammed, Design & implementation of a dual axis solar tracking system researchgate. [Online]. Available: https://www.researchgate.net/publication/276876652\_Design\_Implementation\_of\_a\_Dual\_Axis\_Solar\_Tracking\_System. Accessed 01 Nov 2022
- 112. A.C.R. Soon, S.-H. Chong, C.K. Gan. Design and implementation of a laboratory-scale single axis solar tracking system, in *Proceedings of the 1st ICRIL-International Conference Innov. Sci. Technol.* (IICIST 2015), Kuala Lumpur, Malaysia, 2015, pp. 645–648
- 113. R.R. Patel, A.J. Patil, A.N. Shewale, Intelligent sun tracking system using FLC implemented on FPGA. Int. J. Adv. Found Res. Comput. 2, 33–41 (2015)
- 114. G.C. Lazaroiu, M. Longo, M. Roscia, M. Pagano, Comparative analysis of fixed and sun tracking low power PV systems considering energy consumption. Energy Convers. Manag. **92**, 143–148 (2015). https://doi.org/10.1016/j.enconman.2014.12.046
- 115. F. Huang, L. Li, W. Huang, Optical performance of an azimuth tracking linear Fresnel solar concentrator. Sol. Energy 108, 1–12 (2014). https://doi.org/10.1016/j.solener.2014.06.028
- 116. S. Dheer, G. Kaur, Performance of distributed photovoltaic system at a commercial building. Int. J. Eng. Res. Echnol. 23 Apr 2013. [Online]. Available: https://www.ijert.org/performance-of-distributed-photovoltaic-system-at-a-commercial-building. Accessed 24 Oct 2022.
- 117. M. Neagoe, I. Visa, B.G. Burduhos, M.D. Moldovan, Thermal load based adaptive tracking for flat plate solar collectors. Energy Procedia 48, 1401–1411 (2014). https://doi.org/10.1016/ j.egypro.2014.02.158
- 118. L.M. Gutiérrez-Castro, P. Quinto-Diez, J.G. Barbosa-Saldaña, L.R. Tovar-Galvez, A. Reyes-Leon, Comparison between a fixed and a tracking solar heating system for a thermophilic anaerobic digester. Energy Procedia 57, 2937–2945 (2014). https://doi.org/10.1016/j.egypro.2014.10.329
- 119. J. Song, Y. Zhu, D. Xia, Y. Yang, A photovoltaic solar tracking system with bidirectional sliding axle for building integration. Energy Procedia 61, 1638–1641 (2014). https://doi.org/10.1016/j.egypro.2014.12.315
- 120. Y.-K. Choi, I.-S. Kim, S.-T. Hong, H. Lee, A study on development of azimuth angle tracking algorithm for tracking-type floating photovoltaic system. Adv. Sci. Technol. Lett. 51, 197–202 (2014). https://doi.org/10.1007/s12541-014-0613-5
- 121. Solar Cell, Solar Module, Solar Array. PVeducation.com, 10 July 2014. [Online]. Available: https://pveducation.com/solar-concepts/solar-cells-modules-arrays/. Accessed 01 Nov 2

# **Chapter 6 Toward Geometric Interpretation of Generalized Frequency**



Kota Horizumi

#### 6.1 Introduction

The purpose is to introduce the vector bundle framework of "extended frequencies" that is "geometric algebra"-valued vector fields on surfaces. The aim is to reexamine a geometrical interpretation of the generalized frequency of Milano in the view point of this framework. It is shown that:

**Main Theorem** The class of the generalized frequencies of Milano according to all voltage curves running over a surface S is linearly isomorphic to the vector bundle consisting of all the tangent hyperplanes at any points of the surface S.

The notion of generalized frequency  $F_v$  for a voltage curve v in the n-space  $\mathbb{R}^n$  is presented by F. Milano in the paper [1], which is the sum of the "radial" scalar component  $\rho_v$  of the voltage v and the "azimuthal" vector component  $\Omega_v$  of the voltage:  $F_v = \rho_v + \Omega_v$ . It is also discussed that this quantity is useful for engineering purposes in [2–4]. His geometrical interpretation of the frequencies is that the azimuthal component is the multiple of the curvature and the magnitude of the voltage v.

In our previous research, we introduced the class of the "extended frequencies," and the "extended frequencies" are "geometric algebra" (GA)-valued vector fields on surfaces. They show the characterization theorem that the class of the generalized frequencies of Milano is characterized by the subclass of "tangential" extended frequencies.

The research has been supported by T. Matsuhisa and Y. Hasegawa in useful discussion

In this chapter, we aim to open up to giving an algebraic interpretation of the characterization from the view point of the geometric algebra-valued vector bundle. In this line, we obtain the above theorem.

This chapter is organized as follows. In Sect. 6.2, after reviewing the generalized frequencies of Milano based on the paper [1] together with the basic of the geometric algebra, we propose the notion of "extended frequency" with examples. In addition we present the characterization theorem of the generalized frequencies of Milano by the extended frequencies with an emphasis on the notion of "tangential" frequencies. In Sect. 6.3, we present the geometric algebra  $\mathcal{G}(\mathbb{R}^{n+1})$ -valued bundle to give a geometric structure of our extended frequencies. As a consequence of the characterization theorem, we show the main theorem.

#### 6.2 Model

In this section, after reviewing the generalized frequencies of Milano defined in the paper [1] together with the basic of the geometric algebra, we propose the notion of "extended frequency" with examples. In addition we present the characterization theorem of the generalized frequencies of Milano by the extended frequencies with an emphasis on the notion of "tangential" frequencies.

# 6.2.1 Geometric Algebra

We begin with reviewing the basics of the geometric algebra according to L. C. Grove [5] and C. Doran, A. Lasenby [6].

Let n be a natural number  $n=1,2,3,\cdots$ , and the pair  $(\mathbb{R}^{n+1},\varphi)$  is the nondegenerate quadratic form  $(\mathbb{R}^{n+1},\cdot)$  in which "·" is the canonical inner product  $\mathbf{x}\cdot\mathbf{y}:={}^t\mathbf{x}\mathbf{y}=\sum_{i=1}^{n+1}x_iy_i$  for any  $\mathbf{x}={}^t(x_1,x_2,\cdots,x_n,x_{n+1}),\mathbf{y}={}^t(y_1,y_2,\cdots,y_n,y_{n+1})$  on  $\mathbb{R}^{n+1}$ . Denote by  $\|\mathbf{x}\|$  the **norm**  $\|\mathbf{x}\|:=\sqrt{\mathbf{x}\cdot\mathbf{x}}$  on  $\mathbb{R}^{n+1}$ .

**Definition 1** By the **geometric algebra** on the (n+1)-space  $\mathbb{R}^{n+1}$ , we mean the algebra  $\mathcal{G}(\mathbb{R}^{n+1}) = \langle \mathcal{G}(\mathbb{R}^{n+1}), \varphi \rangle$  of the nondegenerate quadratic form  $(\mathbb{R}^{n+1}, \cdot)$ , which consists of a unitary associative algebra  $\mathcal{G}(\mathbb{R}^{n+1})$  and the canonical inclusion  $\varphi: \mathbb{R}^{n+1} \to \mathcal{G}(\mathbb{R}^{n+1}), x \mapsto \varphi(x) = x$  as an  $\mathbb{R}$ -linear map with the following properties:

- **GA1**  $\mathcal{G}(\mathbb{R}^{n+1})$  has the identity element  $1_{\mathcal{G}(\mathbb{R}^{n+1})} = 1 \in \mathbb{R}$ .
- **GA2**  $\mathcal{G}(\mathbb{R}^{n+1})$  as a ring is generated by  $\varphi(\mathbb{R}^{n+1}) = \mathbb{R}^{n+1}$  and  $1_{\mathcal{G}(\mathbb{R}^{n+1})} (= 1 \in \mathbb{R})$  over  $\mathbb{R}$ .
- **GA3**  $\varphi(x)^2 = x \cdot x$  for any  $x \in \mathbb{R}^{n+1}$ .
- **GA4** [UFP] If  $\langle \mathcal{H}, \rho \rangle$  is another pair satisfying the conditions **CA1** and **CA3**, then there is an  $\mathbb{R}$ -linear ring homomorphism  $f : \mathcal{G}(\mathbb{R}^{n+1}) \to \mathcal{H}$  such that  $\rho = f \circ \varphi$  and  $f(1_{\mathcal{G}(\mathbb{R}^{n+1})}) = 1_{\mathcal{H}}$ .

We call vectors  $x, y \in \mathbb{R}^{n+1}$  **orthogonal** if  $x \cdot y = 0$ , denoted by  $x \perp y$ . We denote by  $\odot$  the algebra product of  $\mathcal{G}(\mathbb{R}^{n+1})$ , i.e.,  $\odot : \mathcal{G}(\mathbb{R}^{n+1}) \times \mathcal{G}(\mathbb{R}^{n+1}) \to \mathcal{G}(\mathbb{R}^{n+1})$ , which is called the **geometric product**.

We prefer to list some properties on the geometric algebra  $\mathcal{G}(\mathbb{R}^{n+1})$ : Let  $\{e_1, e_2, e_3, \cdots, e_{n+1}\}$  be the canonical orthonormal basis of  $\mathbb{R}^{n+1}$ . For every  $A, B, C \in \mathcal{G}(\mathbb{R}^{n+1})$  and for every  $x, y \in \mathbb{R}^{n+1}$ , the below statements are true:

- 1. There exists the geometric algebra  $\mathcal{G}(\mathbb{R}^{n+1})$  of the canonical quadratic space  $(\mathbb{R}^{n+1}, \cdot)$  uniquely up to  $\mathbb{R}$ -algebra isomorphism.
- 2. We obtain that  $x \odot y + y \odot x = 2x \cdot y$ . In particular  $x^2 = x \odot x = ||x||^2 \in \mathbb{R}$  for every  $x, y \in \mathbb{R}^{n+1}$ .
- 3. For any  $i, j \ (1 \le i, j \le n+1)$ ,

$$e_i \odot e_j = \begin{cases} 1 & (i = j), \\ -e_j \odot e_i & (i \neq j). \end{cases}$$

4. The geometric algebra  $\mathcal{G}(\mathbb{R}^{n+1})$  is the  $\mathbb{R}$ -vector space of dimension  $2^{n+1}$  with the basis:

$$\{1, \mathbf{e}_{i_1} \odot \mathbf{e}_{i_2} \odot \cdots \odot \mathbf{e}_{i_p} \mid 1 \leq i_1 \leq i_2 \leq i_3 \leq \cdots \leq i_p \leq n+1, \\ p = 1, 2, 3, \cdots, n+1\};$$

i.e.,

$$\mathcal{G}(\mathbb{R}^{n+1}) = L_{\mathbb{R}} \left( 1, \mathbf{e}_{i_1} \odot \mathbf{e}_{i_2} \odot \cdots \odot \mathbf{e}_{i_p} \mid 1 \leq i_1 \leq i_2 \leq i_3 \leq \cdots \leq i_p \leq n+1, \right.$$

$$p = 1, 2, 3, \cdots, n+1).$$

- 5.  $A \odot 1 = 1 \odot A = A$ .
- 6.  $A \odot B = A \bullet B + A \wedge B$ .
- 7. The algebra  $\mathcal{G}(\mathbb{R}^{n+1})$  is decomposed into the direct sum of the components, the sub-geometric algebra  $\mathcal{G}^p(\mathbb{R}^{n+1})$  of degree  $p=0,1,2,\cdots,n+1$ ; i.e.,

$$\mathcal{G}(\mathbb{R}^{n+1}) = \mathbb{R} \oplus \mathbb{R}^{n+1} \oplus \mathcal{G}^2(\mathbb{R}^{n+1}) \oplus \cdots$$
$$\cdots \oplus \mathcal{G}^p(\mathbb{R}^{n+1}) \oplus \cdots \oplus \mathcal{G}^{n+1}(\mathbb{R}^{n+1}),$$

in which each component  $\mathcal{G}^p(\mathbb{R}^{n+1})$  is the  $\mathbb{R}$ -vector space of dimension  $_{n+1}C_p$ :

$$\mathcal{G}^{0}(\mathbb{R}^{n+1}) = L_{\mathbb{R}}(1_{\mathbb{R}}) = \mathbb{R},$$

$$\mathcal{G}^{1}(\mathbb{R}^{n+1}) = L_{\mathbb{R}}(\boldsymbol{e}_{1}, \boldsymbol{e}_{2}, \boldsymbol{e}_{3}, \cdots, \boldsymbol{e}_{n+1}) = \mathbb{R}^{n+1},$$

$$\mathcal{G}^{p}(\mathbb{R}^{n+1}) = L_{\mathbb{R}}\left(\boldsymbol{e}_{i_{1}} \odot \boldsymbol{e}_{i_{2}} \odot \cdots \odot \boldsymbol{e}_{i_{p}} \middle| 1 \leq i_{1} \leq i_{2} \leq i_{3} \leq \cdots \leq i_{p} \leq n+1\right)$$
for  $p = 2, 3, \dots, n+1$ .

The **extended inner product** (or simply *inner product*)  $\bullet$  on  $\mathcal{G}(\mathbb{R}^{n+1})$  is the bilinear map  $\bullet : \mathcal{G}(\mathbb{R}^{n+1}) \times \mathcal{G}(\mathbb{R}^{n+1}) \to \mathcal{G}(\mathbb{R}^{n+1})$  defined by

$$A \bullet B := \frac{1}{2} \{ A \odot B + B \odot A \}$$
 for every  $A, B, \in \mathcal{G}(\mathbb{R}^{n+1})$ .

The **extended outer product** (or simply *outer product*)  $\wedge$  on  $\mathcal{G}(\mathbb{R}^{n+1})$  is the bilinear map  $\wedge : \mathcal{G}(\mathbb{R}^{n+1}) \times \mathcal{G}(\mathbb{R}^{n+1}) \to \mathcal{G}(\mathbb{R}^{n+1})$  defined by

$$A \wedge B := \frac{1}{2} \{ A \odot B - B \odot A \} \text{ for every } A, B, \in \mathcal{G}(\mathbb{R}^{n+1}).$$

**Remark 1** For vectors x, y in the 3-space  $\mathbb{R}^3$ , we can canonically identify

$$x \odot y = x \cdot y + x \times y$$
,

where the symbol " $\times$ " means the outer product (the cross product) on  $\mathbb{R}^3$ .

# 6.2.2 Generalized Frequency of F. Milano

In this chapter, by a **differentiable** map (function) or  $\mathcal{C}^{\infty}$ -map ( $\mathcal{C}^{\infty}$ -function), we mean an infinitely many differentiable map (function). We shall review the generalized frequency of Milano in the paper [1].

A voltage curve is a  $C^{\infty}$ -map v of an interval  $I \subseteq \mathbb{R}$  to  $\mathbb{R}^{n+1}$  (i.e.,  $v \in C^{\infty}(I, \mathbb{R}^{n+1})$ ):

$$\mathbf{v}: I \to \mathbb{R}^{n+1}, t \mapsto \mathbf{v}(t) = {}^t(v_1(t), v_2(t), \cdots, v_{n+1}(t))$$

provided that both  $v(t) \neq 0$  and  $v'(t) \neq 0$  almost everywhere. The **magnitude** of a voltage v is the nonnegative number defined by

$$v = |\mathbf{v}| = \sqrt{\mathbf{v} \bullet \mathbf{v}}.$$

The **frequency**  $\Omega_v$  of a voltage v is

$$\mathbf{\Omega}_{\mathbf{v}} := \frac{1}{v^2} \left( \mathbf{v} \wedge \mathbf{v}' \right).$$

The magnitude of frequency  $\Omega_v$  is

$$\omega_{\boldsymbol{v}} := |\boldsymbol{\Omega}_{\boldsymbol{v}}|.$$

<sup>&</sup>lt;sup>1</sup> By this we mean in this chapter that the set of all the  $t \in I$  such that either v(t) = 0 or v'(t) = 0 is a discrete set.

The **radial frequency**  $\rho_{v}$  of a voltage v is

$$\rho_{\boldsymbol{v}} := \frac{1}{v^2} \left( \boldsymbol{v} \cdot \boldsymbol{v}' \right).$$

The **generalized frequency** of Milano associated with a voltage curve v on an interval I of  $\mathbb{R}$  is the function  $F: \mathcal{C}^{\infty}(I, \mathbb{R}^{n+1}) \to \mathcal{C}^{\infty}(I, \mathcal{G}(\mathbb{R}^{n+1}))$  defined by

$$F(\mathbf{v}(t)) = F_{\mathbf{v}}(t) = (\rho_{\mathbf{v}} + \boldsymbol{\Omega}_{\mathbf{v}})(t).$$

When P = v(0), we denote by F(P) the generalized frequency at P

$$F(P) = F_{\boldsymbol{v}}(0) = \frac{1}{\left|\boldsymbol{v}(0)\right|^2} \left(\boldsymbol{v}(0) \cdot \boldsymbol{v}'(0) + \boldsymbol{v}(0) \wedge \boldsymbol{v}'(0)\right).$$

Further we obtain

$$F(\mathbf{v}) = \rho_{\mathbf{v}} + \mathbf{\Omega}_{\mathbf{v}} = \frac{1}{v^2} (\mathbf{v} \odot \mathbf{v}').$$

**Example 1 (Example 2 in Milano [1])** Let v(t) be the voltage curve in the 3-space  $\mathbb{R}^3$  given by

$$\mathbf{v}(t) = {}^{t}(\sin{(\omega_0 t)}, \sin{(\omega_0 t - \alpha)}, \sin{(\omega_0 t + \alpha)}),$$

where constants  $\omega_0 > 0$ ,  $\alpha = \frac{2}{3}\pi$ . On noting that  $\mathbf{v} \cdot \mathbf{v}' = 0$ , it is observed that

$$\mathbf{v} \odot \mathbf{v}' = \frac{\sqrt{3}}{2} \omega_0(\mathbf{e}_1 \wedge \mathbf{e}_2 - \mathbf{e}_1 \wedge \mathbf{e}_3 + \mathbf{e}_2 \wedge \mathbf{e}_3).$$

Since  $v_1^2 + v_2^2 + v_3^2 = \frac{3}{2}$ , it follows that the generalized frequency of Milano is given as

$$F(\mathbf{v}(t)) = (\rho_{\mathbf{v}} + \mathbf{\Omega}_{\mathbf{v}})(t) := \frac{1}{v^2} \mathbf{v}(t) \odot \mathbf{v}'(t)$$
$$= \frac{\omega_0}{\sqrt{3}} (\mathbf{e}_1 \wedge \mathbf{e}_2 - \mathbf{e}_1 \wedge \mathbf{e}_3 + \mathbf{e}_2 \wedge \mathbf{e}_3).$$

Furthermore, it can be seen that the magnitude  $\omega_{\nu}$  of frequency is

$$\omega_{\boldsymbol{v}} = |\boldsymbol{\Omega}_{\boldsymbol{v}}| = \frac{1}{v^2} |\boldsymbol{v}(t) \wedge \boldsymbol{v}'(t)| = \frac{1}{v^2} |\boldsymbol{v}(t) \odot \boldsymbol{v}'(t)| = \omega_0.$$

# 6.2.3 Extended Frequency on n-Surface

Let D be a non-empty open domain in  $\mathbb{R}^{n+1}$  with  $n=1,2,3,\cdots$  and let  $f:D\to\mathbb{R}$  be a  $\mathcal{C}^{\infty}$ -function on D, i.e.,  $f\in\mathcal{C}^{\infty}(D,\mathbb{R})$ . A **vector field** X on D is a  $\mathcal{C}^{\infty}$ -map  $X:D\to\mathbb{R}^{n+1}$ ; i.e.,  $X\in\mathcal{C}^{\infty}(D,\mathbb{R}^{n+1})$ .

By an *n*-surface  $\tilde{S}$ , we mean  $\tilde{S} = f^{-1}(0)$  defined by f, which is the set of all the points  $\mathbf{x} = (x_1, x_2, \dots, x_{n+1}) \in \mathbb{R}^{n+1}$  with  $f(x_1, x_2, \dots, x_{n+1}) = 0$  provided that  $(\nabla f)(P) \neq \mathbf{0}$  for every point  $P \in \tilde{S}$ . Let denote by  $\mathcal{S}(\mathbb{R}^{n+1})$  the class of all *n*-surfaces in  $\mathbb{R}^{n+1}$ , i.e.,

$$\begin{split} \mathcal{S}(\mathbb{R}^{n+1}) &:= \\ \left\{ \tilde{S} = f^{-1}(0) \mid f(\boldsymbol{x}) \in \mathcal{C}^{\infty}(D, \mathbb{R}) \text{ with } (\nabla f)(\boldsymbol{x}) \neq \boldsymbol{0} \right. \\ \text{for any } \boldsymbol{x} \in \tilde{S}, \ D \text{ is a non-empty open domain of } \mathbb{R}^{n+1} \right\}. \end{split}$$

By an **extended frequency** associated with a differentiable vector field  $X \in \mathcal{C}^{\infty}(S, \mathbb{R}^{n+1})$ , we mean a pair  $\langle S, F_X \rangle$  in which S is a subsurface of  $\tilde{S}$ ,  $X(P) \neq \mathbf{0}$  on S almost everywhere, and  $F_X$  is the  $\mathcal{G}(\mathbb{R}^{n+1})$ -valued vector field defined by

$$F_X := \frac{1}{|I|^2} I \odot X \in \mathcal{C}^{\infty}(S^*, \mathcal{G}(\mathbb{R}^{n+1})),$$

where  $S^* := S \setminus \{0\}$  and I is the identity map on S. The extended frequency at  $P \in S^*$  is

$$F_X(P) = \frac{1}{|I(P)|^2} I(P) \odot X(P)$$
$$= \frac{1}{|P|^2} (P \bullet X(P) + P \wedge X(P)).$$

# 6.2.4 Tangential Frequency

Let S be a subsurface of the n-surface  $\tilde{S}$  defined by a  $\mathcal{C}^{\infty}$ -function  $f(x_1, x_2, \cdots, x_{n+1}) = 0$  on an open set U in  $\mathbb{R}^{n+1}$  for  $n = 1, 2, 3, \cdots$ , and let  $Q \in U$ . We denote by  $[(\nabla f)(Q)]^{\perp}$  the set of all nonzero vectors  $Y \in \mathbb{R}^{n+1} \setminus \{\mathbf{0}\}$  such that  $Y \cdot (\nabla f)(Q) = 0$ , i.e.,

$$[(\nabla f)(Q)]^{\perp} := \left\{ Y \in \mathbb{R}^{n+1} \setminus \{ \boldsymbol{0} \} \mid Y \cdot (\nabla f)(Q) = 0 \right\}.$$

An extended frequency  $\langle S, F_X \rangle$  is called **tangential at**  $P \in S^*$  if  $X(P) \in [\nabla f(P)]^{\perp}$ , i.e.,  $X(P) \cdot \nabla f(P) = 0$ . It is also called **tangential on** S (or simply **tangential**) if it is tangential at every  $P \in S^*$ .

**Example 2 (Tangential Extended Frequency)** Let  $\tilde{S}$  be the sphere of radius  $\sqrt{\frac{3}{2}}$  and center the origin:

$$\tilde{S} = \left\{ x = {}^{t}(x, y, z) \in \mathbb{R}^{3} \middle| f(x, y, z) = x^{2} + y^{2} + z^{2} = \frac{3}{2} \right\};$$

the 2-surface  $\tilde{S} = f^{-1}(0)$  defined by  $f(x, y, z) = x^2 + y^2 + z^2 - \frac{3}{2}$ . Let X be the differentiable vector field on  $\tilde{S}$  given by

$$X(x) := \frac{\omega_0}{2\sqrt{3}} {}^{t} (2(z-y), 3x + y - z, -3x + y - z).$$

Denote

$$H := \{ \mathbf{x} = {}^{t}(x, y, z) \in \mathbb{R}^{3} \mid x + y + z = 0 \} \subseteq [(\nabla f)(\mathbf{x})]^{\perp}$$

for any  $x \in \tilde{S}$ . Set the surface S by  $S = \tilde{S} \cap H$ . Then it is plainly seen that the pair  $(S, F_X)$  is a *tangential* extended frequency, and  $F_X(P)$  on S is obtained as

$$F_X(P) = \frac{\omega_0}{\sqrt{3}} (\mathbf{e}_1 \wedge \mathbf{e}_2 - \mathbf{e}_1 \wedge \mathbf{e}_3 + \mathbf{e}_2 \wedge \mathbf{e}_3)$$

for  $P \in S$  with its magnitude  $|F_X(P)| = \omega_0$ .

# 6.2.5 Characterization of Generalized Frequencies of F. Milano

We can obtain that:

**Theorem 1** The generalized frequency of Milano associated with each voltage curve can be represented almost everywhere by a tangential extended frequency, and vice versa.

**Remark 2** The "tangential" condition on an extended frequency in Theorem 1 plays an essential role.

# **6.3** Toward Geometric Structure of Frequencies

We actually have started our research to reexamine the geometric interpretation of generalized frequencies in [1, 7]. In this chapter we will give the brief description in the below.

# Geometric Algebra-Valued Bundle

Notation and assumptions being the same as above, we will construct the geometric algebra-valued bundle  $\mathfrak{G}(S, \mathcal{G}(\mathbb{R}^{n+1}))$  on an *n*-surface as follows.

**Definition 2** By the geometric algebra  $\mathcal{G}(\mathbb{R}^{n+1})$ -valued bundle  $\mathfrak{G}(S, \mathcal{G}(\mathbb{R}^{n+1}))$ over an *n*-surface S, we mean the structure  $(\mathfrak{G}(S, \mathcal{G}(\mathbb{R}^{n+1})), \pi)$ , in which:

The n-surface S is defined by a differentiable function f on an open domain of  $\mathbb{R}^{n+1}$ .

**GB2** For any point  $P \in S^* := S \setminus \{0\}$ , the stalk  $\mathfrak{G}_P(S) = \mathfrak{G}_P(S, \mathcal{G}(\mathbb{R}^{n+1}))$  at Pis the injective limit of  $\mathcal{C}^{\infty}(U,\mathcal{G}(\mathbb{R}^{n+1}))$  as open  $U\subseteq S^*$  tends to P:

$$\mathfrak{G}_P(S,\mathcal{G}(\mathbb{R}^{n+1})) := \inf_{P \in U} \lim_{C} C^{\infty}(U,\mathcal{G}(\mathbb{R}^{n+1})).$$

**GB3** The  $\mathcal{G}(\mathbb{R}^{n+1})$ -bundle  $\mathfrak{G}(S,\mathcal{G}(\mathbb{R}^{n+1}))$  is the disjoint union of all stalks  $\mathfrak{G}_P(S)$  over all  $P \in S^*$ :

$$\mathfrak{G}(S,\mathcal{G}(\mathbb{R}^{n+1})) := \bigsqcup_{P \in S^* = S \setminus \{\mathbf{0}\}} \mathfrak{G}_P(S,\mathcal{G}(\mathbb{R}^{n+1})).$$

**GB4** The canonical projection  $\pi: \mathfrak{G}(S, \mathcal{G}(\mathbb{R}^{n+1})) \to S, X \in \mathfrak{G}_P(S, \mathcal{G}(\mathbb{R}^{n+1}))$  $\mapsto P$ .

We prefer to list some properties:

- 1.  $\mathfrak{G}_P(S)$  has the geometric algebraic structure, so the bundle  $\mathfrak{G}(S, \mathcal{G}(\mathbb{R}^{n+1}))$ becomes an infinite-dimensional geometric algebra.
- 2.  $\mathfrak{G}(S, \mathcal{G}(\mathbb{R}^{n+1}))$  has the topology induced from the surface S via the projection  $\pi$ being continuous.

**Definition 3** By the subbundle  $\mathfrak{F}(S, \mathcal{G}(\mathbb{R}^{n+1}))$ , we mean the pair  $(\mathfrak{F}(S, \mathcal{G}(\mathbb{R}^{n+1})),$  $\pi$ ), in which:

$$\begin{split} \mathfrak{F}_P(\wedge^q\mathbb{R}^{n+1}) &:= \operatorname{inj} \operatorname{lim}_{P \in U} \mathcal{C}^\infty(U, \wedge^q\mathbb{R}^{n+1}) \text{ for } 0 \leq q \leq n+1. \\ \mathfrak{F}^q(S, \mathcal{G}(\mathbb{R}^{n+1})) &:= \bigsqcup_{P \in S} \mathfrak{F}_P(\wedge^q\mathbb{R}^{n+1}). \\ \mathfrak{F}(S, \mathcal{G}(\mathbb{R}^{n+1})) &:= \bigoplus_{q=0}^{n+1} \mathfrak{F}^q(S, \mathcal{G}(\mathbb{R}^{n+1})). \end{split}$$

 $\pi$  is the canonical projection from  $\mathfrak{F}(S,\mathcal{G}(\mathbb{R}^{n+1}))$  to S. SB4

We list some properties:

- 3.  $\mathfrak{F}_P(S)$  has the geometric algebraic structure, so the bundle  $\mathfrak{F}(S,\mathcal{G}(\mathbb{R}^{n+1}))$ becomes an infinite-dimensional geometric algebra.
- 4.  $\mathfrak{F}(S,\mathcal{G}(\mathbb{R}^{n+1}))$  is a sub-geometric algebra-bundle and a sub-geometric algebraalgebra of  $\mathfrak{G}(S, \mathcal{G}(\mathbb{R}^{n+1}))$ .

# 6.3.2 Geometric Interpretation of Generalized Frequencies

Let  $\mathcal{E}_S$  be the set of all extended frequencies on S:

$$\mathcal{E}_S := \left\{ F_X \mid X \in \mathcal{C}^{\infty}(S^*, \mathbb{R}^{n+1}) \right\},\,$$

and  $\mathcal{E}^{Fr}$  the class of all extended frequencies defined by the disjoint union of the components  $\mathcal{E}_S$  over all  $S \in \mathcal{S}(\mathbb{R}^{n+1})$ :

$$\mathcal{E}^{Fr} = \bigsqcup_{S \in \mathcal{S}(\mathbb{R}^{n+1})} \mathcal{E}_S.$$

Denote by  $\mathcal{F}^{0,2}(S,\mathcal{G}(\mathbb{R}^{n+1}))$  the subbundle

$$\mathcal{F}^{0,2}(S,\mathcal{G}(\mathbb{R}^{n+1})) := \mathfrak{F}^0(S,\mathcal{G}(\mathbb{R}^{n+1})) \oplus \mathfrak{F}^2(S,\mathcal{G}(\mathbb{R}^{n+1})),$$

and

$$\mathcal{F}^{0,2}(\mathcal{G}(\mathbb{R}^{n+1})):=\bigsqcup_{S\in\mathcal{S}(\mathbb{R}^{n+1})}\mathcal{F}^{0,2}(S,\mathcal{G}(\mathbb{R}^{n+1})).$$

It is worthy of notice that  $\mathcal{E}_S \subseteq \mathcal{F}^{0,2}(S,\mathcal{G}(\mathbb{R}^{n+1}))$ , and so  $\mathcal{E}^{Fr} \subseteq \mathcal{F}^{0,2}(\mathcal{G}(\mathbb{R}^{n+1}))$ . We can understand a geometric interpretation of generalized frequency will be given by characterizing the class  $\mathcal{E}_S$  in the framework of geometric algebra-bundle  $\mathcal{F}^{0,2}(S,\mathcal{G}(\mathbb{R}^{n+1}))$ . Furthermore, we have a possibility to reexamine the geometric interpretation of generalized frequency.

#### 6.3.3 Characterization Theorem Revisited

Let *S* be an *n*-surface defined by  $f(x_1, x_2, \dots, x_{n+1}) = 0$ , and *P* any point of  $S^* := S \setminus \{0\}$ . We denote by  $\mathcal{T}_P(S)$  the class of all tangential extended frequencies at  $P \in S^*$ , i.e.,

$$\mathcal{T}_P(S) := \left\{ F_X(P) \in \mathcal{G}(\mathbb{R}^{n+1}) \mid F_X \in \mathcal{E}_S, \right.$$
$$X \in \mathcal{C}_P^{\infty}(S^*, \mathbb{R}^{n+1}) \cap [(\nabla f)(P)]^{\perp} \right\}.$$

It is noted that  $\mathcal{T}_P(S)$  is a  $\mathbb{R}$ -vector subspace of  $\mathcal{F}_P^{0,2}(S,\mathcal{G}(\mathbb{R}^{n+1}))$ .

**Definition 4** By the **tangential** vector bundle of the generalized frequencies **over** an *n*-surface *S*, we mean the sub-vector bundle  $\mathcal{T}(S)$  of  $\mathcal{F}^{0,2}(S, \mathcal{G}(\mathbb{R}^{n+1}))$ , which

consists of the sum of the stalks  $\mathcal{T}_P(S)$  over all  $P \in S$  with the canonical projection  $\pi : \mathcal{T}(S) \to S$ , i.e.,

$$\mathcal{T}(S) := \bigsqcup_{P \in S^* = S \setminus \{\mathbf{0}\}} \mathcal{T}_P(S).$$

The **tangential** vector bundle of the generalized frequencies is the pair  $(\mathcal{T}, \pi)$  consisting of:

**TB1** 
$$\mathcal{T}(\mathbb{R}^{n+1}) := \bigsqcup_{S \in \mathcal{S}} \mathcal{T}(S).$$
  
**TB2**  $\pi : \mathcal{T}(\mathbb{R}^{n+1}) \to \mathcal{S}, \ Q(\in \mathcal{T}_P(S)) \mapsto P \in S \in \mathcal{S}.$ 

It is worthy of notice that:

**Remark 3**  $\mathcal{T}(\mathbb{R}^{n+1})$  has the geometric algebra-valued vector bundle that is the direct product of the components of the geometric algebra-valued bundles  $\mathcal{T}(S)$  where S runs over S.

Let  $V_0(\mathbb{R}^{n+1})$  be the set of all voltage curves on  $\mathbb{R}^{n+1}$  and let  $\mathcal{M} = \mathcal{M}(\mathbb{R}^{n+1})$  denote the class of all generalized frequencies of Milano according with voltage curve in  $\mathbb{R}^{n+1}$ :

$$\mathcal{M} = \mathcal{M}(\mathbb{R}^{n+1}) = \left\{ F_{\boldsymbol{v}}(t) \mid \boldsymbol{v} = \boldsymbol{v}(t) \in \mathbf{V}_{\mathbf{0}}(\mathbb{R}^{n+1}) \right\}.$$

*Note 1* We can observe that

$$\mathcal{M}(\mathbb{R}^{n+1}) = \bigsqcup_{P \in \mathbb{R}^{n+1} \setminus \{\mathbf{0}\}} \mathcal{M}_P(\mathbb{R}^{n+1}),$$

in which

$$\mathcal{M}_{P}(\mathbb{R}^{n+1}) = \bigsqcup_{v \in \mathbf{V}_{\mathbf{0}}(\mathbb{R}^{n+1})} \{ F(P) = F_{v}(0) \mid P = v(0) \}.$$

In the circumstances, we can obtain a vector-bundle interpretation of Theorem 1, and which is expected to give a geometric reinterpretation of generalized frequencies of Milano.

**Theorem 2** The class  $\mathcal{M}(\mathbb{R}^{n+1})$  of all generalized frequencies of Milano coincides with the tangential vector bundle  $\mathcal{T}(\mathbb{R}^{n+1})$  of  $\mathcal{F}^{0,2}(\mathcal{G}(\mathbb{R}^{n+1}))$  in the geometric algebra  $\mathcal{G}(\mathbb{R}^{n+1})$ -valued bundle, i.e.,  $\mathcal{M}(\mathbb{R}^{n+1}) = \mathcal{T}(\mathbb{R}^{n+1}) \subseteq \mathcal{F}^{0,2}(\mathcal{G}(\mathbb{R}^{n+1}))$ . Especially for any  $P \in \mathbb{R}^{n+1} \setminus \{\mathbf{0}\}$ , there exists an n-surface  $S_P$  such that  $\mathcal{M}_P(\mathbb{R}^{n+1}) = \mathcal{T}_P(S_P)$ .

The proof can be plainly given by modifying the proof of Theorem 1. As consequences, we give geometric interpretations of the frequencies of Milano as below.

**Corollary 1** The class of the generalized frequencies of Milano at any point  $P \in \mathbb{R}^{n+1} \setminus \{0\}$  is linearly isomorphic to the tangent hyperplane  $H_P(S_P)$  of some n-surface  $S_P$  at P.

**Proof** Let  $P, S_P$  be the same in Theorem 2. In viewing that  $C_P^{\infty}(S_P, \mathbb{R}^{n+1}) \cong \mathbb{R}^{n+1}$ , it is plainly seen that  $W_P(S_P) := C_P^{\infty}(S_P, \mathbb{R}^{n+1}) \cap [(\nabla f)(P)]^{\perp}$  is identified with the tangent hyperplane  $H_P(S_P)$  of the n-surface  $S_P$  at P.

On noting that  $\mathcal{T}_P(S_P)$  is a  $\mathbb{R}$ -linear space, it follows that  $\mathcal{T}_P(S_P)$  and  $H_P(S_P)$  are linearly isomorphic to each other. In fact, it can be plainly seen that  $\mathcal{T}_P(S_P)$  and  $W_P(S_P)$  are vector spaces and that the map  $\mathcal{T}_P(S_P) \to H_P(S_P) \cong W_{P(S_P)} := \mathcal{C}_P^{\infty}(S_P, \mathbb{R}^{n+1}) \cap [(\nabla f)(P)]^{\perp}$ ,  $F_X(P) \mapsto X(P)$  is linear. Furthermore, on noting  $P \neq \mathbf{0}$ , it is plainly seen that the map is bijective. Therefore by Theorem 2, it follows that the class  $\mathcal{M}_P(\mathbb{R}^{n+1})$  of all the generalized frequencies of Milano at P is linearly isomorphic to the tangent hyperplane  $H_P(S_P)$ , in completing the proof.

We let  $V_0(S)$  denote the set of all voltage curves on a subsurface S of the n-surface  $\tilde{S} = f^{-1}(0)$  defined by  $f = f(x) \in \mathcal{C}^{\infty}(S, \mathbb{R})$ . Let  $\mathcal{M}(S)$  be the class of all the generalized frequencies of Milano according to all voltage curves running over S.

$$\mathcal{M}(S) = \{ F_{\boldsymbol{v}}(t) \mid \boldsymbol{v} = \boldsymbol{v}(t) \in \mathbf{V}_{\mathbf{0}}(S) \}.$$

It can be plainly observed that  $\mathcal{M}(S)$  has the bundle structure:

$$\mathcal{M}(S) = \bigsqcup_{P \in S^* = S \setminus \{0\}} \mathcal{M}_P(S),$$

in which

$$\mathcal{M}_{P}(S) = \bigsqcup_{v \in \mathbf{V}_{0}(S)} \{ F(P) = F_{v}(0) \mid P = v(0) \}.$$

We can now show the main theorem in Sect. 6.1 that gives another geometric interpretation of the frequencies of Milano as below.

**Corollary 2** Let S be a subsurface of the n-surface  $\tilde{S} = f^{-1}(0)$  defined by  $f = f(x) \in C^{\infty}(S, \mathbb{R})$ . The class  $\mathcal{M}(S)$  of the generalized frequencies of Milano according to all voltage curves running over a surface S is linearly isomorphic to the vector bundle  $\mathcal{H}(S)$  consisting of all the tangent hyperplanes at any points of the surface S;  $\mathcal{H}(S) = \bigsqcup_{P \in S^* = S \setminus \{0\}} H_P(S)$ .

**Proof** On noting that any voltage curve  $v \in V_0(S)$  lies globally on S, we can take  $S_P$  in Theorem 2 as  $S_P = S$ . Therefore  $\mathcal{M}_P(S) \cong H_P(S)$ , and Corollary 2 follows immediately, in completing the proof.

It ends well this section with reconsidering Example 2.

**Example 3** Notation and assumptions being the same in Example 2, let *S* be the subsurface *S* of the sphere of radius  $\sqrt{\frac{3}{2}}$  and center the origin:

$$S = \left\{ t(x, y, z) \in \mathbb{R}^3 \,\middle|\, x^2 + y^2 + z^2 = \frac{3}{2}, x + y + z = 0 \right\}.$$

Then the class  $\mathcal{M}_P(S)$  of the generalized frequencies of Milano according to all voltage curves running over the surface S is linearly isomorphic to the tangent bundle on S, i.e.,

$$\mathcal{M}_{P}(S) \cong \mathcal{H}(S) = \bigsqcup_{P = {}^{t}(p_{1}, p_{2}, p_{3}) \in S} \left\{ {}^{t}(x, y, z) \in \mathbb{R}^{3} \mid p_{1}x + p_{2}y + p_{3}z = 0 \right\}.$$

# 6.4 Concluding Remarks

In this chapter we propose the structure of the geometric algebra-valued vector bundles. By using this framework we address a geometric interpretation problem of generalized frequencies of Milano. We can obtain the interpretation as that the class of the generalized frequencies is linearly isomorphic to the tangent hyperplane at each point on some n-surface.

Our experience has taught us the bundle structure is a useful technique to investigate the geometric structure. This chapter is on line of this teaching. So we can expect a further advanced study on the geometric algebra-valued bundle on surfaces will give taking new aspects of the geometrical interpretation of frequencies.

Indeed it can be seen the generalized frequencies of Milano have an orthogonalgeometry structure on the geometric algebra-valued bundle, which means that the class of generalized frequencies is a normed linear space on which the "invariant" orthogonal group acts isometrically.

**Acknowledgments** The authors cordially thank Ibaraki University Library, Mito campus, for providing a space in the "Common Learning Room" for our working seminar.

#### References

F. Milano, A geometric interpretation of frequency. IEEE Trans. Power Syst. 37(1), 816–819 (2022). https://doi.org/10.1109/tpwrs.2021.3108915

- F. Milano, G. Tzounas, I. Dassios, M.A.A. Murad, T. Kërçi, Using differential geometry to revisit the paradoxes of the instantaneous frequency. IEEE Open Access J. Power Energy 2, 501–513 (2022)
- F. Milano, B. Alhanjari, G. Tzounas, Enhancing frequency control through rate of change of voltage feedback. IEEE Trans. Power Syst. 39(1), 2385–2388 (2024)
- A. Alshawabkeh, G. Tzounas, F. Milano, Instantaneous frequency estimation in unbalanced systems using affine differential geometry. IEEE Trans. Power Delivery. Under review. Submitted. https://doi.org/10.48550/arXiv.2206.12091
- L.C. Grove, Classical groups and geometric algebra. Graduate Studies in Mathematics, vol. 39
   (American Mathematical Society, Providence, 2002), x+169 pp. ISBN: 0-8218-2019-2, Zbl 0990.20001, MR1859189
- C. Doran, A. Lasenby, Geometric Algebra for Physicists (Cambridge University Press, Cambridge, 2003), xiv+578pp. Zbl 1078.53001, MR1998960. https://doi.org/10.1017/ cbo9780511807497
- F. Milano, G. Tzounas, I. Dassios, T. Kërçi, Applications of the Frenet frame to electric circuits. IEEE Trans. Circuits Syst. 69(4), 1668–1680 (2022). https://doi.org/10.1109/tcsi.2021.3133948

# Chapter 7 Cluster Metric Sensitivity to Irrelevant Features



Miles N. F. McCrory and Spencer A. Thomas

#### 7.1 Introduction

Clustering is an important unsupervised machine learning method and can be applied in pattern recognition, image segmentation and data mining problems [1]. Clustering algorithms group similar points together based on a measure of distance or similarity of the features within the points, such as the Euclidean distance between their values or attributes. In many applications of clustering, the ground truth labels are not available, and the algorithms are used in a data exploration methodology or pattern recognition. Therefore, in order to have confidence in the resulting groupings, we must understand the impact of input data on the clustering results. Datasets are increasing in volume, dimensionality and complexity, often with distinct possible clustering tasks of interest based on subsets of the data. As such, for a given task of interest, the input data can contain redundant or irrelevant variables for that specific task. Feature selection methods can help identify and remove irrelevant features and have been widely used in supervised learning tasks [2–7]. However, these require ground truth labels in order to assess the impact of removing a feature for the learning task, such as increased accuracy (classification) or reduced error (regression) [8]. For unsupervised tasks, such as clustering, neither these labels are available, nor there is a clear objective to assess feature selection. Therefore, it is important to understand how sensitive clustering metrics are to the inclusion of irrelevant features for a task when assessing assigned clusters [9]. Understanding these sensitivities can potentially identify candidate metrics for performing unsupervised feature selection, by providing a suitable objective to optimise. In practice, we are unlikely to know a priori, if variables in the data are uncorrelated to a given task. Typically, exploratory data analysis is used to identify patterns and key features in the data that are then used to inform feature selection and downstream analysis. However, many real-world problems are highly complex, and the relationship between a feature and the target of interest may be unknown. Furthermore, individual inputs alone may not correlate to the task or output, but there may exist a non-linear combination of inputs that describes the task well. Similarly, random variables can negatively impact clustering, as the random distances will mask any useful information in the data [10]. From a practical perspective, we may not know which of the variables are or are not important, but we would like our evaluation metrics to reflect if the data contains non-informative features. This at least provides confidence in our interpretation of the metric values as 'good' or 'bad'. Additionally, this can enable feature selection through optimisation of the metric, thus providing an automated way to remove redundant or irrelevant features in an unsupervised data-driven way. There exists a range of clustering algorithms that can be used effectively for specific tasks and applications [11]. k-means is a centroid-based algorithm and is one of the most popular methods, as it is quick to run and easy to implement [1, 12]. The k-means algorithm minimises the distance of points within clusters, the within-cluster sum of squares, but maximises the distance of points between clusters, the between-cluster sum of squares. The algorithm iterates through a two-step process, firstly assigning each point to the nearest clusters and then updating the calculated centroids [13]. The k-means algorithm requires the user to state the number of clusters a priori. If this is not known, the number k of clusters can be estimated using the socalled 'elbow plots', such as the inflection point of total sum squared distances to cluster centroids as a function of k [14], maximising metrics such as the Silhouette Coefficient as a function of k, or directly using data-driven embedding [15]. Densitybased clustering methods such as DBSCAN [16] avoid the need to know the number of clusters a priori, however, they do require the selection of a minimum number of points and radius parameter. This replaces one unknown parameter with two, which additionally may not be easy or intuitive to optimise.

Due to the cluster number being a comparatively simple and interpretable parameter to optimise and the algorithms ubiquitous use in clustering problems, in this work we focus on k-means. In this work, we investigate the sensitivity of the k-means clustering algorithm to increasing levels of random variables in the input data in order to study the impact on clustering performance. This is effectively increasing the level of impact of the so-called 'curse of dimensionality' [9]. We conduct experiments on datasets with ground truth labels to verify useful metrics for practical applications where such information is not available. By artificially adding increasing amounts of random variables to input data, we can determine the impact of these irrelevant features relative to the informative features in the data. We define irrelevant here as features that are uncorrelated with the cluster label, are modelled as randomly generated values and are added across all cluster groups. Our results cover several datasets of different dimensions, and we monitor the ratio of random variables to informative features, evaluating clustering performance using several metrics. We investigate Gaussian and uniformly generated random values, as well

as the effect of scaling the data. This work could easily be extended to other types of clustering algorithms and different distributions for sampling random numbers. To the best of our knowledge, this has not been investigated previously with the literature surrounding clustering sensitivity examining the internal parameters of clustering algorithms, that is, ablation studies or (hyper) parameter tuning [17–20] or sensitivity analysis [21–23].

#### 7.2 Problem Formulation

#### 7.2.1 Data

The datasets used in the experiments are called the Dim-sets datasets [24]. There are four different datasets available; each with a different number of dimensions, D = (32, 64, 128, 256), referred to as Dim-D, where D is the dimensionality. The datasets all have 1024 data points and 16 clusters, and each is made up of 64 data points. These clusters are generated to have a Gaussian distribution with clusters that are well separated in all dimensions. All of these datasets have associated ground truths, and the initial clustering metric scores for these datasets can be used as a baseline reference point for all other datasets, when irrelevant features are iteratively added.

#### 7.2.2 Evaluation Metrics

There are various metrics that can be used to measure the performance of clustering algorithms. Clustering metrics assess performance in two main ways: either by comparison of predicted labels to a ground truth or by measuring spatial distances within and between clusters. In this study, we have the associated ground truth labels and evaluate the clustering results with this information.

Normalised mutual information (NMI) compares a clustering outcome (X) to the ground truth clustering labels (Y) defined as

$$NMI = \frac{MI(X, Y)}{\text{mean}(H(X), H(Y))}$$
(7.1)

where MI() is the mutual information, H(z) is the entropy of z. This has an upper bound of 1, indicating perfect clustering assignment and a lower limit of zero for incorrect clustering results [25].

The Rand index (RI) [26] is a measure of similarity between two sets of data groupings; in our case, this is the similarity between the cluster results and the ground truth labels, and RI is defined as

$$RI = \frac{a+b}{N} \tag{7.2}$$

here a and b are the number of true positives and true negatives, respectively. N is the total number of points in the data. As we are investigating the impact of random variables on clustering results, we use the adjusted Rand index (ARI)

$$ARI = \frac{RI - E[RI]}{\max(RI) - E(RI)}$$
 (7.3)

where  $E[\ ]$  is the expectation value due to the random elements in the k-means initialisation leading to differing a and b across runs. This formulation ensures that random labels will have scores near zero. This has an upper bound of 1 indicating perfect clustering assignment. The Silhouette Coefficient (S) measures the clustering results, assuming the desired outcome is dense and separated clusters. It is defined using the mean distance between a point and all the points within the same cluster  $(d_w)$  and the mean distance between a point and all other points in the nearest cluster  $(d_n)$ 

$$S = \frac{d_n - d_w}{\max(d_n, d_w)} \tag{7.4}$$

This has a lower limit of -1, sparse and overlapping clusters, and 1 for dense well-separated clustering. The Davies–Bouldin Index (DB) [27] compares the similarity of each cluster with the next most similar cluster within the dataset, averaged over all k clusters. The DB is calculated using the average distance of all points to the centroid ( $\delta$ ) within each cluster and the distance between centroids for pairs of clusters ( $\Delta_{ii}$ ),

$$DB = \frac{1}{k} \sum_{i=1}^{k} \max_{j \neq i} \left( \frac{\delta_i + \delta_j}{\Delta_{ij}} \right)$$
 (7.5)

The perfect Davies–Bouldin score is 0, which means clusters are well separated, clearly defined and dense. There is no upper bound for the Davies–Bouldin metric, but higher scores means that clusters are poorly defined and overlap.

# 7.2.3 Experiments

To assess the impact of random variables on clustering performance, we use a set of well-defined clusters with associated ground truth labels outlined in Sect. 7.2.2 as our baseline. For each dataset, we iteratively append one random variable to each instance in the dataset, increasing its dimensionality by one each time. Within the iteration cycle, we perform k-means clustering on the data and evaluate the results with the metrics outlined in Sect. 7.2.2. The experimental workflow is summarised in Fig. 7.1. We then obtain the distribution of each metrics as a function

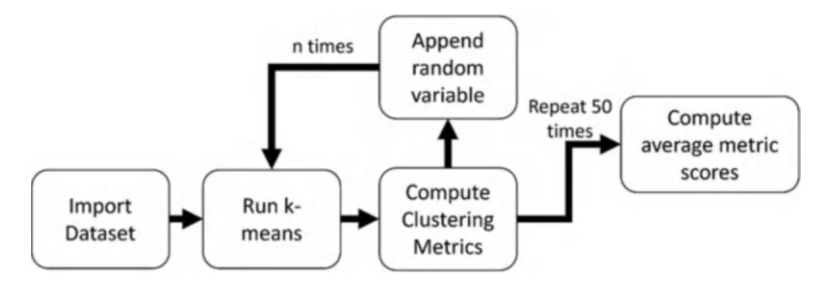


Fig. 7.1 Workflow for the experimentation used in this work

of additional random variables. We represent the additional variables as a ratio of random variables to 'real' features in the data for comparison across different dataset dimensions. This will highlight the dependence of clustering performance on the proportion of random variables in the data.

Since we have the ground truth, we know how many clusters are there in the datasets. Moreover, as the clusters are well defined and separated, we can compare clustering performance to this baseline, and therefore, attribute any difference directly to the inclusion of the random variables. As we are iteratively increasing the dimensionality by adding random variables and have several baseline datasets of increasing dimensionality of 'real' features (all of which well-defined clusters), we are also able to examine general properties such as proportion of random numbers. We generate random numbers using the mean  $(\mu)$  and standard deviation  $(\sigma)$  of the features in the original data. We compare the effect of random numbers generated from a Gaussian distribution,  $R_G$ 

$$R_G \sim N\left(\mu_r, \sigma_r^2\right)$$

where

$$\mu_r = \mathrm{sign} \left( \; \mu + \sigma \; \right) \eta$$

$$\sigma_r = \sigma (1 \operatorname{sign} \eta)$$

Here  $\eta$  is a random number [0, 1), and sign represents the sign ( $\pm$ ) determined by an additional random number,  $R \in [0, 1)$ ,

$$sign = \begin{cases} +, & \text{if } R \ge 0.5 \\ -, & \text{otherwise} \end{cases}$$

These are generated for each random value added; hence, for the Gaussian distributed values, each random value added has a different mean  $(\mu_r)$  and standard

deviation  $(\sigma_r)$ . We also consider random variables generated from a uniform distribution for identifying any impact due to noise distribution. For the uniformly distributed random variable,  $R_U$ , we sample random numbers for the range  $[-(\mu + 2\sigma), + (\mu + 2\sigma)]$ . Finally, as scaling has been shown to affect clustering results [10], we also examine these effects in our experiments. We compare unscaled data, generated with the distributions outlined above, with popular scaling methods. Specifically, we consider Centred data, where each variable has the mean subtracted yielding a mean of zero in the scaled data, and Standardised Centred data, where the variables are centred and scaling to have unit variance. Through the rest of the article, we refer to these scaling as 'Centred' and 'Standardised', respectively.

We perform k-means with k specified from the ground truth labels in the data, that is, 16 in our case. As our choice of implementation is the popular k-means++ [25]. We repeat each clustering experiments 50 times for each appended random variable to find an average clustering metrics and provide confidence bounds for these values. We have used Euclidean distance as our measure in all clustering experiments. The proportion of added random variables is reported as a ratio of random variable to meaningful features in the baseline dataset. For instance, a ratio of 0:1 represents the baseline datasets in all cases, that is, no added random variables, whereas a ratio of 2:1 means that there are twice as many random variables in the data as there are informative features. In the case of a 2:1 ratio, Dim-32 has 64 random variables and 32 informative features, whereas Dim-128 has 256 random variables and 128 informative features. This allows comparisons to be made across the varying dimensionality datasets and generalisation of the results.

#### 7.3 Results

Figure 7.2 illustrates the results of this work and summarises the dependence of appended random values on clustering performance metric under different scaling methods and when using different distributions to sample the random numbers. For clarity, we also look at the standard deviation of these curves in Fig. 7.3 that follows the same structure as Fig. 7.2. Overall, we observe the same behaviour in centred and unscaled data for all metrics and both random number distributions. Each of the four dataset demonstrates the same dependence when unscaled or centred, indicating that dimensionality does not influence this. We also see comparable values and dependencies in the standard deviation plots in Fig. 7.3, which shows both unscaled and centred data for random number distributions. It is worth reiterating the appended random variables generated from the Gaussian distribution; each has a different mean and variance. As such the unscaled and centred data are different but appear to have the same dependency on appended random variables. Therefore, there is no observable benefit in centred the data when investigating random or uninformative features in the data for unsupervised tasks. For all metrics, standardising the data removes any discrepancy between random variables generated from a Gaussian and uniform distribution. Moreover, standardising the

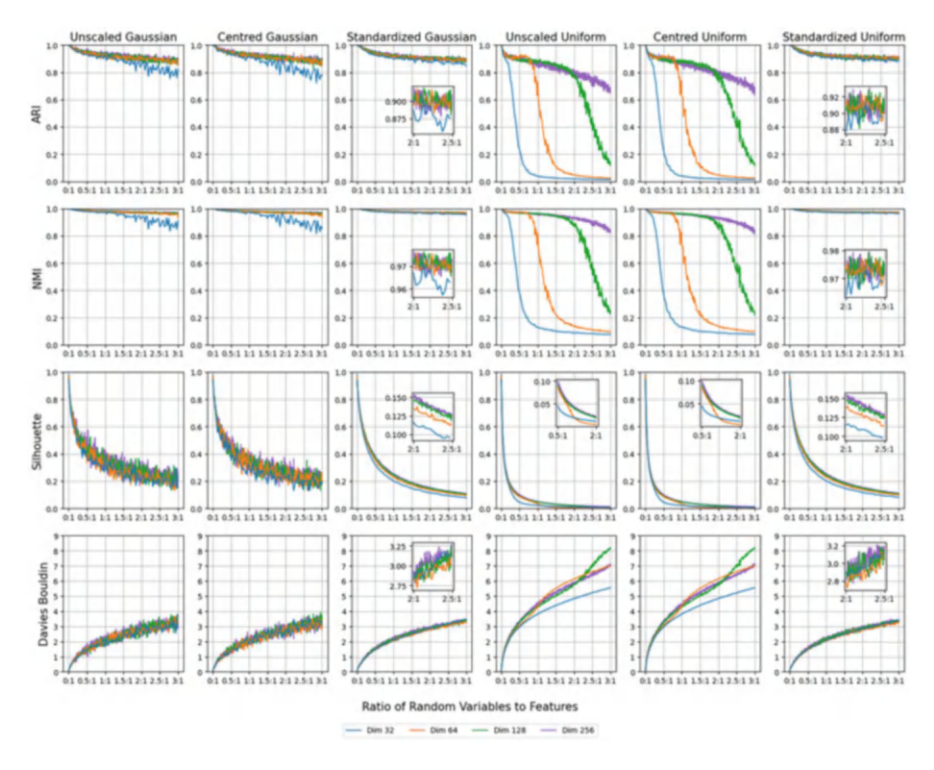


**Fig. 7.2** A comparison of clustering performance with different random number generations and data scaling methods. Columns depict different scaling and random number generation methods, and rows illustrate clustering performance metrics averaged over 50 independent runs. The ratio of random variables to informative features ranges from 0:1 (baseline model) to 3:1, where 75% of the input data is randomly generated and therefore does not correlated to the cluster label. Note that higher Davies–Bouldin scores indicate worse clustering performance unlike the other metrics

data reduces the standard deviation in performance scores in repeated runs for all configurations, with the exception of the Silhouette Coefficient for uniform random variables that are comparable.

ARI and NMI behave qualitatively the same across all configurations in Fig. 7.2. When considering Gaussian random variables, scaling has little or no effect, with standardised data reducing the larger gradient of Dim-32 compared to the higher dimensional datasets making the dependence on appended random variables comparable across all dimensions. The larger gradient of Dim-32 is accompanied by increasing variation in ARI and NMI with increasing proportions of random variables, see Fig. 7.3. Both metrics are insensitive to large proportions of random variables, indicating high-quality clustering performance even when 75% of the data is random noise. When considering uniformly distributed random variables, scaled and centred data exhibit greater sensitivity to added random variables when assessed by ARI and NMI (noted by the steeper initial gradient in the curves in

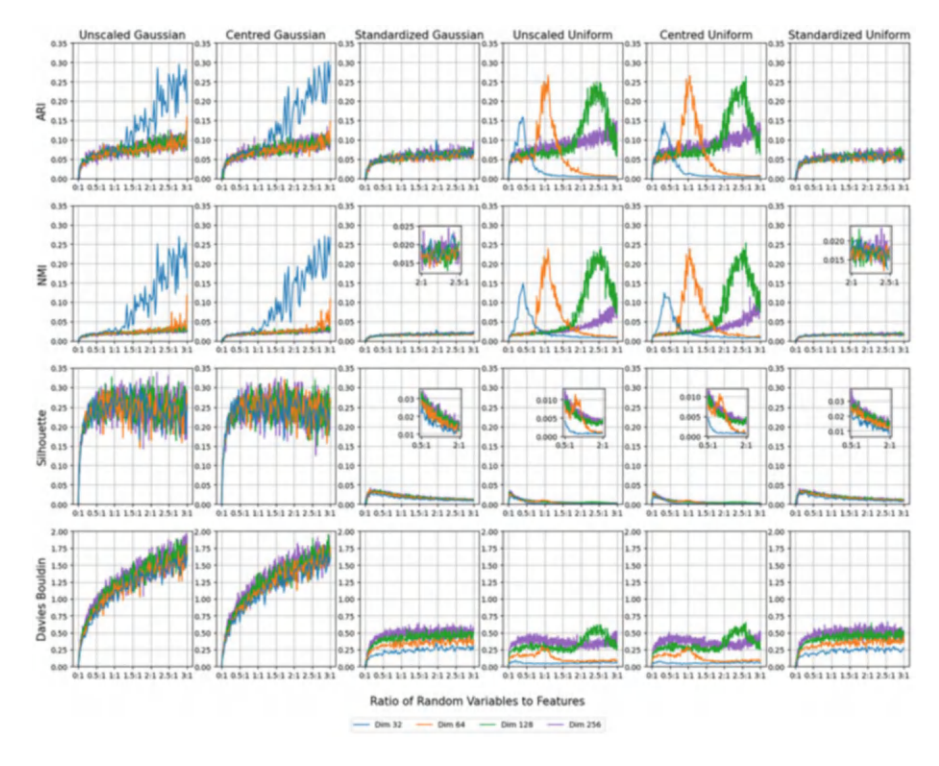


**Fig. 7.3** Standard deviation ( $\sigma$ ) value of clustering metrics score for 50 independent repeats. As in Fig. 7.2, we plot these values as a function of the proportion of random variables to features. Rows and columns are as in Fig. 7.2

Fig. 7.2). However, there is a 'tipping point', where the scores rapidly decrease to near zero. The location of this tipping point appears to be dependent on the dimensionality of the baseline data. Higher dimensions exhibit tipping points at higher proportions of random variables to features, and the rate of reduction of score appears to be reduced. The start of these tipping points manifests as an abrupt increase in standard deviation (Fig. 7.3). The inflection point in Fig. 7.2 also corresponds with a maximum in the standard deviation in Fig. 7.3. Standardising the data removes this dependency completely, and the standardised uniform curves closely resemble the standardised Gaussian curves in terms of scores (Fig. 7.2) and their variability (Fig. 7.3). The Silhouette Coefficient and the Davies-Bouldin scores show clear dependence on the proportion of random variables, both showing larger gradients initially before reducing to a lower rate of change as observed in Fig. 7.2. The Silhouette Coefficient shows a rapid decrease in score from the baseline before indicating a plateau, this is more noticeable in the uniform random number data. The Davies-Bouldin score has a comparatively lower initial gradient but appears to not to plateau, again more noticeable in the uniform data. This may be due to the increase in intra-cluster distance with the addition of the random variables in line with the curse of dimensionality. Specifically for the Gaussian random variables, standardising data for both Silhouette Coefficient and Davies-Bouldin metrics reduces the variability seen in the curves in Fig. 7.2, see Fig. 7.3. Similar to the scores, the standard deviation plateaus for the Silhouette Coefficient and continues to increase for Davies-Bouldin. When using the standardised data, the Silhouette Coefficient yields scores at the lower end of the range seen in the unscaled and centred data, indicating lower quality clustering with increasing number of random variables added. Whereas, for the Davies-Bouldin metric, standardised data appear to have comparable values to the unscaled and centred data. For both metrics, standardised data drastically reduces the variability between runs (Fig. 7.3), and in the case of the Davies-Bouldin the standard deviation plateaus. For the uniform random variables, both Silhouette Coefficient and Davies-Bouldin show rapid degradation of score with increasing proportions of random variables. This dependence is stronger and exhibits much lower variation than in the Gaussian case. For unscaled and centred data, both metrics also show some subtle structure in the curves that is dependent on the dimensionality of the baseline data. This results in clustering performance being worse for lower dimensional data at certain proportions of random variables. For example, 1.5:1 Dim-64 has a higher Davies-Bouldin score than Dim-128 and Dim-256, whereas at 2.5:1 the Dim-128 curve has overtaken Dim-64 and Dim-256. At 3:1, it appears that Dim-256 is higher than Dim-64 and may exhibit the same pattern, though this is outside of the range of our analysis. This dependence on dimensionality manifests as peaks in the standard deviation plots in Fig. 7.3, albeit much smaller peaks than seen in ARI and NMI. The Silhouette Coefficient shows similar patterns, but these are obfuscated by the dynamic range of these curves and are visible in the insets in Figs. 7.2 and 7.3. standardising the data removes this structure for both metrics and leads to curves resembling the standardise Gaussian data.

#### 7.4 Conclusion

These results indicate that the Silhouette Coefficient and the Davies–Bouldin score are the most sensitive to irrelevant features in all cases. The Silhouette Coefficient exhibits rapid decrease in value in response to comparatively low levels of added irrelevant features indicating that it is the most sensitive from a perfect feature set baseline. The Davies–Bouldin score also exhibits a rapid increase when irrelevant features are added, and its trend implies that it will not plateau. Both the Silhouette Coefficient and Davies–Bouldin score provide useful measurements of cluster quality that are sensitive to the addition of irrelevant features. As these metrics do not require ground truth labels, they are well suited as objective functions to optimise in feature selection for unsupervised tasks with unknown amounts of irrelevant features or when a perfect feature baseline is not available. Conversely, ARI and NMI show a resilience to irrelevant features. For uniform random numbers, this resilience is up to a critical point, which appears to be dependent on the

dimensionality of the data. No critical points were observed with Gaussian random numbers, and ARI and NMI maintained very high scores even at high proportions of irrelevant features relative to informative features in the data. This indicates that these metrics may not be useful for evaluating the clustering of noisy data, particularly, if the noise is Gaussian distributed. Finally, we also observe that Standardised data reduces the variability of the clustering results between runs and also provides comparable results between Gaussian and uniformly distributed random variables. It also removes the appearance of tipping points in the uniform random numbers that is dependent on the dimensionality of the baseline data.

**Acknowledgements** Spencer Thomas designed the study and experiments. Miles McCrory and Spencer Thomas implemented and conducted all experiments. All authors interpreted the results and prepared the manuscript. The authors would like to thank Sam Bilson and Peter M Harris (NPL) for useful feedback on the manuscript. This work was funded by the Department for Science, Innovation and Technology through the National Measurement System.

#### References

- 1. P. Berkhin, A survey of clustering data mining techniques, in *Grouping Multidimensional Data*, ed. by J. Kogan, C. Nicholas, M. Teboulle, (Springer, 2006), pp. 25–71
- N. Papaioannou, A. Tsimpiris, C. Talagozis, L. Fragidis, A. Angeioplastis, S. Tsakiridis, D. Varsamis, Parallel feature subset selection wrappers using k-means classifier. WSEAS Trans. Inf. Sci. Appl. 20, 76–86 (2023) Publisher: WSEAS
- 3. S. Wang, J. Tang, H. Liu, Feature selection, in *Encyclopedia of machine learning and data mining*, ed. by C. Sammut, G.I. Webb, (Springer, Boston, 2016), pp. 1–9
- N. Pudjihartono, T. Fadason, A.W. Kempa-Liehr, J.M. O'Sullivan, A review of feature selection methods for machine learning-based disease risk prediction. Front. Bioinf. 2, 927312 (2022)
- J. Zabalza, J. Ren, J. Zheng, H. Zhao, C. Qing, Z. Yang, D. Peijun, S. Marshall, Novel segmented stacked autoencoder for effective dimensionality reduction and feature extraction in hyperspectral imaging. Neurocomputing 185, 1–10 (2016)
- Z.M. Hira, D.F. Gillies, A review of feature selection and feature extraction methods applied on microarray data. Adv. Bioinforma. 2015, 198363 (2015)
- 7. Y. Saeys, I. Inza, P. Larrañaga, A review of feature selection techniques in bioinformatics. Bioinformatics **23**(19), 2507–2517 (2007)
- 8. M. Dash, H. Liu, Feature selection for classification. Intell. Data Anal. 1(1), 131–156 (1997)
- M.E. Houle, H.-P. Kriegel, P. Kröger, E. Schubert, A. Zimek, Can shared-neighbor distances defeat the curse of dimensionality? in *Scientific and Statistical Database Management*, Lecture Notes in Computer Science, ed. by M. Gertz, B. Ludäscher, (Springer, Berlin/Heidelberg, 2010), pp. 482–500
- 10. L. Kaufman, P.J. Rousseeuw, Finding groups in data: An introduction to cluster analysis, in *Finding Groups in Data: An Introduction to Cluster Analysis*, (Wiley, 1990), pp. 1–67
- D. Cheng, Q. Zhu, J. Huang, W. Quanwang, L. Yang, A local cores-based hierarchical clustering algorithm for data sets with complex structures. Neural Comput. & Applic. 31, 8051–8068 (2019)
- 12. D. Arthur, S. Vassilvitskii, K-means++: The advantages of careful seeding, in *Proceedings* of the Eighteenth Annual ACM-SIAM Symposium on Discrete Algorithms, SODA '07, USA, January 2007, pp. 1027–1035. Society for Industrial and Applied Mathematics
- D.J.C. MacKay, Information Theory, Inference, and Learning Algorithms (Cambridge University Press, 2003)

- 14. C. Yuan, H. Yang, Research on K-value selection method of K-means clustering algorithm. J **2**(2), 226–235 (2019) Publisher: Multidisciplinary Digital Publishing Institute
- 15. S.A. Thomas, Fast data driven estimation of cluster number in multiplex images using embedded density outliers, in 2022 IEEE Conference on Computational Intelligence in Bioinformatics and Computational Biology (CIBCB), 2022, pp. 1–8
- M. Ester, H.-P. Kriegel, J. Sander, X. Xu. A density-based algorithm for discovering clusters in large spatial databases with noise, in KDD'96: Proceedings of the Second International Conference on Knowledge Discovery and Data Mining, 1996, pp. 226–231
- D. Peng, Z. Gui, D. Wang, Y. Ma, Z. Huang, Y. Zhou, H. Wu, Clustering by measuring local direction centrality for data with heterogeneous density and weak connectivity. Nat. Commun. 13(1), 5455 (2022)
- M. Krzak, Y. Raykov, A. Boukouvalas, L. Cutillo, C. Angelini, Benchmark and parameter sensitivity analysis of single-cell RNA sequencing clustering methods. Front. Genet. 10, 1253 (2019)
- P. Peng, Y. Yoshida, Average sensitivity of spectral clustering, in *Proceedings of the 26th ACM SIGKDD International Conference on Knowledge Discovery & Data Mining*, 2020, pp. 1132–1140
- S. Roux, S. Buis, F.Ç. Lafolie, M. Lamboni, Cluster-based GSA: Global sensitivity analysis of models with temporal or spatial outputs using clustering. Environ. Model Softw. 140, 105046 (2021)
- 21. M. Kristiansen, M. Korpas, P. Härtel, Sensitivity analysis of sampling and clustering techniques in expansion planning models, in 2017 IEEE International Conference on Environment and Electrical Engineering and 2017 IEEE Industrial and Commercial Power Systems Europe (EEEIC/I&CPS Europe). IEEE, 2017, pp. 1–6
- 22. I. Hajnal, G. Loosveldt, The sensitivity of hierarchical clustering solutions to irrelevant variables. Bull. Sociol. Methodol./Bulletin de M'ethodologie Sociologique **50**(1), 56 (1996)
- 23. P.O. Olukanmi, B. Twala, Sensitivity analysis of an outlier-aware k-means clustering algorithm, in 2017 Pattern Recognition Association of South Africa and Robotics and Mechatronics (PRASA-RobMech), 2017, pp. 68–73
- 24. P. Fränti, O. Virmajoki, V. Hautamäki, Fast agglomerative clustering using a k-nearest neighbor graph. IEEE Trans. Pattern Anal. Mach. Intell. **28**(11), 1875–1881 (2006)
- F. Pedregosa, G. Varoquaux, A. Gramfort, V. Michel, B. Thirion, O. Grisel, M. Blondel, P. Prettenhofer, R. Weiss, V. Dubourg, J. Vanderplas, A. Passos, D. Cournapeau, M. Brucher, M. Perrot, E. Duchesnay, Scikit-learn: Machine learning in python. J. Mach. Learn. Res. 12, 2825–2830 (2011)
- 26. W.M. Rand, Objective criteria for the evaluation of clustering methods. J. Am. Stat. Assoc. **66**(336), 846–850 (1971)
- 27. D.L. Davies, D.W. Bouldin, A cluster separation measure. Conf Name IEEE Trans. Pattern Anal. Mach. Intell. **PAMI-1**(2), 224–227 (1979)

# **Chapter 8 Orthogonal Geometry on Generalized Frequencies**



Yuichi Hasegawa and Kota Horizumi

Facit indignatio versum D. L. Luvenalis

Facit indignatio proficit investigationis
T. M.

### 8.1 Introduction

The purpose is to bring the hidden geometric structure of "frequencies" into light. To this end we investigate the structure of "extended frequencies." The "extended frequencies" are "geometric algebra"-valued vector fields on surfaces. The aim is to give a metric-geometrical interpretation of the generalized frequency of Milano in the paper [1] in the framework.

F. Milano actually proposed his extended notion of frequency, *generalized* frequency  $F_v$ , for a voltage curve v in the n-space  $\mathbb{R}^n$  in the paper [1], which is

The research has been supported by T. Matsuhisa in useful discussion

Major in Electrical and Electronic System, Undergraduate School of Engineering, Ibaraki University, Hitachi-shi, Japan

#### K. Horizumi

Major in Electrical and Electronic System, Graduate School of Science and Engineering, Ibaraki University, Hitachi-shi, Ibaraki-ken, Japan

Y. Hasegawa (⊠)

defined as the sum of the "radial" scalar component  $\rho_v$  of the voltage v and the "azimuthal" vector component  $\Omega_v$  of the voltage:  $F_v = \rho_v + \Omega_v$ .

The former radial component is well known as the "instantaneous bandwidth" in time frequency analysis and signal processing, and the latter azimuthal component is the binormal vector defined by the fraction of the cross product of the vector  $\mathbf{v}$  and the tangent vector  $\mathbf{v}'$  by the square of the magnitude of the voltage  $\mathbf{v}$ . It is also discussed that this quantity is useful for engineering purposes in the papers [2, 3], and [4].

Especially, F. Milano et al. gave their geometrical interpretation of the generalized frequencies by pointing out that the azimuthal component can be geometrically interpreted as the binormal vector with amplitude given as the multiple of the curvature and the magnitude of the voltage v in the papers [1] and [5].

This chapter adopt a new approach to geometrical interpretation of the generalized frequencies. In fact, Horizumi and Hasegawa in 2023 introduced the class of the "extended frequencies" that generalized the "generalized frequency" introduced by F. Milano in the paper [1], and they show that the subclass of "tangential" extended frequencies characterizes the "generalized frequency." Further, Horizumi opens up an algebraic interpretation of the characterization from the view point of the geometric algebra-valued vector bundle.

In this chapter, we focus on the geometry on the class of those frequencies by highlighting the vector bundle structure on surfaces, and it is shown that:

**Main Theorem** The class of all the extended frequencies is a normed linear space on which the orthogonal group acts isometrically, and thus the class of all generalized frequencies of Milano is interpreted as an invariant orthogonal geometry.

The chapter is organized as follows. In Sect. 8.2, after reviewing the generalized frequencies of Milano based on the paper [1] together with the basic of the geometric algebra, we propose the notion of "extended frequency" with examples. In Sect. 8.3, we present the geometric algebra  $\mathcal{G}(\mathbb{R}^{n+1})$ -valued bundle to give a geometric structure of our extended frequencies and to revise the characterization theorem that every generalized frequency of Milano can be expressed by a "tangential" extended frequency. In Sect. 8.4 we consider a certain group action on the class of all extended frequencies. This leads us to introduce the orthogonal-geometric structure in the extended frequencies and to give a certain geometrical interpretation of the generalized frequencies of Milano as the above theorem.

#### 8.2 Model

In this section, we review the generalized frequencies of Milano according to the paper [1] together with the basic of the geometric algebra, and we propose the notion of "extended frequency" with examples. In addition presented is the characterization

theorem of the generalized frequencies of Milano by the extended frequencies with an emphasis on the notion of "tangential" frequencies.

# 8.2.1 Geometric Algebra

We begin with reviewing the basics of the geometric algebra according to L. C. Grove [6] and C. Doran, A. Lasenby [7].

Let n be a natural number  $n=1,2,3,\cdots$ , and the pair  $(\mathbb{R}^{n+1},\varphi)$  is the nondegenerate quadratic form  $(\mathbb{R}^{n+1},\cdot)$  in which "·" is the canonical inner product  $\mathbf{x}\cdot\mathbf{y}:={}^t\mathbf{x}\mathbf{y}=\sum_{i=1}^{n+1}x_iy_i$  for any  $\mathbf{x}={}^t(x_1,x_2,\cdots,x_n,x_{n+1}),\mathbf{y}={}^t(y_1,y_2,\cdots,y_n,y_{n+1})$  on  $\mathbb{R}^{n+1}$ . Denote by  $\|\mathbf{x}\|$  the **norm**  $\|\mathbf{x}\|:=\sqrt{\mathbf{x}\cdot\mathbf{x}}$  on  $\mathbb{R}^{n+1}$ .

**Definition 1** By the **geometric algebra** on the (n+1)-space  $\mathbb{R}^{n+1}$ , we mean the algebra  $\mathcal{G}(\mathbb{R}^{n+1}) = \langle \mathcal{G}(\mathbb{R}^{n+1}), \varphi \rangle$  of the nondegenerate quadratic form  $(\mathbb{R}^{n+1}, \cdot)$ , which consists of a unitary associative algebra  $\mathcal{G}(\mathbb{R}^{n+1})$  and the canonical inclusion  $\varphi: \mathbb{R}^{n+1} \to \mathcal{G}(\mathbb{R}^{n+1}), x \mapsto \varphi(x) = x$  as a  $\mathbb{R}$ -linear map with the following properties:

- **GA1**  $\mathcal{G}(\mathbb{R}^{n+1})$  has the identity element  $1_{\mathcal{G}(\mathbb{R}^{n+1})} = 1 \in \mathbb{R}$ .
- **GA2**  $\mathcal{G}(\mathbb{R}^{n+1})$  as a ring is generated by  $\varphi(\mathbb{R}^{n+1}) = \mathbb{R}^{n+1}$  and  $1_{\mathcal{G}(\mathbb{R}^{n+1})} (= 1 \in \mathbb{R})$  over  $\mathbb{R}$ .
- **GA3**  $\varphi(x)^2 = x \cdot x$  for any  $x \in \mathbb{R}^{n+1}$ .
- **GA4** [UFP] If  $\langle \mathcal{H}, \rho \rangle$  is another pair satisfying the conditions **CA1** and **CA3**, then there is a  $\mathbb{R}$ -linear ring homomorphism  $f : \mathcal{G}(\mathbb{R}^{n+1}) \to \mathcal{H}$  such that  $\rho = f \circ \varphi$  and  $f(1_{\mathcal{G}(\mathbb{R}^{n+1})}) = 1_{\mathcal{H}}$ .

We call vectors  $x, y \in \mathbb{R}^{n+1}$  **orthogonal** if  $x \cdot y = 0$ , denoted by  $x \perp y$ . We denote by  $\odot$  the algebra product of  $\mathcal{G}(\mathbb{R}^{n+1})$ ; i.e.,  $\odot : \mathcal{G}(\mathbb{R}^{n+1}) \times \mathcal{G}(\mathbb{R}^{n+1}) \to \mathcal{G}(\mathbb{R}^{n+1})$ , which is called the **geometric product**.

We prefer to list some properties on the geometric algebra  $\mathcal{G}(\mathbb{R}^{n+1})$ : Let  $\{e_1, e_2, e_3, \cdots, e_{n+1}\}$  be the canonical orthonormal basis of  $\mathbb{R}^{n+1}$ . For every  $A, B, C \in \mathcal{G}(\mathbb{R}^{n+1})$  and for every  $x, y \in \mathbb{R}^{n+1}$ , the below statements are true:

- 1. There exists the geometric algebra  $\mathcal{G}(\mathbb{R}^{n+1})$  of the canonical quadratic space  $(\mathbb{R}^{n+1}, \cdot)$  uniquely up to  $\mathbb{R}$ -algebra isomorphism.
- 2. We obtain that  $x \odot y + y \odot x = 2x \cdot y$ . In particular  $x^2 = x \odot x = ||x||^2 \in \mathbb{R}$  for every  $x, y \in \mathbb{R}^{n+1}$ .
- 3. For any  $i, j \ (1 \le i, j \le n + 1)$ ,

$$\mathbf{e}_{i} \odot \mathbf{e}_{j} = \begin{cases} 1 & (i = j), \\ -\mathbf{e}_{j} \odot \mathbf{e}_{i} & (i \neq j). \end{cases}$$

4. The geometric algebra  $\mathcal{G}(\mathbb{R}^{n+1})$  is the  $\mathbb{R}$ -vector space of dimension  $2^{n+1}$  with the basis:

$$\{1, \mathbf{e}_{i_1} \odot \mathbf{e}_{i_2} \odot \cdots \odot \mathbf{e}_{i_p} \mid 1 \leq i_1 \leq i_2 \leq i_3 \leq \cdots \leq i_p \leq n+1, \\ p = 1, 2, 3, \cdots, n+1\};$$

i.e.,

$$\mathcal{G}(\mathbb{R}^{n+1}) = L_{\mathbb{R}} \left( 1, \mathbf{e}_{i_1} \odot \mathbf{e}_{i_2} \odot \cdots \odot \mathbf{e}_{i_p} \mid 1 \leq i_1 \leq i_2 \leq i_3 \leq \cdots \leq i_p \leq n+1, \right.$$

$$p = 1, 2, 3, \cdots, n+1).$$

- 5.  $A \odot 1 = 1 \odot A = A$ .
- 6.  $A \odot B = A \bullet B + A \wedge B$ .
- 7. The algebra  $\mathcal{G}(\mathbb{R}^{n+1})$  is decomposed into the direct sum of the components, the sub-geometric algebra  $\mathcal{G}^p(\mathbb{R}^{n+1})$  of degree  $p = 0, 1, 2, \dots, n+1$ ; i.e.,

$$\mathcal{G}(\mathbb{R}^{n+1}) = \mathbb{R} \oplus \mathbb{R}^{n+1} \oplus \mathcal{G}^2(\mathbb{R}^{n+1}) \oplus \cdots$$
$$\cdots \oplus \mathcal{G}^p(\mathbb{R}^{n+1}) \oplus \cdots \oplus \mathcal{G}^{n+1}(\mathbb{R}^{n+1}),$$

in which each component  $\mathcal{G}^p(\mathbb{R}^{n+1})$  is the  $\mathbb{R}$ -vector space of dimension  $_{n+1}C_p$ :

$$\mathcal{G}^{0}(\mathbb{R}^{n+1}) = L_{\mathbb{R}}(1_{\mathbb{R}}) = \mathbb{R},$$

$$\mathcal{G}^{1}(\mathbb{R}^{n+1}) = L_{\mathbb{R}}(\boldsymbol{e}_{1}, \boldsymbol{e}_{2}, \boldsymbol{e}_{3}, \cdots, \boldsymbol{e}_{n+1}) = \mathbb{R}^{n+1},$$

$$\mathcal{G}^{p}(\mathbb{R}^{n+1}) = L_{\mathbb{R}}\left(\boldsymbol{e}_{i_{1}} \odot \boldsymbol{e}_{i_{2}} \odot \cdots \odot \boldsymbol{e}_{i_{p}} \middle| 1 \leq i_{1} \leq i_{2} \leq i_{3} \leq \cdots \leq i_{p} \leq n+1\right)$$
for  $p = 2, 3, \dots, n+1$ .

The **extended inner product** (or simply *inner product*)  $\bullet$  on  $\mathcal{G}(\mathbb{R}^{n+1})$  is the bilinear map  $\bullet : \mathcal{G}(\mathbb{R}^{n+1}) \times \mathcal{G}(\mathbb{R}^{n+1}) \to \mathcal{G}(\mathbb{R}^{n+1})$  defined by

$$A \bullet B := \frac{1}{2} \{ A \odot B + B \odot A \} \text{ for every } A, B, \in \mathcal{G}(\mathbb{R}^{n+1}).$$

The **extended outer product** (or simply *outer product*)  $\wedge$  on  $\mathcal{G}(\mathbb{R}^{n+1})$  is the bilinear map  $\wedge : \mathcal{G}(\mathbb{R}^{n+1}) \times \mathcal{G}(\mathbb{R}^{n+1}) \to \mathcal{G}(\mathbb{R}^{n+1})$  defined by

$$A \wedge B := \frac{1}{2} \{ A \odot B - B \odot A \} \text{ for every } A, B, \in \mathcal{G}(\mathbb{R}^{n+1}).$$

**Remark 1** For vectors x, y in the 3-space  $\mathbb{R}^3$ , we can canonically identify

$$x \odot v = x \cdot v + x \times v$$
.

where the symbol " $\times$ " means the outer product (the cross product) on  $\mathbb{R}^3$ .

#### 8.2.2 Generalized Frequency of F. Milano

By a **differentiable** map (function) or  $C^{\infty}$ -map ( $C^{\infty}$ -function), we mean an infinitely many differentiable map (function). We shall review the generalized frequency of Milano in the paper [1].

A voltage curve is a  $\mathcal{C}^{\infty}$ -map  $\boldsymbol{v}$  of an interval  $I \subseteq \mathbb{R}$  to  $\mathbb{R}^{n+1}$  (i.e.,  $\boldsymbol{v} \in \mathcal{C}^{\infty}(I, \mathbb{R}^{n+1})$ ):

$$\mathbf{v}: I \to \mathbb{R}^{n+1}, t \mapsto \mathbf{v}(t) = {}^{t}(v_1(t), v_2(t), \cdots, v_{n+1}(t))$$

provided that both  $v(t) \neq 0$  and  $v'(t) \neq 0$  almost everywhere. The **magnitude** of a voltage v is the nonnegative number defined by  $v = ||v|| := \sqrt{v \cdot v}$ .

The **generalized frequency** of Milano associated with a voltage curve v on an interval I of  $\mathbb{R}$  is the function  $F: \mathcal{C}^{\infty}(I, \mathbb{R}^{n+1}) \to \mathcal{C}^{\infty}(I, \wedge \mathbb{R}^{n+1})$  defined by

$$F(\mathbf{v}) = \frac{1}{\|\mathbf{v}\|^2} \left( \mathbf{v} \odot \mathbf{v}' \right) = \frac{1}{v^2} \left( \mathbf{v} \bullet \mathbf{v}' + \mathbf{v} \wedge \mathbf{v}' \right).$$

The frequency  $\Omega_{v}$  of a voltage v is  $\Omega_{v} := \frac{1}{v^{2}}(v \wedge v')$ . The magnitude of frequency  $\Omega_{v}$  is  $\omega_{v} := |\Omega_{v}|$ . The radial frequency  $\rho_{v}$  of a voltage v is  $\rho_{v} := \frac{1}{v^{2}}(v \cdot v')$ . Thus it follows that

$$F(\mathbf{v}) = (\rho_{\mathbf{v}} + \mathbf{\Omega}_{\mathbf{v}}),$$

and so  $F(\mathbf{v}(t)) = F_{\mathbf{v}}(t) = (\rho_{\mathbf{v}} + \mathbf{\Omega}_{\mathbf{v}})(t)$ . When  $P = \mathbf{v}(0)$ , we denote by F(P) the generalized frequency at P

$$F(P) = F_{\mathbf{v}}(0) = \frac{1}{\|\mathbf{v}(0)\|^2} \left( \mathbf{v}(0) \bullet \mathbf{v}'(0) + \mathbf{v}(0) \wedge \mathbf{v}'(0) \right).$$

**Example 1 (Example 2 in the Paper [1])** Let v(t) be the voltage curve in the 3-space  $\mathbb{R}^3$  given by

$$\mathbf{v}(t) = {}^{t}(\sin{(\omega_0 t)}, \sin{(\omega_0 t - \alpha)}, \sin{(\omega_0 t + \alpha)}),$$

where constants  $\omega_0 > 0$ ,  $\alpha = \frac{2}{3}\pi$ . On noting that  $\mathbf{v} \bullet \mathbf{v}' = \mathbf{v} \cdot \mathbf{v}' = 0$ , it is observed that

$$\mathbf{v} \odot \mathbf{v}' = \frac{\sqrt{3}}{2} \omega_0 (\mathbf{e}_1 \wedge \mathbf{e}_2 - \mathbf{e}_1 \wedge \mathbf{e}_3 + \mathbf{e}_2 \wedge \mathbf{e}_3).$$

By this we mean in this article that the set of all the  $t \in I$  such that either v(t) = 0 or v'(t) = 0 is a discrete set.

Since  $v_1^2 + v_2^2 + v_3^2 = \frac{3}{2}$ , it follows that the generalized frequency of Milano is given as

$$F(\mathbf{v}(t)) = (\rho_{\mathbf{v}} + \mathbf{\Omega}_{\mathbf{v}})(t) := \frac{1}{v^2} \mathbf{v}(t) \odot \mathbf{v}'(t)$$
$$= \frac{\omega_0}{\sqrt{3}} (\mathbf{e}_1 \wedge \mathbf{e}_2 - \mathbf{e}_1 \wedge \mathbf{e}_3 + \mathbf{e}_2 \wedge \mathbf{e}_3).$$

Furthermore, the magnitude  $\omega_{\nu}$  of frequency is

$$\omega_{\boldsymbol{v}} = \|\boldsymbol{\Omega}_{\boldsymbol{v}}\| = \frac{1}{v^2} \|\boldsymbol{v}(t) \wedge \boldsymbol{v}'(t)\| = \frac{1}{v^2} \|\boldsymbol{v}(t) \odot \boldsymbol{v}'(t)\| = \omega_0.$$

### 8.2.3 Extended Frequency on n-Surface

Let D be a non-empty open domain in  $\mathbb{R}^{n+1}$  with  $n=1,2,3,\cdots$  and let  $f:D\to\mathbb{R}$  be a  $\mathcal{C}^{\infty}$ -function on D, i.e.,  $f\in\mathcal{C}^{\infty}(D,\mathbb{R})$ . A **vector field** X on D is a  $\mathcal{C}^{\infty}$ -map  $X:D\to\mathbb{R}^{n+1}$ , i.e.,  $X\in\mathcal{C}^{\infty}(D,\mathbb{R}^{n+1})$ . By an n-surface  $\tilde{S}$ , we mean  $\tilde{S}=f^{-1}(0)$  defined by f, which is the set of all the points  $\mathbf{x}=(x_1,x_2,\cdots,x_{n+1})\in\mathbb{R}^{n+1}$  with  $f(x_1,x_2,\cdots,x_{n+1})=0$  provided that  $(\nabla f)(P)\neq \mathbf{0}$  for every point  $P\in \tilde{S}$ . Let denote by  $\mathcal{S}(\mathbb{R}^{n+1})$  the class of all (n+1)-surfaces in  $\mathbb{R}^{n+1}$ , i.e.,

$$\mathcal{S}(\mathbb{R}^{n+1}) := \{ S \mid \mathbf{0} \notin S : \text{a compact sub-surface of } \tilde{S} = f^{-1}(0), \ f(\mathbf{x}) \in \mathcal{C}^{\infty}(D, \mathbb{R})$$
 with  $(\nabla f)(\mathbf{x}) \neq \mathbf{0}$  for every  $\mathbf{x} \in \tilde{S} \left( \emptyset \neq D \text{ is a open domain of } \mathbb{R}^{n+1} \right) \}$ .

**Definition 2** By an **extended frequency** (EF) associated with a differentiable vector field  $X \in \mathcal{C}^{\infty}(S, \mathbb{R}^{n+1})$ , we mean a pair  $(S, F_X)$  in which S is a *compact* subsurface of  $\tilde{S}$  not containing the origin  $\mathbf{0}$  with respect to the relative topology,  $X(P) \neq \mathbf{0}$  on S almost everywhere, and  $F_X$  is the  $\mathcal{G}(\mathbb{R}^{n+1})$ -valued vector field defined by

$$F_X := \frac{1}{|I|^2} I \odot X \in \mathcal{C}^{\infty}(S, \mathcal{G}(\mathbb{R}^{n+1})),$$

where I is the identity map on S.

# 8.2.4 Tangential Frequency

Let S be a closed subsurface of the n-surface  $\tilde{S}$  defined by a  $C^{\infty}$ -function  $f(x_1, x_2, \dots, x_{n+1}) = 0$  on a non-empty open domain D in  $\mathbb{R}^{n+1}$  for  $n = 1, 2, 3, \dots$ , and let  $Q \in D$ . We denote by  $[(\nabla f)(Q)]^{\perp}$  the set of all nonzero vectors  $Y \in \mathbb{R}^{n+1} \setminus \{\mathbf{0}\}$  such that  $Y \cdot (\nabla f)(Q) = 0$ . That is,

$$[(\nabla f)(Q)]^{\perp} := \left\{ Y \in \mathbb{R}^{n+1} \mid Y \cdot (\nabla f)(Q) = 0 \right\}.$$

An extended frequency  $(S, F_X)$  is called **tangential at**  $P \in S$  if  $X(P) \in [\nabla f(P)]^{\perp}$ ; i.e.,  $X(P) \cdot \nabla f(P) = 0$ . It is also called **tangential on** S (or simply **tangential**) if it is tangential at every  $P \in S$ .

**Example 2 (Tangential Extended Frequency)** Let  $\tilde{S}$  be the sphere of radius  $\sqrt{\frac{3}{2}}$  and center the origin:

$$\tilde{S} = \left\{ \boldsymbol{x} = {}^{t}(x, y, z) \in \mathbb{R}^{3} \mid f(x, y, z) = x^{2} + y^{2} + z^{2} - \frac{3}{2} = 0 \right\};$$

the 2-surface  $\tilde{S} = f^{-1}(0)$  defined by  $f(x, y, z) = x^2 + y^2 + z^2 - \frac{3}{2}$ . Let X be the differentiable vector field on  $\tilde{S}$  given by

$$X(x) := \frac{\omega_0}{2\sqrt{3}} {}^{t}(2(z-y), 3x+y-z, -3x+y-z).$$

Denote

$$H := \{ x = {}^{t}(x, y, z) \in \mathbb{R}^{3} \mid x + y + z = 0 \} \subseteq [(\nabla f)(x)]^{\perp},$$

for every  $x \in \tilde{S}$ . Set the compact subsurface S by  $S = \tilde{S} \cap H$ . Then it is plainly seen that the pair  $\langle S, F_X \rangle$  is a *tangential* extended frequency, and  $F_X(P)$  on S is obtained as

$$F_X(P) = \frac{\omega_0}{\sqrt{3}} (\mathbf{e}_1 \wedge \mathbf{e}_2 - \mathbf{e}_1 \wedge \mathbf{e}_3 + \mathbf{e}_2 \wedge \mathbf{e}_3)$$

for  $P \in S$  with its magnitude  $||F_X(P)|| = \omega_0$ .

# 8.3 Geometric Algebra-Valued Bundle of Frequencies

Let  $\tilde{S}$  be the closed *n*-surface  $\tilde{S}=f^{-1}(0)$  defined by a  $\mathcal{C}^{\infty}$ -function  $f(x_1,x_2,\cdots,x_{n+1})$  on an open domain of  $\mathbb{R}^{n+1}$  and S a compact subsurface of  $\tilde{S}$ 

not containing the origin **0**. We let denote by  $\mathcal{E}_S$  the set of all extended frequencies on S:

$$\mathcal{E}_S := \left\{ F_X \mid X \in \mathcal{C}^{\infty}(S, \mathbb{R}^{n+1}) \right\}.$$

As regards this class, we have a possibility to reexamine the geometric interpretation of generalized frequency.

Let P be any point of S. We denote by  $\mathcal{T}_P(S)$  the class of all tangential extended frequencies at  $P \in S$ , i.e.,

$$\mathcal{T}_P(S) := \left\{ F_X(P) \in \mathcal{G}(\mathbb{R}^{n+1}) \; \middle|\; F_X \in \mathcal{E}_S, X \in \mathcal{C}_P^\infty(S, \mathbb{R}^{n+1}) \cap [(\nabla f)(P)]^\perp \right\}.$$

By the **tangential** vector bundle of the generalized frequencies **over** the compact subsurface S, we mean the pair  $(\mathcal{T}(S), \pi)$ , which consists of the sum of the stalks  $\mathcal{T}_P(S)$  over all  $P \in S$  and the canonical projection  $\pi : \mathcal{T}(S) \to S$ , i.e.,

$$\mathcal{T}(S) := \bigsqcup_{P \in S} \mathcal{T}_P(S), \quad \pi : \mathcal{T}(S) \to S, \ \mathcal{Q}(\in \mathcal{T}_P(S)) \mapsto P \in S.$$

The **tangential** vector bundle of the generalized frequencies is the pair  $(\mathcal{T}(\mathbb{R}^{n+1}), \pi)$  consisting of:

**TVB1** 
$$\mathcal{T}(\mathbb{R}^{n+1}) := \bigsqcup_{S \in \mathcal{S}} \mathcal{T}(S).$$
  
**TVB2**  $\pi : \mathcal{T}(\mathbb{R}^{n+1}) \to \mathcal{S}, \ Q(\in \mathcal{T}_P(S)) \mapsto P \in S \in \mathcal{S}.$ 

It is worthy of notice that:

*Note 1*  $\mathcal{T}(\mathbb{R}^{n+1})$  has the geometric algebra-valued vector bundle that is the direct product of the components of the GA-valued bundles  $\mathcal{T}(S)$  where S runs over S.

Let  $V_0(\mathbb{R}^{n+1})$  be the set of all voltage curves on  $\mathbb{R}^{n+1}$  and let  $\mathcal{M} = \mathcal{M}(\mathbb{R}^{n+1})$  denote the class of all generalized frequencies of Milano according with voltage curve in  $\mathbb{R}^{n+1}$ :

$$\mathcal{M} = \mathcal{M}(\mathbb{R}^{n+1}) = \left\{ F_{\boldsymbol{v}}(t) \mid \boldsymbol{v} = \boldsymbol{v}(t) \in \mathbf{V}_{\mathbf{0}}(\mathbb{R}^{n+1}) \right\}.$$

Note 2 We can observe that

$$\mathcal{M}(\mathbb{R}^{n+1}) = \bigsqcup_{P \in \mathbb{R}^{n+1} \setminus \{\mathbf{0}\}} \mathcal{M}_P(\mathbb{R}^{n+1}),$$

in which

$$\mathcal{M}_{P}(\mathbb{R}^{n+1}) = \bigsqcup_{v \in \mathbf{V}_{\mathbf{0}}(\mathbb{R}^{n+1})} \{ F(P) = F_{v}(0) \mid P = v(0) \}.$$

In the circumstances we can obtain a vector bundle interpretation, and which is expected to give a geometric reinterpretation of generalized frequencies of Milano.

**Theorem 1** The class  $\mathcal{M}(\mathbb{R}^{n+1})$  of all generalized frequencies of Milano coincides with the tangential vector bundle  $\mathcal{T}(\mathbb{R}^{n+1})$  in the geometric algebra  $\mathcal{G}(\mathbb{R}^{n+1})$ -valued bundle, i.e.,  $\mathcal{M}(\mathbb{R}^{n+1}) = \mathcal{T}(\mathbb{R}^{n+1})$ . Especially for every  $P \in \mathbb{R}^{n+1} \setminus \{\mathbf{0}\}$ , there exists a compact n-surface  $S_P$  such that  $\mathcal{M}_P(\mathbb{R}^{n+1}) = \mathcal{T}_P(S_P)$ .

**Corollary 1** The class of the generalized frequencies of Milano at any point  $P \in \mathbb{R}^{n+1} \setminus \{\mathbf{0}\}$  is linearly isomorphic to the tangent hyperplane  $H_P(S_P)$  of some compact n-surface  $S_P$  at P.

**Remark 2** The "tangential" condition on an extended frequency in Theorem 1 plays an essential role.

# 8.4 Orthogonal Geometry of Generalized Frequencies

# 8.4.1 Group Action on Geometric Algebra

Let  $\mathfrak{G}$  be a subgroup of the (n+1)-generalized linear group  $\mathbf{GL}_{n+1}(\mathbb{R})$ . The group  $\mathfrak{G}$  acts on the geometric algebra  $\mathcal{G}(\mathbb{R}^{n+1})$  as follows.

The algebra  $\mathcal{G}(\mathbb{R}^{n+1})$  is decomposed into the direct sum of the components, the p-th sub-geometric algebra  $\mathcal{G}^p(\mathbb{R}^{n+1})$  of degree p for  $p = 0, 1, 2, \dots, n+1$ ; i.e.,

$$\mathcal{G}(\mathbb{R}^{n+1}) = \mathbb{R} \oplus \mathbb{R}^{n+1} \oplus \mathcal{G}^2(\mathbb{R}^{n+1}) \oplus \cdots \oplus \mathcal{G}^p(\mathbb{R}^{n+1}) \oplus \cdots \oplus \mathcal{G}^{n+1}(\mathbb{R}^{n+1}),$$

in which each component  $\mathcal{G}^p(\mathbb{R}^{n+1})$  is the  $\mathbb{R}$ -vector space of dimension  $_{n+1}C_p$ :

$$\mathcal{G}^{p}(\mathbb{R}^{n+1}) = L_{\mathbb{R}} \left( \mathbf{e}_{i_{1}} \odot \mathbf{e}_{i_{2}} \odot \cdots \odot \mathbf{e}_{i_{p}} \middle| 1 \leq i_{1} \leq i_{2} \leq i_{3} \leq \cdots \leq i_{p} \leq n+1 \right).$$

The group  $\mathfrak{G}$  actually acts on each component  $\mathcal{G}^p(\mathbb{R}^{n+1})$  as follows: For every  $(n+1)\times (n+1)$ -invertible matrix  $G\in\mathfrak{G}$ ,

$$G \cdot (x_{i_1} \odot x_{i_2} \odot \cdots \odot x_{i_p}) := Gx_{i_1} \odot Gx_{i_2} \odot \cdots \odot Gx_{i_p}.$$

By the  $\binom{i_1\ i_2\ \cdots\ i_p}{j_1\ j_2\ \cdots\ j_p}$ -minor of  $G=(g_{ij})_{1\le i,j\le n+1}\in\mathfrak{G}$ , we mean the determinant defined by

$$D_{G}\begin{pmatrix} i_{1} \ i_{2} \cdots i_{p} \\ j_{1} \ j_{2} \cdots j_{p} \end{pmatrix} := \begin{pmatrix} g_{i_{1}j_{1}} \ g_{i_{1}j_{2}} \ \cdots \ g_{i_{1}j_{l}} \cdots g_{i_{1}j_{p}} \\ \vdots \\ g_{i_{k}j_{1}} \ g_{i_{k}j_{2}} \ \cdots \ g_{i_{k}j_{l}} \cdots g_{i_{k}j_{p}} \\ \vdots \\ g_{i_{p}j_{1}} \ g_{i_{p}j_{2}} \ \cdots \ g_{i_{p}j_{l}} \cdots g_{i_{p}j_{p}} \end{pmatrix}.$$

It is noted that

$$G \cdot (\mathbf{e}_{i_1} \odot \mathbf{e}_{i_2} \odot \cdots \odot \mathbf{e}_{i_p})$$

$$= \sum_{1 \leq j_1 \leq j_2 \leq \cdots \leq j_p \leq n+1} D_G \begin{pmatrix} i_1 & i_2 & \cdots & i_p \\ j_1 & j_2 & \cdots & j_p \end{pmatrix} \mathbf{e}_{j_1} \odot \mathbf{e}_{j_2} \odot \cdots \odot \mathbf{e}_{j_p}.$$

### 8.4.2 Inner Product on Geometric Algebra

The geometric algebra  $\mathcal{G}(\mathbb{R}^{n+1})$  possesses the inner product  $(\cdot,\cdot):\mathcal{G}(\mathbb{R}^{n+1})\times\mathcal{G}(\mathbb{R}^{n+1})\to\mathbb{R}$  defined by the bilinearly extension of the inner product on  $\mathcal{G}^p(\mathbb{R}^{n+1})$  as below:

$$\begin{cases} (x, y) := xy & \text{for } x, y \in \mathcal{G}^0(\mathbb{R}^{n+1}) = \mathbb{R} \\ (\boldsymbol{e}_{i_1} \odot \cdots \odot \boldsymbol{e}_{i_p}, \boldsymbol{e}_{j_1} \odot \cdots \odot \boldsymbol{e}_{j_p}) := \prod_{k=1}^p \boldsymbol{e}_{i_k} \cdot \boldsymbol{e}_{j_k} & (p \ge 1); \end{cases}$$

i.e.,

$$(\boldsymbol{e}_{i_1} \odot \cdots \odot \boldsymbol{e}_{i_p}, \boldsymbol{e}_{j_1} \odot \cdots \odot \boldsymbol{e}_{j_p}) = (\boldsymbol{e}_{i_1} \cdot \boldsymbol{e}_{j_1})(\boldsymbol{e}_{i_2} \cdot \boldsymbol{e}_{j_2}) \cdots (\boldsymbol{e}_{i_p} \cdot \boldsymbol{e}_{j_p}) \quad (p \geq 1).$$

For any elements  $A, B \in \mathcal{G}(\mathbb{R}^{n+1})$  with

$$A = a_0 + \sum_{p=1}^{n+1} \sum_{1 \leq i_1 \leq i_2 \leq \dots \leq i_p \leq n+1} a_{i_1 i_2 \dots i_p} \boldsymbol{e}_{i_1} \odot \boldsymbol{e}_{i_2} \odot \dots \odot \boldsymbol{e}_{i_p}$$

$$(a_0 \in \mathcal{G}^0(\mathbb{R}^{n+1}) = \mathbb{R})$$

$$B = b_0 + \sum_{q=0}^{n+1} \sum_{1 \leq j_1 \leq j_2 \leq \dots \leq j_q \leq n+1} b_{j_1 j_2 \dots j_q} \boldsymbol{e}_{j_1} \odot \boldsymbol{e}_{j_2} \odot \dots \odot \boldsymbol{e}_{j_q}$$

$$(b_0 \in \mathcal{G}^0(\mathbb{R}^{n+1}) = \mathbb{R}),$$

we define the inner product on  $\mathcal{G}(\mathbb{R}^{n+1})$  by

$$(A, B) := a_0 b_0 + \sum_{p=0}^{n+1} \sum_{1 \le i_1 \le \dots \le i_p \le n+1, \ 1 \le j_1 \le \dots \le j_p \le n+1} \sum_{a_{i_1 \dots i_p} b_{j_1 \dots j_p} (e_{i_1} \odot e_{i_2} \odot \dots \odot e_{i_p}, e_{j_1} \odot e_{j_2} \odot \dots \odot e_{j_p}).$$

Therefore, it follows that for every  $G \in \mathfrak{G}$ ,

$$(G \cdot (\boldsymbol{e}_{i_1} \odot \boldsymbol{e}_{i_2} \odot \cdots \odot \boldsymbol{e}_{i_p}), G \cdot (\boldsymbol{e}_{j_1} \odot \boldsymbol{e}_{j_2} \odot \cdots \odot \boldsymbol{e}_{j_p})) := \prod_{k=1}^{p} (G \boldsymbol{e}_{i_k}) \cdot (G \boldsymbol{e}_{j_k})$$

and

$$(GA, GB) := a_0b_0 + \sum_{p=0}^{n+1} \sum_{1 \leq i_1 \leq \dots \leq i_p \leq n+1, \ 1 \leq j_1 \leq \dots \leq j_p \leq n+1} \sum_{a_{i_1 \dots i_p} b_{j_1 \dots j_p} (G \cdot (\mathbf{e}_{i_1} \odot \dots \odot \mathbf{e}_{i_p}), G \cdot (\mathbf{e}_{j_1} \odot \dots \odot \mathbf{e}_{j_p})).$$

**Remark 3** The geometric algebra  $\mathcal{G}(\mathbb{R}^{n+1})$  is a normed space with its **norm**  $\|\cdot\|_{\mathcal{G}}$  defined by  $\|A\|_{\mathcal{G}} = \sqrt{(A,A)}$ . It can be easily seen that the algebra operators of  $\mathcal{G}(\mathbb{R}^{n+1})$  are continuous with respect to the norm, so  $\mathcal{G}(\mathbb{R}^{n+1})$  is a normed algebra.

# 8.4.3 Normed Space of Generalized Frequencies

We shall introduce the norm on the vector bundle  $\mathcal{T}(S)$  generated by all tangential extended frequencies on a compact subsurface S of an n-surface.

We let set the bilinear extension  $(\cdot, \cdot)_P : \mathcal{T}_P(S) \times \mathcal{T}_P(S) \to \mathbb{R}$  on the linear space  $\mathcal{T}_P(S) = L_{\mathbb{R}}(\mathcal{T}_P(S))$  of the inner product  $(\cdot, \cdot)_{\mathcal{G}(\mathbb{R}^{n+1})}$  on  $\mathcal{G}(\mathbb{R}^{n+1})$ , which is defined by  $(F_X(P), F_Y(P))_P := (F_X(P), F_Y(P))_{\mathcal{G}(\mathbb{R}^{n+1})}$ . We denote  $||F_X(P)||_{\mathcal{T}_P(S)} = \sqrt{(F_X(P), F_X(P))_P}$ .

**Definition 3** For every  $F_X \in \mathcal{T}(S)$ , the **norm** of  $F_X$  is defined by

$$||F_X|| := \sup_{P \in S} ||F_X(P)||_{\mathcal{T}_P(S)} = \sup_{P \in S} \sqrt{(F_X(P), F_X(P))_P}.$$

The **distance function** dist :  $\mathcal{T}(S) \times \mathcal{T}(S) \to \mathbb{R}$  is defined by

$$dist(F_X, F_Y) := ||F_X - F_Y||,$$

whose value is called the **distance** between two members  $F_X$  and  $F_Y$ .

**Remark 4** It should be noticed that the norm  $\|\cdot\|$  and the distance function dist are well defined. In fact, since each member in  $\mathcal{T}(S)$  is a continuous map from the compact surface S to the normed space  $\mathcal{G}(\mathbb{R}^{n+1})$ , it follows that the member is bounded on S, and thus  $\|F_X\| = \sup_{P \in S} \|F_X(P)\|_{\mathcal{T}(S)_P} \nleq +\infty$ , as claimed.  $\square$ 

It follows immediately that:

**Proposition 1** The pair  $(\mathcal{T}(S), \|\cdot\|)$  of the vector bundle generated by all the tangential extended frequencies on an n-surface S is a normed linear space, and the pair  $(\mathcal{T}(S), \text{dist})$  with the distance function  $\text{dist}(\cdot, \cdot)$ , is a metric space.

### 8.4.4 Invariant Action on Surface S

Let  $\mathfrak{G}$  be a subgroup of the (n + 1)-generalized linear group  $\mathbf{GL}_{n+1}(\mathbb{R})$ , and let  $L_{\mathbb{R}}(\mathcal{E}_S)$  be the linear vector space generated by  $\mathcal{E}_S$ , denoted simply by  $\mathcal{E}_S$  without fear of confusion.

**Definition 4** The group  $\mathfrak{G}$  acts on the normed linear space  $\mathcal{E}_S$  as follows.

$$\cdot : \mathfrak{G} \times \mathcal{E}_{S} \to \mathcal{E}_{S}, (G, F_{X}) \mapsto G \cdot F_{X}, 
(G \cdot F_{X})(P) := F_{GX}(GP) = \frac{1}{\|GP\|_{\mathcal{G}}^{2}} GP \odot GX(GP).$$

Let *S* be a compact subsurface of the *n*-surface  $\tilde{S} = f^{-1}(0)$  defined by a  $C^{\infty}$ -function  $f(x_1, x_2, \dots, x_{n+1})$  and let  $\mathfrak{G}$  be a subgroup of the  $\mathbf{GL}_{n+1}(\mathbb{R})$ .

A group  $\mathfrak{G}$  is said to act **transitively** on the subsurfaces S if  $G \cdot S \subseteq S$  for every  $G \in \mathfrak{G}$ , i.e.,

$$\left\{G\cdot P\in\mathbb{R}^{n+1}\mid G\in\mathfrak{G},\,P\in S\right\}\subseteq S.$$

A group  $\mathfrak{G}$  is said to be **invariant** on S if f(Gx) = f(x) for every  $x \in S$  and for every  $G \in \mathfrak{G}$ . Let  $\mathfrak{O}_{n+1}(f)$  be an invariant subgroup of the orthogonal group  $\mathbf{O}_{n+1}(\mathbb{R})$  on a compact subsurface S of the n-surface  $\tilde{S} = f^{-1}(0)$  defined by a function  $f = f(x) \in \mathcal{C}^{\infty}(S, \mathbb{R})$ .

It is worthy of notice that:

**Proposition 2** Let  $\mathfrak{G}$  be an invariant group on a compact subsurface S of the n-surface  $\tilde{S} = f^{-1}(0)$  defined by a function  $f = f(x) \in \mathcal{C}^{\infty}(S, \mathbb{R})$ . Then  $\mathfrak{G}$  acts transitively on the surface S. Hence any invariant subgroup  $\mathfrak{D}_{n+1}(f)$  does also on S too.

Now we can obtain the former part of the main theorem in Sect. 8.1 as below.

**Theorem 2** Let S be the n-surface  $S = f^{-1}(0)$  defined by  $f = f(\mathbf{x}) \in C^{\infty}(S, \mathbb{R})$ . Then any invariant orthogonal group  $\mathfrak{D}_{n+1}(f)$  acts isometrically on the normed linear space  $\mathcal{T}(S)$ .

**Proof** On noting  $||F_{G \cdot X}|| = ||F_X||$  for every  $G \in \mathfrak{D}_{n+1}(f)$ , it plainly follows from  $G \cdot S = S$  that  $||G \cdot F_{\cdot X} - G \cdot F_Y|| = ||F_{G \cdot X} - F_{G \cdot Y}|| = ||F_X - F_Y||$ , and the theorem follows immediately, in completing the proof.

# 8.4.5 Geometrical Interpretation of Generalized Frequencies Revisited

We further proceed with giving another geometrical interpretation of generalized frequencies of Milano in the above line.

Let  $V_0(S)$  denote the set of all voltage curves on a subsurface S of the n-surface  $\tilde{S} = f^{-1}(0)$  defined by  $f = f(x) \in \mathcal{C}^{\infty}(S, \mathbb{R})$ . Let  $\mathcal{M}(S)$  be the class of all the generalized frequencies of Milano according to all voltage curves running over S:

$$\mathcal{M}(S) = \{ F_{\boldsymbol{v}}(t) \mid \boldsymbol{v} = \boldsymbol{v}(t) \in \mathbf{V}_{\mathbf{0}}(S) \}.$$

It can be plainly observed that  $\mathcal{M}(S)$  has the bundle structure:

$$\mathcal{M}(S) = \bigsqcup_{P \in S} \mathcal{M}_P(S),$$

in which

$$\mathcal{M}_{P}(S) = \bigsqcup_{v \in \mathbf{V}_{0}(S)} \{ F(P) = F_{v}(0) \mid P = v(0) \}.$$

We can verify the latter part of the main theorem in Sect. 8.1 as below.

**Theorem 3** Let S be a compact subsurface of the n-surface  $\tilde{S} = f^{-1}(0)$  defined by  $f = f(x) \in \mathcal{C}^{\infty}(S, \mathbb{R})$ , and let  $\mathfrak{O}_{n+1}(f)$  be an invariant subgroup of the orthogonal group  $\mathbf{O}_{n+1}(\mathbb{R})$ . Then the class  $\mathcal{M}(S)$  of all generalized frequencies of Milano according to all voltage curves running over S is an invariant orthogonal geometry via the group  $\mathfrak{O}_{n+1}(f)$  action on the surface S.

That is, the group  $\mathfrak{O}_{n+1}(f)$  acts isometrically on the normed linear space  $\mathcal{M}(S)$  of all the generalized frequencies of Milano according to all voltage curves running over S.

**Proof** On noting that any voltage curve  $v \in V_0(S)$  lies globally on S, we can take  $S_P$  in Theorem 1 as  $S_P = S$ . It follows from Theorem 1 that  $\mathcal{M}_P(S) = \mathcal{T}_P(S)$ , and thus  $\mathcal{M}(S) = \mathcal{T}(S)$ . Further it can be plainly observed that the transitive group  $\mathfrak{O}_{n+1}(f)$  acts isometrically on the right-hand side  $\mathcal{T}_P(S)$ , which follows immediately what we want to show.

It ends well this article with reconsidering Example 2.

**Example 3** Notation and assumptions being the same in Example 2, let *S* be the subsurface of the sphere of radius  $\sqrt{\frac{3}{2}}$  and center the origin:

$$S = \left\{ \mathbf{x} = {}^{t}(x_{1}, x_{2}, x_{3}) \in \mathbb{R}^{3} \middle| x_{1}^{2} + x_{2}^{2} + x_{3}^{2} = \frac{3}{2}, x_{1} + x_{2} + x_{3} = 0 \right\}.$$

Then the class  $\mathcal{M}(S)$  of the generalized frequencies of Milano according to all voltage curves running over the surface S is linearly isomorphic to the tangent bundle on S, i.e.,

$$\mathcal{M}(S) \cong \mathcal{T}(S) = \bigsqcup_{P = {}^{t}(p_{1}, p_{2}, p_{3}) \in S} \left\{ {}^{t}(x_{1}, x_{2}, x_{3}) \in \mathbb{R}^{3} \mid p_{1}x_{1} + p_{2}x_{2} + p_{3}x_{3} = 0 \right\},$$

via the map

$$\mathcal{M}_P(S) \ni F_v(0) = F_X(P) \mapsto X(P) = {}^t(x_1(P), x_2(P), x_3(P)) \quad (v(0) = P).$$

The distance on  $\mathcal{M}(S)$  between two generalized frequencies  $F_v$  and  $F_w$  is given by

$$dist(F_v, F_w) = \sup_{P \in S} \sqrt{\sum_{i=1}^{3} (x_i(P) - y_i(P))^2},$$

in which  $F_v(0) = F_X(P) \mapsto X(P) = {}^t(x_1(P), x_2(P), x_3(P))$  is as above, and

$$\mathcal{M}_P(S) \ni F_{\mathbf{w}}(0) = F_Y(P) \mapsto Y(P) = {}^t(y_1(P), y_2(P), y_3(P)) \quad (\mathbf{w}(0) = P).$$

It is noted that  $\operatorname{dist}(F_{\boldsymbol{v}}, F_{\boldsymbol{w}}) \leq \sqrt{\frac{3}{2}}$ .

Further it is observed that the orthogonal group  $\mathbf{O}_3(\mathbb{R})$  acts transitively on the surface S, and that it is invariant on S; thus  $\mathfrak{O}_3 = \mathbf{O}_3(\mathbb{R})$  acts isometrically on  $\mathcal{M}_P(S)$ . This gives a geometry of the generalized frequencies of Milano.  $\square$ 

# 8.5 Concluding Remarks

Our aim is to give a geometrical interpretation of the generalized frequencies of Milano. In this chapter, we propose the metric-geometrical structure of the extended frequencies with emphasis on geometric algebra-valued vector bundles playing an important role.

By our experience, the bundle structure is known as a useful technique to understand the geometric structure of mathematical subjects. So we have taken a step forward the geometrical interpretation of the generalized frequencies of Milano as its construction of the algebraic bundle structures on frequencies by Horizumi and as an orthogonal geometry in this chapter, which means that the class is a normed linear space on which the "invariant" orthogonal group acts isometrically. In the next agenda, we will proceed to investigate the geometric bundle structure on frequencies.

**Acknowledgments** The authors cordially thank Ibaraki University Library, Mito campus, for providing a space in the "Common Learning Room" for our working seminar.

### References

- F. Milano, A geometric interpretation of frequency. IEEE Trans. Power Syst. 37(1), 816–819 (2022). https://doi.org/10.1109/tpwrs.2021.3108915
- F. Milano, G. Tzounas, I. Dassios, M.A.A. Murad, T. Kërçi, Using differential geometry to revisit the paradoxes of the instantaneous frequency. IEEE Open Access J. Power Energy 2, 501–513 (2022)
- F. Milano, B. Alhanjari, G. Tzounas, Enhancing frequency control through rate of change of voltage feedback. IEEE Trans. Power Syst. 39(1), 2385–2388 (2024)
- A. Alshawabkeh, G. Tzounas, F. Milano, Instantaneous frequency estimation in unbalanced systems using affine differential geometry. IEEE Trans. Power Delivery. Under review. Submitted. https://doi.org/10.48550/arXiv.2206.12091
- F. Milano, G. Tzounas, I. Dassios, T. Kërçi, Applications of the Frenet frame to electric circuits. IEEE Trans. Circuits Syst. 69(4), 1668–1680 (2022). https://doi.org/10.1109/tcsi.2021.3133948
- L.C. Grove, Classical groups and geometric algebra. Graduate Studies in Mathematics, vol. 39
   (American Mathematical Society, Providence, 2002), x+169 pp. ISBN: 0-8218-2019-2, Zbl 0990.20001, MR1859189
- C. Doran, A. Lasenby, Geometric Algebra for Physicists (Cambridge University Press, Cambridge, 2003), xiv+578pp. Zbl 1078.53001, MR1998960. https://doi.org/10.1017/ cbo9780511807497

# Chapter 9 A Hybrid Probabilistic–Fuzzy Programming for Integrated Production Planning and Raw Material Procurement in Post-Pandemic Time



S. Sutrisno , Purnawan Adi Wicaksono , S. Solikhin , and Abdul Aziz

### 9.1 Introduction

Excess demands for some products such as medical products happened during the COVID-19 pandemic. In the post-pandemic time, some products/services such as hospitality products tend to have excess demands. Furthermore, some factors such as prices, quality, and safety tend to be uncertain due to some reasons such as restrictions [1]. Therefore, managers in manufacturing and retail industries need to have new decision-making support that suits these conditions in optimizing their production and selling activities to earn the optimal profit. Two important activities in manufacturing industries that need to be optimized are raw material procurement and production. Operational costs for these activities significantly contribute to the profit earned by the company. Therefore, they should be optimized in any situation including excess demands and uncertainties after a pandemic. Therefore, the manager needs a new model to solve these two problems.

The common approach that suits process optimization is using a mathematical optimization model. Many companies rely on this approach in optimizing their activities. Some examples include chemical product companies [2–5], portfolio and accounting entities [6–9], and energies [10–14]. The basic step in process optimization using this approach is modeling the problem as a mathematical optimization model and calculating the optimal decision using an optimization algorithm.

Department of Mathematics, Diponegoro University, Semarang, Indonesia e-mail: s.sutrisno@live.undip.ac.id

P. A. Wicaksono

Department of Industrial Engineering, Diponegoro University, Semarang, Indonesia

S. Sutrisno (⋈) · S. Solikhin · A. Aziz

S. Sutrisno et al.

For the raw material procurement and production planning problems, some mathematical optimization models have been proposed to solve this problem independently based on the specifications of the problem. Some examples include single supply chain networks [15], two-echelon networks [16], periodic buyback schemes [17], hierarchical approach [18], and variable prices [19]. However, those problems were considered in deterministic environments, meaning that all parameters were fully certain. In more complex situations, more advanced models have been proposed. This includes situations of product rejections [20–23] and risk management [24, 25].

Some more advanced models have been developed to handle uncertainties of some parameters. The model depends also on the specifications of the problem. Numerous examples are available in the literature, for example, the energy-based model [26], order acceptance scheme [27], aggregate production model [28, 29], and references therein. Reports on applications are also available in various sectors such as crude oil refinery [30] and textile industries [31].

Nevertheless, there is still no model that integrates the raw material procurement and production planning problems with excess demands and hybrid uncertainties in which some parameters are fuzzy and some other parameters are probabilistic. This research gap is filled in this paper, that is, this study aimed to propose a new mathematical optimization model with hybrid uncertainties as a decision-making support for integrated raw parts procurement and production planning problems with excess demands and probabilistic–fuzzy parameters. Numerical experiment results will be presented to show how the problem was solved by using the proposed model.

# 9.2 Methodology and Mathematical Model

To be precise, the problem together with the assumptions considered in this study is specified in the following subsection. The methodology and the proposed model will follow in the subsequent subsections.

# 9.2.1 Problem Setting

Consider that some types of raw materials/parts will be purchased from several suppliers. These parts will be used to make several product brands. The flow of the products is illustrated in Fig. 9.1. The suppliers have various capacities, prices, raw part qualities, and delivery performances. The company sells produced products to buyers. To fit post-pandemic situations with excess demands, the production capacities are less than the demands, that is, all produced products are sold. The decision-maker has to make an optimal decision for the amount of each raw part type that will be purchased from each supplier and the amount of each product brand

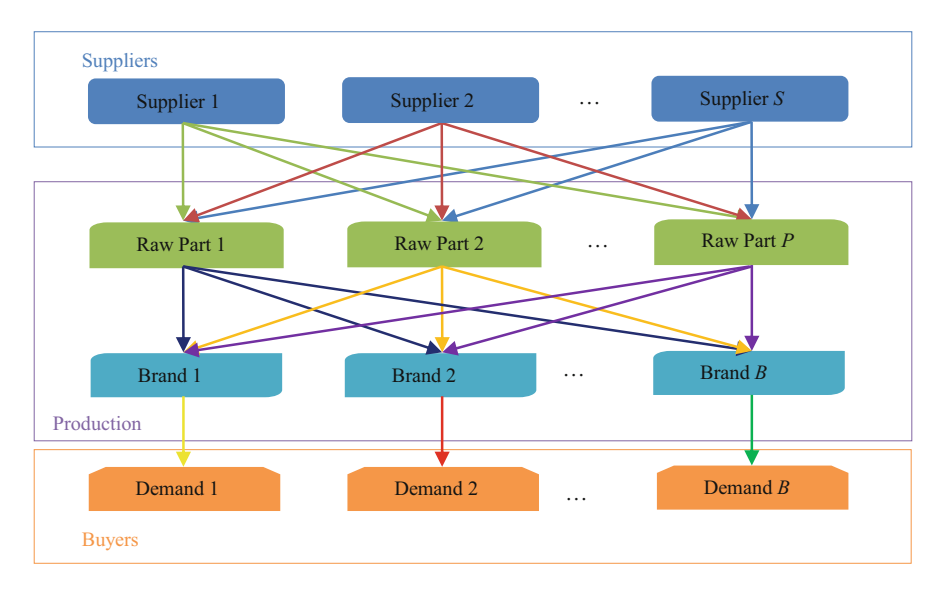


Fig. 9.1 The flow of raw parts and products in the supply chain

that will be made such that the profit is expected to be maximal. The decision-maker can only maximize the expectation of the profit, since the problem is solved under uncertainty of some parameters, see the mathematical model for further details.

The mathematical model of the problem described above was formulated under the following assumptions. First, in maximizing the profit, demands do not need to be fully satisfied due to excess demand situations. Second, late-delivered raw parts are not used in production, however, are used in the subsequent production cycle. Third, rejected raw parts and products are vanished. The reminders of raw parts and products, if any, are omitted and thus do not contribute to the profit function.

# 9.2.2 Methodology

Figure 9.1 shows the methodology implemented in this study. It contains the problem-solving steps. The problem is solved, in general, with four steps. First, the problem-defining step specifies the integrated raw parts procurement and production planning problem; this is already explained in the previous section. The second step is mathematical modeling, in which the defined problem is transformed into a mathematical optimization model; this is presented in the following subsection. The third step is calculating the optimal decision via the formulated model by using an optimization algorithm. Uncertain programming based on an interior point algorithm was used in this step, where all computations were performed in LINGO 20.0 optimization software. The final step is evaluating the model and

S. Sutrisno et al.



Fig. 9.2 The problem-solving procedure

implementation. The model is modified, if needed, based on the changes in the problem. When the optimal decision has been derived, it can then be implemented by the decision-maker. The problem-solving procedure is presented in Fig. 9.2.

### 9.2.3 Nomenclature

### Indices:

$p \in \{1, 2, \dots, P\}$	:	Raw material parts
$s \in \{1, 2, \ldots, S\}$	:	Vendors or suppliers
$b \in \{1, 2, \ldots, B\}$	:	Product or service brands

# Decision variables:

$Y_b$	:	Number of product or service brand b that will be made
$X_{sp}$	:	Number of raw material parts $p$ that will be procured from supplier $s$
$Z_s$	:	Indicator variables representing whether a supplier or vendor <i>s</i> is selected to supply raw material parts
$S_s$	:	Number of deliveries to transport raw material parts from supplier or vendor <i>s</i>

# Fuzzy parameters:

$\widetilde{DE}_b$	:	Demands from buyers or customers for product brand b
$\widetilde{BP}_b$	:	Product brand b's unit price
$\widetilde{PP}_{sp}$	:	Raw part p's unit price at supplier s
$\widetilde{TC}_s$	:	One truck's transportation cost for delivering raw parts from supplier s
$\widetilde{SC}_{sp}$	:	The capacity of supplier s for raw part p

# Probabilistic parameters:

$\overline{AC}_b$	:	Cost to product one unit product brand b
$\overline{LR}_{sp}$	:	Rates of late-delivered raw parts from suppliers
$\overline{DR}_{sp}$	:	Rates of rejected raw parts ordered from supplier
$\overline{DY}_b$	:	Rates of rejected products from production

# Deterministic parameters:

$RP_{pb}$	:	Required number of raw part $b$ to produce one unit of product brand $b$
$\overline{C}$		Maximum capacity of trucks used in transporting raw parts from suppliers
	:	to the manufacturer
$O_s$	:	Cost to order raw parts to the supplier
$PD_p$	:	Penalty cost for one unit of rejected raw parts
$PL_p$	:	Penalty cost for one unit of late-delivered raw parts

### Others:

$\mathcal{E}[\cdot]$	:	Hybrid probabilistic-fuzzy expectation value
----------------------	---	--

S. Sutrisno et al.

### 9.2.4 Mathematical Model

The problem specified in the previous section is modeled as mathematical programming, where the objective function is the expectation of the profit. Some constraint functions are modeled based on the conditions that should be satisfied. The profit expectation function is simply formulated as the income expectation minus the total operational cost expectation. First, the income, denoted by  $F_1$ , is formulated as the unit product price  $\widetilde{BP}_b$  times the number of nonrejected produced products  $(1 - \overline{DY}_b) Y_b$ , that is,

$$F_1 = \sum_{b=1}^{B} \left( \widetilde{BP}_b \times \left( 1 - \overline{DY}_b \right) Y_b \right). \tag{9.1}$$

The problem is assumed to have excess demands, meaning that all of the available products will be sold. The first operational cost component is the cost to produce one unit of product, which is denoted by  $F_2$  and is formulated as follows:

$$F_2 = \sum_{b=1}^{B} \left( \overline{AC}_b \times Y_b \right). \tag{9.2}$$

The second operational cost component is the procurement cost for raw parts; this is denoted by  $F_3$  and is formulated as the unit price times the amount of order, that is,

$$F_3 = \sum_{p=1}^{P} \sum_{s=1}^{S} \left( \widetilde{PP}_{sp} \times X_{sp} \right) \tag{9.3}$$

The next operational cost component included in the model is the penalty costs for rejected and delayed raw parts, which is denoted by  $F_4$  and is formulated as follows:

$$F_4 = \sum_{p=1}^{P} \sum_{s=1}^{S} \left[ \left( PD_p \times \overline{DR}_{sp} \times X_{sp} \right) + \left( PL_p \times \overline{LR}_{sp} \times X_{sp} \right) \right]. \tag{9.4}$$

The other operational cost components are the ordering and transportation costs, which is denoted by  $F_5$  and is formulated as follows:

$$F_5 = \sum_{s=1}^{S} \left[ \left( \overline{O}_s \times Z_s \right) + \left( \widetilde{TC}_s \times S_s \right) \right]. \tag{9.5}$$

Thus, the profit can be formulated as:

$$Z = F_1 - F_2 - F_3 - F_4 - F_5 \tag{9.6}$$

where  $F_1$  is the income,  $F_2$ ,  $F_3$ ,  $F_4$ , and  $F_5$  are operational costs.

Note that due to the presence of probabilistic and fuzzy parameters, the actual profit function Z is not possible to be maximized before the realization of those uncertain parameters. Instead, the decision-maker can only maximize the expectation of the profit. Furthermore, the decision that maximizes the expectation of the profit must satisfy the conditions that have been specified in the problem set. Altogether, this is modeled as the following optimization problem where explanations for the constraint functions will follow afterward:

$$\max_{\{X_{SP}, Y_b\}} \mathcal{E}[Z] \tag{9.7}$$

subject to:

$$\sum_{s=1}^{S} \left[ X_{sp} - \left( \overline{LR}_{sp} \times X_{sp} \right) - \left( \overline{DR}_{sp} \times X_{sp} \right) \right] \ge \sum_{b=1}^{B} \left( RP_{pb} \times Y_{b} \right),$$

$$\forall p = 1, 2, \dots, P$$
(9.8)

$$Y_b - \overline{DY}_b \times Y_b \le \widetilde{DE}_b, \quad \forall b = 1, 2, \dots, B$$
 (9.9)

$$X_{sp} \le \widetilde{SC}_{sp}, \forall p = 1, 2, \dots P, \forall s = 1, 2, \dots, S$$
 (9.10)

$$\sum_{p=1}^{P} X_{sp} \le C \times S_s, \forall s = 1, 2, \dots, S$$
 (9.11)

$$Z_{s} = \begin{cases} 1, & \text{if } \sum_{p=1}^{P} X_{sp} > 0 \\ 0, & \text{others} \end{cases} \quad \forall s = 1, 2, \dots, S$$
 (9.12)

$$X_{sp}, Y_b \ge 0$$
 and integer  $\forall s = 1, 2, ..., S, \ \forall p = 1, 2, ..., P, \forall b = 1, 2, ..., b.$  (9.13)

The constraint functions (9.8)–(9.13) are explained as follows. The first constraint function, the inequality (9.8), states that the nonrejected raw parts that arrived at the manufacturer are enough for production. This is formulated as the number of raw parts ordered to suppliers minus the delayed raw parts minus the rejected raw parts is no less than the required number of raw parts needed to produce products. The second constraint, inequality (9.9), states that the number of nonrejected products is not larger than the demand, meaning that the demand is not necessarily to be satisfied; this is due to an excess demand situation in which loss of some demand is allowed as long as the profit is expected to be maximal. The next constraint function (9.11) is utilized to decide the number of trucks used to transport

S. Sutrisno et al.

raw parts from each supplier. Meanwhile, the constraint (9.10) is the upper bound of the number of raw parts that can be procured from suppliers. The binary function (9.12) is designed to indicate whether  $Z_s$  should be 1 if the corresponding supplier is selected or 0 otherwise; this is used to calculate the order cost in the  $F_5$ . The last constraint is nonnegativity and integer for all decision variables: the number of raw parts that must be produced by each supplier and the number of products that must be produced in the production.

The programming model (9.7) together with its constraints contains both probabilistic and fuzzy parameters. It belongs to uncertain programming. To calculate the optimal decision, the uncertain programming method is utilized. For calculating the expectation value of a probabilistic parameter, standard formulas from probability theory are used, for example, see Ref. [32] for technical details. Meanwhile, for each fuzzy parameter  $\eta$ , consider the following discrete membership function:

$$\mu_{\eta}(x) = \begin{cases} \mu_{\eta^{(1)}}, & \text{if } \eta = \eta^{(1)} \\ \mu_{\eta^{(1)}}, & \text{if } \eta = \eta^{(2)} \\ \vdots \\ \mu_{\eta^{(m)}}, & \text{if } \eta = \eta^{(m)} \end{cases}$$

where  $\eta^{(1)}$ ,  $\eta^{(2)}$ , ...,  $\eta^{(m)}$  are distinct and  $\eta^{(1)} < \eta^{(2)} < \cdots < \eta^{(m)}$ . Then, the expectation value  $\eta$  is calculated as  $\mathcal{E}[\eta] = \sum_{i=1}^m w_i \eta^{(i)}$ , where for  $i = 1, 2, \ldots, m$ , the weights  $w_i$  is calculated via

$$w_i = \frac{1}{2} \left( \max_{1 \le j \le i} \mu^{(j)} - \max_{1 \le j < i} \mu^{(j)} + \max_{1 \le j \le m} \mu^{(j)} - \max_{1 < j \le m} \mu^{(j)} \right);$$

One may refer to Ref. [33] for further technical details. Note that this discrete membership function approach for the fuzzy parameters is one alternative that decision-makers can choose. Other types of membership functions such as triangular and trapezoidal membership functions can also be implemented, see Sect. 9.4 for further details.

# 9.3 Simulation Experiment Results

To test the model proposed in this study, simulations were carried out in a laboratory; data used in the experiments were randomly generated. The numbers of suppliers, raw part types, and product brands are five each. Values for deterministic parameters are shown in Tables 9.1, 9.2, 9.3, and 9.4. Probability distributions of probabilistic parameters are normal; their means and standard deviations are shown in Table 9.5. Meanwhile, each fuzzy parameter  $\eta$  has a discrete membership function of the form

**Table 9.1** Required number of raw parts for making one unit of products  $(RP_{pb})$ 

	Product brand type				
Raw material/part type	<i>B1</i>	B2	<i>B3</i>	B4	B5
P1	2	2	1	2	1
P2	2	1	2	1	2
P3	1	2	3	3	3
P4	2	1	2	1	3
P5	3	2	1	2	2

**Table 9.2** Penalty costs for rejected raw parts  $(PD_p)$ 

	Part ty	Part type				
Supplier	P1	P2	P3	P4	P5	
S1	2.00	1.00	1.00	1.00	2.00	
S2	1.00	0.50	1.00	0.50	2.00	
S3	2.00	0.50	0.50	1.00	0.75	
S4	1.00	1.00	1.00	2.00	0.75	
S5	0.75	0.75	2.00	0.75	0.50	

**Table 9.3** Penalty costs for delayed raw parts  $(PL_p)$ 

	Raw material/part type					
Supplier	<i>P1</i>	P2	P3	P4	P5	
S1	0.75	1.00	0.50	1.00	2.00	
S2	1.00	1.50	0.75	1.50	1.50	
S3	0.75	1.50	0.50	1.00	2.50	
S4	1.00	2.00	1.00	1.26	1.00	
S5	0.75	1.00	0.50	1.50	1.00	

Table 9.4 Transport costs, order costs, and truck capacity

Supplier	Order costs $(O_s)$	Transportation costs $(TC_s)$	Truck capacity (C)
S1	50	250	100
S2	60	300	
S3	55	240	
S4	50	320	
S5	45	275	

$$\mu_{\eta} = \begin{cases} \mu_{\eta^{(1)}} & \text{if } \eta = \eta^{(1)}; \\ \mu_{\eta^{(2)}} & \text{if } \eta = \eta^{(2)}; \\ \vdots \\ \mu_{\eta^{(5)}} & \text{if } \eta = \eta^{(5)}. \end{cases}$$

where values for  $\eta^{(i)}$  for each fuzzy parameter are shown in Tables 9.6, 9.7, 9.8, 9.9, and 9.10. The optimal decision is calculated (9.7) using LINGO 20.0 software, where the uncertain programming algorithm was utilized. The results are shown in Figs. 9.3 and 9.4.

S. Sutrisno et al.

**Table 9.5** Values of mean and standard deviation for the normally distributed probabilistic parameters

Probabilistic parameter	Mean (µ)	Standard deviation $(\sigma)$
$\overline{AC}_b$	20	10
$\overline{LR}_{sp}$	0.1	0.05
$\frac{\overline{LR_{sp}}}{\overline{DR_{sp}}}$ $\overline{DY_b}$	0.1	0.05
$\overline{DY}_b$	0.075	0.025

**Table 9.6** Values for possible realizations and weights for the fuzzy parameter demands  $(\widetilde{DE}_b)$ 

i	$\widetilde{DE}_{b}^{(i)}$	$\mu_{\widetilde{DE}_{h}^{(i)}}$	$w_{\widetilde{DE}_b}^{(i)}$
1	50	0.30	0.150
2	60	0.50	0.100
3	70	0.80	0.150
4	80	1.00	0.250
5	100	0.70	0.350

**Table 9.7** Values for possible realizations and weights for the fuzzy parameter products' prices  $(\widetilde{BP}_b)$ 

i	$\widetilde{BP}_b^{(i)}$	$\mu_{\widetilde{\mathit{BP}}_b^{(i)}}$	$w_{\tilde{BP}_b}^{(i)}$
1	375	0.35	0.175
2	500	0.55	0.100
3	425	1.00	0.450
4	450	0.55	0.150
5	475	0.25	0.125

**Table 9.8** Values for possible realizations and weights for the fuzzy parameter raw parts' prices  $(\widetilde{PP}_{sp})$ 

i	$\widetilde{PP}_{sp}^{(i)}$	$\mu_{\widetilde{PP}_{sp}^{(i)}}$	$w_{\widetilde{PP}_{sp}}^{(i)}$
1	25	0.10	0.050
2	26	0.20	0.050
3	32	1.00	0.700
4	33	0.40	0.050
5	34	0.30	0.150

Table 9.9	Values for	
possible re	alizations and	
weights for the fuzzy		
parameter	transportation costs	
$(\widetilde{TC}_s)$		

i	$\widetilde{TC}_s^{(i)}$	$\mu_{\widetilde{TC}_s^{(i)}}$	$w_{\widetilde{TC}_s}^{(i)}$
1	110	0.10	0.050
2	120	0.30	0.100
3	180	1.00	0.575
4	190	0.55	0.165
5	200	0.22	0.110

For procurement planning, the optimal decision is shown in Fig. 9.3. It is shown that only S1, S3, S4, and S5 were chosen to supply raw material parts. No parts were purchased from supplier S2. This decision was due to in aggregate, supplier S2 being the worst supplier. Nevertheless, not all raw part types were purchased from all selected suppliers. For example, only raw part types P1 and P4 were purchased from supplier S5. This shows that it is not a good decision to purchase raw part types

**Table 9.10** Values for possible realizations and weights for the fuzzy parameter suppliers' capacities  $(SC_{sp})$ 

i	$\widetilde{SC}_{sp}^{(i)}$	$\mu_{\widetilde{SC}_{sp}^{(i)}}$	$w^{(i)}_{\widetilde{SC}_{sp}}$
1	200	0.45	0.225
2	220	0.70	0.125
3	230	1.00	0.275
4	240	0.75	0.125
5	250	0.50	0.250

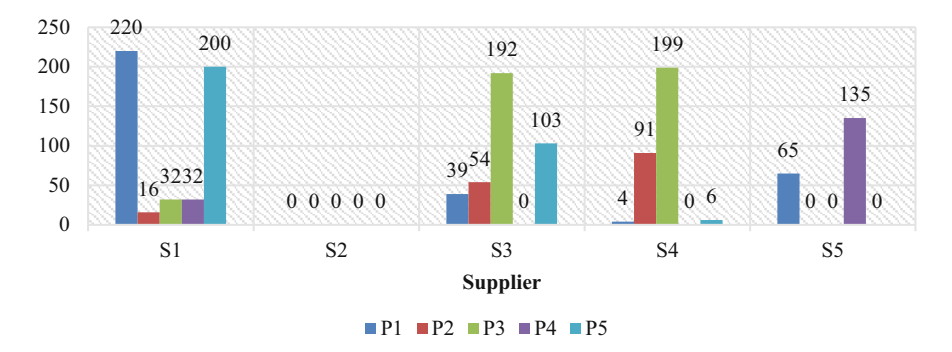


Fig. 9.3 The optimal raw part procurement



Fig. 9.4 The optimal decision regarding the production

P2, P3, and P5 from supplier S5, and it is better to purchase those part types from the other selected suppliers. This decision provides the maximal expectation of the profit. This indeed is not obvious, and the optimal allocation cannot be made without using such a mathematical optimization model. In Fig. 9.4, the optimal decision regarding the production is depicted. Only brand B2, B3, and B4 were decided to be produced. Even though it is only one unit of B3 to be produced, it still contributes to the profit. Brands B1 and B5 were not decided to be produced; this was due to it contributing negatively to the profit. In particular, the expectation of the profit is 3046.91.

S. Sutrisno et al.

### 9.4 Discussion

Based on the mathematical optimization model formulated in the previous section and the numerical experiment results, the following managerial insights can be considered by decision-makers during implementation. First, the mathematical model could be modified following the needs of the decision-maker and the specifications of the problem. For example, some other operational costs could be added such as costs to make contracts with suppliers or carriers. Other constraints functions could also be added such as limitations on the production cost and transportation cost.

Second, other probability distribution functions such as Poisson could also be considered for the probabilistic parameters; however, this depends on the probability test results from the data. Nevertheless, the problem-solving step is still the same. Meanwhile, other types of membership functions for the fuzzy parameters could also be utilized. For example, some fuzzy parameters could have triangular membership or trapezoidal functions. This depends on the decision-maker's intuition in deciding which membership function types fit the situation the best. Mathematically speaking, this is the best that decision-makers can do due to a lack of data. Nevertheless, decision-makers can decide this based on their experience in dealing with similar problems.

Third, if the decision-maker still has time for computation, the calculation in LINGO 20.0 could be done multiple times with the same or different values for the uncertain parameters, for example, with different membership functions. Different calculations with the same parameters could provide different decisions, however, it will provide the same expectation of the profit. However, if different parameters for the uncertain parameters are used, it could also provide different expectations of the profit; this is due to uncertainty. For example, if for the fuzzy parameter demands, different membership functions are used in the optimization, they could provide different expectations of the profit. Nevertheless, in the end, the decision-maker decides which decision will be implemented.

The fourth insight is that the actual profit gained by the manufacturer might be different from the profit expectation provided by the mathematical model. Note that the actual profit can only be known, after the exact values of all uncertain parameters are known. This is due to the activities being carried out under uncertainties; and mathematically, this is the best that the decision-maker can do to optimize the activities.

The next insight is about the computer used in the computation. In the numerical experiments performed in this study, only a common computer was used with common specifications. All computations were done in minutes. However, if the size of the problem is sufficiently large, for example, with hundreds of suppliers and tens of product brands, the computational time will increase and could take hours or even days. In this case, if a common computer does not solve the problem in time, the decision-maker could consider a high-performance computer to decrease the computational time. Another option could be utilizing heuristic algorithms; this

is rather out of the scope of this study; however, it is interesting to study in the future.

Last, the mathematical model proposed in this study can be implemented for any kind of raw parts and products or services; however, slight modification would be needed in implementations, when different specifications are faced by the decision-maker. For example, if the measurement follows real numbers, then the integer constraints for decision variables might be not needed.

# 9.5 Summary and Future Works

A newly built novel mathematical model in the form of hybrid probabilistic–fuzzy programming is proposed in this study, which is useful for optimizing procurement and production planning problems with excess demand and uncertainties. The proposed model fits extraordinary situations such as recovery time after a pandemic, in which demands are bigger than supplies and most of the parameters are uncertain with or without data availability. Numerical experiments have been carried out to test the proposed model, and results showed that the model successfully provided the optimal decision that provided the maximal expectation of the profit. This concludes that the proposed model can be utilized by managers or decision-makers in industries.

As a future research direction, the model can be further developed such that it also includes other parties that are not involved yet in the model proposed in this study, such as warehouses and distributors. Furthermore, it can also be further developed with multiple time observation periods, in which decisions are made for multiple procurement and production cycles.

**Acknowledgments** This work was funded by Universitas Diponegoro via the RPI Research Grant under project no. 185-83/UN7.6.1/PP/2023.

### References

- L. Wang, Food supply chain sustainability strategy for fresh retailer and multi-output random fresh suppliers after COVID-19. Sustainability (Switzerland) 15 (2023). https://doi.org/ 10.3390/su15010546
- L. Gelain, L. van der Wielen, W.M. van Gulik, G. da Cruz, J. Pradella, A. Carvalho da Costa, Mathematical modelling for the optimization of cellulase production using glycerol for cell growth and cellulose as the inducer substrate. Chem. Eng. Sci. X. 8, 100085 (2020). https:// doi.org/10.1016/j.cesx.2020.100085
- M. Shutaywi, Z. Shah, Mathematical modeling and numerical simulation for nanofluid flow with entropy optimization. Case Stud. Therm. Eng. 26, 101198 (2021). https://doi.org/10.1016/ j.csite.2021.101198

 R. Pierott, A.W.A. Hammad, A. Haddad, S. Garcia, G. Falcón, A mathematical optimisation model for the design and detailing of reinforced concrete beams. Eng. Struct. 245, 112861 (2021). https://doi.org/10.1016/j.engstruct.2021.112861

126

- N. Sanghvi, D. Vora, J. Patel, A. Malik, Optimization of end milling of Inconel 825 with coated tool: A mathematical comparison between GRA, TOPSIS and fuzzy logic methods. Mater Today Proc. 38, 2301–2309 (2021). https://doi.org/10.1016/j.matpr.2020.06.413
- M. Gutiérrez, Making better decisions by applying mathematical optimization to cost accounting: An advanced approach to multi-level contribution margin accounting. Heliyon 7, e06096 (2021). https://doi.org/10.1016/j.heliyon.2021.e06096
- H.D. Perez, S. Amaran, E. Erisen, J.M. Wassick, I.E. Grossmann, Optimization of extended business processes in digital supply chains using mathematical programming. Comput. Chem. Eng. 152, 107323 (2021). https://doi.org/10.1016/j.compchemeng.2021.107323
- B.C. Barroso, R.T.N. Cardoso, M.K. Melo, Performance analysis of the integration between portfolio optimization and technical analysis strategies in the Brazilian stock market. Expert Syst. Appl., 115687 (2021). https://doi.org/10.1016/J.ESWA.2021.115687
- R. Faia, T. Pinto, Z. Vale, J.M. Corchado, Portfolio optimization of electricity markets participation using forecasting error in risk formulation. Int. J. Electr. Power Energy Syst. 129, 106739 (2021). https://doi.org/10.1016/J.IJEPES.2020.106739
- M.J. Dehghani, C.K. Yoo, Three-step modification and optimization of Kalina power-cooling cogeneration based on energy, pinch, and economics analyses. Energy 205, 118069 (2020). https://doi.org/10.1016/J.ENERGY.2020.118069
- F. Guo, Y. Li, Z. Xu, J. Qin, L. Long, Multi-objective optimization of multi-energy heating systems based on solar, natural gas, and air- energy. Sustain Energy Technol Assess 47, 101394 (2021). https://doi.org/10.1016/J.SETA.2021.101394
- J.A. Okolie, E.I. Epelle, S. Nanda, D. Castello, A.K. Dalai, J.A. Kozinski, Modeling and process optimization of hydrothermal gasification for hydrogen production: A comprehensive review. J. Supercrit. Fluids 173, 105199 (2021). https://doi.org/10.1016/ J.SUPFLU.2021.105199
- J. Zhou, Y. Wu, Z. Zhong, C. Xu, Y. Ke, J. Gao, Modeling and configuration optimization of the natural gas-wind-photovoltaic-hydrogen integrated energy system: A novel deviation satisfaction strategy. Energy Convers. Manag. 243, 114340 (2021). https://doi.org/10.1016/ J.ENCONMAN.2021.114340
- R. Liu, Y. Lin, G. Xu, Y. Li, R. Premalatha, K. Chandran, Optimized hybridized mathematical model for wastewater treatment and energy generation using microbial fuel cells. Sustain Energy Technol Assess 47, 101348 (2021). https://doi.org/10.1016/J.SETA.2021.101348
- N.R. Ware, S.P. Singh, D.K. Banwet, A mixed-integer non-linear program to model dynamic supplier selection problem. Expert Syst. Appl. 41, 671–678 (2014). https://doi.org/10.1016/ j.eswa.2013.07.092
- M.T. Ahmad, S. Mondal, Dynamic supplier selection model under two-echelon supply network. Expert Syst. Appl. 65, 255–270 (2016). https://doi.org/10.1016/j.eswa.2016.08.043
- M. Farhat, A. Akbalik, A.B. Hadj-Alouane, N. Sauer, Lot sizing problem with batch ordering under periodic buyback contract and lost sales. Int. J. Prod. Econ. 208, 500–511 (2019). https://doi.org/10.1016/J.IJPE.2018.12.013
- N. Goker, M. Dursun, A comparative analysis of disaggregation types in hierarchical production planning. WSEAS Trans. Comput. Res. 10, 55–61 (2022). https://doi.org/10.37394/232018.2022.10.8
- Z. Babić, T. Perić, B. Marasović, Z. Babić, T. Perić, B. Marasović, Production planning through multi-objective De Novo programming with variable prices. WSEAS Trans. Bus. Econ. 20, 1581–1599 (2023). https://doi.org/10.37394/23207.2023.20.139
- L.E. Cárdenas-Barrón, J.L. González-Velarde, G. Treviño-Garza, A new approach to solve the multi-product multi-period inventory lot sizing with supplier selection problem. Comput. Oper. Res. 64, 225–232 (2015). https://doi.org/10.1016/j.cor.2015.06.008

- D. Choudhary, R. Shankar, A goal programming model for joint decision making of inventory lot-size, supplier selection and carrier selection. Comput. Ind. Eng. 71, 1–9 (2014). https://doi.org/10.1016/j.cie.2014.02.003
- D. Choudhary, R. Shankar, Modeling and analysis of single item multi-period procurement lotsizing problem considering rejections and late deliveries. Comput. Ind. Eng. 61, 1318–1323 (2011)
- Choudhary, D., Shankar, R.: Joint decision of procurement lot-size, supplier selection, and carrier selection. J. Purch. Supply Manag. 19, 16–26 (2013). https://doi.org/10.1016/j.pursup.2012.08.002
- M. Firouz, B.B. Keskin, S.H. Melouk, An integrated supplier selection and inventory problem with multi-sourcing and lateral transshipments. Omega (Westport) 70, 77–93 (2017). https:// doi.org/10.1016/j.omega.2016.09.003
- 25. W. Chen, Y. Zou, An integrated method for supplier selection from the perspective of risk aversion. Appl. Soft Comput. 54, 449–455 (2017). https://doi.org/10.1016/j.asoc.2016.10.036
- M. Rodoplu, T. Arbaoui, A. Yalaoui, Joint energy capacity and production planning optimization in flow-shop systems. Appl. Math. Model. 102, 706–725 (2022). https://doi.org/10.1016/ J.APM.2021.09.036
- T. Aouam, K. Geryl, K. Kumar, N. Brahimi, Production planning with order acceptance and demand uncertainty. Comput. Oper. Res. 91, 145–159 (2018). https://doi.org/10.1016/ J.COR.2017.11.013
- J. Jang, B. Chung, Do: Aggregate production planning considering implementation error: A robust optimization approach using bi-level particle swarm optimization. Comput. Ind. Eng. 142, 1–12 (2020). https://doi.org/10.1016/J.CIE.2020.106367
- E.B. Tirkolaee, N.S. Aydin, I. Mahdavi, A bi-level decision-making system to optimize a robust-resilient-sustainable aggregate production planning problem. Expert Syst. Appl. 228, 1–15 (2023). https://doi.org/10.1016/J.ESWA.2023.120476
- F. Li, F. Qian, W. Du, M. Yang, J. Long, V. Mahalec, Refinery production planning optimization under crude oil quality uncertainty. Comput. Chem. Eng. 151, 1–12 (2021). https://doi.org/ 10.1016/J.COMPCHEMENG.2021.107361
- A. Guise, J. Oliveira, S. Teixeira, Â. Silva, Development of tools to support the production planning in a textile company. Procedia Comput Sci. 219, 889–896 (2023). https://doi.org/ 10.1016/J.PROCS.2023.01.364
- 32. S. Prasad, Elementary. Stat. Methods. (2023). https://doi.org/10.1007/978-981-19-0596-4
- B. Liu, Uncertainty Theory (Springer, Berlin/Heidelberg, 2015). https://doi.org/10.1007/978-3-662-44354-5

# Chapter 10 Curve Identification and Digitization for the Reconstruction of Ship Hulls from 2D Drawings



Argiris I. Delis, Ioannis K. Nikolos, Eleftherios S. Zografos, Charilaos S. Zografos, Sotirios S. Sarakinos, Alexandros N. Konstantinis, Petros Manousis, and Dimitra N. Pochani

### 10.1 Introduction

Maritime transport, being one of the most energy-efficient means of transport, is in the middle of a procedure to transform into a greener and less polluting industry. In this framework, the shipping companies are obliged to comply with stricter rules and regulations, regardless of the fact that ship emissions are much lower compared to other transport sections. The rapid development of simulation-based engineering especially Simulation-Based Design (SBD) [1], Computational Fluid Dynamics (CFD), and Computational Structural Dynamics (CSD), supported by the corresponding developments in computer hardware, empowered the development of more energy-efficient and less polluting ships. However, such computational methodologies necessitate the existence of accurate three-dimensional (3D) models of the ship's hull geometries, even for existing vessels (e.g., if trimming optimization is required, or modifications to an existing ship hull are to be applied). However, shipowners usually have available only two-dimensional (2D) hull drawings, with insufficient information and details; therefore, intense work is required by specialized personnel to accurately reproduce the 3D ship hull shapes from the available simplified two-dimensional drawings.

This work proposes a solution to the aforementioned requirement, through the development of a novel methodology and the corresponding software, which allows for the semiautomatic (but very efficient) detection of ship hull curves in two-dimensional scanned drawings and their subsequent transformation into three-

A. I. Delis · I. K. Nikolos (⋈)

School of Production Engineering & Management, Technical University of Crete, Chania, Greece e-mail: inikolos@tuc.gr

E. S. Zografos  $\cdot$  C. S. Zografos  $\cdot$  S. S. Sarakinos  $\cdot$  A. N. Konstantinis  $\cdot$  P. Manousis  $\cdot$  D. N. Pochani ZETA AND CO E.P.E., Ioannina, Greece

dimensional parametric surfaces of the hull [2, 3]. It has to be emphasized here that image tracing is a fundamental module in many other engineering applications, for example, in graphic design and computer animation, used to transform hand-drawn images to a set of smooth (parametric) curves, which may be further processed, to produce complicated geometrical entities.

Scanned images of 2D drawings can easily produce unorganized data (point clouds) of various geometrical entities; however, such data form is not suitable to be further used for the recognition of specific geometrical entities. For the conversion of unorganized data to geometrical entities of parametric form (B-splines, NURBS [4]), the identification of sets of ordered points is usually required.

Several computer graphics or geometry processing methods utilize spatially varying directional information. Such directional fields take various forms; some fields specify a direction and a magnitude, while others consider multiple directions per point, including some notion of symmetry; a detailed taxonomy of several types of directional fields is given in Ref. [5], and in the included references. Such directional fields can be used for surface parameterization, mesh generation, texture synthesis, flow simulation, fabrication, architectural geometry, and illustration [5]. In Ref. [6], Bessmeltsev and Solomon try to find a smooth frame field, where at least one direction is aligned with nearby contours of the drawing; around junctions, the two directions of the field are aligned with the two intersecting contours. Then, the topology of the drawing is extracted by grouping traced curves into strokes, while a vectorization is created. However, different approaches are also used. In Ref. [7], a method based on the Delaunay Triangulation of data points was utilized for the identification of connected components, while in Ref. [8], an improved moving least-squares technique is proposed to approximate a set of unorganized points, using Euclidean minimum spanning tree, region expansion, and refining iteration. In Ref. [9], a quad-tree of the data points is constructed, extracting a grid-like boundary, which is subsequently smoothed using a Laplacian-like method.

In this work, a part of the developed computational procedure is presented, for the semiautomatic reconstruction of three-dimensional ship hulls from scanned two-dimensional drawings. First, the filtering procedure for the scanned images is presented, which is based on standard image filtering algorithms. Then, a clustering procedure is presented, which is used to identify different pixel clusters on the image; it is used for both filtering of unnecessary background texturing or noise and the identification of different lines (as point sets) in the drawing. Several examples demonstrate its effectiveness. The procedure used for the automatic digitization of lines from a cluster of points has been previously presented in Refs. [2, 3]. In this work, further details are provided, concerning the information that is interactively provided by the user to assist the production of ordered point sets for each curve and its transformation to a parametric curve. Finally, some details on the structure of the developed software are also provided, along with a discussion.

Detailed three-dimensional models of ship hulls are often required by the shipowners for several purposes, such as trim and ballast optimization [10–13], determination of the effects of the ship hull fouling [14], and application of shiphull modifications (which require the detailed geometry for several simulations)

[15]. Although the proposed numerical procedure utilizes some already existing methodologies and tools (like the various image filtering tools, or the parameterization of the ship hull lines in the form of B-spline and NURBS curves), the whole procedure is a novel one. To the authors' best knowledge, such an integrated methodology for the semiautomatic reconstruction of three-dimensional ship hulls from two-dimensional drawings has not been presented so far.

# **10.2** The Developed Filtering Procedure

The 2D ship plans (drawings) should be initially transformed to a digital form (a digital picture) in order to be used by the developed software tools. However, usually, such plans (drawings) are not in perfect condition; moreover, the digitization procedures (e.g., scanning with a digital scanner) usually introduce errors and imperfections to the produced digital picture. Therefore, a filtering procedure is needed to enhance the clarity and quality of the corresponding picture and make it more suitable for the subsequent numerical procedures developed for identifying the geometrical entities contained (in the picture). These numerical procedures necessitate a high quality and clarity from the picture, to identify the contained geometrical entities with the minimum interaction from the user.

The filtering software developed utilizes each picture as an RGB (Red-Green-Blue) file, that is, the corresponding RGB values for each pixel of the picture (including its intensity). Further,  $N_i$  is the number of pixels in the horizontal direction,  $N_j$  is the number of pixels in the vertical direction, while  $N_i \times N_j$  is the total number of pixels in the digitized picture. A uniform Cartesian computational grid is then defined for the digitized picture (drawing). The construction of the uniform Cartesian computational grid upon the digitized drawing is illustrated in Fig. 10.1. The nodes of the computational grid are positioned at the center of each pixel. The gray color of each pixel in Fig. 10.1 corresponds to its intensity value I(i,j). The discretization step of the grid is uniform and equal in both directions (Fig. 10.1):

$$\Delta x = \Delta y = 1 \tag{10.1}$$

The x(i) and y(j) grid coordinates for each grid point are defined as follows:

$$x(1) = 0.5$$

$$y(1) = 0.5$$

$$x(i) = x (i - 1) + \Delta x$$

$$y(j) = y (j - 1) + \Delta y$$
(10.2)

The digital picture many times contains (besides the ship lines) Cartesian axes with numbers, grid lines, legends, arrows, etc. Such information is useful, however,

132 A. I. Delis et al.

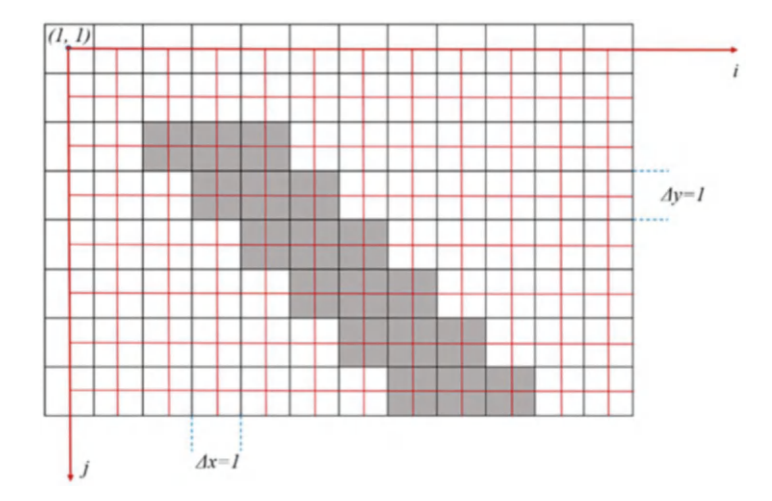


Fig. 10.1 The construction of the uniform Cartesian computational grid (in red color) upon the digitized drawing, represented with its pixels in RGB format; the nodes of the computational grid are positioned at the center of each pixel, while the color of each pixel corresponds to its intensity

the automation of the identification of the contained geometrical entities complicates a lot. Not all the drawings are of the same type (some are in gray scale, others contain colored lines, they may have background grid lines of the same or different colors, dashed or solid, etc.). Therefore, it is impossible to develop a unique and global procedure, to deal with all the different types of drawings. The approach that is followed here is to develop several filtering tools that will be available to the user, which may be applied in various combinations and sequences, according to the drawing type and the contained imperfections and/or problematic regions.

Most of the developed filtering tools are standard filters from the open literature. However, the combination of filters and the correct selection of their parameters for the application at hand is the most crucial part of this work.

The developed filters (incorporated in the developed software) are listed below:

- 1. *Color\_Balance* (changes the color balance of the picture): an image's color balance can be modified by adjusting the values of pixels' components (Red, Green, and Blue) by different amounts.
- 2. *Laplacian\_Smoothing* (applies a Laplacian smoothing operator): the Laplacian smoothing operator replaces the pixel's components with the mean values of the corresponding components of the surrounding pixels. It has a smoothing effect on the image.
- 3. *Brightness* (modifies the brightness of the picture): to increase a color's brightness by a certain percentage, the software adds to each pixel's component the aforementioned percentage times the difference between each component and its largest possible value of 255. To decrease a color's brightness by a

- certain percentage, the software subtracts from each pixel's components the aforementioned percentage times the component's value.
- 4. *Gray\_Scale* (transforms a colored picture to gray scale): to convert a pixel's color to a grayscale value, we set the pixel's red, green, and blue color components to the average of the three values.
- 5. *Complement* (computes the complement of the picture): to produce the complement of an image, we simply subtract each pixel's red, green, and blue component values from the largest possible value of 255.
- 6. *Self\_Subtract* (applies a self-subtract filter): the self-subtraction of an image is used for edge detection. The image is first shifted by one pixel in *x* and *y* directions. Subsequently, the software simply subtracts the three color components of the images' corresponding pixels. Where the image contains an edge between two colors, the shifted image and the original one have different pixel values, so the subtraction gives a bright result.
- 7. *Binary\_Contrast* (applies a binary-contrast filter): this filter examines each pixel in an image and compares the pixel's brightness to a cutoff value. It subsequently produces pixels that are brighter than the cutoff value of white. It makes the other pixels black. The result can often separate two parts of the image that differ in brightness by only a small amount.
- 8. *Kernel\_low* (makes a low-pass kernel for unsharpening (softening) the picture): a low-pass filter determines a pixel's output value by taking a symmetric average of the nearby pixels, which has a smoothing or blurring effect on the image.
- 9. Unsharp\_Masking (applies unsharp masking filter, for sharpening the picture): unsharp masking is used to sharpen an image by subtracting a scaled version of the result of low-pass filtering from the original image. It enhances the changes in high-frequency areas, making those areas more noticeable and making the image appear sharper.
- 10. *Kernel\_high* (makes high-pass kernel, for sharpening the picture): high-pass kernels have a relatively large center coefficient (corresponding to the pixel under modification), while the surrounding coefficients are negative; this gives the filter its detail-enhancement effect.
- 11. *Kernel\_Edge* (makes an edge detection kernel (Laplacian edge detection)): the Laplacian edge detection method uses a symmetric kernel to detect edges in all directions at the same time. Laplacian edge detection kernels are similar to those of high-pass filters, except the sum of the coefficients is zero than one. This makes the values of most output pixels black and makes brighter the regions where the filter detects high-frequency features (rapid changes of the pixels' components).
- 12. *Kernel\_Emb* (makes embossing kernel): an embossing filter is similar to an edge detection filter; most of the embossing filter's kernel coefficients are zero. One coefficient on the edge of the kernel has a value of 1, and the opposite coefficient has a value of -1. The resulting image has bright highlights, where the image grows darker as we move from the direction of the 1 coefficient toward the -1 coefficient. In places where the image grows lighter, the kernel

134 A. I. Delis et al.

produces a negative value, therefore, the results at those positions are rounded up to zero (black). The three-dimensional appearance of the result is enhanced by adding 127 to each pixel's color components; in this way, background areas (that would be turned black) now have a medium gray color.

# **10.3** The Developed Clustering Procedure

In addition to the aforementioned filters, a clustering algorithm was developed, to identify the different clusters of pixels inside the picture. The clustering algorithm plays two roles. The first role is to identify the clusters consisting of a small number of pixels (like dashed-lines/dashes or numbers inside the picture) and delete them in a subsequent stage. This role is a filtering-like procedure. The second role is to identify discrete lines inside the picture (this feature is not currently utilized, but maybe used in the future).

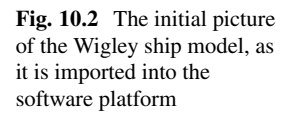
The clustering algorithm sweeps the picture (actually its pixels) in alternative directions and searches for adjacent pixels, as to produce clusters of pixels with dark color, in contrast to the white background. The final clustering contains only those pixels belonging to the identified clusters, while the white pixels of the background are not included in any cluster. The application of such a clustering algorithm necessitates the existence of a picture with high clarity and high contrast, so as the features of the two-dimensional drawing to be easily recognizable. Therefore, a preprocessing of the drawing is usually required, which is achieved with an initial application of some of the aforementioned filters.

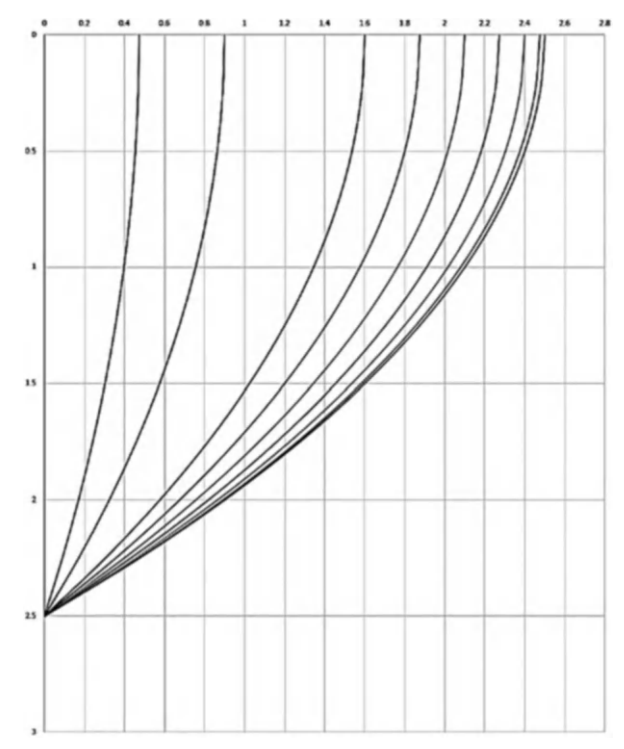
The filtering-like procedure of the clustering algorithm is demonstrated in Figs. 10.2, 10.3, 10.4 and 10.5, as it is applied through the Graphical User Interface (GUI) of the integrated software platform. Figure 10.2 contains the initial picture of the Wigley ship model. Figure 10.3 contains the picture of the Wigley ship model, after applying a 0.30 intensity threshold. This filter effectively removes most of the background gray-colored grid lines.

Figure 10.4 depicts the picture of the Wigley ship model, after applying the clustering procedure and after removing all the clusters with less than 20 pixels. Figure 10.5 depicts the picture of the Wigley ship model, after applying the clustering procedure and after removing all the clusters with less than 160 pixels; as it can be revealed, all the numbers of the drawing have been effectively removed.

In the following, the effectiveness of the developed clustering procedure will be demonstrated in additional specific test cases, which correspond to actual ship drawings. Figure 10.6 contains a part of a scanned 2D ship drawing, with letters, numbers, vectors, and dashed grid lines. Figure 10.7 contains the same drawing after the application of *Contrast* and *Unsharp\_Masking* filters. Subsequently, the clustering algorithm is applied, to identify several clusters, delete clusters of a small number of pixels (dashes), and identify other clusters (like numbers) (Fig. 10.8).

In Figs. 10.9 and 10.10, an additional test case is presented. Figure 10.9 contains the original picture of the 2D ship hull drawing. Figure 10.10 contains





the result of the successive application of *Binary\_Contrast* (parameter value: 0.65), *Laplacian\_Smoothing*, *Binary\_Contrast* (parameter value: 0.9), and clustering. As it can be observed, the resulting width of each line was increased (through the *Laplacian\_Smoothing* procedure), to render easier the subsequent geometry identification procedures.

It should be emphasized here that the presented automated filtering and clustering procedure does not exclude the (additional) manual editing of the picture (e.g., "deleting" dark pixels or regions of pixels); nevertheless, such manual editing would be much easier and efficient after the described automated filtering and clustering procedures.

# 10.4 The Automatic Digitization of Lines

The curved lines included in the digital form of a 2D drawing are in the form of a collection of pixels. This format is useless for the reconstruction of the 3D geometry, which is the target of this work. Therefore, the lines should be converted to a vector-like format. This includes the digitization of several points along each

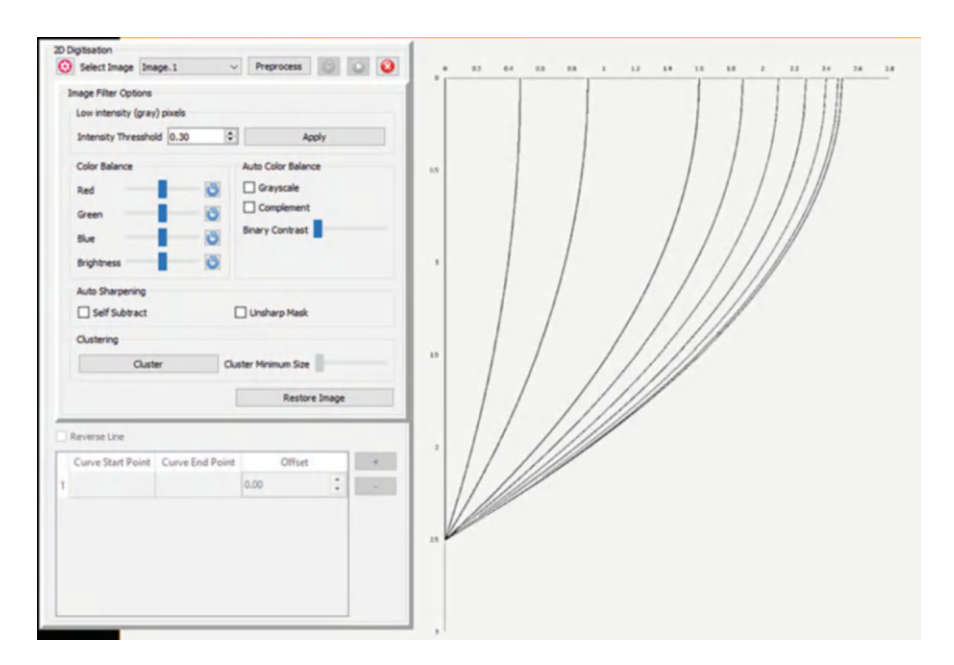


Fig. 10.3 The picture of the Wigley ship model, after applying a 0.30 intensity threshold

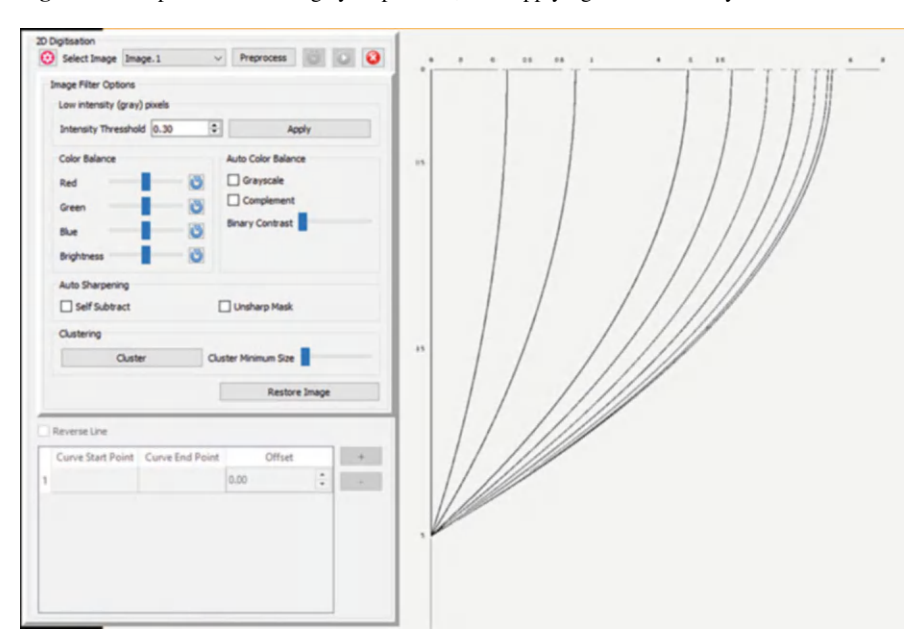


Fig. 10.4 The picture of the Wigley ship model, after applying the clustering procedure and after removing all the clusters having less than 20 pixels

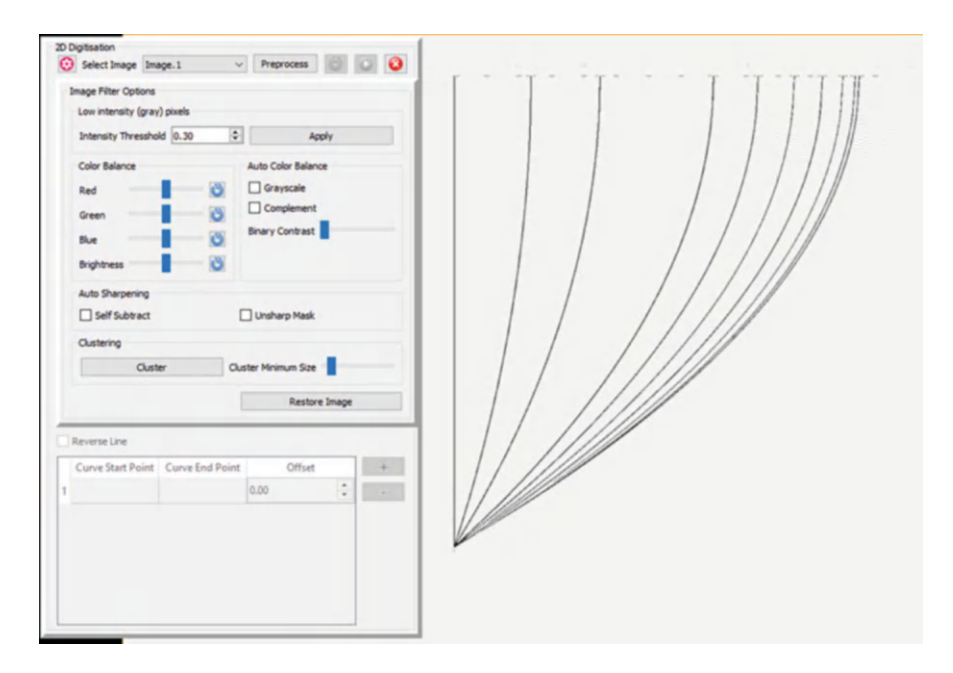
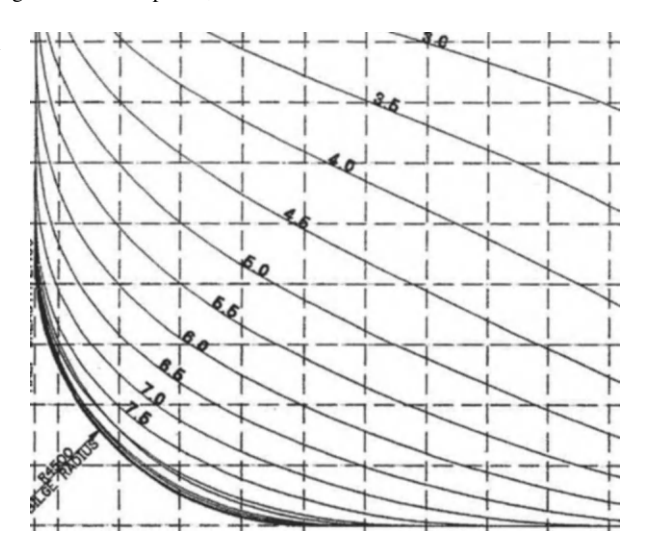


Fig. 10.5 The picture of the Wigley ship model, after applying the clustering procedure and after removing all the clusters having less than 160 pixels; all the numbers have been removed

**Fig. 10.6** A part of an actual scanned 2D ship drawing



line, which will be subsequently used as interpolation points for parametric curves (like B-splines and NURBS) [2, 3].

The developed procedure and the corresponding software deal with the automatic digitization of points along each line. The basic information that is utilized is the RGB format of the digital picture (as it has been previously modified by the

Fig. 10.7 The ship drawing of Fig 10.6, after the application of *Contrast* and *Unsharp\_Masking* filters

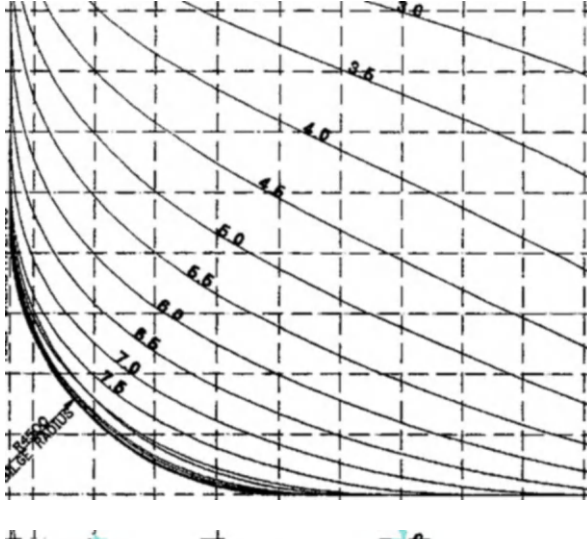
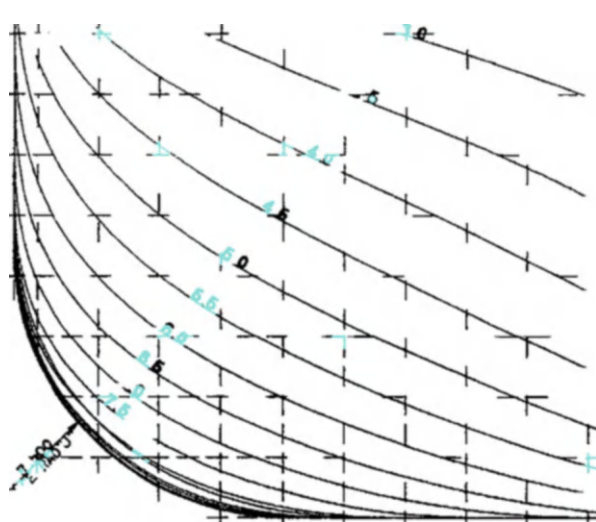


Fig. 10.8 The ship drawing of Fig 10.7, after the application of the clustering procedure; in light blue color, the clusters with less than a certain number of pixels are depicted (which will be, subsequently, deleted)



filtering procedure, presented in the previous sections—an example is depicted in Fig. 10.11). Besides the previous, some additional information is required by the user:

- 1. The number of specific "Direction Points," which will be used to guide the software, to produce the nominal direction for each line (and, subsequently, the inverted one).
- 2. The (pixel) coordinates of each "Direction Point." A positive sign corresponds to a "Starting Direction Point—SDP," while a negative sign corresponds to an "Ending Direction Point—EDP." Direction Points are required to guide the numerical procedure to produce successive discrete (digitized) points along each

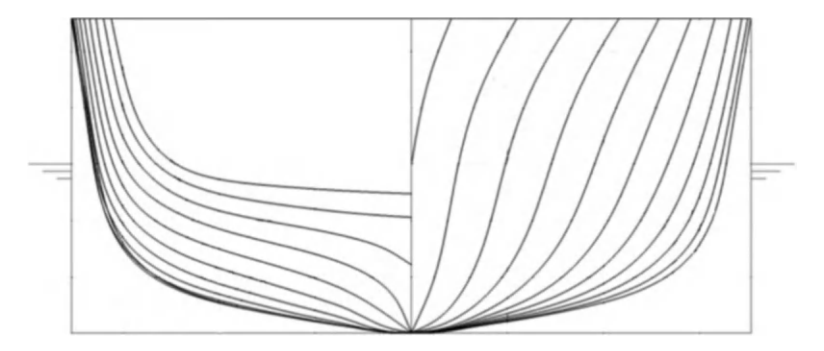
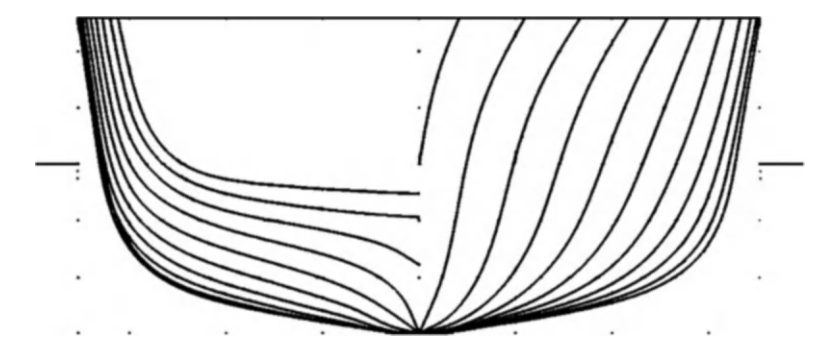


Fig. 10.9 The original ship hull drawing, used for testing the algorithm



**Fig. 10.10** The ship hull drawing of Fig. 10.9, after the application of *Binary\_Contrast* (0.65), *Laplacian\_Smoothing*, *Binary\_Contrast* (0.9), and clustering operators

line in a preferred direction (Fig. 10.12). In principle, each open line needs an *SDP* and an *EDP*, except for cases where lines have a common start or end. In those cases, a single *SDP* or *EDP*, respectively, would suffice (see Fig. 10.16). The produced direction (from *SDP* toward *EDP*) can be inverted for some lines, as will be discussed in the following.

- 3. The number of lines in the picture that will be scanned with the *nominal direction*.
- 4. The (approximate) coordinates of points (pixel coordinates) at the beginning and the end of each of the aforementioned lines (Fig. 10.13).
- 5. The number of lines in the picture that will be scanned with the *inverted direction*.
- 6. The (approximate) coordinates of points (pixel coordinates) at the beginning and the end of each of the aforementioned (inverted) lines.

There is no restriction regarding the number of "Starting Direction Points—SDPs" and "Ending Direction Points—EDPs"; the mix of such points depends on the number of lines in the picture and their (possible) connectivity. For example, a picture may necessitate the insertion of three "Starting Direction Points" and five "Ending Direction Points" (Fig. 10.12).

140 A. I. Delis et al.

**Fig. 10.11** The ship hull drawing of a Capesize Bulk Carrier (Bow lines)

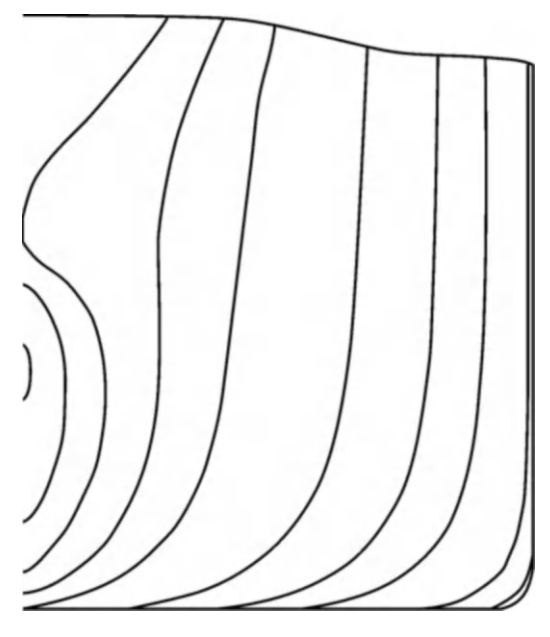
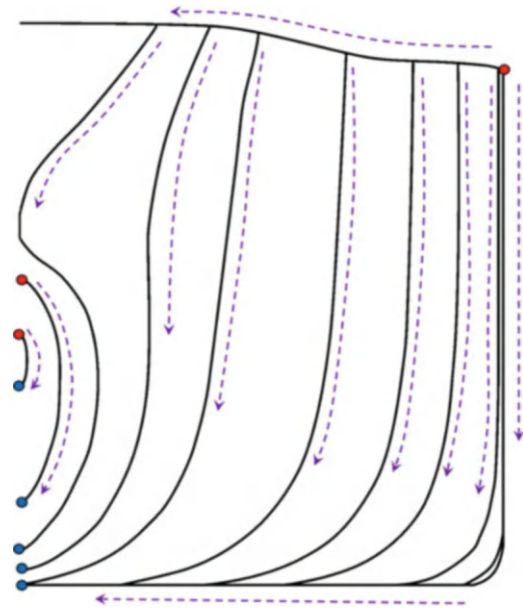
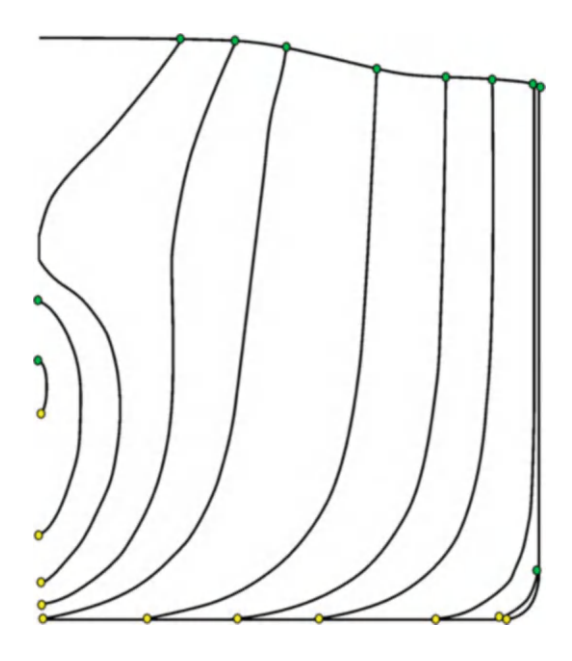


Fig. 10.12 The ship hull drawing of Fig. 10.11; the positions of the "Starting Direction Points" are depicted with red dots, while the positions of the "Ending Direction Points" are depicted with blue dots, while the dashed arrows depict the produced directions for the contained lines



Lines that are connected usually require fewer "Direction Points." This will be demonstrated through the use of specific test cases. Single lines, which are not connected to other ones, usually require a single "Starting Direction Point" and a single "Ending Direction Point."

Fig. 10.13 is the ship hull drawing of Fig. 10.11; the positions of the initial point of each line are depicted with green dots (where the digitization process begins for the corresponding line), while the positions of the final point of each line are depicted with yellow dots (where the digitization procedure ends for the corresponding line)



In the following, several test cases will be presented, to clarify the procedure and demonstrate its capabilities (and possible limitations).

Figure 10.11 contains the lines of a Capesize Bulk Carrier (Bow), after the application of a filtering procedure. As can be observed, most of the curves are connected, and only two of them are isolated. For this test case, no direction inversion was required. Eight "Direction Points" were introduced (three being SDPs and five being EDPs). In Fig. 10.12, the positions of the SDPs are depicted with red dots, while the positions of the EDPs are depicted with blue dots. Figure 10.13 demonstrates the positions of the initial point of each line, depicted with green dots (where the digitization process begins), while the positions of the final point of each line are depicted with yellow dots (where the digitization procedure ends for the corresponding line). The resulting digitized lines are presented in Fig. 10.14.

The produced digital points for each line (Fig. 10.14) are more than the actual size of the required interpolation points for the construction of the relative parametric curve. Therefore, the number of produced points can be automatically reduced to a much smaller one, before the construction of the parametric curve (B-spline or NURBS).

For the second test case, a slightly different approach is used. Less "Direction Points" (only two) are used, combined with the invert direction procedure. Figure 10.15 contains the lines of a Capesize Bulk Carrier (Stern), after the application of a filtering procedure. As it can be observed (similar to the previous case), most of the curves are connected, and only one of them is isolated. For this test case, a direction inversion was required. Only two "Direction Points" were introduced (one being *SDP* and one being *EDP*). In Fig. 10.16, the position of the *SDP* is depicted with

142 A. I. Delis et al.

Fig. 10.14 is the ship hull drawing of Fig. 10.11; the resulting digitized lines—the picture is inverted in the vertical direction

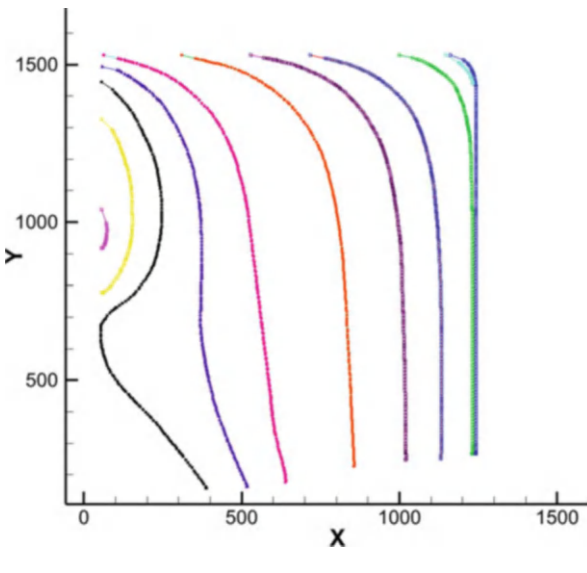
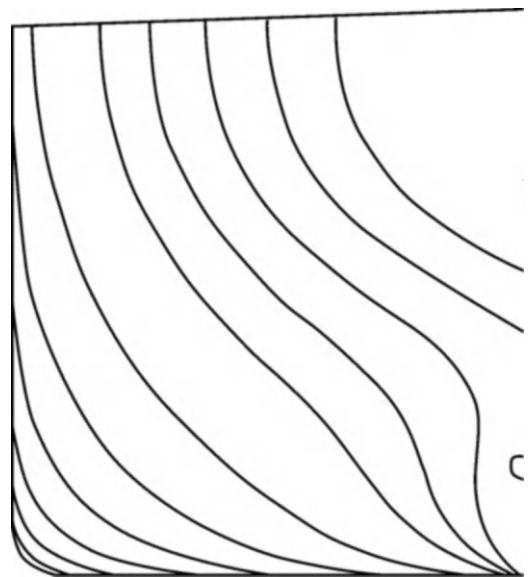


**Fig. 10.15** The ship hull drawing of a Capesize Bulk Carrier (Stern lines)



a red dot, while the position of the *EDP* is depicted with a blue dot. The resulting digitized lines are presented in Fig. 10.17. The 12 main lines were produced with the nominal direction, while an additional 6 lines (in the flat bottom) were produced with the inverted direction.

Fig. 10.16 The ship hull drawing of Fig. 10.15; the position of the "Starting Direction Point" is depicted with a red dot, while the position of the "Ending Direction Point" is depicted with a blue dot

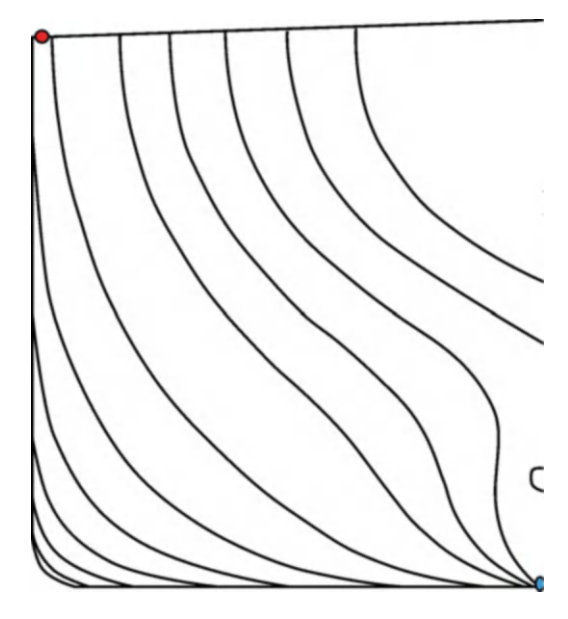
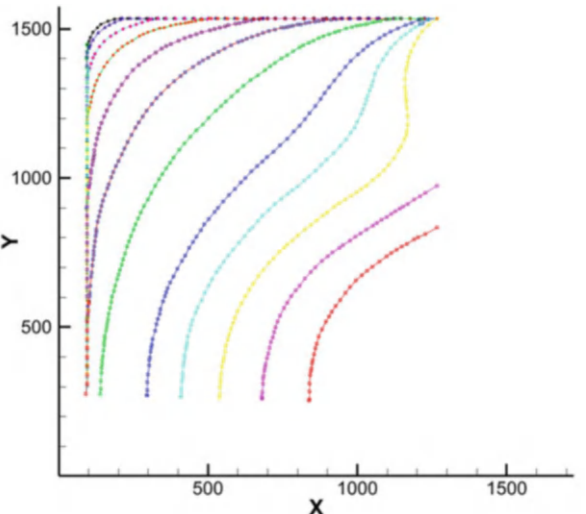


Fig. 10.17 The ship hull drawing of Fig. 10.15; the resulting digitized lines—the picture is inverted in the vertical direction



# 10.5 The Developed Software

The developed interactive software (in C++) can be described as the sum of four main parts, namely, the Graphical User Interface (GUI), the Sketch Recognition Application, a two-dimensional Design Application, and a three-dimensional Design Application.

144 A. I. Delis et al.

To render the software as easy as possible for the final user, an interactive Graphical User Interface was developed. Apart from the main menus, it consists of a model browser area, an entity properties viewer area, and a 3D geometry viewer. All the functions that the user can perform are available through the main menus, prompting the corresponding "tool-guides." In those "tool-guides," the user enters the necessary arguments and performs the requested geometrical functions. Some Graphical User Interface customization options are also available, such as background colors choice, unit system selection, as well as keys and shortcuts customization options. Nevertheless, the user can import, export, and save his work in the available file formats.

Regarding the Sketch Recognition Application, it takes the form of a twodimensional geometric viewer. The drawing is initially imported in image format and placed on the desired plane. Several filters (as described in a previous section) can be applied for the enhancement of the quality of the image, as part of the preprocessing; the result should be an image easier to recognize with precision. Subsequently, the image recognition algorithms may be applied, while the final result is in the form of several sets of points, corresponding to the traced curves depicted in the drawings, which can be exported in a native file format (to be later imported into the CAD environment).

The two-dimensional Design Application takes the points exported by the image recognition process as input and subsequently proceeds with their parametric expression in the two-dimensional space. The ability to define additional geometries, such as lines and conics (elliptical, parabolic, and hyperbolic shapes), is also offered, together with the ability to create curves of all the known parametric curves families, such as Bezier, B-Splines, and NURBS.

Finally, in the three-dimensional Design Application, the user may use the previously created 2D curves as an input for the creation of 3D surfaces, through a skinning process, thereby concluding the three-dimensional reconstruction of the ship hull geometry. Additional functionalities for the creation of other 3D surfaces, such as extrusions and fills, are available (including geometrical tools for their modification, like split and trim functions). The final geometrical entities can be saved both in native file format and in standard STEP file format, to be easily imported to third-party CAD/CAE software.

### 10.6 Discussion

A numerical methodology and the corresponding software were presented in this work, developed for the detection (and reconstruction) of curves from two-dimensional ship hull drawings in a semiautomatic manner and their subsequent transformation to parametric curves, such as B-splines and NURBS. The procedure is part of a sophisticated software, under development, for supporting naval engineers to reconstruct the entire 3D shape of a ship hull in the form of fully parametric geometrical entities, to be further used in Computer-Aided Design (CAD) and

Computer-Aided Engineering (CAE) software, for simulation purposes. As it was described in the previous sections, the methodology starts with importing 2D ship hull two-dimensional drawings in the form of pixelated images; various image filtering procedures can be subsequently applied to the imported scanned drawing, to render the ship hull lines more easily recognizable. Additionally, a simple clustering algorithm is applied, to separate the ship hull lines from background noise or unwanted features (such as background grid lines or numbers). Then, a computational methodology is applied to semiautomatically discretize the resulting curves and produce ordered points for each line. Such points will be consequently used as interpolation points for the production of parametric curves, such as B-splines and NURBS. To clarify the presented procedure, characteristic test cases were presented, which also verified its effectiveness and ease of application. The proposed numerical methodology is already part of a software platform, being at an advanced development level before commercialization.

**Acknowledgments** This research has been co-financed by the European Regional Development Fund of the European Union and Greek national funds, through the Operational Program Competitiveness, Entrepreneurship and Innovation, under the call RESEARCH—CREATE—INNOVATE (project code: T2EDK-03906).

### References

- E.F. Campana, D. Peri, Y. Tahara, F. Stern, Shape optimization in ship hydrodynamics using computational fluid dynamics. Comput. Methods Appl. Mech. Eng. 196(1-3), 634–651 (2006)
- A.I. Delis, E.S. Zografos, C.S. Zografos, S.S. Sarakinos, A.N. Konstantinis, I.K. Nikolos, A numerical methodology for the identification and digitization of curves from 2D drawings, in *Proceeding of the 21st International Conference of Numerical Analysis and Applied Mathematics*, Heraklion, Crete, Greece, September 11–17, 2023
- G. Koini, A.I. Delis, I.K. Nikolos, E.S. Zografos, C.S. Zografos, S.S. Sarakinos, P. Manousis, Reconstruction of 3-dimensional ship hull geometries from 2-dimensional drawings, in Proceeding of the 19th International Conference of Computational Methods in Sciences and Engineering, Heraklion, Crete, Greece, May 23–26, 2023
- 4. L. Piegl, W. Tiller, *The NURBS book* (Springer, New York, 1997)
- A. Vaxman, M. Campen, O. Diamanti, D. Panozzo, D. Bommes, K. Hildebrandt, M. Ben-Chen, Directional field synthesis, design, and processing. Comput. Graph. Forum 35(2), 545–572 (2016)
- M. Bessmeltsev, J. Solomon, Vectorization of line drawings via polyvector fields. ACM Trans. Graph. 38(1), article 9 (2019)
- 7. P. Bo, G. Luo, K. Wang, A graph-based method for fitting planar B-spline curves with intersections. J. Comput. Des. Eng. 3, 14–23 (2016)
- 8. I.-K. Lee, Curve reconstruction from unorganized points. Comput. Aided Geom. Des. **17**(2), 161–177 (2000)
- 9. J. Wang, Z. Yu, W. Zhang, M. Wei, C. Tan, N. Dai, X. Zhang, Robust reconstruction of 2D curves from scattered noisy point data. Comput-Aided Des **50**, 27–40 (2014)
- MTCC-Asia (Maritime Technology Cooperation Centre for Asia), Guidelines on Ship Trim Optimization – Based on Machine Learning Method, 2019
- 11. X. Lv, X. Wu, J. Sun, H. Tu, Trim optimization of ship by a potential-based panel method. Adv. Mech. Eng., Article ID 378140 (2013)

A. Drouet, P. Sergent, D. Causeur, P. Corrignan, Trim optimisation in waves, in *Proceeding of the VII International Conference on Computational Methods in Marine Engineering*, MARINE 2017

- 13. T. Panagiotakopoulos, I. Filippopoulos, C. Filippopoulos, E. Filippopoulos, Z. Lajic, A. Violaris, S.P. Chytas, Y. Kiouvrekis, Vessel's trim optimization using IoT data and machine learning models, in *Proceeding of the 13th International Conference on Information, Intelligence, Systems & Applications (IISA)*, Corfu, Greece, 2022, pp. 1–5
- 14. S. Song, Y.K. Demirel, C. De Marco Muscat-Fenech, T. Tezdogan, M. Atlar, Fouling effect on the resistance of different ship types. Ocean Eng. **216**, 107736 (2020)
- 15. F. Djamaluddin, Optimization of ship fender under axial load using Taguchi. WSEAS Trans. Appl. Theor. Mech. 17 (2022)

# Chapter 11 Multiple Subset Problem as an Encryption Scheme for Communication



Yair Zadok, Nadav Voloch, Noa Voloch-Bloch, and Maor Meir Hajaj

## 11.1 Introduction and Related Work

The methods of encryption have been widely used in the past decades for various purposes, from financial transactions to working with databases, internet communication, etc. Different encryption schemes fit different purposes. The basic encryption idea is to create a scheme that will be secure from possible untrustworthy third parties, who intend to approach our data. For that, the data being transferred is usually in a form that is not understandable to someone who does not have the knowledge of the encryption algorithm, or certain keys, that the receiver of the message does have. In this paper, we further develop our encryption scheme that is based on a variant of the multiple-subset problem and was presented in Ref. [1]. We implement this method as a secure communication protocol, which has a unique and novel method of encrypting and decrypting data.

The subset sum problem (SSP) is a specific instance of the knapsack problem within the field of computational complexity theory. It encompasses various variations and is known to be NP-complete (as described in Ref. [2], which analyzes all sorts of NP-complete problems). The classic problem, as shown in Ref. [3], is described as follows: Let  $A = \{a_1, a_2, \ldots, a_m\}, a_i \in \mathbb{N}$ , and  $s \in \mathbb{N}$ , find  $B \subseteq A$ , for

Y. Zadok

Achva Academic College, MP. Shikmim, Israel

N. Voloch (⊠)

Ruppin Academic Center, Emek Hefer, Kfar Monash, Israel

e-mail: voloc@post.bgu.ac.il

N. Voloch-Bloch

Voloch Knowledge Horizons, Tel Aviv, Israel

M. M. Hajaj

University of Haifa, Haifa, Israel

148 Y. Zadok et al.

which  $\sum_{ai \in B} a_i = s$ . Meaning for a given set of integers A, and an integer s, find a subset of items from A summing up to s.

SSP, being *NP-complete*, has a naïve exponential time solution of cycling all of the possible subsets and a slightly better  $(O(2^{n/2}))$  solution shown in research that handles Computing Partitions with Applications to the Knapsack Problem [4].

The existence of subsets that add up to the required sum can be determined using pseudopolynomial dynamic programming solutions, which utilize an array with Boolean values, resulting in more efficient solutions, as presented in Ref. [5], that shows a new technique called *balancing* for the solution of Knapsack Problems. The research proves that an optimal solution to the Knapsack Problem is balanced, and thus only balanced feasible solutions need to be enumerated to solve the problem to optimality, Ref. [6] presents a new algorithm that is the fastest general algorithm for this problem, and a modified algorithm for cyclic groups, which computes all the realizable subset sums within the group. Efficient approximation algorithms are also shown in Ref. [7], which covers different approximation algorithms for combinatorial problems, Subset Sum is one of them, and Ref. [8] focuses on the subset sum problem, finds a complete polynomial approximation scheme for it, and shows their results accordingly. An alternative form of SSP is the multiple-subset problem (MSSP), wherein a set of items is chosen and distributed among multiple identical bins, ensuring that the capacity of each bin is not surpassed, while aiming to maximize the total weight of the items. Approximation algorithms for MSSP were demonstrated in Ref. [9], which is the first research that formulates the problem and its possible approximation solutions. A special case of MSSP is the equal subset problem (ESS), in which given a set  $A = \{a_1, a_2, \dots, a_m\}, a_i \in \mathbb{N}$ , and  $s \in \mathbb{N}$ , the problem is to decide whether two disjoint subsets  $A_1, A_2 \subseteq A$  exist whose elements sum up to the same value, meaning  $\sum_{ai \in A_1} a_i = s$  and  $\sum_{ai \in A_2} a_i = s$ . In Ref. [10], Woeginger and Zhongliang introduce a problem and propose an approximation algorithm to solve it. Ref. [11] discusses various problems and variations derived from ESS, while Ref. [12] presents an efficient approximation algorithm for it.

There is some novel state-of-the-art encryption research such as Ref. [13], which describes the principles and methods underlying the creation of an application in secure operating systems, which provides reliable data encryption. The research aims to analyze and indicate the specifics of encryption methods and algorithms based on domestic standards in open-source operating systems. Cryptanalysis was used in the article, as this avoids vulnerabilities identified in previously created implementations. In the article, the authors draw attention to the fact that 7-Zip uses CBC encryption (concatenation of encrypted text blocks), but the Counter Mode is supported. The same support was provided in the encrypt implementation. Since the key expansion function initially fills the special array created by p7zip with round keys using a unique property of the domestic standard, only one round encryption function was created (performed both during encryption and decryption).

This method is also used in various modes. In many cases, initialization time deviations depending on the selected mode are insignificant. The created cryptographic module was tested to meet the domestic standard, which contains several test cases. It was confirmed during the tests that the created module implements

the algorithm of the domestic standard. The article shows a way to implement a fairly convenient graphical interface for accessing the cryptographic module, which enables the user not to call the command line and remember the sequence and types of parameters passed to p7zip. This implementation also takes into account the verification of the correctness of decryption and the reading of other error codes.

There are also different types of encryptions, like hybrid encryption, that are described and used in another state-of-the-art scheme in Ref. [14], which discusses the integration of the Internet of Things (IoT) with cloud computing (CC) to improve efficiency in service delivery. The integration is achieved through the development of an integrated IoT system with cloud computing, using a hybrid encryption mechanism for security. The proposed system has been implemented, and its performance has been evaluated using various metrics such as power consumption, packet delivery ratio, and algorithm execution time. The system also shows resilience against attacks like the black hole attack.

In this paper, we focus on a different problem that is similar to ESS but deals with a collection of sets instead of a single set of integers. Additionally, we aim to determine an unknown parameter (s) for the sum. This problem has a cryptographic application, which will be discussed in the subsequent sections of this paper.

While previous studies have addressed ESS and provided efficient approximation algorithms for it, there is a need to explore and propose solutions for this related problem and its cryptographic implications. It is this research gap that the current study seeks to fill.

Our contribution to this paper is of several aspects: First, we formulate the Multiple Integrated Subset Problem (MISSP), with examples of it. Second, we describe an encryption methodology scheme based on this problem, and last, we show a communication implementation that uses this encryption scheme.

# 11.2 Multiple Integrated Subset Problem

A problem arises, when ESS is addressed in a different manner that is as follows: For a given family of sets of integers  $A = \{A_1, A_2, ..., A_n\}$ , find an integer s, such that for every set  $A_i$  some of its subsets is summed up to s if such an integer exists. We denote this problem as the *MISSP*—Multiple Integrated Subset Problem.

The similarity between this problem and ESS lies in the requirement of finding a comparable sum in various subsets. However, the difference lies in the constraints, where the problem deals with a collection of sets (2D array) instead, implying a predefined and consistent number of elements in each part of the problem (each set).

Furthermore, the sum (s) is a parameter that is not known and needs to be determined for each set. This condition leads to an O(n) complexity increase, as SSP needs to be performed for every possible value of s.

The subsequent sections of this paper will demonstrate an enhancement in efficiency for this increase. Table 11.1 shows a few examples of integrated sets on a

150 Y. Zadok et al.

2D set	Set	Set items	S	Summations
A	$A_1$	{22, 4, 23, 16}	49	22 + 23 + 4 = 49
	$A_2$	{8, 3, 17, 21}	49	17 + 21 + 8 + 3 = 49
	$A_3$	{8, 13, 9, 19}	49	13 + 9 + 8 + 19 = 49
В	$B_1$	{22, 3, 20, 15}	None	None
	$B_2$	{5, 1, 17, 21}	None	None
	$B_3$	{8, 10, 7, 19}	None	None
	$B_4$	{23, 5, 26, 19, 4}	None	None
C	$C_1$	{8, 15, 11, 9, 1}	10; 21	9+1=10; 9+1+11=21
	$C_2$	{13, 2, 7, 1}	10; 21	7 + 2 + 1 = 10; 7 + 1 + 13 = 21
	<i>C</i> <sub>3</sub>	{18, 11, 10,19}	10; 21	10 = 10; 10 + 11 = 21

Table 11.1 Small-scale examples for MISSP with unknown parameters

small scale. As seen, implementing SSP for finding sums on multiple integrated sets is not injective, thus multiple results of s can appear (like in set C), or none (like in set B).

The probability of obtaining at least one result of s decreases as the number of sets (n) increases, since there are fewer opportunities for the sets to have equal sums. Conversely, the probability of obtaining at least one result of s increases as the number of items in each set (m) increases, as there are more possibilities for equal sums between the sets. This is because there are inevitably more options for creating such a sum. This problem has a cryptographic application when the sets have equal sizes (m), and each integer in the sets has the same number of digits (d). In this application, the cipher text is represented by the sets, the private keys consist of two of the parameters m, n, and d, and the encrypted plain text is the resulting sum s. To accurately decrypt the cipher text, it is necessary to obtain a single result of s.

The complete algorithm for efficiently solving MISSP, along with its proof of correctness and analysis of its complexity, can be found in our previous work [1].

# 11.3 Encryption with MISSP

The classic SSP in cryptography, known as the Merkle–Hellman knapsack cryptosystem [15], was one of the earliest created. It was derived from the knapsack problem with SSP as a special case [16]. This fundamental cryptosystem relied on constructing a super-increasing set, where each number is larger than the sum of all preceding numbers. The SSP was then solved using a greedy polynomial time algorithm [17]. However, this cryptosystem was later compromised, leading to the development of more intricate versions of SSP for stronger cryptosystems [18]. In this context, we propose the utilization of MISSP as a relatively robust cryptosystem based on two symmetric private keys.

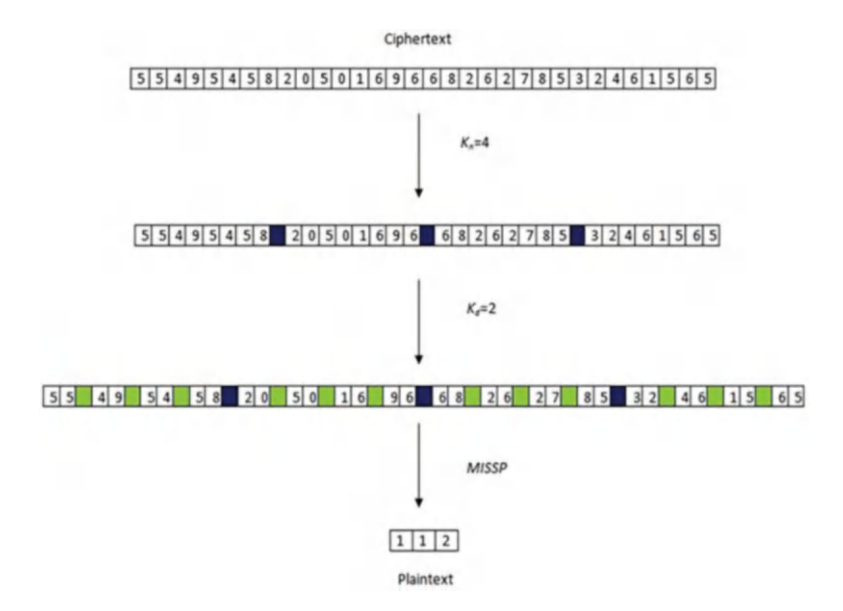


Fig. 11.1 MISSP cipher text decomposed to sets of integers by the private keys and decrypted by the MISSP algorithm

MISSP has a cryptographic application for equal sizes of sets (m), from which we derive the number of sets (n), and an equal number of digits of every integer in the sets (d). In this particular application, the cipher text refers to the series of provided sets, while the private symmetric keys consist of two parameters: m, n, and d.

The encrypted plain text is represented by the sum s obtained from these parameters. To ensure an accurate decryption of the cipher text, a singular result of s is essential. Figure 11.1 demonstrates the decryption process, which comprises three distinct steps. The first step involves decomposing the cipher text into n distinct sets. In the example of the figure, the cipher text is 55495458205016966826278532461565,  $K_n$  (that is the first private key, representing n in the algorithm, which is the number of sets) is 4, and hence, the cipher text is decomposed to  $\{55495458, 20501696, 68262785, 32461565\}$ . The second stage is decomposing the resulting sets into d-size items. In the example  $K_d = 2$  ( $K_d$  is the second private key, representing d in the algorithm, which is the number of digits of every integer in the sets) the sets are decomposed to the 2D set of two-digit integers, on which the MISSP algorithm will run, and it is  $\{55, 49, 54, 58\}$ ,  $\{20, 50, 16, 96\}$ ,  $\{68, 26, 27, 85\}$ ,  $\{32, 46, 15, 65\}$ }. For the last part, we run MISSP on the 2D set. Its result is the actual plain text. In the example, it is 112 for the following summations: 54 + 58, 96 + 16, 85 + 27, and 65 + 15 + 32.

There are two important points to note.

First, the selection of keys *n* and *d* is essentially the same as any combination of *m* and *d* or *m*. Second, the decomposition process yields the same 2D set, albeit with

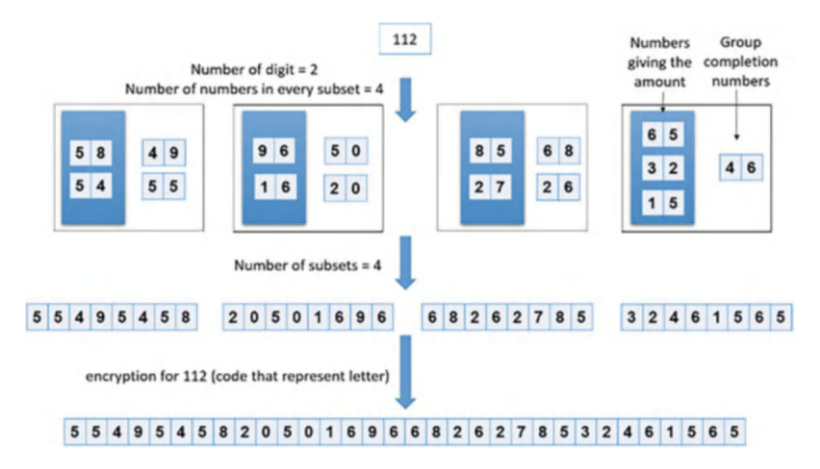


Fig. 11.2 Plain text encrypted to sets of integers by the private keys by the MISSP algorithm

different stages of decomposition. Additionally, the division of the cipher text (C) can be conducted either for the integers or for the sets first. This is attributed to the fact that the size of the cipher text, denoted as |C|, is equal to mnd, where m represents the item size, n represents the size of each set, and d represents the number of sets.

Second, there is a singularity constraint for the resulting plain text, meaning *MISSP* necessarily has to have exactly one result. For example, set *A* in Table 11.1 is suitable for *MISSP* encryption (1 result), but sets *B* (0 results) and *C* (2 results) are not suitable.

We can see the reverse process of decryption of the same values (112 as plain text to 55495458205016966826278532461565 as the cipher text in Fig. 11.2) using, of course, the same private keys for the different parameters of *MISSP*.

### 11.4 Results

Today, there are accepted and well-known methods for encrypting over the Internet. These methods are known and are a target for hacking and attacks by many factors, such as private hackers, organizations, and even countries, so it is important to renew these methods all the time.

For this research, we have developed a communication application that incorporates a modern form of encryption that is not based on an existing mechanism. The application performs the encryption and decryption based on the *MISSP* algorithm. The app is installed on the Client's endpoint, and it enables loading the relevant files (dictionary, keys, and data file) and then selects an encryption or decryption operation.



Fig. 11.3 Communication application system architecture for encryption with MISSP algorithm

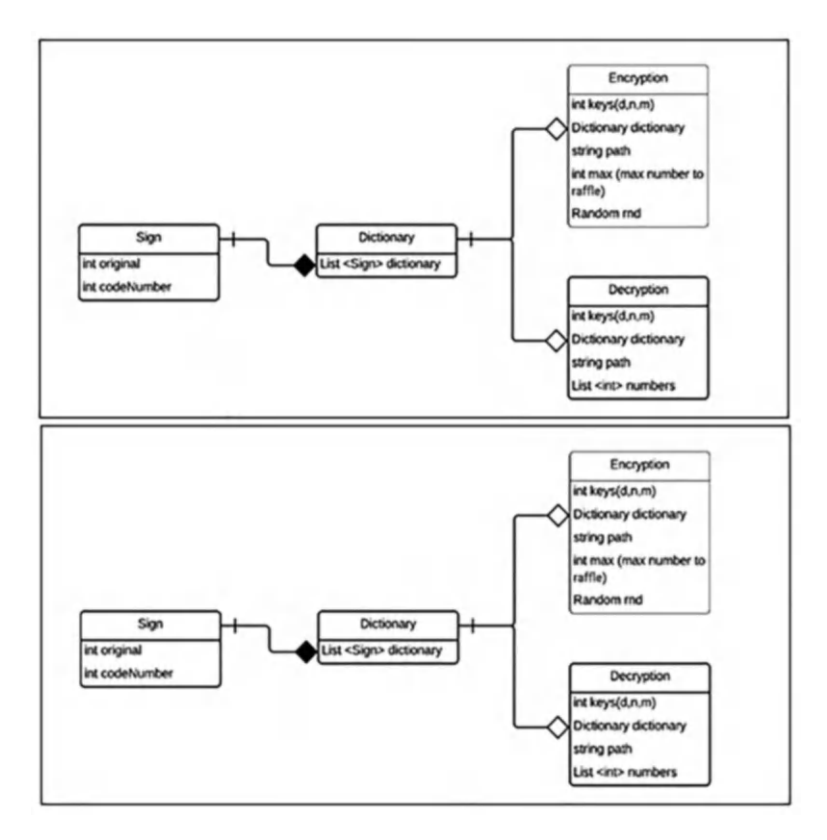


Fig. 11.4 Class application design for MISSP algorithm communication encryption

Once the desired operation is completed, it is possible to send the file created through the network.

The basic technological architecture of the communication application is described in Fig. 11.3. As we can see in the figure, for the UI and algorithm implementation, .NET technology was used, and for the communication protocol, we used Oracle's Virtual Box.

In Fig. 11.4, we can see the class application design for the communication protocol, with the following classes:

154 Y. Zadok et al.

Sign Class—for defining a sign in the dictionary. Original: the original sign codeNumber: code in the dictionary.

Dictionary Class—for defining a dictionary that the inserted text (that we want to encrypt) is written in. dictionary: a list of Signs.

*Encryption Class*—The class contains the encryption algorithm, continues the encryption keys and dictionary, and returns encrypted text.

Decryption Class—The class contains the decryption algorithm, contains the decryption keys and dictionary, and returns decrypted text.

We achieved a fully operational application that displays all relevant data, sends and receives data, and accepts user preferences. The code for this application is presented in Ref. [19]. In the implementation itself, we have devised a dictionary for the plaintext to be established, creating some known equal subsets for the purpose of encryption. In Tables 11.2 and 11.3, we can see more results and examples of using MSSIP encryption.

**Table 11.2** MISSP decryption for C = 3549313174881315445873652855274070486229 82282929545549589854514066844221964433115138492922182856793451481685316125836 92956543931393165971925901260799466515318973136998975301895

				s (plain	
n/m	d	sets	Set items	text)	Summations
4/11	4	$A_1$	{3549, 3131, 7488, 1315, 4458, 7365, 2855, 2740, 7048, 6229, 8228}	26931	3549 + 7365 + 2740 + 7048 + 6229
4/11	4	$A_2$	{2929, 5455, 4958, 9854, 5140, 6684, 4221, 9644, 3311, 5138, 4929}	26931	2929 + 5455 + 4958 + 5140 + 3311 + 5138
4/11	4	$A_3$	{2218, 2856, 7934, 5148, 1685, 3161, 2583, 6929, 5654, 3931, 3931}	26931	2218 + 1685 + 2583 + 6929 + 5654+ 3931 + 3931
4/11	4	$A_4$	{6597, 1925, 9012, 6079, 9466, 5153, 1897, 3136, 9989, 7530, 1895}	26931	6597 + 9012 + 1897 + 7530 + 1895

**Table 11.3** MISSP decryption for C = 799983342767152577242663441740985671678720845 472559646208978678249295875506162204711109183474250893534771926

n/m	d	sets	Set items	s (plain text)	Summations
4/9	3	$A_1$	{799, 983, 342, 767, 152, 577, 242, 663, 441}	2942	342 + 767 + 152 + 577 + 663 + 441
4/9	3	$A_2$	{740, 985, 671, 678, 720, 845, 472, 559, 646}	2942	985 + 678 + 720 + 559
4/9	3	$A_3$	{208, 978, 678, 249, 295, 875, 506, 162, 204}	2942	978 + 678 + 249 + 875 + 162
4/9	3	$A_4$	{711, 109, 183, 474, 250, 893, 534, 771, 926}	2942	711 + 534 + 771 + 926

### 11.5 Conclusion and Future Work

This paper introduces the problem of finding a common subset sum for integrated sets (*MISSP*). The objective is to identify a sum that can be achieved by all sets within a 2D set, if such a sum exists. Additionally, a robust cryptosystem utilizing symmetric private keys was proposed for situations where the numbers and sets are of equal sizes. The implementation of this cryptosystem in a communication application was also discussed.

For future work, we intend to improve the *MISSP* encryption algorithm using some newer results in solving subset problems, such as Refs [20–22], and trying to combine the encryption algorithm in other nonstandard communication protocols such as TOR (Onion Routing) and solve existing problems as described in Ref. [23]. Another interesting aspect of this research is analyzing attack scenarios on this encryption to test its strength. This could help show the robustness of the scheme and demonstrate its strength in juxtaposition to other known encryption schemes.

**Acknowledgments** The authors acknowledge the assistance of Offir Zeevi and Hadar Krispel from Ruppin Academic Center in the implementation of this research and Ruppin Academic Center for its support in the different stages of this research.

### References

- N. Voloch, MSSP for 2-D sets with unknown parameters and a cryptographic application. Contemp. Eng. Sci. 10(19), 921–931 (2017)
- M.R. Garey, D.S. Johnson, Computers and Intractability: A Guide to the Theory of NP-Completeness (W.H. Freeman, 1979) ISBN 0-7167-1045-5.A3.2: SP13, p. 223
- 3. T.H. Cormen, C.E. Leiserson, R.L. Rivest, C. Stein, 35.5: The subset-sum problem, in *Introduction to Algorithms*, 2nd edn., (MIT Press and McGraw-Hill, (2001) [1990])
- E. Horowitz, S. Sahni, Computing partitions with applications to the knapsack problem. J. Assoc. Comput. Mach. 21, 277–292 (1974)
- D. Pisinger, Linear Time Algorithms for Knapsack Problems with Bounded Weights. Journal of Algorithms 33(1), 1–14 (1999)
- K. Koiliaris, C. Xu, AA Faster Pseudopolynomial Time Algorithm for Subset Sum. arXiv:1507.02318 (2015)
- D.S. Johnson, Approximation algorithms for combinatorial problems. J. Comput. Syst. Sci. 9(3), 256–278 (1974)
- H. Kellerer, R. Mansini, U. Pferschy, M.G. Speranza, An efficient fully polynomial approximation scheme for the subset-sum problem, in *Proceedings of the 8th ISAAC Symposium*, Springer Lecture Notes in Computer Science, vol. 1350, (1997), pp. 394–403
- A. Caprara, H. Kellerer, U. Pferschy, The multiple subset sum problem. SIAM J. Optim. 11(2), 308–319 (2000)
- G.J. Woeginger, Y. Zhongliang, On the equal-subset-sum problem. Inf. Process. Lett. 42(6), 299–302 (1992)
- M. Cieliebak, S. Eidenbenz, A. Pagourtzis, K. Schlude, On the complexity of variations of equal sum subsets. Nordic. J. Comput. 14(3), 151–172 (2008)

- 12. C. Bazgan, M. Santha, Z. Tuza, Efficient approximation algorithms for the subset-sums equality problem, in *International Colloquium on Automata, Languages, and Programming*, (Springer, Berlin/Heidelberg, 1998), pp. 387–396
- M.M. Karimov, N.N.U. Ochilov, A.E. Tangirov, Encryption methods and algorithms based on domestic standards in open-source operating systems. WSEAS Trans. Inf. Sci. Appl. 20, 42–49 (2023)
- 14. N. Chahin, A. Mansour, Improving the IoT and cloud computing integration using hybrid encryption. WSEAS Trans Des Constr Maint 3, 1–6 (2023)
- 15. R. Merkle, M. Hellman, Hiding information and signatures in trapdoor knapsacks. IEEE Trans. Inf. Theory **24**(5), 525–530 (1978)
- S. Martello, P. Toth, 4 Subset-sum problem, in Knapsack Problems: Algorithms and Computer Interpretations, (Wiley-Interscience, 1990), pp. 105–136
- A. Shamir, A polynomial-time algorithm for breaking the basic Merkle Hellman cryptosystem. IEEE Trans. Inf. Theory 30(5), 699–704 (1984)
- A. Kate, I. Goldberg, Generalizing cryptosystems based on the subset sum problem. Int. J. Inf. Secur. 10(3), 189–199 (2011)
- 19. https://github.com/nadavvoloch/SUSU\_encryption/
- A. Antonopoulos, A. Pagourtzis, S. Petsalakis, M. Vasilakis, Faster algorithms for k-SUBSETSUM and variations, in *Frontiers of Algorithmics: International Joint Conference*, *IJTCS-FAW 2021, Beijing, China, August 16–19, 2021, Proceedings*, (Springer, Cham, 2022), pp. 37–52
- N. Melissinos, A. Pagourtzis, A faster FPTAS for the subset-sums ratio problem, in Computing and Combinatorics: 24th International Conference, COCOON 2018, Qing Dao, China, July 2-4, 2018, Proceedings 24, (Springer, 2018), pp. 602–614
- 22. A. Antonopoulos, A. Pagourtzis, S. Petsalakis, M. Vasilakis, Faster algorithms for k-subset sum and variations. J. Comb. Optim. **45**(1), 1–21 (2023)
- N. Voloch, M.M. Hajaj, Handling exit node vulnerability in onion routing with a zero-knowledge proof, in *Information integration and web intelligence: 24th international conference, iiWAS 2022, virtual event, November 28–30, 2022, proceedings*, (Springer Nature Switzerland, Cham, 2022), pp. 399–405

# Chapter 12 State Feedback Controller of a Self-Balancing Bicycle



I. I. Siller-alcalá, J. U. Liceaga-Castro, R. A. Alcántara-ramírez, and S. Calzadilla-Ayala

### 12.1 Introduction

In the last two decades, scientists have focused on achieving the goal of balancing a two-wheeled bicycle. The problem of unmanned balancing the bicycle at a certain speed or zero speed is very attractive to systems control researchers [1–3], because it presents two interesting problems for this community: the system is unstable and the presence of disturbances. To solve these problems, authors usually use a robust control algorithm and mechanical devices, such as flywheels or gyroscopes to add them to the bicycle to stabilize it at zero speed wheel [4–11].

In this work, the prototype of an autonomous bicycle is stabilized at zero speed, so the bicycle is treated as an inverted pendulum. This prototype is one of the three mechatronic systems that can be assembled using a kit called "Arduino Engineering Kit Rev2" [11], developed by Mathworks and Arduino. The two control strategies selected to stabilize the bicycle are PID and state feedback controllers. These controllers were chosen for easy implementation, because they are well suited for an engineering context. Additionally, the state feedback controller is a natural option, because the prototype allows access to all process states. In this context, the article is divided into the following sections: In Sect. 12.2, the dynamic model of the self-balancing bicycle based on the Lagrange formalism that also includes the actuator electric DC motor is presented. In Sect. 12.3, the designs of the PID controller and the state feedback controller are shown. In Sect. 12.4, the performance of the designed controllers is verified through simulations and the implementation of the controller. Finally, in Sect. 12.5, the conclusion of the research is presented.

I. I. Siller-alcalá (⊠) · J. U. Liceaga-Castro · R. A. Alcántara-ramírez · S. Calzadilla-Ayala Departamento de Electrónica, Área de Control de Procesos, Universidad Autónoma Metropolitana, México D.F., México

e-mail: sai@azc.uam.mx

# 12.2 Mathematical Model of a Self-Balancing Bicycle

In this section, the model of the unmanned bicycle system is presented, the development is based on the principle of the inertial wheel pendulum to obtain simplified Lagrange dynamic equations. Subsequently, the nonlinear differential equations are linearized at an equilibrium point. These linear differential equations are the basis for carrying out the design of the two linear controller approaches. The bicycle to be stabilized is shown in Fig. 12.1.

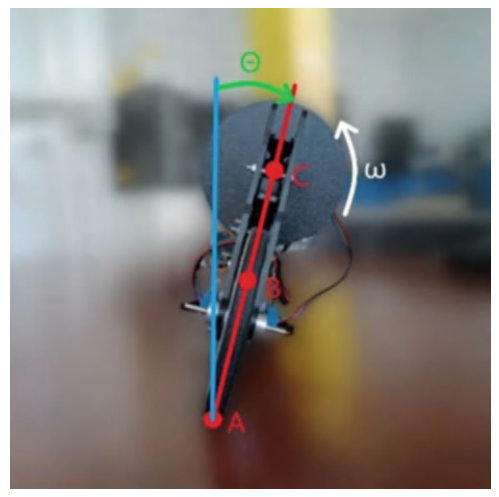
To obtain the equations that describe the dynamics of the system, a behavior alike an inverted pendulum with a flywheel is assumed.

The variables and coordinate system that were used are shown in Fig. 12.2, from the front view of the robotic bicycle, where:

**Fig. 12.1** Complete robotic bicycle



Fig. 12.2 Front view of the robotic bicycle and reference coordinate system.



 $\theta$ : It is the angle of inclination of the robotic bicycle concerning the vertical axis.

 $\omega$ : It is the angular velocity of the flywheel or reaction wheel.

A: It is the axis of rotation of the inverted pendulum, in this case, the robotic bicycle.

B: It is the center of mass of the robotic bicycle.

First, the model of the electric DC motor actuator is developed. Using the basic circuit that represents a DC motor, the equation below is obtained as follows:

$$V = R_a i_a + L_a \frac{di_a}{dt} + E_a \tag{12.1}$$

where V is the motor supply voltage,  $R_a$  and  $L_a$  are the armature coil resistance and inductance, respectively,  $i_a$  is the armature current, and  $E_a$  is the counter-electromotive force, given by the following equation:

$$E_a = K_a \omega \tag{12.2}$$

where  $\omega(t)$  is the rotor and therefore flywheel angular velocity, and  $K_a$  is the electromotive constant. In DC motors, it is generally assumed that the generated torque is proportional to the current provided; this relationship is illustrated in the following equation:

$$\tau_m = K_m i_a \tag{12.3}$$

where  $\tau_m(t)$  is the torque generated by the motor and  $K_m$  is the torque constant of the motor; the following equation is obtained by substituting (12.1) into (12.3):

$$\tau_m = \frac{K_m}{R_a} \left( V - L_a \frac{di_a}{dt} - E_a \right) \tag{12.4}$$

It is considered that the term corresponding to the inductance  $L_a$  can be neglected, since its value is much lower than that of the resistance  $R_a$ , considering this and substituting (12.2) into (12.4), the following equation is obtained:

$$\tau_m = \frac{K_m}{R_a} \left( V - K_a \omega \right) \tag{12.5}$$

Using the Lagrange formalism, the following equations that describe the mechanical dynamics of the system are given.

The torque about a given axis of rotation is the sum of all the torques that act in the system on this axis and is defined as:

$$\tau_N = \sum \tau_{si} = I_s \ddot{\theta}_s \tag{12.6}$$

where.

 $\tau_N$ : It is the net torque applied to the axis of rotation.

 $\tau_{si}$ : These are the torques applied on the axis of rotation.

 $I_s$ : Moment of inertia of the system.

 $\ddot{\theta}_s$ : Angular acceleration of the system.

If no external torque acts on the robotic bicycle, other than that due to gravitational acceleration, we have two torques that act on the bicycle:

 $\tau_g$ : Torque due to gravitational acceleration.

 $\tau_{vi}$ : Torque due to the flywheel.

Therefore, the net torque on the bicycle with respect to the axis of rotation A, Fig. 12.2, results in:

$$\tau_{Bnet} = I_B \ddot{\theta} = \tau_g - \tau_{vi} \tag{12.7}$$

where  $I_B$  is the moment of inertia of the bicycle. The torque provided by the flywheel, which in turn is generated by the DC motor, must be of equal magnitude but in the opposite direction to the torque  $\tau_g$ , in such a way that the angular momentum of the robotic bicycle is conserved. Expanding the terms of Eq. (12.7), we obtain:

$$I_B \ddot{\theta} = m_b g l_{AB} \operatorname{sen}(\theta) + m_{vi} g l_{AC} \operatorname{sen}(\theta) - I_{vi}^C \dot{\omega}$$
 (12.8)

The torque  $\tau_{vi}$  provided by the flywheel can be described by the following equation:

$$\tau_{vi} = I_{vi}^{C} \left( \dot{\omega} + \ddot{\theta} \right) \tag{12.9}$$

Subsequently, adding Eqs. (12.5) to (12.8) and (12.9), we obtain:

$$I_B \ddot{\theta} = m_b g l_{AB} \operatorname{sen}(\theta) + m_{vi} g l_{AC} \operatorname{sen}(\theta) - \left( \frac{K_m}{R_a I_{vi}^C} \left( V - K_a \omega \right) - I_{vi}^C \ddot{\theta} \right)$$
(12.10)

$$\tau_{vi} = 0.5 m_{vi} R^2 \left( \dot{\omega} + \ddot{\theta} \right) = \tau_m = \frac{K_m}{R_a} \left( V - K_a \omega \right) v \tag{12.11}$$

Defining states  $x_1 = \theta$ ,  $x_2 = \theta'$ ,  $x_3 = \omega$ , and linearizing the nonlinear Eqs. (12.10) and (12.11) around the equilibrium point:  $x_1 = 0$ ,  $x_2 = 0$ ,  $x_3 = 0$ , the state space representation,  $\dot{X} = AX + Bu$ , y = CX, for this system dynamic is given by:

$$\begin{bmatrix} \dot{x}_{1} \\ \dot{x}_{2} \\ \dot{x}_{3} \end{bmatrix} = \begin{bmatrix} 0 & 1 & 0 \\ \frac{m_{B}gI_{AB} + m_{vi}gI_{AC}}{I_{B} - I_{vi}^{C}} & 0 & \frac{K_{m}K_{a}}{R_{a}(I_{B} - I_{vi}^{C})} \\ -\frac{m_{b}gI_{AB} + m_{vi}gI_{AC}}{I_{B} - I_{vi}^{C}} & 0 - \frac{K_{m}K_{a}I_{B}}{I_{vi}^{C}R_{a}(I_{B} - I_{vi}^{C})} \end{bmatrix} \begin{bmatrix} x_{1} \\ x_{2} \\ x_{3} \end{bmatrix} + \begin{bmatrix} 0 \\ -\frac{K_{m}}{R_{a}(I_{B} - I_{vi}^{C})} \\ \frac{K_{m}I_{B}}{I_{vi}^{C}R_{a}(I_{B} - I_{vi}^{C})} \end{bmatrix}$$

$$y = \begin{bmatrix} 1 & 0 & 0 \end{bmatrix} \begin{bmatrix} x_{1} \\ x_{2} \\ x_{3} \end{bmatrix}$$

$$(12.12)$$

Substituting the values of the parameters provided by the prototype maker (Table 12.1), we obtain the state space linear model:

$$\begin{bmatrix} \dot{x}_1 \\ \dot{x}_2 \\ \dot{x}_3 \end{bmatrix} = \begin{bmatrix} 0 & 1 & 0 \\ 96.5795 & 0 & 0.0195 \\ -96.5795 & 0 & -0.6608 \end{bmatrix} \begin{bmatrix} x_1 \\ x_2 \\ x_3 \end{bmatrix} + \begin{bmatrix} 0 \\ -1.0241 \\ 34.7768 \end{bmatrix} u$$

$$y = \begin{bmatrix} 1 & 0 & 0 \end{bmatrix} \begin{bmatrix} x_1 \\ x_2 \\ x_3 \end{bmatrix}$$
(12.13)

**Table 12.1** Dynamic parameters

Parameter	Value
g	9.8067 m/s <sup>2</sup>
$I_b^A$	0.00169 kg·m <sup>2</sup>
$I_b^B$	0.000445 kg·m <sup>2</sup>
$I_{vi}^A$	0.00126 kg·m <sup>2</sup>
$I_{vi}^C$	0.00008687 kg·m <sup>2</sup>
1	0.13 m
$l_{AB}$	0.065 m
$l_{AC}$	0.13 m
$\overline{l_{AD}}$	0.13 m
$m_b$	0.2948 kg
$m_{vi}$	0.0695 kg
r	0.02 m
R	0.05 m
$\overline{I_B}$	0.00295 kg·m <sup>2</sup>
$K_m$	0.019 N*m/A
$K_a$	0.019 V*s/rad
$R_a$	6.48 Ω

# 12.3 Control Design

In this section, the design of two linear controllers is presented. The PID and state feedback controllers were chosen. Both controllers were chosen mainly because of their well-proven effectiveness, for the PID controller, and because there is complete access to the state vector, in the case of state feedback controller. Also, both controllers are easy to implement and are well suited for engineering context.

# 12.3.1 PID Control Design

The Transfer Function associated to the linear state space mode of Eq. (12.13) is as follows:

$$G(s) = \frac{-1.024s}{s^3 + 0.6608s^2 - 96.5795s - 61.9366}$$
(12.14)

Rewriting the above equation:

$$G(s) = \frac{-1.024s}{(s - 9.818)(s + 9.838)(s + 0.6412)}$$
(12.15)

The system is unstable with a pole at 9.818, two stable poles  $\{9.838, 0.6412\}$ , and a zero at zero. The root locus of G(s) is presented in Fig. 12.3.

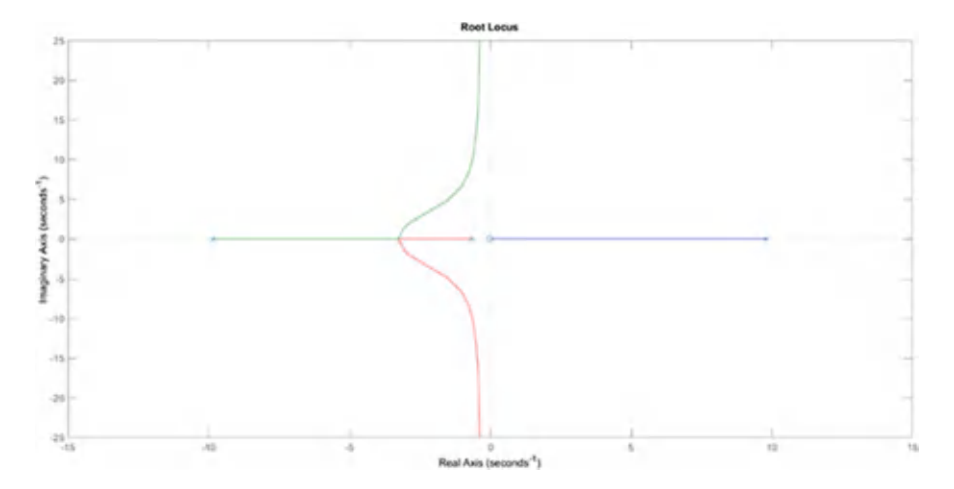


Fig. 12.3 Root locus of G(s)

The closed-loop poles lie on the right-half of s plane making the system unstable. In addition, there is zero at the origin, which becomes an uncomfortable issue, because it represents a derivative behavior in the system and may impel to stabilize the system using a PID controller.

From the observations made to the graph of the root locus of the system, the following transfer function was designed for the bicycle's PID controller:

$$C(s) = \frac{s^2 + 10s + 30}{s} \tag{12.16}$$

The pole at the origin in C(s) has the purpose of removing the origin zero in G(s), while the complex conjugate zeros must be responsible for determining the trajectory of the root locus, so that, with a certain gain, all the poles will lie on the left-hand plane. The transfer function of the open-loop system is given by:

$$G_{LA}(s) = C(s)G(s) = \frac{-1.024s^3 - 10.24s^2 - 30.72s}{s^4 + 0.661s^3 - 96.58s^2 - 61.94s}$$
(12.17)

The roots of the closed-loop system can be analyzed by using the root locus.

As seen in the graph in Fig. 12.4, when adding the controller, the roots locus changes according to plan, with a gain greater than 11.7, the closed-loop poles will lie in the left half-plane, so the system becomes closed-loop stable. However, a stable closed-loop pole close to the origin may affect the performance of the control

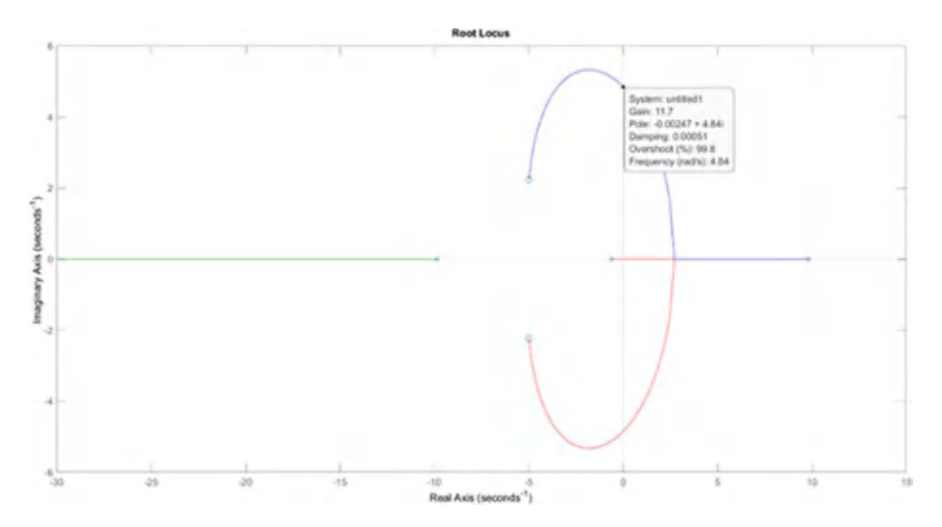


**Fig. 12.4** Root locus of  $G_{LA}(s)$ 

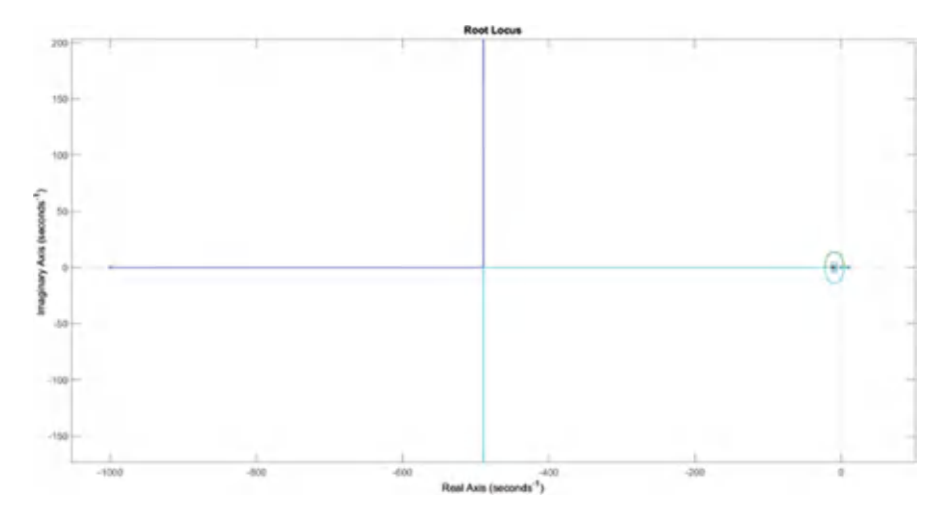


Fig. 12.5 Root locus with new controller

system due to its very large steady-state time. Therefore, redesigning the controller to reduce the steady-state time of the dominant pole results in:

$$C(s) = \frac{s^2 + 20s + 104}{0.001s^2 + s}$$
 (12.18)

With this new controller design, the root locus is shown in Fig. 12.5.

In this graph, it is observed that the pole introduced by the controller at -1000 causes one of the poles closest to the origin to move away, and finally around -500 both poles separate from the real axis symmetrically.

Figure 12.6 shows a close-up of the trajectories of the poles that are closest to the origin.

Finally, a gain of 28 has been chosen, so that the poles are in the left half-plane, thereby ensuring the stability of the system.

To assess the performance of the control system based on the controller of Eq. (12.18), a digital simulation based on the nonlinear model of Eqs. (12.10) and (12.11), assuming an obvious reference signal of  $o^{\circ}$  and constant disturbances of  $\pm 6^{\circ}$  with a frequency of 0.5 rad/s. Figure 12.7 shows that controller (12.18) stabilizes the system with an excellent disturbance rejection achieving the objective.

# 12.3.2 Pole Placement State Feedback Control Design

It is well-known that the stability and control performance of a closed-loop system depends on its pole locations. In this section, the pole placement method will be

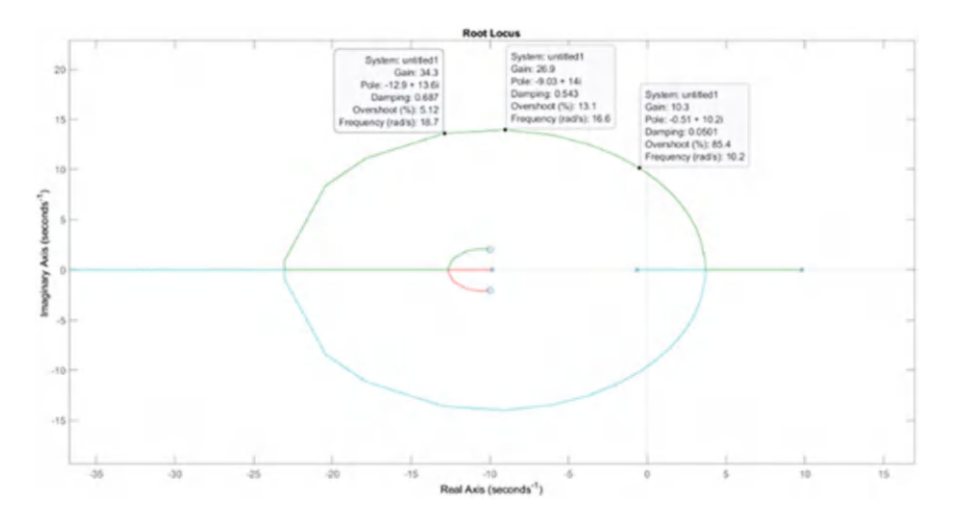


Fig. 12.6 Root locus with new controller

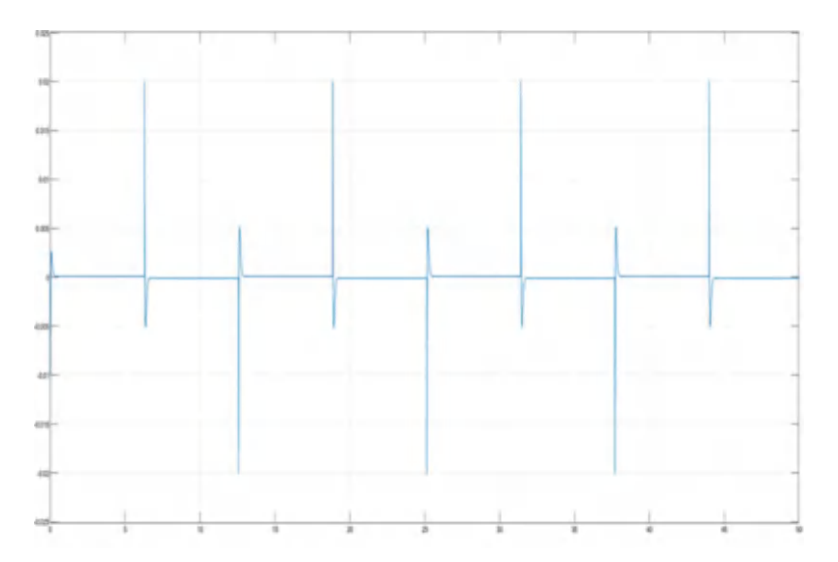


Fig. 12.7 Output signal corresponding to the inclination angle

used to place the poles of the closed-loop system in the desired positions by state feedback controller. To achieve this, the sufficient and necessary condition for the existence of the state feedback controller is that the system must be controllable.

To know if this system, represented by the state Eqs. (12.12), is controllable, it is necessary to check that the controllability matrix  $C_M$  is full range. For this system, the matrix  $C_M$  is defined as:

$$C_M = \left[ B \ AB \ A^2B \right] \tag{12.19}$$

The rank of the controllability matrix is equal to the number of linearly independent rows or columns; therefore, the  $C_M$  matrix is full rank, if its determinant is different from zero.

The controllability matrix of this system:

$$C_{M} = \begin{bmatrix} 0 & \frac{K_{m}K_{a}}{R_{a}(I_{B}-I_{vi}^{C})} & \frac{K_{m}^{2}K_{a}I_{B}}{I_{vi}^{C}R_{a}^{2}(I_{B}-I_{vi}^{C})^{2}} \\ -\frac{K_{m}}{R_{a}(I_{B}-I_{vi}^{C})} & \frac{K_{m}^{2}K_{a}I_{B}}{I_{vi}^{C}R_{a}^{2}(I_{B}-I_{vi}^{C})^{2}} & -\frac{(m_{b}gI_{AB}+m_{vi}gI_{AC})K_{m}I_{vi}^{C^{2}}R_{a}^{2}(I_{B}-I_{vi}^{C})+K_{m}^{3}K_{a}^{2}I_{B}^{2}}{I_{vi}^{C^{2}}R_{a}^{3}(I_{B}-I_{vi}^{C})^{3}} \\ -\frac{K_{m}I_{B}}{I_{vi}^{C}R_{a}(I_{B}-I_{vi}^{C})} & -\frac{K_{m}^{2}K_{a}I_{B}^{2}}{I_{vi}^{C^{2}}R_{a}^{2}(I_{B}-I_{vi}^{C})^{2}} & \frac{(m_{b}gI_{AB}+m_{vi}gI_{AC})K_{m}I_{vi}^{C^{3}}R_{a}^{2}(I_{B}-I_{vi}^{C})+K_{m}^{3}K_{a}^{2}I_{B}^{3}}{I_{vi}^{C^{3}}R_{a}^{3}(I_{B}-I_{vi}^{C})^{3}} \end{bmatrix}$$

$$(12.20)$$

The determinant is given by:

$$|C_M| = \frac{(m_b g l_{AB} + m_{vi} g l_{AC}) K_m^3}{R_a^3 I_{vi}^C (I_B - I_{vi}^C)^3} = 143.5352 \times 10^3.$$
 (12.21)

Since the determinant of  $C_M$  is not zero, its rank is equal to 3, equal to the order of the system; so, the system is controllable, and therefore, state feedback control exists.

The system dynamics given by (12.13) are used for the design of the linear controllers as follows.

Let the control given by:

$$u = r - kx \tag{12.22}$$

where u is the control signal, r is the reference signal, and k is the state feedback gain vector.

The closed-loop system is as follows:

$$\dot{x} = (A - Bk) x + Br;$$
  

$$y = Cx$$
(12.23)

Rewriting:

$$\dot{x} = A_{LC}x + Br$$

$$v = Cx$$
(12.24)

where  $A_{LC} = A - Bk$ , and the input is the reference r.

The state feedback gain vector k should be chosen in such a way that eigenvalues are placed on the desired closed-loop poles.

The position of the closed-loop poles was chosen according to the following equation:

$$(s+10)(s+5)(s+1) = s^3 + 16s^2 + 65s + 50 = 0$$
 (12.25)

That is, with a dominant overdamped closed-loop pole at -1. The two non-dominant poles at  $\{-5, -10\}$  were chosen trying not to obtain excessive high-state feedback gains, as this may render saturation on the system input signal.

The state feedback gain vector k obtained is given by:

$$k = [-157.799, -16.1466, -0.03441]$$
 (12.26)

Digital simulations are presented to show the efficiency of the controller, and the following model in Simulink simulates the state feedback control system composed of:

$$\begin{bmatrix} \dot{x}_1 \\ \dot{x}_2 \\ \dot{x}_3 \end{bmatrix} = \begin{bmatrix} 0 & 1 & 0 \\ 96.5795 & 0 & 0.0195 \\ -96.5795 & 0 & -0.6608 \end{bmatrix} \begin{bmatrix} x_1 \\ x_2 \\ x_3 \end{bmatrix} + \begin{bmatrix} 0 \\ -1.0241 \\ 34.7768 \end{bmatrix} u$$

$$y = \begin{bmatrix} 1 & 0 & 0 \end{bmatrix} \begin{bmatrix} x_1 \\ x_2 \\ x_3 \end{bmatrix} \text{ and } u = r - kx$$

$$(12.27)$$

Figures 12.9, 12.10, and 12.11 show the graphs obtained by simulation using the Simulink program shown in Fig. 12.8.

As seen in the graphs of Figs. 12.9, 12.10 and 12.11, the simulations of the state feedback control system show good performance. Although the state initial conditions that were implemented in the integrators (Fig. 12.10) start from nonideal or initial conditions values, the controller was capable of taking the output to 0, maintaining bicycle balance.

In Fig. 12.11, it is observed that the control signal, which represents the voltage that would be applied to the DC motor of the flywheel, has a very large magnitude, and this is because the states begin with values far from ideals.

To show the performance of the state feedback controller, in the presence of output angle variations, with magnitudes that could occur in the real model, a disturbance was added to the diagram in Fig. 12.8 in state  $x_1 = \theta$ , which corresponds to the tilt angle of the system, as shown in Fig. 12.12.

The disturbance is a pulse with an amplitude of 0.1745, which would correspond to an inclination of  $10^{\circ}$ . Furthermore, it occurs 6 s after the simulation starts and has a duration of 0.1 s. Figure 12.13 shows the graphs of the simulation carried out.

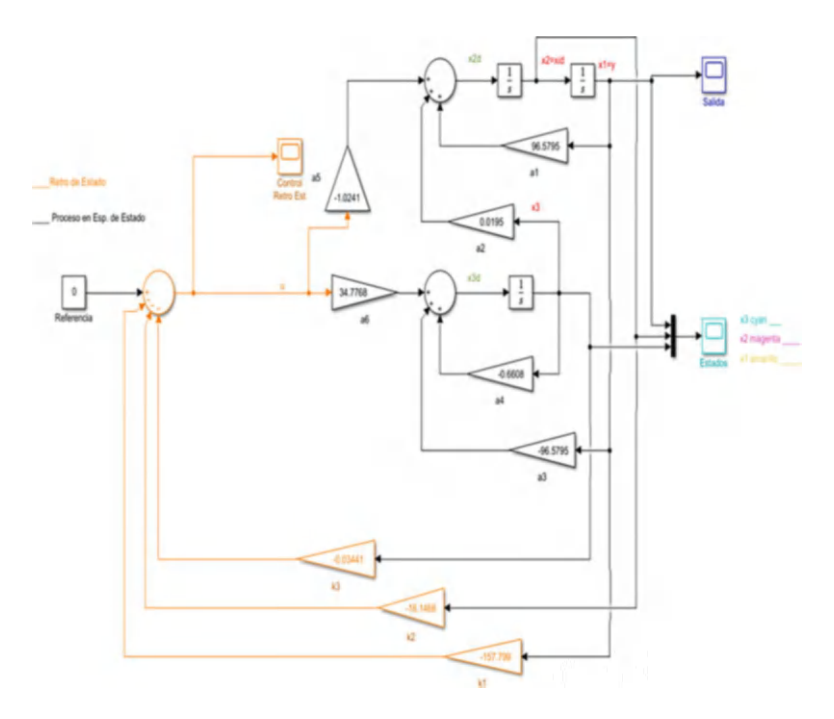


Fig. 12.8 Simulink diagram of the bicycle state feedback control system

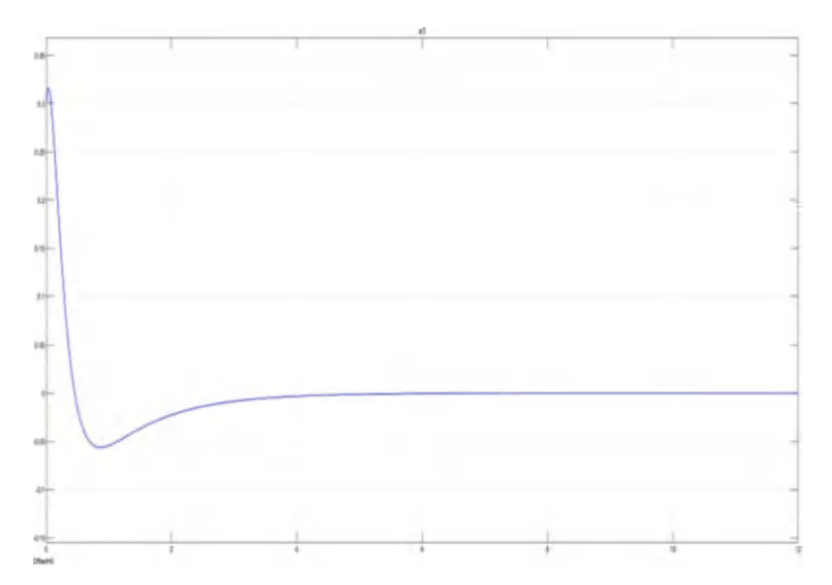
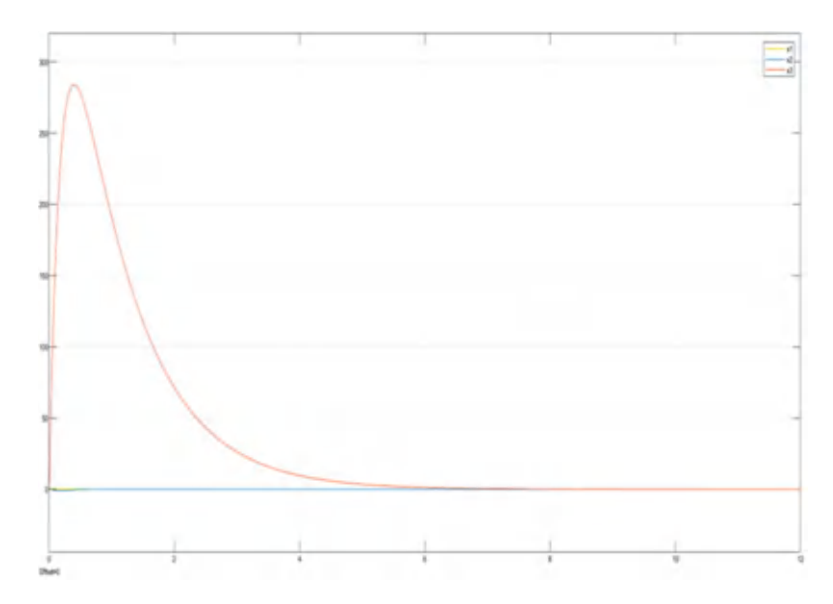


Fig. 12.9 System output that corresponds to the system inclination angle



**Fig. 12.10** System states:  $x_1 = \theta$  (orange line),  $x_2 = \theta$  (blue line),  $x_3 = \omega$  (red line)

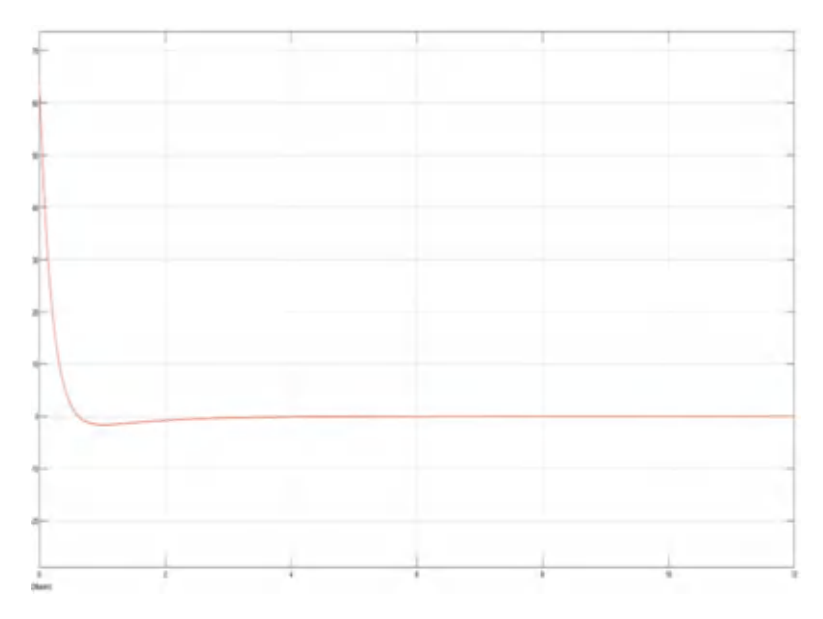


Fig. 12.11 State feedback control signal

With the results of this second simulation of Figs. 12.13, 12.14 and 12.15, it was confirmed that the feedback system behaves correctly. The effort made by the controller, which is observed in Fig. 12.14, is because the disturbance signal

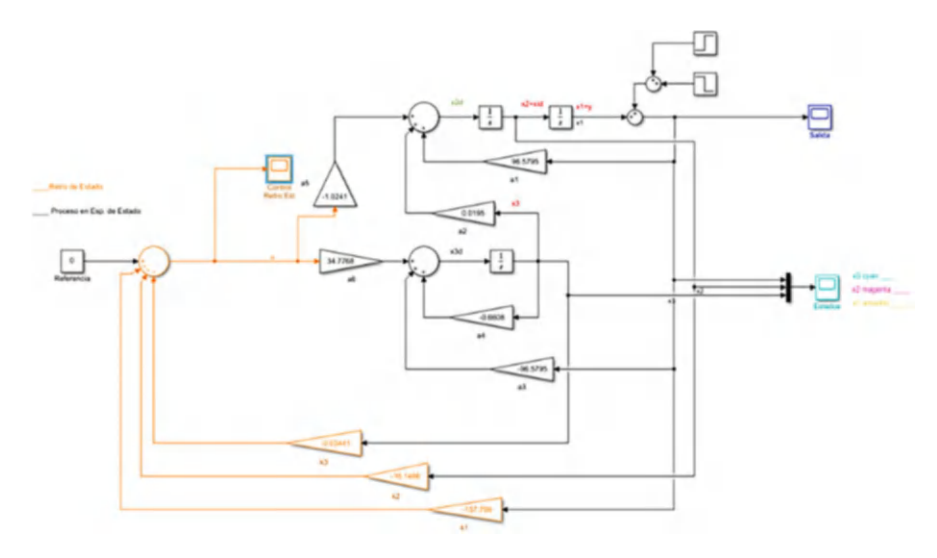
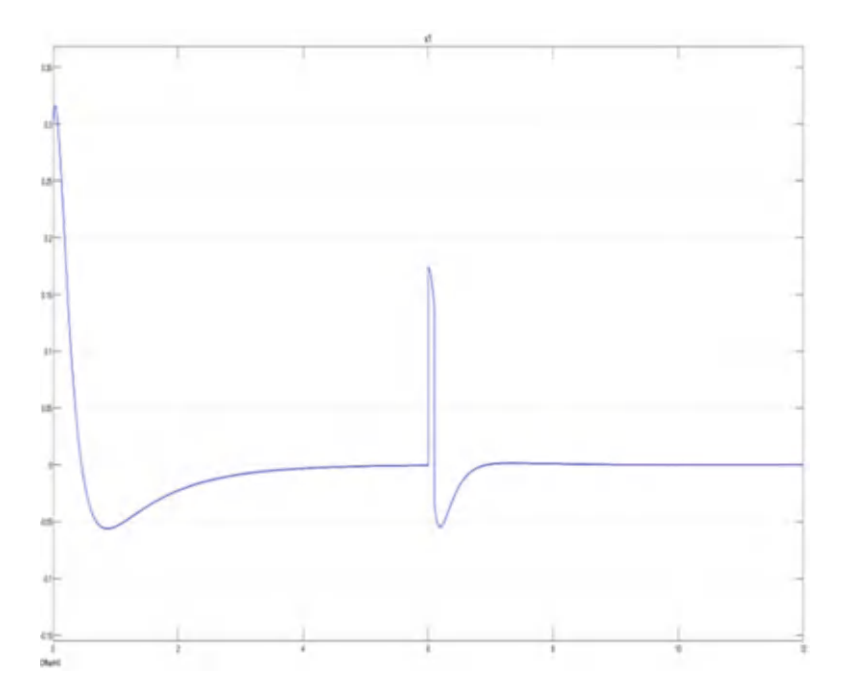
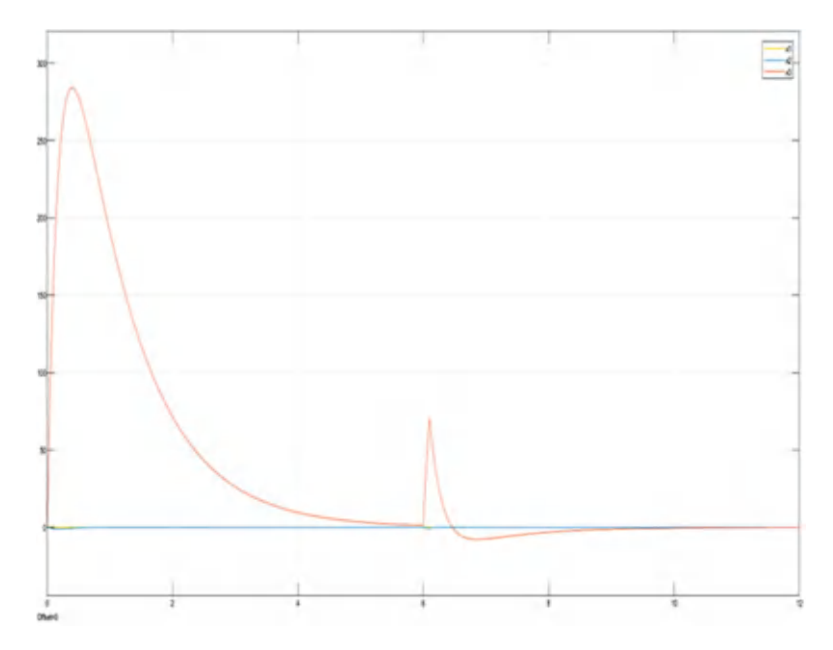


Fig. 12.12 Simulink diagram of the bicycle state feedback control system with perturbations in state  $x_1=\theta$ 



 ${\bf Fig.~12.13~}$  System output that corresponds to the system inclination angle in the presence of perturbation



**Fig. 12.14** System states:  $x_1 = \theta$  (orange line),  $x_2 = \theta$  (blue line),  $x_3 = \omega$  (red line) in the presence of perturbation

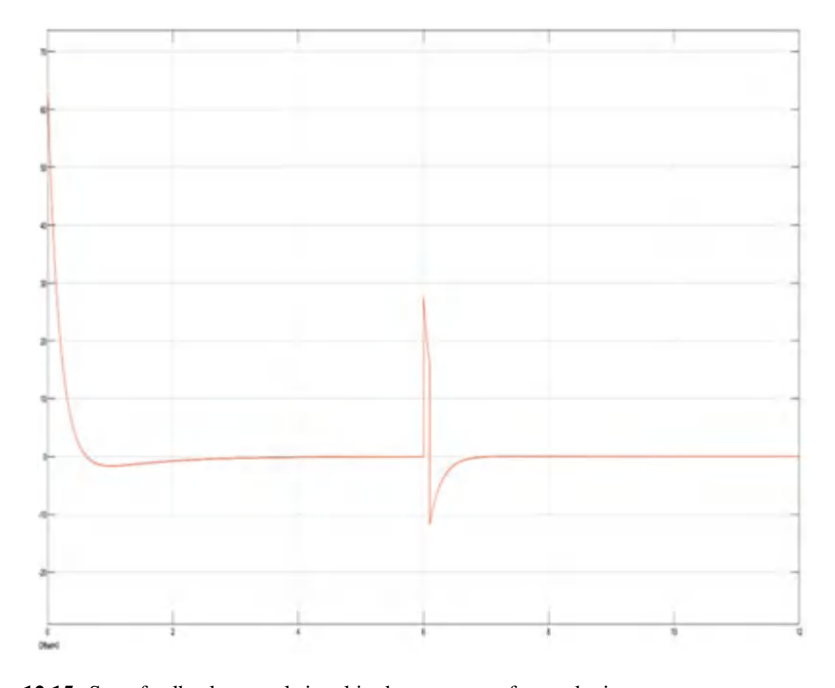


Fig. 12.15 State feedback control signal in the presence of perturbation

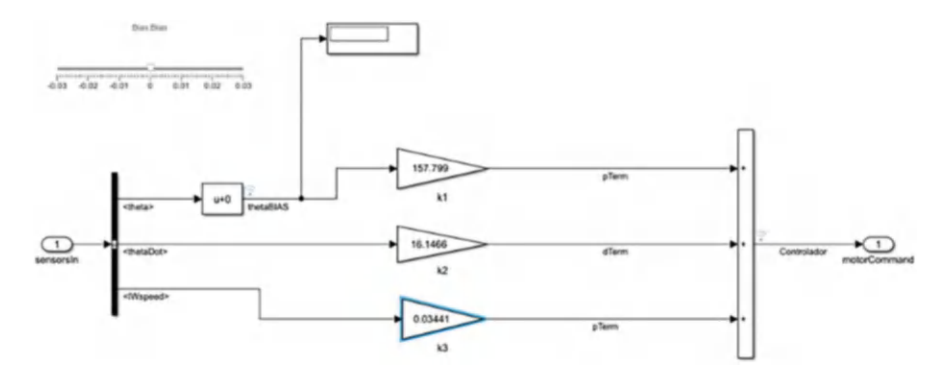


Fig. 12.16 Implementation of the state feedback controller

is square, but the disturbances or changes in the inclination angle of the real system are not so abrupt, so it was considered that the feedback loop behaves correctly.

# 12.4 Implementation of the State Feedback Controller

The software configuration shown in Fig. 12.16 provided by Arduino [11] for the operation of the bicycle has the advantage that the state feedback controller designed in this work is easily implemented. The software configuration was developed using Matlab's Simulink, with the sampling time used equal to T = 0.01 s.

Figure 12.17 shows the graphics of the results: inclination angle  $\theta$ , inclination angle rate  $\theta$ , angular velocity of the flywheel  $\omega$ , and the control signal produced by the state feedback controller.

Figure 12.17 shows that the state feedback controller can maintain bicycle verticality under real-time conditions, that is, with initial conditions far from the ideal and sensor noise. This explains the high-frequency components and the almost "chattering" control signal behavior. Excessive control effort could be reduced, if dominant closed-loop poles are placed with larger steady-state time, although this could reduce the possibility of reaching stability. That is, the bicycle could lose verticality, before the controller has enough time to recover it.

### 12.5 Conclusions

The PID and state feedback controllers were designed to stabilize a self-balancing bicycle. These controllers were chosen because of their well-proven effectiveness, simplicity, and easy implementation.

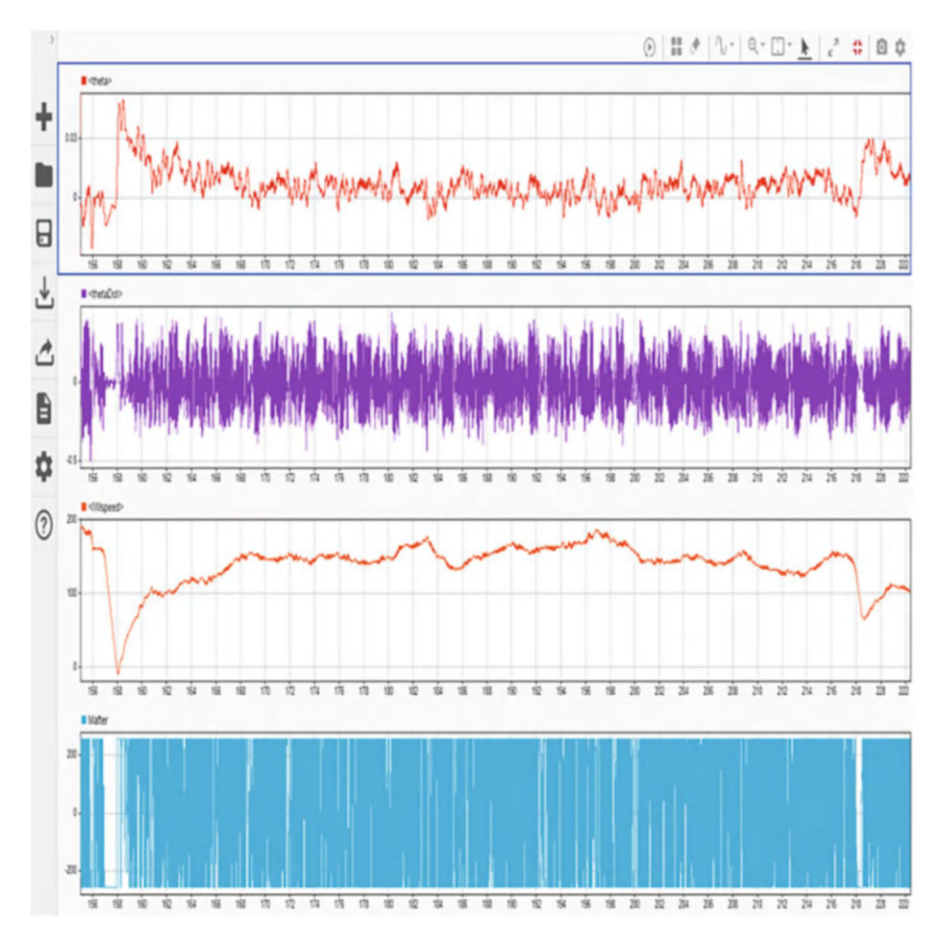


Fig. 12.17 Signals provided by the bicycle sensors while it is balancing:  $\theta$  (red line),  $\dot{\theta}$  (purple line),  $\omega$  (orange line), and control signal u (blue line)

However, the real-time implementation of the PID controller could not be carried out, due to the cancelation of the pole at the origin; that is, the exact pole/zero cancellation at zero could not be guaranteed due to the approximation of the integral action in a digital implementation, obtaining an unstable response. Further analysis or a more complex linear controller is required to avoid canceling the process zero at zero. On the other hand, the state feedback controller has excellent behavior without the need for cancellations. Although it does not include an integral action, it achieves the desired outputs, because the signal reference is r=0, and the state feedback assures exponential and asymptotical stability in all the states, so  $x_1=\theta \to 0$ . Therefore, the bicycle maintains verticality.

Nevertheless, and taking advantage of having access to the entire state vector, it would be advisable to design and implement a nonlinear state feedback control such

as "Back Stepping" control. In this way, a more direct control could be designed for each state. However, as shown by Eqs. (12.10), (12.11), and (12.15), this may not be a simple task as the system degree is 3 while its relative degree is 2. Also, Sliding Mode control with "super twist" could be analyzed.

## References

- 1. P. Govardhan et al., Survey on self-balancing two-wheel electric prototype. Int. J. Eng. Res. Gen. Sci 5(5), 32–36 (2017)
- 2. C.-H. Chiu, W. Chi-Yuan, Bicycle robot balance control based on a robust intelligent controller. IEEE Access 8, 84837–84849 (2020)
- L. Chen et al., Extreme-learning-machine-based robust integral terminal sliding mode control of bicycle robot. Control. Eng. Pract. 121, 105064 (2022)
- S.H. Park, S.Y. Yi, Active balancing control for unmanned bicycle using scissored-pair control moment gyroscope. Int. J. Control. Autom. Syst. 18, 217–224 (2020)
- 5. Y. Liu et al., Self-balance control of bicycle with inertial wheel pendulum based on linear ADRC, in 2022 China Automation Congress (CAC), (IEEE, 2022)
- W. Deng et al., Towards automated bicycles: Achieving self-balance using steering control, in *Dynamic Systems and Control Conference*, vol. 51906, (American Society of Mechanical Engineers, 2018)
- Z. Yongli, Y. Liu, G. Yi, Model analysis of unmanned bicycle and variable gain lqr control, in 2020 IEEE 9th Joint International Information Technology and Artificial Intelligence Conference (ITAIC), vol. 9, (IEEE, 2020)
- 8. N. He et al., Self-balancing bicycle based on control moment gyroscope, in 2023 42nd Chinese Control Conference (CCC), (IEEE, 2023)
- 9. S. He, J. Zeng, Y. Guan, Self-balance control of an Essboard-like Robot with a Flywheel, in 2022 IEEE International Conference on Mechatronics and Automation (ICMA), (IEEE, 2022)
- N. Marios Patsouras, Modelling and Control of a Self-Balancing Motorcycle, Diploma Thesis, University of Thessaly, School of Engineering, Department of Mechanical Engineering, Greece, 2022
- Arduino Education, Kit de Ingeniería Arduino Rev2, Arduino, 2021. https://www.arduino.cc/education/engineering-kit

# **Index**

A Acoustic NDE, 1–14 After pandemic, 113, 125 Artificial intelligence for biomedical	Dependent subsets, 20 Diagnosis, 2, 12
engineering	E Efficiency, 20, 34, 53, 54, 58, 62, 63, 149, 167 Encryption, 147–155
В	Energy, 51–57, 59, 61–63, 129
Balancing control, 157–174	Excess demand, 113–115, 118, 119, 125
Best Master Clock Algorithm (BMCA), 41–48	Extended frequency (EF), 71, 72, 76, 77, 79, 97–99, 102–105, 107, 108, 110
Bicycle robot, 158–160 Bile acid loss, 33–39	
Bounded homomorphisms, 26	F
B-splines, 130, 131, 137, 144	Finitely generated abelian groups, 27 Fractional Gaussian noise (fGn), 41–48
c	
Clustering evaluation, 87–88	G
Clustering metrics, 85–94	Generalized frequency of Milano, 71, 72,
Clustering sensitivity, 85–94	74–75, 77, 80–82, 97–99, 101–102,
Clustering uncertainty	104, 105, 109, 110
Communication, 19, 41, 42, 147–155 Composite materials, 2	Geometric algebra, 71–74, 78, 79, 98–100, 105–107
Composite technology	Geometric algebra valued vector bundle, 71,
Computational algebra	72, 78, 80, 82, 97, 98, 103–105, 110
Computational modeling	Geometrical interpretation, 71-82, 97, 98, 105,
Computer modeling	109–110
Cryptography, 149–151	Geometry identification, 130, 132, 135
D	Н
Delaminations, 1–14	Heisenberg groups, 21, 22

© The Editor(s) (if applicable) and The Author(s), under exclusive license to Springer Nature Switzerland AG 2025

N. E. Mastorakis et al. (eds.), *Computational Problems in Science and Engineering II*, https://doi.org/10.1007/978-3-031-78416-3

176 Index

Homomorphic image of a group, 27 Hybrid Probabilistic-Fuzzy optimization, 113–125

#### T

IEEE1588v2 Image filtering, 130, 131, 145 Image processing, 20 Independent subsets, 20 Irrelevant features, 85–94

### K

k-means, 86, 88, 90

### L

Logistics and supply chain management

#### N

Noisy data, 94 Normed geometry NP-complete problems, 147 Numerical methods, 2 Numerical modeling, 114 NURBS, 130, 131, 137, 141, 144, 145

#### O

Order-allocation problem Orthogonal geometry, 82, 97–110

#### P

Packet delay variation (PDV), 4, 41–45, 47 Parametric curves, 130, 137, 141, 144, 145 Photovoltaic (PV), 51–63 Pixel clustering, 130, 134–136, 138 Pooled samples, 33–39 Precision time protocol (PTP), 41–48 Production planning, 113–125

#### R

Reaction wheel, 159 Renewable energy

### S

Scientific computing
Sensitivity, 2, 34, 35, 37, 38, 85–94
Serum 7-alpha-hydroxy-4-cholesten-3-one, 35
Ship hull geometry reconstruction, 129–145
Short bowel syndrome (SBS), 36
Simulation, 3, 5–9, 35, 36, 47, 120–123, 130, 145, 157, 164, 167, 169
Simulation methods for biomedical engineering
Solar, 51–63
Solar power, 51, 52, 62, 63
Specificity, 34, 35, 37, 38
State feedback controller, 157–174
Subset problem, 147–155
Supplier selection

#### T

Tracking, 51–63 2-normed groups, 17–29

#### U

Unsupervised feature selection, 85, 93

#### V

Vector fields on surface, 71, 97